Fundamental study of immiscible Ti-Mg system: ball milling experiments and *ab initio* modelling

By

Maje Jacob Phasha

THESIS submitted in fulfillment of the requirements for the degree of

Doctor of Philosophy

in

Physics

in the

FACULTY OF SCIENCE & AGRICULTURE

(School of Physical & Mineral Sciences)

at the

UNIVERSITY OF LIMPOPO

Supervisors: Prof P.E. Ngoepe

: Dr W Du Preez

2013

DECLARATION

I, Maje Jacob Phasha, declare that the thesis hereby submitted to the University of Limpopo, for the degree of Doctor of Science in Physics, has not previously been submitted by me for a degree at this or any other university; that it is my work in design and in execution, and that all material contained herein has been duly acknowledged.

---------- ----------

Phasha MJ **Date**

DEDICATIONS

This work is dedicated to the following people:

My two adorable children, **Dumisani** and **Ofentse**

My beloved, wonderful & supportive wife **Zanele**

My entire physical and spiritual family.

ACKNOWLEDGEMENTS

First and foremost, I would like to acknowledge my supervisors, Prof. P.E. Ngoepe and Dr W Du Preez for their help, guidance and courageous support throughout the course of my studies. They always had astute words of advice when needed and provided valuable inputs which kept my work on track.

I also like to express my sincere gratitude to A.S. Bolokang, Dr D Mkhonto and Dr Maweja Kasonde, for their honest friendship, fruitful and stimulating scientific discussions. I am also grateful to services of S. Camagu, C. Oliphant and Dr D.E. Motaung, for their help on characterization techniques. The continued support of Dr HR Chauke is also acknowledged.

The Powder Metallurgy group of Light Metals competence area of Materials Science and Manufacturing (MSM) unit within Council for Scientific & Industrial Research (CSIR), is highly acknowledged for providing state-of-the-art laboratory facilities. All the calculations in this work were carried at CSIR as well as Materials Modelling Center (MMC) hosted within the School of Physical and Mineral Sciences, University of Limpopo.

I am indebted to the financial support provided by the National Research Foundation (NRF), Department of Science and Technology (DST) of South Africa and CSIR, without which this study could not have been completed.

Mostly, I am very thankful to my wonderful wife, who stood by through difficult and challenging times, and our lovely children, for their patience throughout the period of my study. Lastly, my colleagues, friends and everyone who might have contributed to the success of this work in one way or another, are duly thanked.

Thanks to you all!

ABSTRACT

A combination of ball milling experiments and *ab initio* calculations in this study successfully yielded results that shed light into understanding the fundamental basis for immiscibility and the concept of mechanical alloying in Ti-Mg system. In addition, the conditions for achieving extended solid solubility in elements that usually do not dissolve in each other under thermodynamic equilibrium conditions have been predicted using ultrasoft (US) and norm-conserving (NC) pseudopotentials. Hydostatic pressures required to stabilize ordered phases were determined. Our new systematic representation of martensitic transformation (MT) paths as a result of dislocation necessary to induce α→FCC, α→BCC and α→ω phase transitions led to, for the first time, a direct determination of CRSS and tensile strength for Ti and Mg HCP metals. Furthermore, a new ω phase which is less stable than α phase at 0 GPa is proposed. Based on this phase, α→ω deformation path which yielded the onset of uniaxial transition pressure of 4.167 GPa is reported.

Attempts of synthesizing Ti-Mg solid solutions by means of Simoloyer high energy ball mill were not successful; however, nanocrystalline Mg-TiH_{2-x} composites were instead formed. These results were attributed to quick formation of metastable Ti hydrides or cold welding at early stages of BM prior to alloying, thus serving as possible obstacles to forming such solid solutions. The deformed Ti crystals adsorbed H^+ from the stearic acid leading to formation of metastable orthorhombic TiH_{2-x} phase which later transformed to a tetragonal TiH_{2-x} or even cubic TiH_2 when stoichiometric amount of H_2 had been adsorbed. Although the yield was significantly lower, the product of milling a mixture of coarse Mg and fine Ti particles was comprised of Ti particles adhering around ductile Mg particles in a core shell manner. The adhesion of the fine hard titanium particles on the surface of the large ductile magnesium particles impeded the further plastic deformation of the titanium particles, thus suppressing the formation of the faults necessary for mechanical alloying.

Nanocrystalline Ti powder of about 40 nm was produced by 30h ball milling. During BM of Ti powder, solid-state transformation from HCP to FCC occurred in the presence of PCA with lattice parameters of 4.242 and 4.240 Å after 24 and 30 h, respectively,

due to protonation. When Ti powder was milled in the absence of PCA, no phase transformation was observed for both uninterrupted and interrupted milling cycles. In addition, nanocrystalline Mg powder with crystallite size varying between 60 and below 40 nm was produced by ball milling. However, no solid-state transformation took place even if the powder was milled for 90 h. Therefore, we evidently report for the first time that the interstitial H^+ is the driving force for α → FCC phase transformation in ball milled Ti powder.

Our theoretical results predicted the ω phase to be the ground-state structure of Ti at 0K and P=0 GPa, in support of other previously reported calculations. We noticed that the stability of the α phase was surpassed by that of the FCC lattice at ~ 100 GPa, corresponding with sudden sharp rise in *c/a* ratio, hence attributed to α → FCC phase transition. Similar results were obtained for Mg at 50 GPa, although in this case the crossing of lattice energies coincided with minimum *c/a*. However, using our proposed HCP→BCC MT path mechanism for Mg, it is evident that the minimum *c/a* at 50 GPa corresponds to a change in the preferred deformation slip from basal (below 10 GPa) to prismatic rather than phase transition. Nonetheless, the proposed MT model predicts that both elemental Ti and Mg prefer to deform via prismatic slip as indicated by lower shear stress as well as CRSS values compared to those calculated for basal slip.

Theoretical findings from *ab initio* calculations on hypothetical ordered Ti-Mg phases indicated absence of intermetallic phases at equilibrium conditions, in agreement with experimental data. However, the formation becomes possible at 80 GPa and above with respect to *c/a* ratio but requires at least 200 GPa with respect to stable lattices. Using calculated heats of formation, elasticity and DOS, it has been possible to show that $L1_2$ $TiMg_3$ could not form even at high pressure as 250 GPa. Nonetheless, both approaches indicate that forming an intermetallic compound between Ti and Mg requires a crystal structure change, α→FCC for Ti and HCP→BCC for Mg.

Proposed DFT-based solid solution model for predicting phase stability and elastic properties of binary random alloys, with Mg-Li system serving as a test case, successfully yielded reliable results comparable to experimental data. This method was successfully applied to study an immiscible Ti-Mg system and the solubility limit

was for the first time theoretically established. Based on formation energy of Ti-Mg solid solutions, our calculations predicted for the first time that the solubility of up to 60 and 100 at.% Mg into Ti with the use of USP and NCP, respectively, to be thermodynamically favourable with necessary lattice kinetics being the main challenge. Nonetheless, NCP proved to be reliable in predicting structural and elastic properties of disordered alloys.

List of Publications

1. MJ Phasha, PE Ngoepe, **Intermetallics** 21 (2012) 88-96: An alternative DFT-based model for calculating structural and elastic properties of random binary HCP, FCC and BCC alloys: Mg–Li system as test case.

2. K Maweja , M Phasha, N van der Berg, **Powder Technology** 199 (2010) 256–263: Microstructure and crystal structure of an equimolar Mg–Ti alloy processed by Simoloyer high-energy ball mill.

3. M Phasha, K Maweja, C Babst, **Journal of Alloys and Compounds** 492 (2010) 201–207: Mechanical alloying by ball milling of Ti and Mg elemental powders: Operation condition considerations.

4. M Phasha , S. Bolokang, P.E. Ngoepe, **Materials Letters** 64 (2010) 1215–1218: Solid-state transformation in nanocrystalline Ti induced by ball milling..

5. S Bolokang, M Phasha, **International Journal of Refractory Metals & Hard Materials** 28 (2010) 610-615: Formation of titanium nitride produced from nanocrystalline titanium powder under nitrogen atmosphere.

6. MJ Phasha, PE Ngoepe, HR Chauke, DG Pettifor, D Nguyen-Mann, **Intermetallics** 18 (2010) 2083-2089: Link between structural and mechanical stability of fcc- and bcc-based ordered Mg-Li alloys.

7. MJ Phasha, W du Preez, PE Ngoepe, Effect of high pressure on the cohesive, electronic and elastic properties of hypothetical equilibrium ordered Ti-Mg phases, *submitted.*

8. MJ Phasha, W du Preez, PE Ngoepe, Martensitic transformations originating from alpha titanium phase: *ab initio* study, *submitted*.

9. MJ Phasha, W du Preez, PE Ngoepe, First principles predictions of $Ti_{100-x}Mg_x$ solid solutions in HCP, FCC and BCC crystal structures, *submitted*.

Table of Contents

List of Figures

List of Tables

Chapter 1

Introduction

The increasing demand for light weight materials for aerospace, medical engineering and automotive applications has led to a continuous development of alloys with lower density. Among other light metals, titanium (Ti) is a technologically important metal as it exhibits unique properties such as low density, good corrosion resistance and mechanical properties at room and moderately high temperatures. Ti and its alloys have received much attention due to their interesting properties such as high strength-to-weight ratio, environmental stability and elevated temperature capabilities [Boyer 1995, Tanaka *et al* 2006, Chen *et al* 2010]. However, titanium alloys cannot be used in large quantities in automobiles unless the cost of titanium alloy parts is lowered to an acceptable level. The high cost of titanium alloy parts comes from both alloy materials and metalworking, factors which should be considered in order to reduce the cost of titanium alloy parts [Liu *et al* 2006]. The use of blended elemental powders is much more cost-effective, due to affordability of Ti and other elemental powders, without any deterioration of mechanical properties.

1.1 Ti-Mg system

Magnesium (Mg) at a low density of 1740 kg/m^3 is approximately 35% lighter than aluminium (Al) alloys and 65% lighter than Ti alloys. However, the technological use of Mg alloys is limited by generally low ductility (toughness) at room temperature and poor corrosion resistance. Nonetheless, addition of magnesium to titanium could produce very low-density alloys with a high specific strength to weight ratio. In addition, density reduction is by far the most effective parameter in reducing component weight [Froes *et al* 1993] and thus could improve fuel efficiency in transport vehicles. Such light weight alloys would receive extensive use in many applications; such as in aerospace industry, where lightweight is of vital importance.

The addition of Mg is of particular interest in density reduction, however, it has negligible equilibrium mutual solubility of up to 1.6 atomic percent (at. %) in alpha (HCP) phase and between 2.4 and 10 at. % in high temperature beta (BCC) titanium phase [Massalski 1990], as illustrated by the phase diagram in figure 1.1.1 [Vermeulen 2009]. Moreover, solid solubility of Mg in Ti could not be extended by conventional melting techniques since the boiling point of Mg (1380K) is much lower than the melting point of Ti (1941K). Hence Ti and Mg form no compound over the whole composition range. Nonetheless, from theoretical point of view there should be appreciable solid solubility of magnesium in titanium based solely on the Hume-Rothery criteria [Hume-Rothery *et al* 1969] as follows:

(i) the difference in atomic diameter is only 10%, well below 15% difference limit.
(ii) the crystal structures are the identical, HCP in both.
(iii) the difference in electronegativity is within required 0.4 of each other, with Mg having 1.31 and Ti 1.54.
(iv) the only difference being the relative valence effect, in that titanium has 4 valence electrons while magnesium has 2. Thus, based on the above criteria, only the last factor is not favourable for significant solubility to occur.

A metal will dissolve another of higher valency to a greater extent than one of lower valency. Hence studies on Mg-Ti solid solutions (Ti dissolved in Mg) regarded as potential material for hydrogen (H_2) storage has received so much attention in recent years [Asano *et al* 2007, 2009a, b, c, Kalisvaart *et al* 2007, Kalisvaart and Notten 2008, Rousselot *et al* 2008] exceeding that of earlier attempts to dissolve Mg in Ti [Zhou *et al* 1995, Wilkes *et al* 1996]. However, the solute and solvent atoms should typically have the same valence in order to achieve maximum solubility. Despite reported successes in fabricating these alloys via several far-from equilibrium processes, the formation mechanism remains unclear with contradicting conclusions. In addition, the extent of solid solubility is not known so far.

The Ti-rich TiMg alloys, which are expected to be corrosion resistant, have potential to

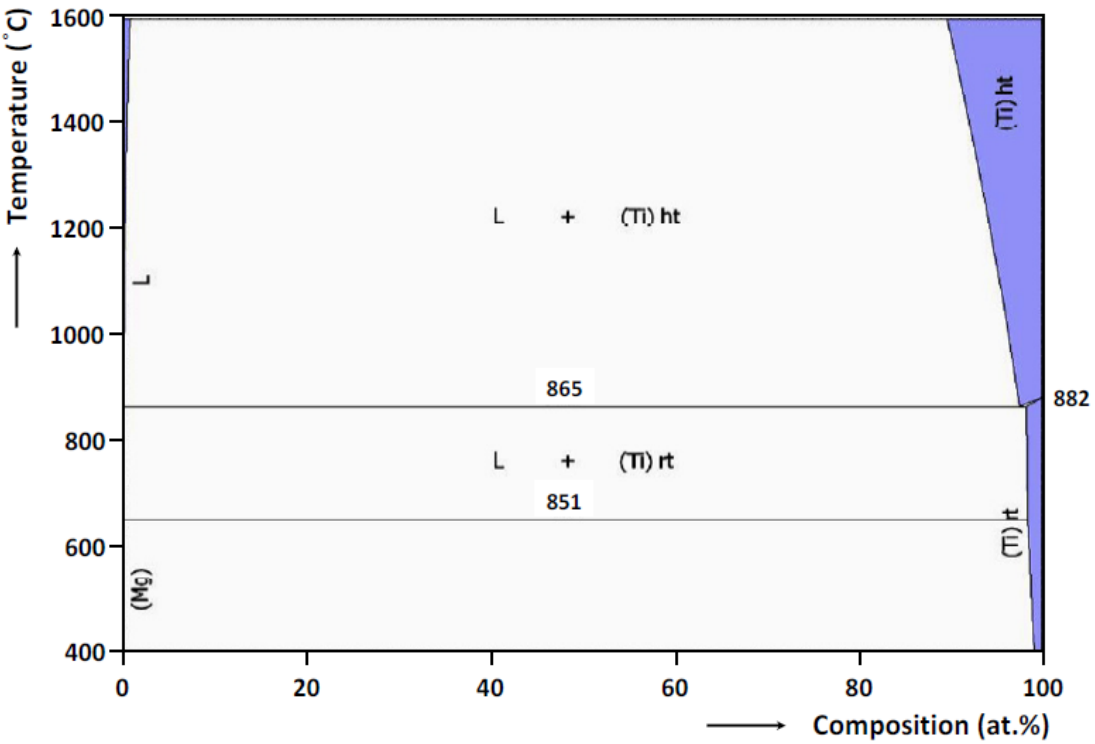

Figure 1.1.1. Ti-Mg phase diagram [Vermeulen 2009]

be used in structural applications in aerospace and automotive industries. Furthermore, Ti-Mg alloys with concentrations towards Mg-rich region possess potential for use as hydrogen storage material [Vermeulen *et al* 2006, Kalisvaart *et al* 2007; Kalisvaart and Notten 2008, Asano *et al* 2007; 2009a, b, c]. Meanwhile, the hcp Mg-rich compositions could be used as a colour-neutral switchable mirror for smart window [Farangis *et al* 2003, Borsa *et al* 2007, Bao *et al* 2008]. The switchable mirror films with variable optical properties are also attractive materials for regulation of light and heat transfer in buildings, vehicles, and satellites and may as well have applications in sensor technologies [Farangis *et al* 2003].

Binary Mg_x–Ti_{1-x} alloys are being investigated worldwide for electrochemical hydrogen storage applications [Asano *et al* 2007, 2009a, b, c, Kalisvaart and Notten 2008, Huang *et al* 2009, Kalisvaart *et al* 2007, Rousselot *et al* 2008]. Addition of Ti to Mg is expected to improve the structural stability of a final Mg–Ti BCC (body-centered cubic) solid solution. It is expected that a final Mg–Ti alloy which would have a BCC structure will

achieve higher hydrogen storage capacity than the close-packed FCC (face-centered cubic) and HCP (hexagonal close-packed) structures. However, the large difference in melting temperature between these two metals makes it difficult to synthesize such alloys by conventional casting routes. Mechanical alloying is an effective far-from equilibrium method capable of mixing even immiscible elements and extends their solid solubility, thus used to achieve solid solutions of Mg–Ti based system [Asano *et al* 2009a, b, c, Kalisvaart and Notten 2008, Huang *et al* 2009, Kalisvaart *et al* 2007, Rousselot *et al* 2008, Sundaresan and Froes 1988, Zhou *et al* 1995, Wilkes *et al* 1996, Senkov *et al* 2000, Sun and Froes 2002, Liang and Schulz 2003, Suryanarayana and Froes 1990]. The microstructure and crystal structure of the alloy powders thus developed would be determinant in hydrogen storage capabilities. Asano and his co-workers used a Fritsch P5 planetary ball mill to synthesize various chemistries of such Mg–Ti binary system using stainless steel or zirconia balls and milling chamber. They have observed that the transformation from the initial HCP structures of elemental Ti and Mg into the HCP, FCC or BCC solid solutions of Ti in Mg were strongly determined by the mixed molar ratios of the two elements and by the dynamic energy which was dependent on the milling setup [Asano *et al* 2009a]. They observed that the crystal structure of Mg–Ti was not affected by iron contamination (up to 5 at. %) from the stainless steel balls and chamber. Hence a BCC product could be formed in a stainless steel milling medium [Asano *et al* 2009b], whereas contamination by a zirconia milling medium was revealed to be detrimental to the formation of the BCC product [Asano *et al* 2009a]. Kalisvaart and Notten (2008) have investigated the effects of using graphite or stearic acid as a process control agent (PCA), in product structures in both low-energy (Uni-Ball-Mill II) and high-energy ball milling (Spex 8000-230) of Mg–Ti and Mg–Ti–Ni systems. From their work it was noted that the transformation from HCP to FCC structures during ball milling was related to a synergy between the process control agent, the impact generated by the milling balls and the dissolution of Ti in Mg. Sun and Froes (2002) reported that the average grain size of the $Ti_{1-x}Mg_x$ alloys decreased with increasing Mg content, whereas the volume fraction of grain boundaries significantly increased as the Mg content increased, suggesting that the grain boundary played an important role in enhancing the solid solubility of Mg in Ti. Repeated plastic deformation

of raw materials was reported in the initial stage of the mechanical alloying of various metallic systems by ball milling. However, common to the above studies, the mechanism and thermodynamics for claimed alloying is still lacking.

Other works showed that particle size is affected by the types and the amount of process control agent, and the milling duration [Zhang *et al* 1999, Byun *et al* 2004]. Kalisvaart and Notten (2008) recently reported the formation of a mixture of two FCC compounds after milling of Ti–Mg mixtures in the presence of a PCA. Whereas HCP products with lattice constants a=3.03 and c=4.84 Å were obtained by solid solution of Ti in Mg when milling was undertaken in the absence of a process control agent using a coarse Mg powder particle size [Kalisvaart *et al* 2007].

On the other hand, ball milling is a complex process and involves the optimization of a number of variables to achieve a desired phase or microstructure. Almost every parameter has an effect on the final constitution of the milled powder, and these process parameters are not completely independent [Suryanarayana 2001]. Milling atmosphere, ball to powder weight ratio, milling speed, milling ball size, milling time, process control agent, starting powder size range, ductility of the initial powders should be considered to achieve the desired production. All these variables usually depend on one another. Many recent studies on the effects of these variables in the mechanical alloying of diverse systems aimed at development of nanocrystalline thermoelectric and magnetic compounds, hydrogen storage materials, structural material, etc., have been successfully conducted worldwide [Zakeri *et al* 2009, Ozdemir *et al* 2008, Feng *et al* 2007, Kamrani *et al* 2007, Miraghaei *et al* 2008, Mousavi *et al* 2008, Gan and Gu 2008, Pallone *et al* 2003]. The claimed alloying of powders during MA process is mainly based on XRD and SEM results, although the basis for the underlying alloying mechanism is not known.

1.2 Far-from equilibrium processes

Different non-equilibrium processing routes such as ion beam mixing (IBM) [Liu *et al*

1993], ball milling [Hida *et al* 1997], solid state reaction (SSR) [Lin *et al* 2000], and high pressure alloying [Dubrovinskaia *et al* 2005], capable of synthesizing metastable, amorphous or nanostructured as well as immiscible alloys have been developed and are nowadays being exploited to produce novel materials having unique properties. These developments led to recent increased attention on the formation of the metastable phases from elements that are immiscible under equilibrium conditions [Ma 2005]. Among these, the processing techniques that ushered notable success in producing titanium-magnesium alloys with extended solid solubility, are physical vapour deposition (PVD) and mechanical alloying (MA). The successful synthesis of Ti-Mg solid solutions containing up to 29 wt. % Mg by means of PVD has been reported [Zheng *et al* 1997, Ward-Close *et al* 1991; 1994]. Until approximately 5 years or less ago, only few attempts of synthesizing Ti-rich Ti-Mg alloys by MA were reported [Zhou *et al* 1995, Wilkes *et al* 1996 and Liang *et al* 2003], with a maximum solid solubility of up to 9 wt. % Mg. Nonetheless, these results confirm that MA can be used as an alternative Ti-Mg alloy synthesis route capable of producing super saturated solid solutions with very fine grained microstructures [Benjamin 1970] and such powders can be consolidated without losing the magnesium by evaporation [Gardiner *et al* 1996].

Among existing non-equilibrium methods (sputtering, vapour deposition, ultra-quenching, etc.), mechanical alloying (MA) is mostly used due to its simplicity, low cost and its ability to produce large volumes [Koch 1997] while achieving chemical and micro-structural homogeneity, as well as allowing direct control over alloy composition. One of the major advantages of MA is in the synthesis of novel alloys, e.g., alloying of normally immiscible elements, which is not possible by any other technique. This is because MA is a completely solid-state processing technique and therefore limitations imposed by phase diagrams do not apply here [Suryanarayana *et al* 2001]. By using such technique as mechanical alloying or milling, it has been shown that the mechanical properties can be increased by the reduction in grain size and the increase in homogeneity of the particle distribution [Lu and Lai 1995]. So far, the MA process using ball-mill has received much attention as a powerful tool for fabrication of several advanced materials, including equilibrium, nonequilibrium (e.g., amorphous,

quasicrystals, nanocrystalline, etc.) and composite materials [El-Eskandarany *et al* 1991, 1998]. In fact, MA is a unique process in that a solid state reaction takes place between the fresh powder surfaces of the reactant materials at room temperature. Consequently, it is reported to produce alloys and compounds that are difficult or impossible to be obtained by conventional melting and casting techniques [El-Eskandarany *et al* 1990]. However, the mechasnism for such alloying is not understood.

1.3 Ball milling of Ti and Mg elemental metal powder

Ti and its alloys are still in demand in many structural applications; such as in aerospace, automotive and medical industries, due to their low density, high strength-to-weight ratio, and good corrosion resistance. On the other hand, Mg and its alloys continue to be very attractive as the lightest structural materials and have great potential for applications in automotive, aerospace and electronic industries. However, the usage of both metals is limited due to some undesirable properties of castings (such as strength, ductility, creep and corrosion resistance) and few fabricating methods besides conventional ingot metallurgy processing. Since grain refinement is generally believed to have beneficial effect on mechanical properties, fabrication of nc metals and alloys using powder metallurgical process such as ball milling (BM), which has proven to be an effective processing technique for producing nanocrystalline (nc) metals, has attracted considerable attention in recent years. Moreover, at nano-scale these properties are expected to improve considerably and as such widen application options.

So far, metastable FCC Ti was obtained by various techniques such as ultrathin films deposited on aluminum substrate [Shechtman *et al* 1994, Van Heerden *et al* 1996, Kim *et al* 1996, Banerjee *et al* 1999], multilayers of nickel [Josell *et al* 1995] and silver [Tepper *et al* 1997], respectively. The lattice parameters of the stabilized FCC Ti varies between 4.15 Å [Kim *et al* 1996] and 4.42Å on Ti-Al alloys [Van Heerden *et al* 1996], respectively. Alternatively, in Ti-Ni and Ti-Ag multilayers the corresponding lattice parameters were 4.40 and 4.34 Å respectively [Josell *et al* 1995, Tepper *et al* 1997], while in sputter deposition of Ti-Al-B is 4.21 Å [Lofvander *et al* 1995]. Recently,

Chakraborty *et al* (2011) synthesized FCC Ti with lattice parameter of 4.1638 Å using DC magnetron sputtering while Aguayo *et al* (2002) reported 4.11 Å from *ab* initio calculations. To date, the basis for such difference in lattice parameter is not accounted for. Subsequently, different authors using the BM process [Chatterjee *et al* 2001a, b, Manna *et al* 2003] later published several articles on the formation of a metastable FCC with varying lattice parameters. In pure Ti, BM does not only reduce the grain size to nanometer level but also induces solid-state transformation, more especially during intense high energy ball milling (HEBM) [Manna *et al* 2003]. In recent years, an increasing number of reports have been published on solid-state transformation achieved by HEBM in elemental metals [Huang *et al* 1995, Chattopadhyay *et al* 2001, Manna *et al* 2002, 2003, Sort *et al* 2003] as well as in binary solid solutions [Froes *et al* 1995, Ma and Atzmon 1995, Koch and Whittenberger 1996, Suryanarayana *et al* 2001, Maweja *et al* 2010, Phasha *et al* 2010b]. Manna *et al* (2003) reported HCP to FCC allotropic transformation in Ti to be governed by lattice expansion (negative hydrostatic pressure) as a result of grain refinement or nanocrystallization during milling. Despite these reports on HCP to FCC allotropic transition in commercially pure (CP) Ti using BM, systematic studies on HCP to FCC transition mechanism are scarce. Most researchers have attributed the stability of FCC phase to impurities such as oxygen, nitrogen and carbon [Seelam *et al* 2009a, b], although the source for these interstitial elements is not well defined. However, after observing a similar FCC allotropic phase using TEM on ball milled Zr powder, Manna *et al* (2002) concluded that the stability of FCC phase is not impurity driven. Furthermore, Vullum *et al* (2009) obtained FCC with a lattice parameter of 4.10 Å after flushing out hydrogen from titanium hydride by electron beam exposure. However, in addition to unclear underlying transformation mechanism, the basis for such a significant difference in the lattice parameter size is not known. Hence, in the current study, the effect of milling on the crystal structure of pure Ti powder is investigated using XRD measurements. The thermal stability of mechanically induced nanocrystalline metastable FCC phase upon annealing will be studied. Furthermore, *ab initio* based model is constructed to demonstrate our proposed HCP → FCC transformation mechanism which attributes different reported lattice parameters of FCC phase to different amounts of protonation.

On the other hand, despite its abundance, low density and low price which render Mg and its alloys very attractive in the automotive and aerospace industries [Polmear 1994], their applications are however limited because of their high sensitivity to oxidation and their relatively low corrosion resistance. Nonetheless, Mg is able to absorb large quantities of hydrogen (7.6 wt. %) which makes it a particularly interesting element for the elaboration of Mg-based metal hydrides as hydrogen source for fuel cells [Huot *et al* 2001, Orimo and Fujii 2001]. For this reason, Mg and its alloys are considered to be some of the most important candidates for reversible storage materials [Sakintuna *et al* 2007, Jain *et al* 2010]. However, in its microcrystalline form it shows slow sorption kinetics. In addition, other impediments in Mg hydrides include high thermodynamic stability and high reactivity toward air and oxygen which is common with most other lightweight metal hydrides [Zeppelin *et al* 2001]. The high thermodynamic stability of MgH_2 results in a relatively high desorption enthalpy, which corresponds to an unfavourable desorption temperature (> 300^{o}C) at 1 bar H_2 [Zeppelin *et al* 2001]. Also, the formation of an oxide layer presents an impenetrable boundary to hydrogen gas molecules [David 2007]. To initiate uptake of hydrogen, the oxide layer must be cracked by activation, which is a long costly process. Even after activation, there is a limited dissociation rate of hydrogen molecules on the metal surface. This is usually improved by a layer of added catalyst, but is also costly. Hydrogenation also depends upon the growth of hydride on the Mg surface. However, this outer layer of the hydride blocks hydrogen from reaching the core or inner unreacted Mg once the layer reaches a thickness of only 100 μm. This means that there is no physical way for Mg to be fully hydrogenated, especially in the microcrystalline form. The solution for these impediments would be to form nanocrystalline magnesium hydride and then a chemical activation. Adjusting the powder size to < 50 μm is thin enough to overcome the hydride blocking issue [Urretavizcaya *et al* 2002]. Hence the recent increased number of research activities that use ball mill process, in which powders are fragmented into very fine particles that are cold welded to form medium sized particles with small grain sizes [Hout *et al* 1999, Gubicza *et al* 2004]. Despite the much improved sorption kinetics of nanocrystalline Mg alloys, most of these studies mill pure Mg under H_2 atmosphere with or without a catalyst [Kwon *et al* 2008, 2010, Song *et al* 2009, David 2007], pure Mg or

MgH_2 in the presence of catalyst under argon atmosphere [Song 1995, Song *et al* 1999, Friedrichs *et al* 2006, Amirkhiz *et al* 2011], which makes it difficult to investigate the effect of milling on pure Mg. As a result, only few studies have been conducted this far on synthesis of nanocystalline pure Mg by ball milling under inert atmosphere [Zaluska *et al* 1999, Hwang *et al* 2001, Grosjean *et al* 2004, Zidoune *et al* 2004, Gerasimov *et al* 2009, Choi *et al* 2010], with no indication of phase transformation.

1.4 Deformation mechanisms for HCP metals

Metallic materials may experience two kinds of deformation: elastic and plastic. Deformation in which stress and strain are proportional is called elastic deformation; a plot of stress (ordinate) versus strain (abscissa) results in a linear relationship [Callister 2001]. The slope of this linear segment corresponds to the modulus of elasticity *E*, which may be thought as stiffness or a material's resistance to elastic deformation. Elastic deformation is nonpermanent, which means that when the applied load is released, the piece returns to its original shape. On the other hand, plastic deformation is permanent, and strength and hardness are measures of a material's resistance to this deformation. On a microscopic scale, plastic deformation corresponds to the net movement of large numbers of atoms in response to an applied stress [Callister 2001]. Furthermore, plastic deformation most often involves the motion of dislocations, linear crystalline defects. However, dislocations do not move with the same degree of ease on all crystallographic planes of atoms and in all crystallographic directions. Ordinarily there is a preferred plane, and in that plane there are specific directions along which dislocation motion occurs. The process by which plastic deformation is produced by dislocation motion is called slip; the crystallographic plane along which the dislocation line traverses is the slip plane. This combination of the slip plane and the slip direction is termed the slip system, as shown in figure 1.4.1. The slip system depends on the crystal structure of the metal and is such that the atomic distortion that accompanies the motion of a dislocation is a minimum. For a particular crystal structure, the slip plane is that plane having the most dense atomic packing, that is, has the greatest planar density. The slip direction corresponds to the direction, in this plane, that is most closely packed

with atoms, that is, has the highest linear density. Metals with FCC or BCC crystal structures have a relatively large number of slip systems (at least 12). Consequently, these metals are quite ductile because extensive plastic deformation is normally possible along the various systems. Conversely, HCP metals, having few active slip systems (less than 5), are normally quite brittle. Plastic deformation in HCP metals commonly occurs by either basal slip B$\langle a \rangle$ along (0001) [11-20] or prismatic P$\langle a \rangle$ slip along (10-10) [11-20] as their principal slip mode in addition to secondary pyramidal slip modes such as $\Pi_1\langle a \rangle$, $\Pi_1\langle c+a \rangle$ and $\Pi_2\langle c+a \rangle$ operating in (10-11)[11-20], (10-11)[11-23] and (11-22)[11-23] slip systems, respectively as shown in figure 1.4.1 [Yoo 1981]. This deformation is induced by applied stress that may be tensile or compressive. The shear components of the applied stress exist at all but parallel or perpendicular alignments to the stress direction. These are termed resolved shear stresses, and their magnitudes depend not only on the applied stress, but also on the orientation of both the slip plane and direction within that plane. In response to an applied tensile or compressive stress, slip in a single crystal commences on the most favourably oriented slip system when the resolved shear stress reaches some critical value, termed the critical resolved shear stress (CRSS). It represents the minimum shear stress required to initiate slip, and is a property of the material that determines when yielding occurs. The single crystal plasticity deforms or yields when the maximum resolved shear stress is equal to the CRSS. The values of CRSS at ambient temperatures for the basal plane slip system is about two orders of magnitude smaller than that of the prismatic plane slip system in Mg [Tonda and Ando 2002]. Hence Mg is expected to be deformed mainly by basal plane slip during ball milling at ambient temperatures. In the case of Ti, however the value of the CRSS of the basal plane slip system is slightly larger than that of the prismatic plane system [Tonda and Ando 2002]. It is therefore anticipated that Ti would deform by prismatic plane slip much more readily than Mg [Yoo 1981], during BM. In addition to slip, plastic deformation in some metallic materials can occur by the formation of mechanical twins, or twinning. The concept of a twin is that, a shear force can produce atomic displacements such that on one side of a plane (the twin boundary), atoms are located in mirror image positions of atoms on the other side. Furthermore, twinning occurs on a definite crystallographic plane and in a specific direction that depend on

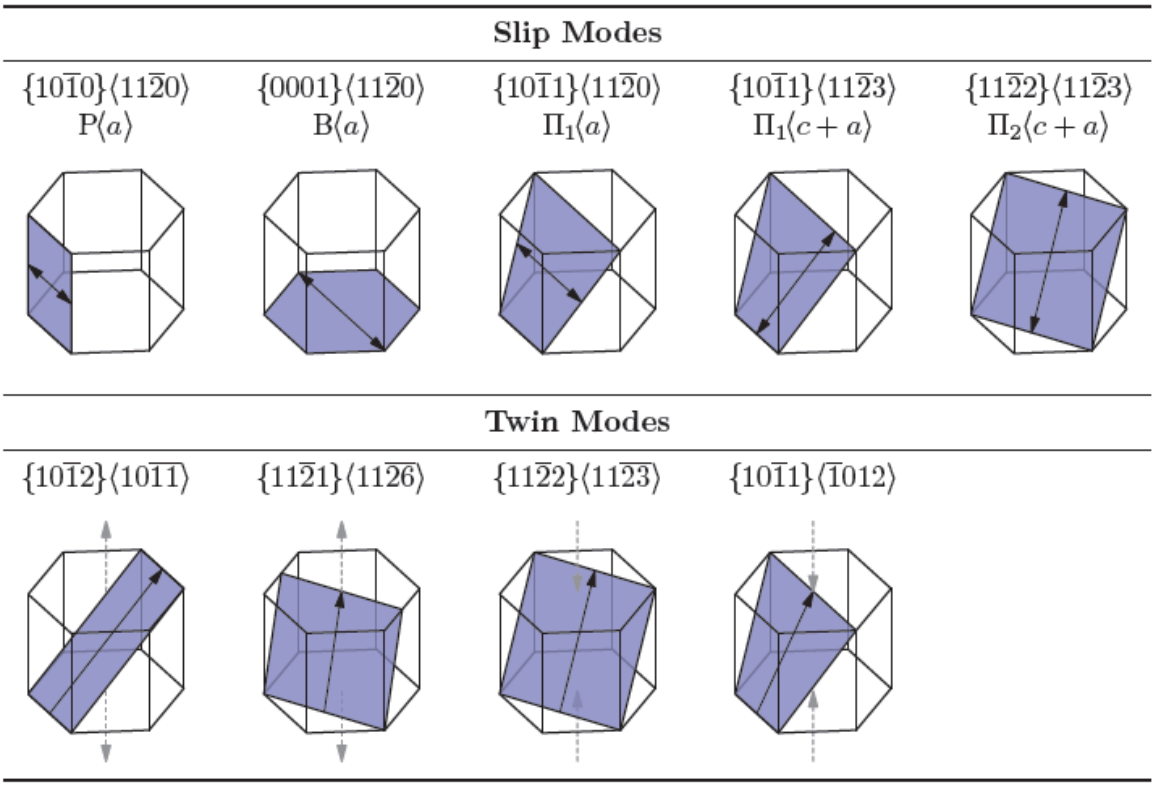

Figure 1.4.1. Slip and twin modes in HCP metals. The shaded area indicates the slip plane while the arrow on the plane indicates the shear direction [Battaini 2008].

crystal structure. The two deformation processes (slip and twinning) differ from one another in several respects. First of all, for slip, the crystallographic orientation above and below the slip plane is the same both before and after the deformation; whereas for twinning, there will be a reorientation across the twin plane. In addition, slip occurs in distinct atomic spacing multiples, whereas the atomic displacement for twinning is less than the interatomic separation. Mechanical twinning occurs in metals that have BCC and HCP crystals structures, at low temperatures, and high rates of loading (shock loading), conditions under which the slip process is restricted; that is, there are few operable slip systems. Therefore, the amount of bulk plastic deformation from twinning is normally small relative to that resulting from slip.

1.5 *Ab initio* modelling

1.5.1. Hypothetical ordered Ti-Mg intermetallic phases

Despite many anticipated technological applications of Ti-Mg alloys, the fundamental studies of this system using state-of-art *ab initio* modelling techniques, to build an understanding of the underlying science and to validate reported experimental results are lacking. It is in the interest of this work to employ *ab initio* modelling to investigate the genesis of solid solutions, their crystal structures as well as the extent of solid solubility in Ti-Mg system. In an equilibrium immiscible system, since there is no thermodynamic driving force for intermixing between the constituent metals, the key issue in initiating an alloying process is to overcome the miscibility barrier (repulsive interaction) characterized by positive heat of formation (ΔH) of the system [de Boer *et al* 1989], thus artificially creating some non-equilibrium alloys. With persisting lack of evidence for establishing the exact extended solid solubility in mechanically induced alloying, the effect of pressure is reported to be a principal mechanism for the intermixing between the immiscible elements [Dubrovinskaia *et al* 2005, Shtremel 2002]. To achieve a thorough understanding of the physical origin of the metastability, namely the structural stability of the artificially created non-equilibrium phases/alloys, is of critical importance from both theoretical and practical points of view [Kong *et al* 2005].

Very recently, another path for overcoming the miscibility barrier between immiscible atoms (iron and magnesium) is proposed, that is, in a series of experiments in diamond anvil cells, high-pressure promotes solubility of Mg in Fe, and the generality of this concept of high-pressure alloying between immiscible elements is demonstrated by its application to Co and Ni with Mg elements [Dubrovinskaia *et al* 2005]. These techniques are employed to study the underlying scientific issue of the solid phase formation and transformation under far-from-equilibrium circumstances, not only in immiscible systems with positive heats of formation but also in the equilibrium miscible metal systems. To obtain an understanding at a depth of electronic structure concerning the stability of the non-equilibrium phases in the immiscible systems, it is necessary to pursue first-principles calculations, which however, is still currently an open issue.

1.5.2. Ideal disordered solid solutions

A solid solution is formed when two metals are completely soluble in liquid state and also completely soluble in solid state. In other words, when homogeneous mixtures of two or more kinds of atoms (of metals) occur in the solid state, they are known as solid solutions. The more abundant atomic form is referred as solvent and the less abundant atomic form is referred as solute. The term “solid solution” is used just as “liquid solution” is used because the solute and solvent atoms are arranged at random. The properties and composition of a solid solution are, however, uniform as long as it is not examined at the atomic or molecular level. Solid solutions in alloy systems may be of two kinds: substitutional and interstitial [Reddy 2008, Callister 2001]. A substitutional solid solution results when the solute atoms take up the positions of the solvent metal in the crystal lattice, as illustrated in figure 1.5.2.1. Solid solubility is governed by the comparative size of the atoms of the two elements, their structure and the difference in electronegativity [Hume-Rothery *et al* 1969]. If the atomic radii of a solvent and solute differ by more than 15% of the radius of the solvent, the range of solubility is very small. When the atomic radii of two elements are equal or differ by less than 15% in size and when they have the same number of valency electrons, substitution of one kind of atom for another may occur with no distortion or negligible distortion of the crystal lattice, resulting in a series of homogeneous solid solutions. Difference of more than 15% may result in locally stressed solid solutions, as demonstrated by figure 1.5.2.2. For an unlimited solubility in the solid state, the radii of the two elements must not differ by more than 8% and both the solute and the solvent elements must have the same crystal structure.

In addition to the atomic size factor, the solid solution is also greatly affected by the electronegativity of elements and by the relative valency factor. The greater the difference between electronegativities, the greater is the tendency to form compounds and the smaller is the solid solubility. Regarding valency effect, a metal of lower valency is more likely to dissolve a metal of higher valency. Solubility usually increases with increasing temperature. This causes precipitation within a homogeneous solid solution

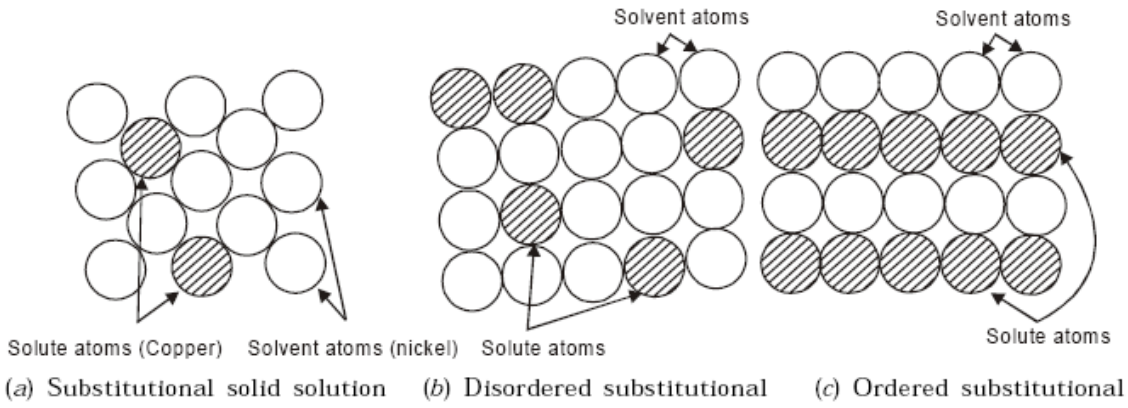

Figure 1.5.2.1. Illustrations of substitutional solid solutions [Reddy 2008].

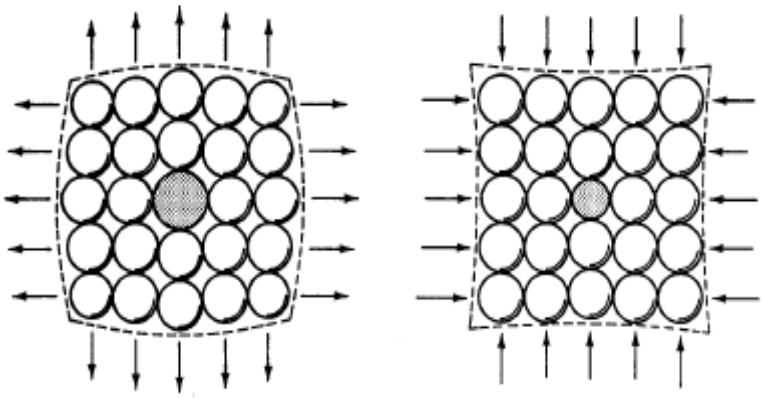

Figure 1.5.2.2. Local stress in substitutional solid solutions.

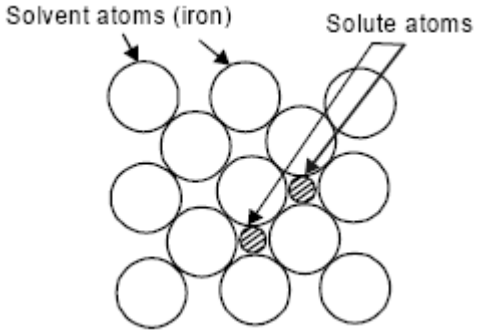

Figure 1.5.2.3. Illustration of interstitial solid solution [Reddy 2008].

phase, resulting in hardening effect of an alloy. When ionic solids are considered, the valency of ions is a very important factor. As shown in figure 1.5.2.3, an interstitial solid solution results when the solute atoms are small enough to fit into the interstices of the metal lattice. The elements that can form interstitial solid solutions with transition metals are hydrogen, carbon, nitrogen and boron.

1.5.2.1. Substitutional Solid Solutions

If the atoms of the solvent or parent metal are replaced in the crystal lattice by atoms of the solute metal then the solid solution is known as substitutional solid solution. For example, copper atoms may substitute for nickel atoms without disturbing the FCC structure of nickel (Fig. 1.5.2.1(*a*)). In the substitutional solid solutions, the substitution can be either disordered or ordered [Ducastelle 1991, Callister 2001, Reddy 2008]. Figure 1.5.2.1(b) shows disordered substitutional solid solution. Here the solute atoms have substituted disorderly for the solvent atoms on their lattice site. Figure 1.5.2.1(c) shows an ordered substitutional solid solution. Here the solute atoms have substituted in an orderly manner for the solvent atoms on their lattice site. Vegard's law has been used extensively in mineralogy, metallurgy and materials science for the past six decades. According to this law, unit cell parameters should vary linearly with composition for a continuous substitutional solid solution in which atoms or ions that substitute for each other are randomly distributed. Although the law was postulated on empirical evidence, several cases of both positive and negative deviations from this law have been documented. Its theoretical foundations have not been critically explored. Presented in this work is an analysis of the law within the framework of solution thermodynamics as well as in far-from equilibrium situation.

1.5.2.2. Mg-Li system

In recent years the problem of environmental conservation and global warming has provided continuous and increasing pressure on the transportation industry to improve fuel economy and reduce emissions of carbon dioxide (CO_2) that are considered to be major contributors to global warming [Meyer 1992]. Among other possibilities for resolving this problem such as use of alternative fuel sources, powertrain enhancements, aerodynamic improvements, etc., lightweight construction seems to be the best cost effective option for significant decrease of fuel consumption and CO_2 emissions [Cole 2003, Aghion *et al* 2001]. It has further been envisaged by auto engineers and designers that a 10 percent (%) reduction in weight will result in a 6-8%

decrease in fuel consumption for any given vehicle [Aghion *et al* 2001, 2004]. As a result, the motor vehicle industry has been attempting to improve fuel efficiency by weight reduction in automobiles, and thereby to reduce emissions of greenhouse effect gas. In order to attain the weight reduction, the improvement of steel strength and the substitution of aluminium (Al) parts for conventional steel parts have been conducted. This has led to some vehicles being equipped with Al parts, such as engine piston, wheel and suspension. However, due to its low density and high specific strength (strength divided by density), the demand for magnesium (Mg) substitution has been increasing in recent years [Mordike and Ebert 2001, Luo 2002, Inoue *et al* 2001, Zhang *et al* 2009, Ganeshan *et al* 2009a, b, Chia *et al* 2009]. Furthermore, Mg alloys are becoming widely recognized as playing an increasingly important role in transportation industry due to strategies of leading car producers which requires the use of lightweight and environmentally friendly materials [Bach *et al* 2003, Furuya *et al* 2003, Leu *et al* 2010]. Consequently, and also owing to the Corporate Average Fuel Efficiency (CAFE) standards and other different government environmental legislation, most automobile producers are planning to increase the use of Mg alloys up to 40-80 kg per vehicle in the near future [Cole 2003, Luo 2001].

Today, since the sustainable energy saving and reduction of CO_2 emissions from transportation by development of advanced technologies for high-performance light-metal-alloy materials for fuel-efficient vehicles is a most important topic for manufactures and scientists working in transportation industry, the need for improving the mechanical properties, formability and corrosion resistance of magnesium alloys have received special attention. Despite possessing the lowest density among all metallic construction materials and other attractive properties (high specific strength as a substrate, good castability and weldability characteristics), the historical setbacks in the development of Mg and its alloys, like other alloys with HCP crystal structure, have been attributed to a number of challenges ranging from processing (formability) to toughness as a result of limited slip planes. Other major contributors hampering Mg alloy development and application are poor wear and corrosion resistance [Liu and Schlesinger 2009]. These difficulties contributed towards Mg alloy development being

deserted as witnessed by the evident drop in Mg production from mid to late 40s [Polmear 1995]. However, addition of lithium (Li) with density of 0.53 g/cm^3 does not only reduce the density of Mg significantly but also improves specific stiffness [Wyss 1988] and forces a useful phase change to BCC phase when alloyed above 30 atomic percent (at.%) concentration [Jackson *et al* 1949, Freeth and Raynor 1953]. The latter property is responsible for the improved ductility and high formability of Mg-Li alloys even at room temperature. The potential lightweight structural applications of Mg-Li alloys were recognized as early as mid 20th century [Grube *et al* 1934, Hume-Rothery *et al* 1945, Jackson *et al* 1949, Freeth and Raynor 1953, Levinson 1955, Jones and Hogg 1956, Herbstein and Averbach 1956a, b]. These early research activities led to first production of Mg-Li alloys in 1960s by NASA for utilization in aerospace fields [Haferkamp *et al* 2000]. However, due to limited ductility in the α region and a combination of poor oxidation resistance and low strength in the β region [Massalski 1992, Bialobrzeski *et al* 2007], this system was abandoned for some time. Nonetheless, because of their undeniable interesting properties such as great weight-saving potential in various engineering applications, the interest in study of ultra light Mg-Li alloys drastically re-emerged strongly in the last two decades [Furui *et al* 2005, Chang *et al* 2006, Bialobrzeski *et al* 2007, Wu *et al* 2009, 2010, Pezda 2009, Meng *et al* 2009, Qu *et al* 2010]. Moreover, Mg-Li alloys are the lightest structural material with high strength-to-weight ratio and therefore are very suitable for applications in the electronics and transportation industries.

Although extensive *ab initio* studies have been carried out in the past [Hafner 1976, Punz and Hafner 1987, Vaks and Trefilov 1988, Korzhavyi *et al* 1995, Salo and Kokko 1993, Rajput *et al* 1993, Sahu 1997] and more recently [Uesugi *et al* 2000, 2001, Counts *et al* 2008, 2009, Anusionwu 2002, Phasha *et al* 2010a, Liang and Gong 2010, Taylor *et al* 2010] on binary Mg-Li alloys, most of these theoretical investigations were conducted using ordered intermetallic phases, with exception of Uesugi et al who used HCP supercell but altered its symmetry by changing the γ angle from 120^o in order to allow insertion of Li atoms [Uesugi *et al* 2000, 2001]. This is so despite the fact that binary Mg-Li alloys form solid solutions rather than intermetallic compounds [Massalski

1990]. Furthermore, to study small additions of Mg and Li to pure Li and Mg metals respectively, the use of ordered phases requires large supercells containing many atoms thus making these calculations computationally expensive. Although a comparison of energy between HCP-, FCC- and BCC-based intermetallic compounds could give a reasonable picture about phase stability, the mechanical properties thereof could be different from those of random alloys since they depend strongly on crystal structure and its corresponding symmetry. Consequently, in the current study, we propose a new approach which allows systematic investigation of random alloys. In this method, only the atomic composition including very small additions is altered while both the correct crystal structure and symmetry are maintained. This approach for disordered alloys is applied to Mg-Li system which has 100% solid solubity as a test case and afterwards will be applied to an immiscible Ti-Mg system which is reported to be formable by non-equilibrium processes, in order to establish the solubility limit.

1.6 Motivation and objectives

The current work is aimed at understanding the basis for immiscibility and the concept of alloying via mechanical ball milling. In addition, we seek to investigate the conditions for achieving extended solid solubility in elements that do not dissolve in each other (immiscible) under normal thermodynamic equilibrium conditions. The Ti-Mg system which is characterized by positive heats of formation is considered. Possibility of forming intermetallic compounds is investigated by subjecting hypothetical binary crystal structures under robust high pressure environment. This work involves the *ab initio* calculations for miscible Mg-Li and immiscible Ti-Mg systems and mechanical milling experiments of Ti-Mg mixtures as well as elemental pure Mg and Ti. The work will be performed as outlined below.

We will test our proposed solid solution (random or disordered alloy) approach on Mg-Li system which is experimentally known to have 100% miscibility under equilibrium conditions. In the current study, various properties such as lattice constants, theoretical density, elastic constants and elastic moduli (mechanical properties), will be determined

as a function of composition. Thereafter, this method will be employed to investigate structural, electronic and mechanical properties of ordered and disordered alloys of Ti-Mg equilibrium immiscible system. This study will be conducted as follows:

1. Experimental attempts to synthesize some of the selected concentrations of interest will be carried out. Different elemental powder mixtures having various compositions are mechanically milled using the horizontal high-energy ball milling (HEBM) machine called Simoloyer.
2. In order to achieve the desired physical and chemical structures, the optimisation of only three milling parameters will be investigated, namely, effect of milling time, speed and starting composition.
3. The milled powder particles will be characterized using X-ray diffraction (XRD) for crystal structure evolution while scanning electron microscope (SEM) equipped with energy dispersive spectrometry (EDS) will be used to trace changes in morphology.
4. In order to understand the genesis of phase transformation in mixed powders, the ball milling experiments on pure elemental metal powders (Ti and Mg) will be carried out.
5. On fundamental basis for immiscibility: *ab initio* calculations will be performed on 34 hypothetical ordered Ti-Mg binary compounds, aimed at confirming their inability to form.
6. Determination of theoretical conditions for forming intermetallic compounds will be obtained by applying hydrostatic pressures on hypothetically ordered crystal structures.
7. Crystallographic solid-state transformations in pure metals (Ti, Mg) via slip deformation mechanism as well as under hydrostatic pressure will be investigated from first-principles calculations.
8. The theoretical model (conditions) for achieving ideal complete solid solubility in HCP, FCC and BCC crystal structures will be developed using Mg-Li system as a test case and then applied to study Ti-Mg system.
9. Based on calculated elastic constants, theoretical mechanical stability of HCP,

FCC and BCC solid solutions spanning the entire concentration range ($Ti_{100-x}Mg_x$) will be determined.

The results of this work may contribute to the fundamental understanding of ordered and disordered binary alloys using *ab initio* technique, as well as synthesis of solid solutions during high-energy ball milling. The latter may be applicable to systematically explain other metal powder products synthesised by HEBM of elemental powders.

1.7. Thesis Outline

In Chapter 1, a brief literature review on Ti-Mg alloys synthesized by different non-equilibrium processes will be given. We highlighted the importance and uses of these alloys as well as the advantages of using mechanical alloying process as compared to other processing routes. In Chapter 2, the process of mechanical milling and alloying, the characterization techniques that will be used are presented. Our experimental procedure and product characterization results are presented in Chapter 3 and 4, for Ti-Mg mixtures and pure elemental powders, respectively. We present the theoretical technique that was used in carrying out the calculations of the Mg-Li and Ti-Mg systems, on the basis of the density functional theory and planewave pseudopotentials method in Chapter 5. In Chapter 6, the predicted equilibrium lattice parameters, heats of formation, electronic structure and elastic properties of hypothetical ordered binary Ti-Mg phases as well as their pressure effects on pure metals (Ti, Mg) are presented. The effects of pressure on phase stability, elastic properties and electronic structure of selected Ti-Mg intermetallic phases are shown in Chapter 7. An alternative DFT-based model for handling random binary HCP, FCC and BCC alloys to predict phase stability and mechanical properties, using Mg-Li system as a test case, is presented in Chapter 8. Based on a proposed model, the structural as well as elastic properties of disordered binary Ti-Mg solid solutions under equilibrium and non-equilibrium conditions are presented in Chapter 9, and compared with the available experimental results. We summarize the findings of this study and make recommendations in Chapter 10.

Chapter 2

Methodology I: Mechanical Milling (MM) process and Characterization tools

2.1. Mechanical Milling

Mechanical milling (MM), more commonly known as ball milling (BM), is a powder metallurgy processing technique involving milling of elemental powder or mixture of elemental powders in the correct proportion to achieve alloying through high energy ball impact in a chamber, thus the alloying obtained in this process is called mechanical alloying (MA) [German 1994, El-Eskandarany 2001]. This technique was traditionally used in mineral processing industries for blending powders or crushing rocks to the ultimate fineness. When used for these purposes, the powder particles either remain unchanged or are fractured into smaller particles. Plastic deformation and cold welding of the powder particles usually occur in the milling process. Due to the lack of dramatic and interesting microstructural changes during milling, the purposes of the process used to be rather simple, thus the traditional use of the process lead to the name “mechanical milling” being used since the process did not yield a new material. The technique was developed around 1966 by John Benjamin and his co-workers at the Inco Paul D. Merica Research Laboratory as part of programme to produce oxide dispersion strengthened (ODS) nickel-base superalloys for gas turbine applications [Benjamin and Vollin 1974]. This method has now become an established commercial technique to produce oxide dispersion strengthened (ODS) nickel- and iron-base superalloys for applications in the aerospace industry [Benjamin 1970, 1976, 1990, 1992].

It was only in the early 1970s that Benjamin and co-workers found that by milling a nickel or aluminium alloy powder in an oxidising atmosphere, new powder with each of the powder particles containing a dispersion of oxide particles was produced [Benjamin

1970, 1976, Benjamin and Vollin 1974]. This meant that during milling the oxide layers formed on the surface of powder particles are fractured and further incorporated into the solid powder particles through cold welding, as illustrated in figure 2.1.1. The cold welding was so perfect that the interfaces formed through cold welding became an integral part of the particle. In the mean-time they also found that excessive plastic deformation occurs during milling. Once excessive plastic deformation and cold welding occur during milling, the nature of the milling process is revolutionalized since the milling process virtually resulted in a new powder material which is totally different from the starting powders. Then Benjamin called the milling process “mechanical alloying”. However, it was not widely accepted at that time that this milling process was a true alloying process since, other than familiar surface oxidation of the particles, no true alloying between elements occurred during milling [Zhang 2004].

In early 1980s, Koch *et al* (1983) published a landmark paper which, for the first time, demonstrated that mechanical milling can facilitate true alloying, and the outcome of the alloying can be a metastable material such as an amorphous alloy. In that study, they milled a mixture of Ni and Nb powders, and found that over time the powder became amorphous Ni-Nb alloy powder. This meant that true alloying does occur during milling. This discovery raised the understanding of mechanical milling as a materials processing to a new level. Since the publishing of Koch *et al*.’s work, the term “mechanical alloying” has been widely accepted and used.

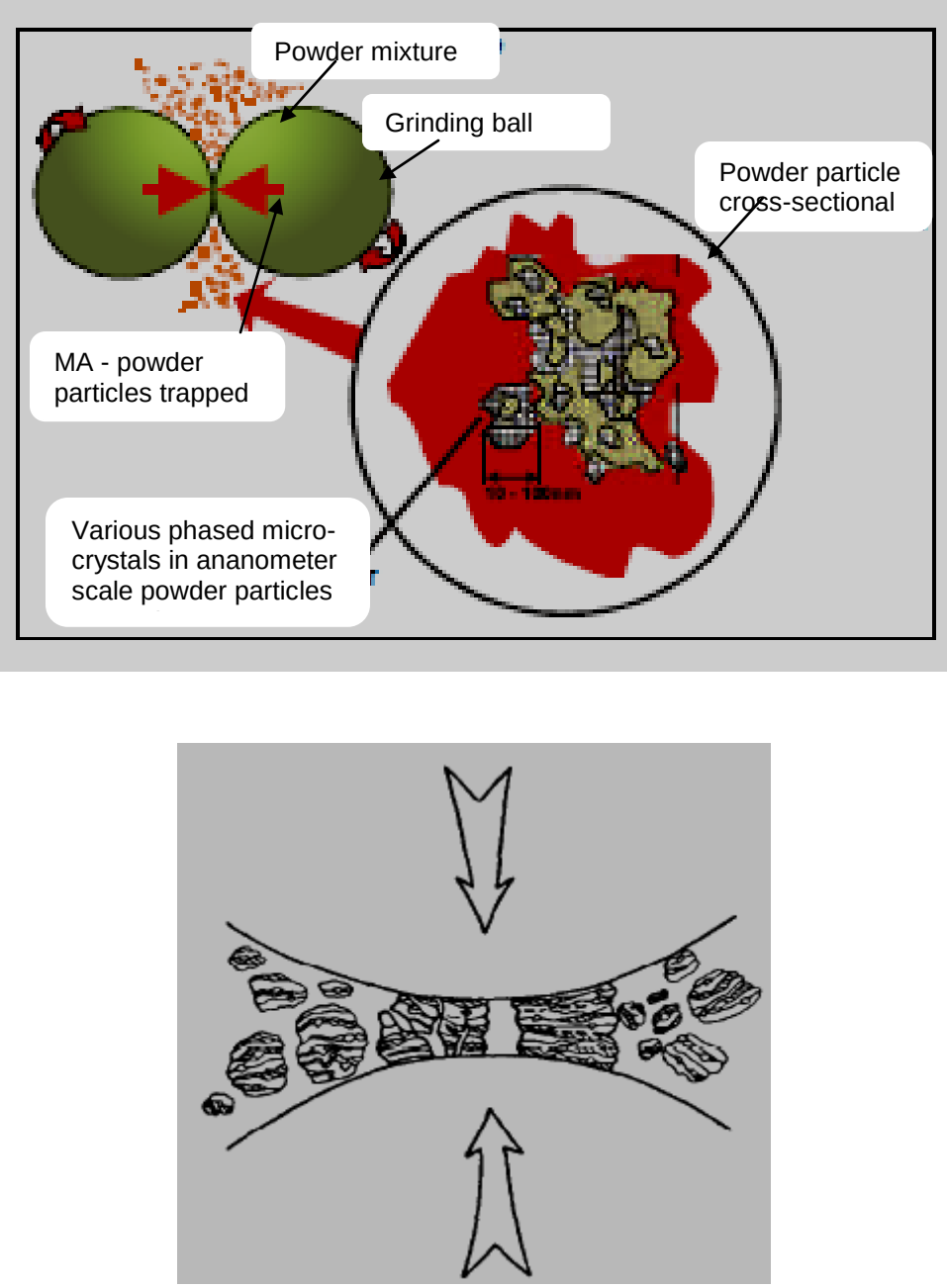

Figure 2.1.1. Schematic diagram of the mechanical milling process [Froes *et al* 1995].

2.2. Mechanical Alloying Mechanism

MA is a solid-state powder processing technique involving repeated welding, fracturing, and re-welding of powder particles in a dry, high energy ball mill under a vacuum or inert atmosphere. During ball milling, powder particles are subjected to high-energy

collision which causes the powder particles to be cold welded together and fracture into fine particles. Cold welding and fracturing enable powder particles to be always in contact with each other and atomically clean surfaces and with minimized diffusion distance.

The MA process has become a solid-state processing technique recently used to synthesize composite, equilibrium and non-equilibrium (amorphous, quasicrystals, nanocrystalline, etc.) materials that are of commercial useful and scientifically interest [Ma 2005, El-Eskandarany 2001, Gardiner *et al* 1996]. The ball mills employed have a chamber containing an agitated media and powder charge. Powder is trapped during media collisions, causing severe plastic deformation, as shown in figure 2.1.1. If two or more different powders are placed in the mill, the particles will aggregate forming a coarse composite and subsequently fragment. Repetition of this process refines the composite structure until fine mixing is achieved and the two powders combine chemically by diffusion or reaction process, creating an alloy in the solid state [Benjamin 1990]. Thermomechanical processing of consolidated material gives the opportunity to develop a wide range of mechanical properties, depending on the alloy composition and the property balance required [Gardiner *et al* 1996].

The energy transfer to powder particles in these mills takes place by grinding/shearing action upon collision between two relatively massive balls or between a milling ball and the inner walls of the vial or milling chamber. The chaotic collisions result in plastic deformation of the particles (producing dislocations, vacancies and atomic disorder), which introduces strain into the particle system. The particles then become cold welded (the joining of materials without the use of heat), which develops lamellar structures with alternate layers of elements. With continued milling, the strain is relieved by fracture (i.e. grain refinement) of the powder. Initially, micro-forging flattens ductile powders into flaky/plate-like particles. As the elemental particles are repeatedly cold welded and then fractured, the lamellar structure is continually refined until a steady state is established between welding and fracturing frequencies and the layers cannot become any thinner. The particle size tends to reach equilibrium. At this stage, alloying begins with a continuous decrease in the inter-lamellar distance of each particle as the thermal

diffusion of one element into the other at layer boundaries occurs to form the alloy. In ductile/ductile systems such as Nb and Sn, the lamellae diffuse to form the alloy Nb_3Sn, provided the correct stoichiometric ratio of constituent elements is present. Ideally, mechanical alloying should result in a homogeneous, amorphous powder.

2.3. Mechanical Alloying of Immiscible system

It is generally thought that homogenisation during high-energy ball milling occurs because a number of conditions that allow solid state reactions to occur at relatively low temperatures are achieved simultaneously during high-energy ball milling [Schaffer and McCormick 1992]. Firstly, an extremely large reaction interfacial area is produced as a result of the microstructural refinement that arises from the process of repeated deformation, fracture and cold welding of powder particles during milling. This interfacial area actually increases during milling as the crystalline size is refined. The same process dynamically maintains the interfacial area during milling, as particles are continually fractured and rewelded, bringing unreacted components into intimate contact. The heavy plastic deformation experienced by the powder particles during milling introduces a high density of crystal defects such as dislocations, vacancies, stacking faults and an increased number of grain boundaries [Schaffer and McCormick 1992]. This defect structure results in an increased rate of diffusion in milled powders. The local temperature increase resulting from collisions between milling media would further assist diffusion behaviour [Suryanarayana 2001].

However, some recent studies have begun to question whether solid state diffusion plays any significant role in the process of high-energy ball milling. Cocco *et al* (2000) examined the high-energy milling process on a quantitative basis, as a function of processing parameters. They concluded that diffusion plays only a minor role in high-energy milling process, involving only short-range atomic rearrangements and relaxation phenomena. Shtremel also queried the significance of diffusion during high-energy milling [Shtremel 2002]. Shtremel began by considering a number of binary metal systems where mutual solid solubility is virtually absent under thermodynamic

equilibrium and yet, in these systems, homogeneous solid solutions can be produced from equiatomic mixtures of pure metals by high-energy milling. Shtremel then noted that diffusion occurs in the direction that lowers the free energy of the system; occurring in the direction of homogenisation in systems with unlimited solubility and in the direction of layering in the absence of solubility in thermodynamic equilibrium. Since homogeneous solid solutions can be produced by high-energy milling in systems with little or no mutual solubility, diffusion cannot be the principal mechanism of high-energy milling. Shtremel supports this claim with estimates that suggest that diffusion during high-energy milling, even allowing for accelerated diffusion due to crystal defects and localised heating, would “cause displacement of the components by a distance not exceeding tens of interatomic distances”. The key point, argued Shtremel, is that any diffusion during high-energy milling should accelerate the homogenisation of the mixture in systems with unlimited solubility and decelerate it in the absence of solubility at equilibrium. Shtremel could not find evidence of this difference in the rates of high-energy milling. Finally, it was proposed that mixing by shear, or “shear displacement”, is the principal mechanism of high-energy milling.

Another work by Lu *et al* (1997) has ascribed mechanical alloying to two key factors, firstly, activation energy which is related to the formation of defects during the collision of powder particles and secondly, crystalline size which is related to the formation of nanometer crystalline during milling. They pointed out that the decrease in activation energy (barrier) can result in an increase in diffusivity at constant temperature, thus a decrease in energy barrier is equivalent to an increase in temperature. Through repeated fracturing and cold-welding of powder particles, crystalline particles of nanometer size can be created and therefore diffusion can occur easily via grain boundaries. It was thus concluded that even elements which are difficult to diffuse may be alloyed using MA technique.

It has now been accepted that the most important reason for the increase in solid solubility is the formation of nanostructures during milling [Suryanarayana *et al* 1990]. The large volume fraction of atoms residing in grain boundaries in these ultrafine-

grained materials is expected to enhance diffusion and, consequently, increase the solid solubility.

2.4. Milling Parameters

Mechanical alloying requires a certain optimisation of various milling parameters in order to achieve the desired physical and chemical structures of a sample.

2.4.1. Milling media

The media used to make a vial is an important factor in milling, since the grinding and impact of the milling balls on the inner surface of the vial can chip away this media, incorporating it into the sample. This can change the stoichiometry of a sample (if vial is of the same media), hence contamination. In order to avoid contamination, it is normal to manufacture the vial from the same material as the sample being milled. However, a stainless steel vial was chosen for milling in this experiment to investigate any contamination effects. Process control agent is used to avoid cold welding on the surfaces of the balls and on the walls of the vial.

2.4.2. Milling atmosphere

Another potential source of contamination during high-energy ball milling is the milling atmosphere. At the high temperature involved during milling, particles expose fresh atomic surfaces throughout the welding and fracturing process, which can introduce oxide and nitride formation in the milling media if milled in air. Contamination is easily prevented by milling in an inert, high purity argon atmosphere. This is made possible by preparing the sample and sealing it air-tight in the vial in an argon filled glove box, which has an oxygen content <3ppm.

2.4.3. Milling speed

The rotation speed of the blades has a huge influence on the milling intensity and hence structural evolution of the sample. Generally, faster rotation speed result in the milling balls transferring more kinetic energy through collisions into the sample. One issue with high milling intensities is that the temperature of the powder may become too high and could form the intermetallic directly through high temperature diffusion of the atoms. Although it has been recorded that high temperatures promote diffusion required for alloying, this also favours the particles recovery from atomic disorder, which means the required microstructure might not be achieved.

2.4.4. Milling time

The milling time is the most important factor in mechanical alloying as ultimately, the formation of the alloy depends on the steady state between cold welding and fracture of the powder particles being achieved. Although the milling time is governed by factors such as the milling intensity and temperature involved, it has been recorded that contamination levels increase with milling time and undesirable phases can be formed if it is longer than required.

2.5. Characterization techniques

2.5.1. SEM, EDS and EBSD analyses: Morphological and microstructural changes

The scanning electron microscope (SEM) is a type of electron microscope that images the sample surface by scanning it with a high-energy beam of electrons in a raster scan pattern. The electrons interact with the atoms that make up the sample producing signals that contain information about the sample's surface topography, composition and other properties such as electrical conductivity.

The types of signals made by an SEM can include secondary electrons, back scattered electrons, characteristic x-rays and light (cathodoluminescence). These signals come from the beam of electrons striking the surface of the specimen and interacting with the sample at or near its surface. In its primary detection mode, secondary electron

imaging, the SEM can produce very high-resolution images of a sample surface, revealing details about 1 to 5 nm in size.

Furthermore, it is necessary to identify the different elements associated with the specimen. This is accomplished by using the “built-in” spectrometer called an Energy Dispersive X-ray Spectrometer (EDS). EDS is an analytical technique which utilizes x-rays that are emitted from the specimen when bombarded by the electron beam to identify the elemental composition of the specimen. To explain further, when the sample is bombarded by the electron beam of the SEM, electrons are ejected from the atoms on the specimen’s surface. A resulting electron vacancy is filled by an electron from a higher shell, and an x-ray is emitted to balance the energy difference between the two electrons. The EDS x-ray detector measures the number of emitted x-rays versus their energy. The energy of the x-ray is characteristic of the element from which the x-ray was emitted. A spectrum of the energy versus relative counts of the detected x-rays is obtained and evaluated for qualitative and quantitative determinations of the elements present.

However, the identification of unknown micron-sized phases in the SEM has been limited by the lack of a robust and simple way to obtain crystallographic information about the unknown while observing the microstructure of the specimen [Goehner and Michael 1996]. However, with the development of charge coupled-device (CCD)-based detectors, backscattered electron Kikuchi patterns (BEKP), commonly referred to as electron backscattered diffraction (EBSD) patterns or simply EBSP, could be easily collected [Schwarzer 1997]. When EBSD is employed as an additional characterization technique to a SEM, enables individual grain orientations, local texture, point-point orientation correlations, and phase identification and distributions to be determined routinely on the surfaces of bulk polycrystals.

In brief, EBSD patterns are generated a phosphor screen by backscatter diffraction of a stationery beam of high-energy electrons from a volume of material of crystal approximately 20 nm deep in the specimen times the projected area of the incident

beam. The characteristic feature of a backscatter Kikuchi pattern is the regular arrangement of parallel bright bands on a steep of continuous background rather than a regular array of diffraction spots as is generated in the TEM in selected area diffraction from a single crystallite. The intersections of Kikuchi bands form prominent and distinct zone axes. The geometry of a Kikuchi pattern can be interpreted as a gnomonic projection of the crystal lattice on the flat phosphor screen. The point of impingement of the primary beam on the specimen surface is the center of projection. The lattice planes can be imagined to be stretched out to intersect the screen in the center of the lines of their related Kikuchi bands. Figure 2.5.1.1 contains a schematic showing the incident beam on the specimen with a given unit cell orientation and a specified diffracting plane giving rise to backscattered Kikuchi diffraction. The two diffracting cones are the edges of the Kikuchi band, and the plane through the center of these cones is the geometric projection of the diffracting plane onto the phosphor screen. When more than one such Kikuchi band is considered, the angles between the projected plane normal orientations correspond to the interplanar angles, and the angular width of a Kikuchi band {*hkl*} is twice the Bragg angle. Thus, the width of the bands is related to the interplanar spacing, d_{hkl}, according to Bragg's law,

$$n.\lambda = 2d_{hkl}\sin\theta_{hkl} \qquad (2.5.1.1)$$

where n is the order of reflection and λ is the wavelength of the incident electron beam, which is dependent on the accelerating voltage of the SEM. The extinction rules for the expected reflections (i.e., Kikuchi bands) of the specific crystal structure are determined by the structure factor of the crystal structure. Phase identification is achieved in the following manner.

First, a feature of interest is identified in the SEM on the tilted specimen using the appropriate imaging signal (backscattered or secondary electrons). An EBSD pattern is then collected from the feature of interest using a stationery beam in the same way that x-ray information is obtained. A flat image is then obtained and used to flat field the raw data image data. Using EDS, compositional data is also obtained from the feature of

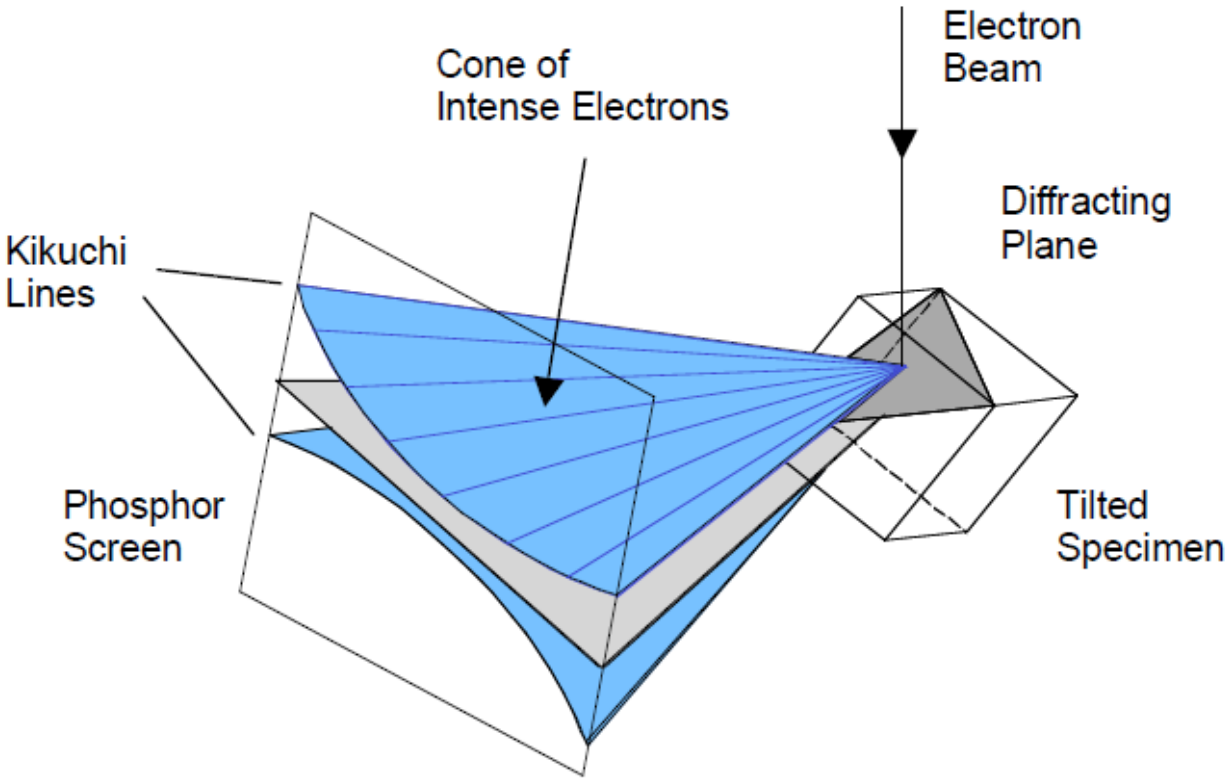

Figure 2.5.1.1. Schematic of the diffraction cones with respect to the reflecting plane, the specimen and the phosphor screen.

interest as this information is used to limit the number of possible candidate materials that could produce EBSD pattern.

Secondly, the interplanar spacings and crystal plane angles are extracted from the EBSD patterns by a Hough transform algorithm. This information is used to derive the reduced cell volume or subcell volume. The subcell volume along with the elemental information is used to search the ICDD's powder diffraction data base. The software takes the results of this search and attempts to assign (*hkl*)'s to the Kikuchi lines that are consistent with the observed (*hkl*)'s from the pattern. Once a candidate phase is identified, its Kikuchi pattern is simulated in the correct orientation and overlaid onto the observed pattern for comparison. If the agreement between the experimental and the simulated pattern is good, then identification is assumed to have been accomplished.

2.5.2. X-ray Diffraction (XRD): phase evolution

The Philips PW 1830 diffractometer which emits x-rays from a monochromatic Cu Kα radiation source at a wavelength, λ=0.15405 nm, will be used in this study. The arrangement of atoms in an ideal crystal structure can be described as having a regular geometrical symmetry and long-range order. The technique of XRD allows various crystal structures present in a sample to be determined. Diffraction is the interference of scattered x-ray waves without energy transfer. This happens through the interaction of incident photons (x-rays) with the electrons of the atoms in the crystal lattice. The scattered waves, which are coherent with the incident wave, constructively interfere at a certain angular positions to a crystal plane known as Bragg angles. These angles can then be used to determine the Miller indices (hkl values) of the particular diffracting plane in question and help determine the structure of the crystal. A series of diffraction peaks are obtained according to Bragg's law,

$$\lambda = 2d_{hkl}\sin\theta \qquad (2.5.2.1)$$

where d_{hkl} is the interplanar spacing in the crystal lattice and θ is the angle between the incident x-rays and scattering planes. The angular position, 2θ, of the diffraction peaks of the x-rays are then matched to standard spectra using computer analysis software connected to the diffractometer. X-ray diffraction can also indicate to the purity of a sample, as any crystalline contaminants are also detected. However, any amorphous phases (described as having an irregular, short-range order of atoms) appear as a smooth background on the diffraction spectra. The grain size and strain of the sample can be extracted from the width of the diffraction peak. Effectively, ball milling reduces the grain size and introduces strain into the sample and although the peak width is dependent on the diffractometer resolution, these physical factors also contribute. These factors are signified by the broadening of the diffraction peaks. The grain size reduction results in less diffracting planes. When crystallites are less than approximately 1000 Å in size, appreciable broadening in the x-ray diffraction lines occurs. These regions may in fact correspond to the actual size of the particles. The observed line broadening can be used to estimate the average size. In the simplest case where the

particles are stress-free, the size is estimated from single diffraction peak. But in those cases where stress may be present, a more robust method involving several diffraction peaks is required. Generally, the x-ray diffraction peak broadening is due to the instrumental broadening, broadening due to crystallite size and lattice strain present in the material. The contributions of each of these effects are convoluted causing an overall broadening of the diffraction peaks. Before estimating the crystallite size and lattice strain, it is necessary to correct the instrumental effect. The instrumental corrected broadening (β_{hkl}) is estimated using the equation

$$\beta_{hkl} = \left[(\beta_{hkl})^2_{measured} - (\beta)^2_{instrumental}\right]^{1/2} \qquad (2.5.2.2)$$

Although it is well known to provide only the lower bound to the crystallite size, the classical Scherrer equation [Warren 1969]:

$$D = \frac{k\lambda}{\beta_{hkl}\cos\theta_{hkl}} \qquad (2.5.2.3)$$

can be used to determine average crystallite size if the analyzed crystals are free from microstrains and defects, in which peak broadening depends only on the crystallite size and diffractometer characteristics. In equation 2.5.2.3, β_{hkl} is the broadening of the *hkl* diffraction peak measured at half of its maximum intensity (in radians), *D* is the crystallite size, λ is the wave length of the X-rays (λ=0.15405 nm for Cu Kα radiation), *k* is the shape factor (*k*=0.9) and θ_{hkl} is the Bragg diffraction angle (degrees).

Alternatively, the crystallite size may also be obtained using the method proposed by Williamson-Hall (1953) through the use of the following equation:

$$\beta_{hkl}\cos\theta_{hkl} = \frac{k\lambda}{D} + 4\varepsilon\sin\theta_{hkl} \qquad (2.5.2.4)$$

where ε is the lattice strain under the assumption that the nature of the crystal is isotropic and the strain present in the material is uniform. In addition to the instrument x-ray peak broadening, lattice strain and crystallite size are the other two independent factors that contribute to the total peak broadening. The strain induced line broadening β_s is given by the relation:

$$\beta_s = 4\varepsilon \tan\theta_{hkl} \qquad (2.5.2.5)$$

Now the total peak broadening is represented by the sum of the contributions of crystallite size and strain present in the material. When a plot is drawn by taking 4sin θ_{hkl} along *X*-axis and β_{hkl} cos θ_{hkl} along *Y*-axis, the strain (ε) present in the material and crystallite size (*D*) are, respectively, extracted from the slope and the *Y*-interecept of the linear fit made to the plot.

Chapter 3

Microstructure and phase evolution of Ti-Mg powder mixtures upon ball milling process

3.1. Introduction

Based on the background in chapter 1 on binary Mg_x-Ti_{1-x} alloys, in this chapter, we firstly investigate the effect of milling speed and the Mg to Ti starting average particle size ratio on morphology and solid solution kinetics during the mechanical alloying process, using SEM and EDS characterizing techniques.

Secondly, the effect of milling speed and time on the evolution of both the microstructure and crystal structure of equimolar mixture of fine elemental Ti and Mg powders using SEM, XRD and TEM techniques is studied. This is aimed at determining the onsets for formation and the distribution of new product phases with new crystal structures during ball milling at high rotation speeds. It is believed that the control of the crystal structure of the Mg–Ti milled product will determine the hydrogen storage performance of the mechanical alloy.

Finally, the effect of starting composition on crystal structure evolution during mechanical milling process using XRD measurements is investigated.

3.2. Experiments

3.2.1. Effect of milling speed and the starting average particle size on morphology

3.2.1.1. Experimental procedure

Ball milling of equiatomic Ti-Mg elemental powders was conducted in a horizontal Simoloyer CM01 fitted with a cylindrical grinding unit (milling chamber) with a 2 L capacity as shown in figures 3.2.1.1.1 and 3.2.1.1.2 respectively, under a pressure of 2 bars in an argon atmosphere.

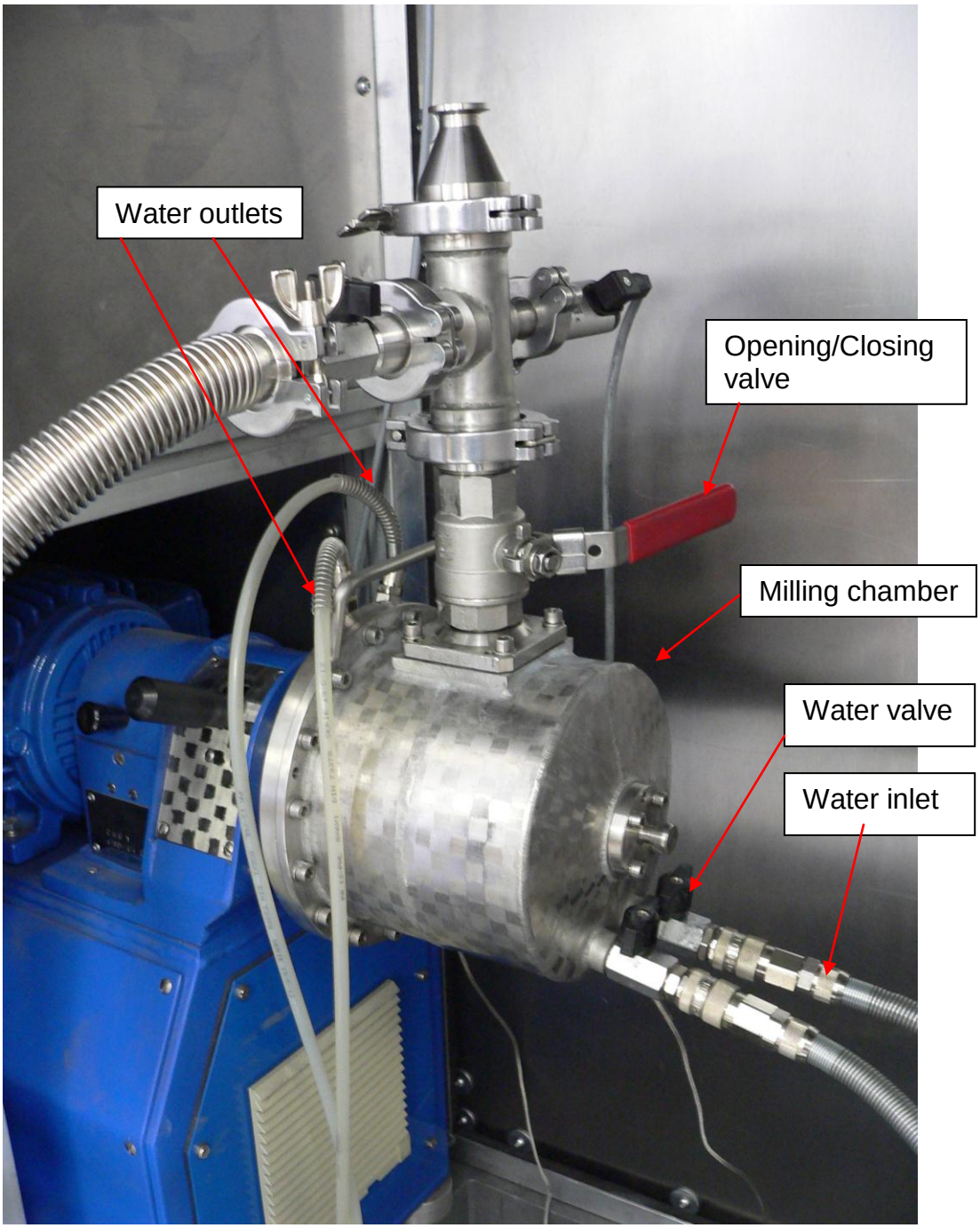

Figure 3.2.1.1.1. Simoloyer ball milling machine supplied by Zoz GmbH.

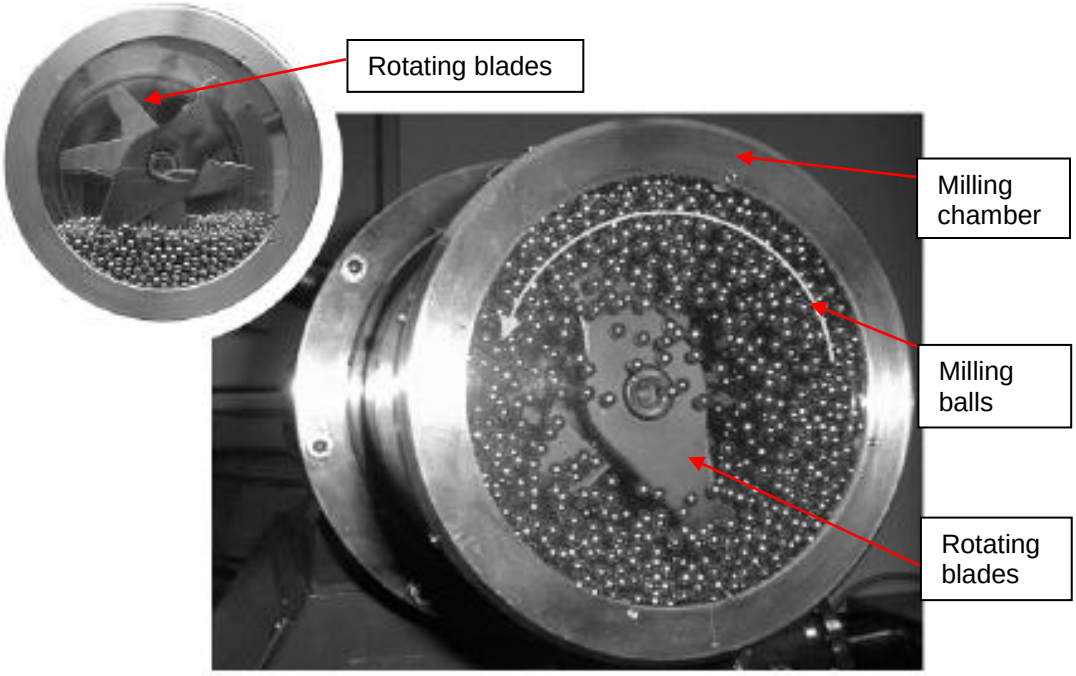

Figure 3.2.1.1.2. Illustration of Simoloyer ball milling process in a grinding unit or milling chamber.

During mechanical milling experiments, the milling chamber is static whereas the milling balls are rolled at high speed by a series of large welded blades on a horizontal rotating shaft. Hence the mechanical energy is transferred from the shaft to the milling balls when in contact with the moving blades. The 4.7 mm diameter 100Cr6 stainless steel balls were used as grinding media. Pure titanium powder (~99.5% purity, < 45 µm) was manually mixed with pure magnesium powder (~99.5% purity). Two starting particle size ranges were considered for the magnesium powders, i.e., coarse: 0.3 - 0.6 mm (300 – 600 µm), and fine: < 45µm. Three different milling speeds (rotation speed of the impellers) i.e. 200, 400 and 800 revolution per minute (rpm) were considered for milling times ranging from 1 to 72 hours. The three rotation speeds represent a low-energy, intermediate and high-energy milling processes, respectively. The ball to powder ratio, on the other hand, was kept constant equal to 10:1. The amount of stearic acid added to the powder mixture, as process control agent (PCA), was also kept constant at 2 weight percent (wt. %). Ball-milling was conducted uninterruptedly for each milling time. The powder transformation during milling, i.e. the evolution of microstructure and crystal

structure of the powder particles and their polished cross sections were analysed using respectively LEO 1525 field-emission scanning electron microscope (FE-SEM coupled with a Robinson Backscatter Electron Detector (RBSD) fitted with an Oxford Link Pentafet energy dispersive x-ray spectroscopy (EDS) detector and Phillips PW 1830 X-ray diffraction (XRD) machine fitted with Cu Kα radiation, and 0.02 step size scanned from 10 to 90^{o} (2θ) was used XRD using a Cu K_{α} source. The yield was determined as the ratio of the weight of the collected powder after milling to the initial weight introduced in the milling chamber.

3.2.1.2. Results and discussion

3.2.1.2.1. Effect of starting magnesium powder particle size and milling speed

The effect of the starting particle size of the magnesium powder was investigated by means of scanning electron microscopy, SEM. The morphology and microstructure of the milled powders evolved with milling time are illustrated in figures 3.2.1.2.1.1(a) through to 3.2.1.2.1.1(d), in the case of a low-energy ball milling (200 rpm). The harder fine titanium powder particles (< 45 μm) were entirely glued on the surface of the ductile coarse magnesium particles (> 300 μm) as shown in figure 3.2.1.2.1.1(a). The powder particles became more equiaxed as low-energy ball milling proceeded (Figure 3.2.1.2.1.1(b) and (c)). In the meantime the finer titanium particles, still not deformed, sunk deeper into the ductile magnesium particles. Plastic deformation and cold welding of the powder particles, essential to mixing by means of solid state diffusion of the titanium and magnesium atoms, was only observed after milling for more than 32h. It also emerged from figure 3.2.1.2.1.1(d), that only the magnesium particles virtually enforced by the insertion of the small titanium particles were plastically deformed enough and produced a layered structure, and a mixing of titanium and magnesium. Those particles became elongated following the deformation axis. The magnesium particles within which titanium particles did not sink deep enough are less deformed and still present as an unmixed core of pure magnesium.

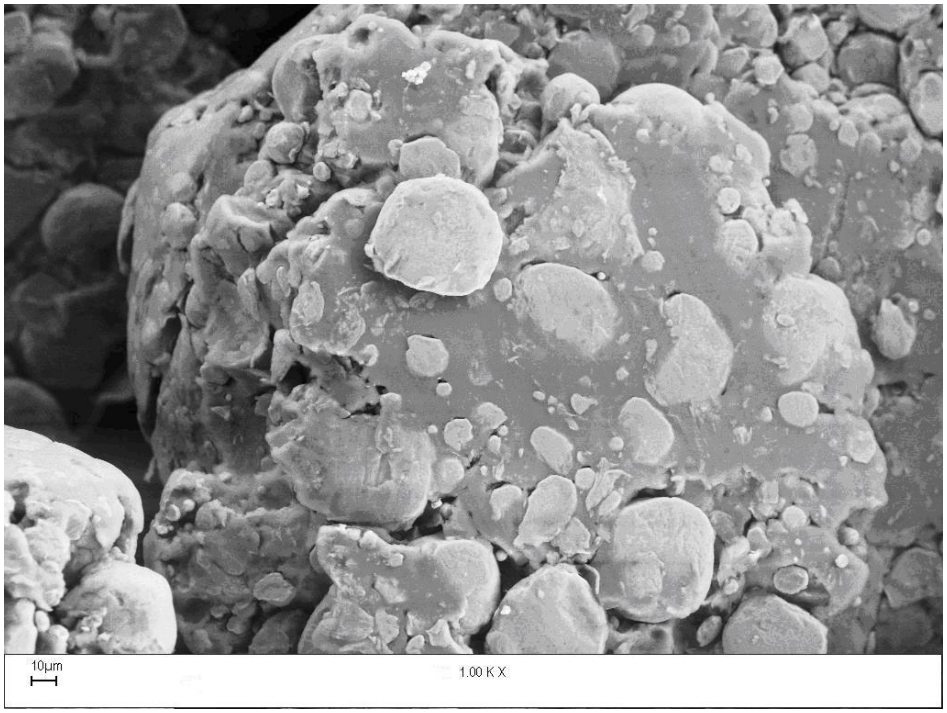

Figure 3.2.1.2.1.1a. SEM image of powder milled for 1h at 200 rpm showing titanium (lighter) particles adhered on the surface of coarse magnesium (darker) particles.

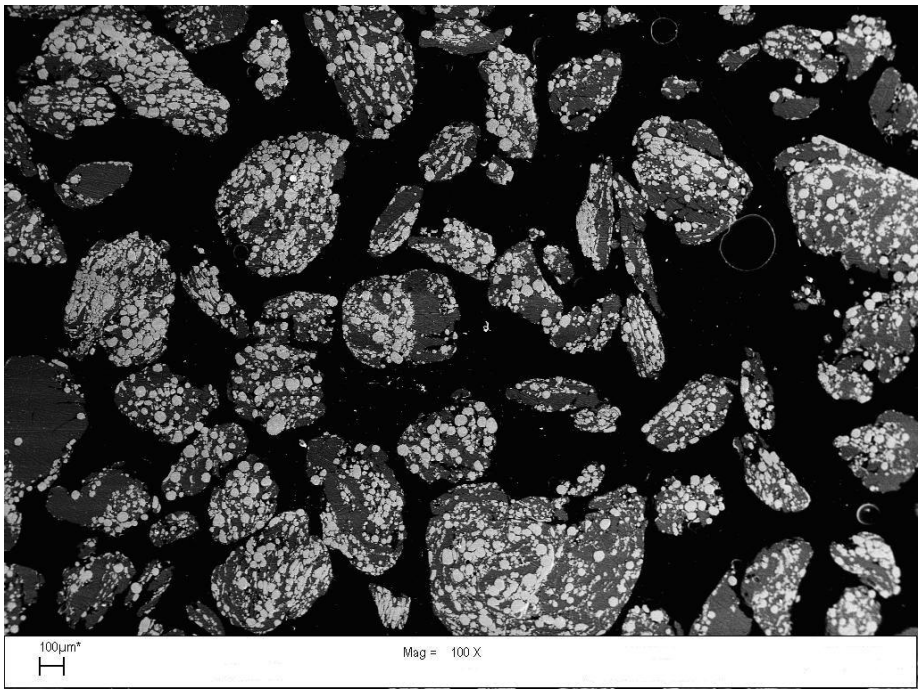

Figure 3.2.1.2.1.1b. SEM image showing the distribution of lighter (Ti) and darker (Mg) particles in the cross section of powder mixture after 8h low-energy ball milling.

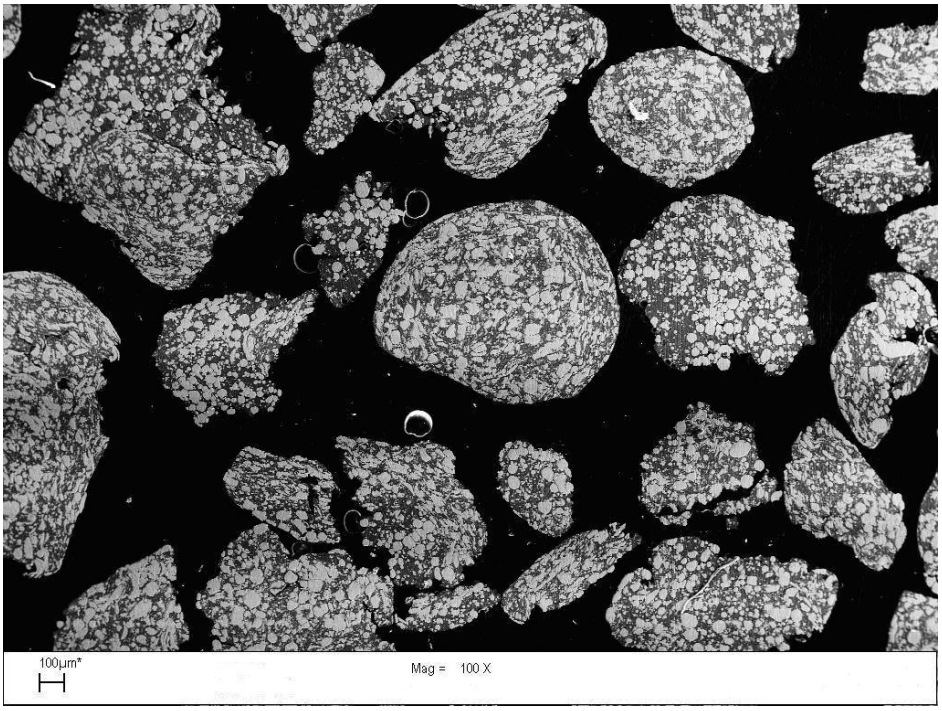

Figure 3.2.1.2.1.1c. SEM picture showing the more equiaxed particles morphology of powder mixture after 16h low-energy ball milling (200 rpm).

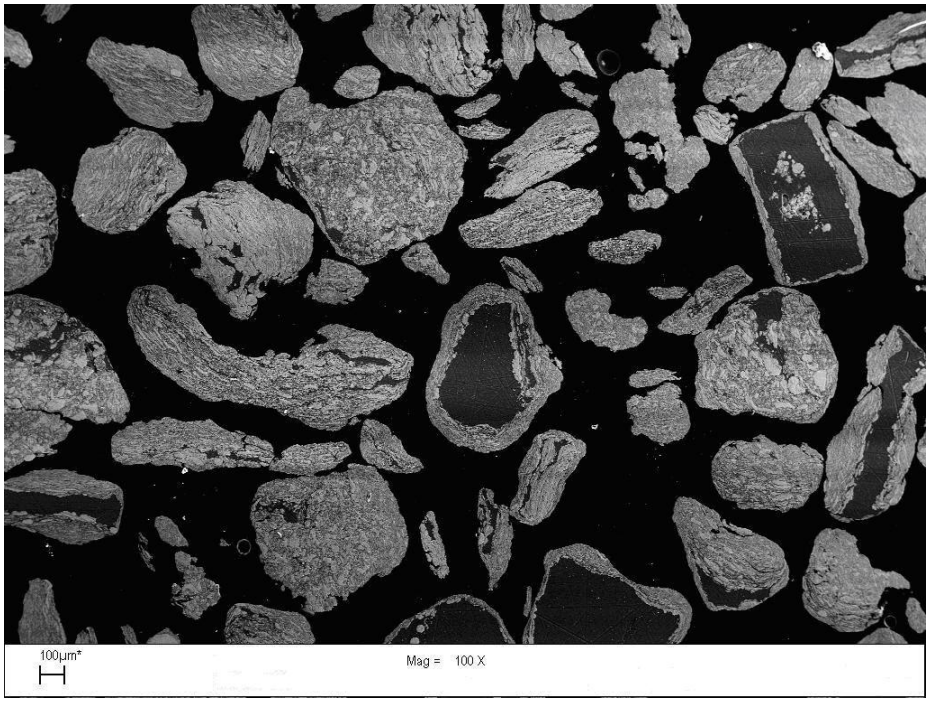

Figure 3.2.1.2.1.1d. SEM image of elongated morphology of powder mixture showing the heterogeneous layer structure formed in the surface of the milled particles and an unmixed core comprised of mainly dark (Mg) particles after 32h low-energy ball milling (200 rpm).

Increasing the milling speed to 400 rpm for 24h led to flattening of both elemental particles in some areas and still coarse in some, as shown in figures 3.2.1.2.1.2(a) and (b) with corresponding EDS spectra indicating slight mixing. The high-energy ball milling of a mixture of fine magnesium (< 45 µm) and titanium powder (< 45 µm), on the other hand, led to a different formation mechanism. Contrary to the insertion and grafting of the hard small particles (Ti: < 45 µm) into the surface of large ductile particles (Mg: >300 µm) as observed when the starting magnesium powder was coarser, the high-energy ball milling of equally fine Ti and Mg particles (< 45 µm) first induced a heavy plastic deformation of both titanium and magnesium particles separately after milling for 1h. The plastic deformation of separated particles was followed by the cold welding of the individual elongated particles and by the formation of the fine layered structure after milling for 4h at 800 rpm as shown in figure 3.2.1.2.1.3(a). The high impact pressure exerted on the titanium particles during high-energy ball milling was enough to even break the plastically deformed particles into ultrafine particles (~2 µm) as illustrated in figure 3.2.1.2.1.3(b). These ultrafine particles present a higher specific surface that may enhance the interdiffusion between titanium and magnesium particles, hence to an effective mechanical alloying process.

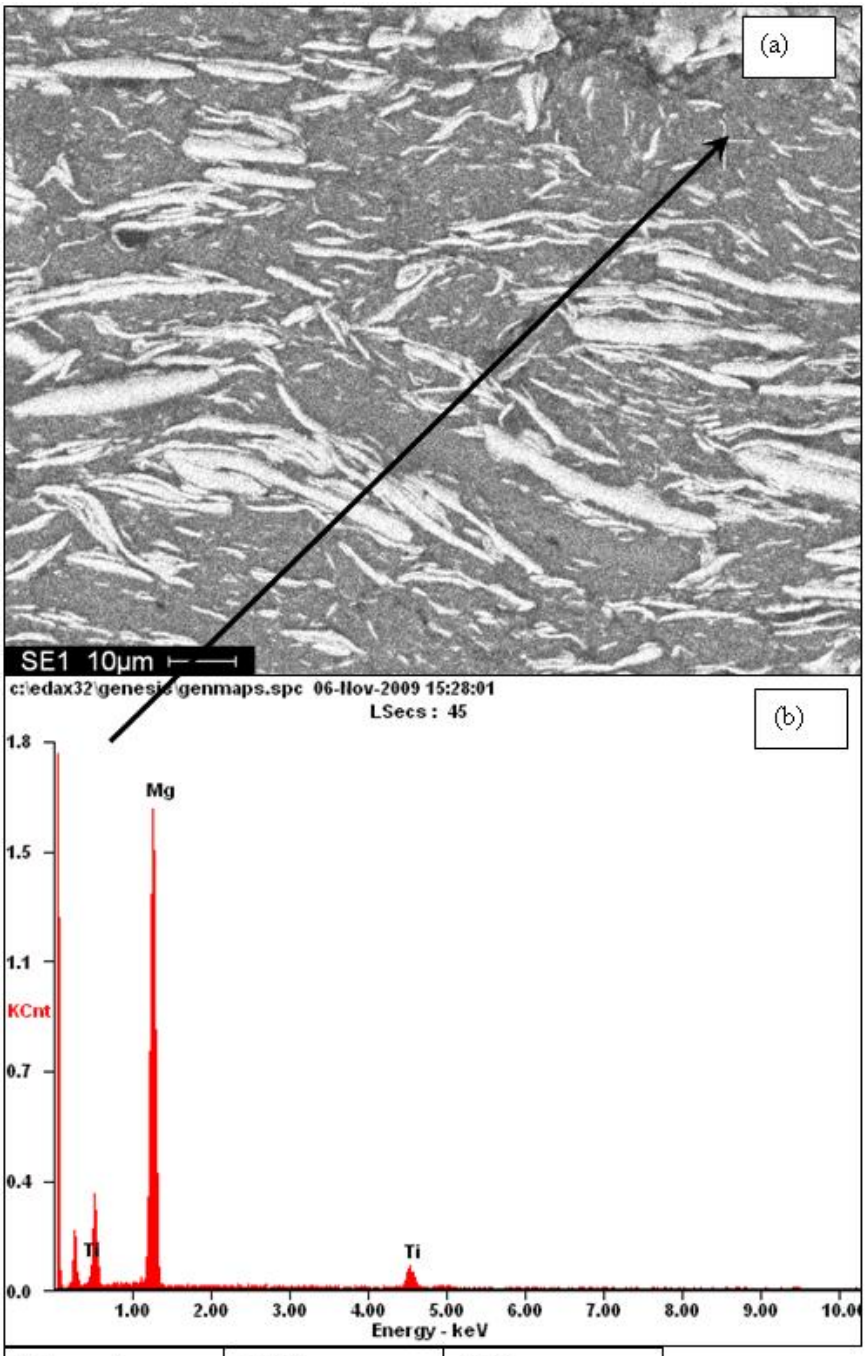

Element	*Wt%*	*At%*
MgK	84.22	91.32
TiK	15.78	08.68

Figure 3.2.1.2.1.2a. SEM image of coarse Mg milled with fine Ti powder at 400 rpm for 24h showing flattened layers of lighter (Ti) particles around Mg (dark) dominated areas, accompanied by the EDS spectrum of Mg-rich dark spot and the attached table showing the spot composition.

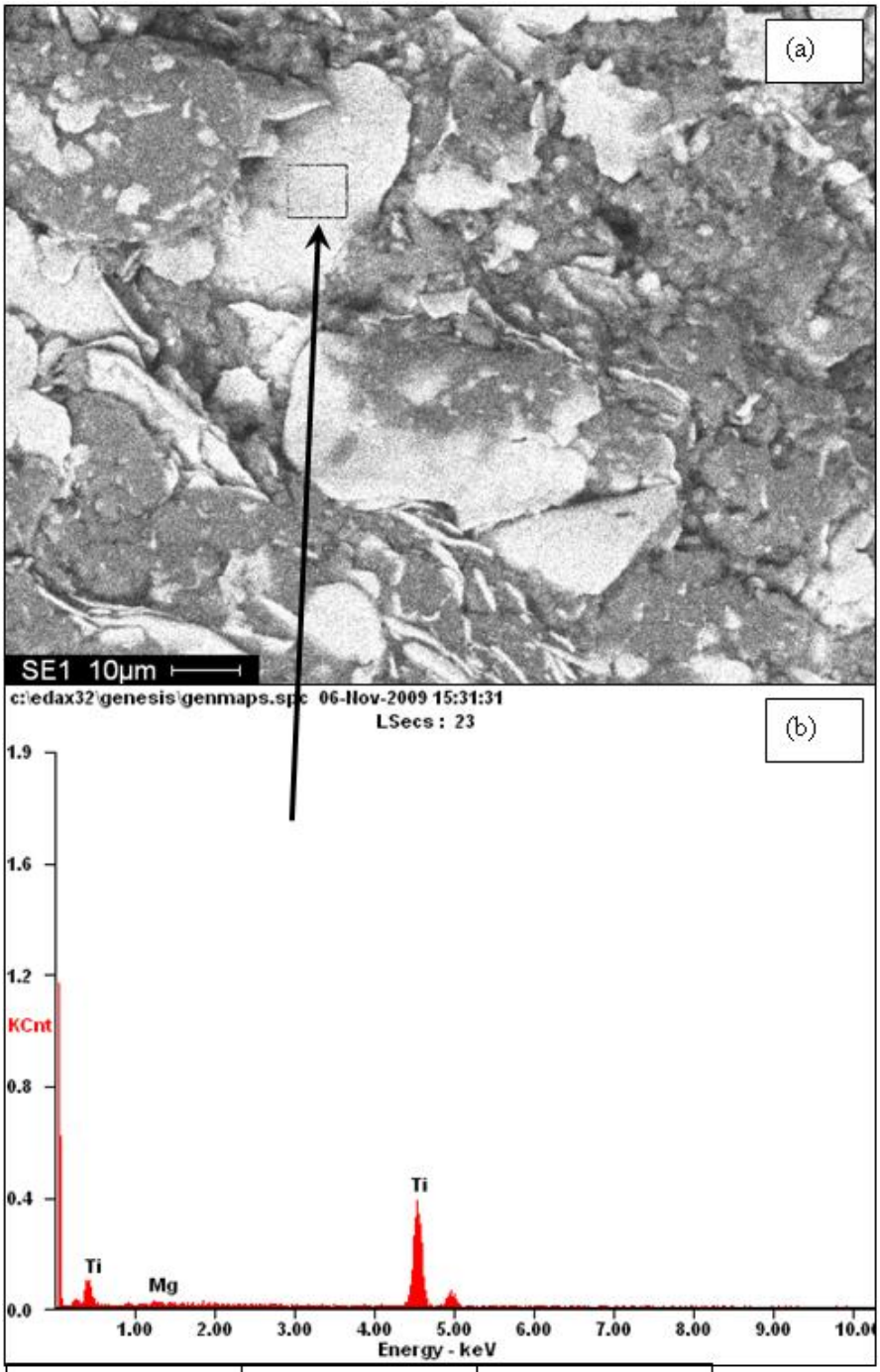

Element	*Wt%*	*At%*
MgK	01.43	02.79
TiK	98.57	97.21

Figure 3.2.1.2.1.2b. SEM image of coarse Mg milled with fine Ti at 400 rpm for 24h indicating coarse Ti (lighter) particles mixed with little Mg (dark) particles, confirmed by accompanied EDS spectrum and its attached chemical composition table.

Figure 3.2.1.2.1.3a. SEM image of high-energy ball milled powder showing fine plastically deformed powder particles of titanium (bright) and magnesium (dark) and some layered structure formed after 4h at 800 rpm.

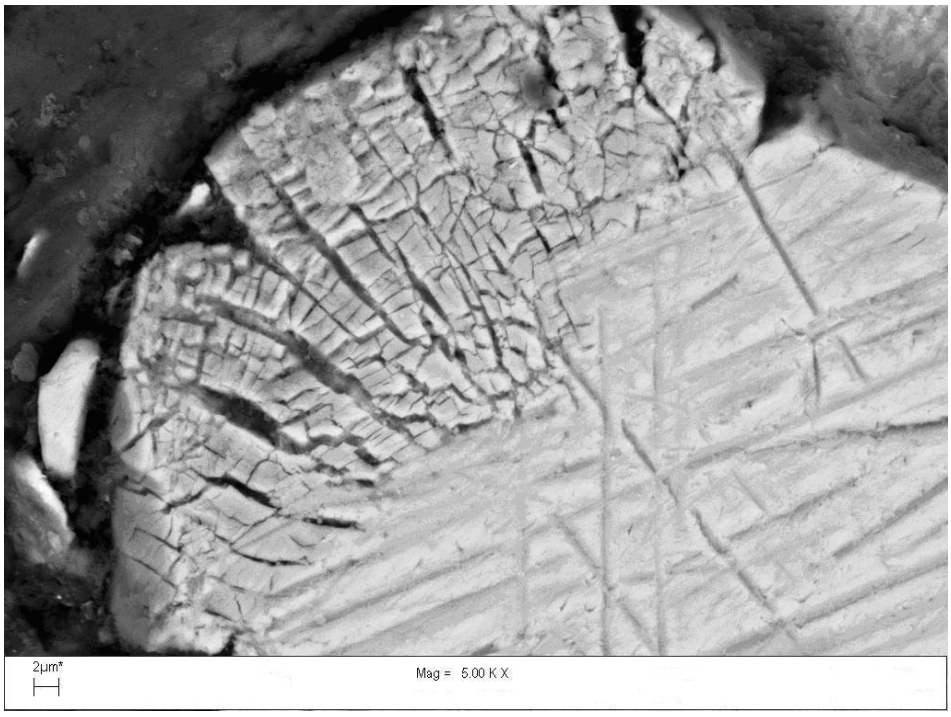

Figure 3.2.1.2.1.3b. SEM picture illustrating the fracturing of the small plastically deformed lighter (Ti) powder particle upon 24h high-energy ball milling (800 rpm).

3.2.1.2.2. Alloying process effectiveness

The ball milling aimed at producing the metastable $Ti_{50}Mg_{50}$ by mechanically alloying of elemental powders was performed. The phase distribution through the cross sections of the milled powders was analysed by means of SEM and the corresponding chemistry determined by EDS (Energy Dispersive X-ray) analysis. Low-energy ball milling (200 rpm) of the coarse magnesium particles and fine titanium particles did not produce a homogeneous microstructure. The spot analyses of different locations in the milled particles are shown in figure 3.2.1.2.2.1(a) while the corresponding EDS spectra are presented in figures 3.2.1.2.2.1(a-1), 3.2.1.2.2.1(a-2), 3.2.1.2.2.1(a-9) and 3.2.1.2.2.1(a-12) and summarized in table 3.2.1.2.2.1. It follows from table 3.2.1.2.2.1 that, ball milling for 32h, starting with coarse ductile magnesium particles (300 – 600 µm), did not induce mechanical alloying of titanium and magnesium. The small traces of C and O are due to presence of stearic acid. The cores of the milled particles were composed of pure magnesium whereas a titanium-rich shell was formed on the surface. The higher SEM magnification (X2000) of the above mentioned shells showed that there was no mixing at all between the two metals. Some fracturing of the heterogeneous layer structure formed on the surface of the coarse magnesium particles was observed in areas of the milled powders where the mixing seemed to have occurred, as shown in figure 3.2.1.2.2.2. On the other hand, milling for more than 32h at 800 rpm produced a homogeneous single phase titanium-magnesium alloy as shown in figure 3.2.1.2.2.3. The chemistry of the single phase varied between $Ti_{56}Mg_{44}$ and $Ti_{50}Mg_{50}$. The typical microstructure of the single phase is illustrated in figure 3.2.1.2.2.3. The summary of SEM observations at different milling parameters is tabled in table 3.2.1.2.2.2.

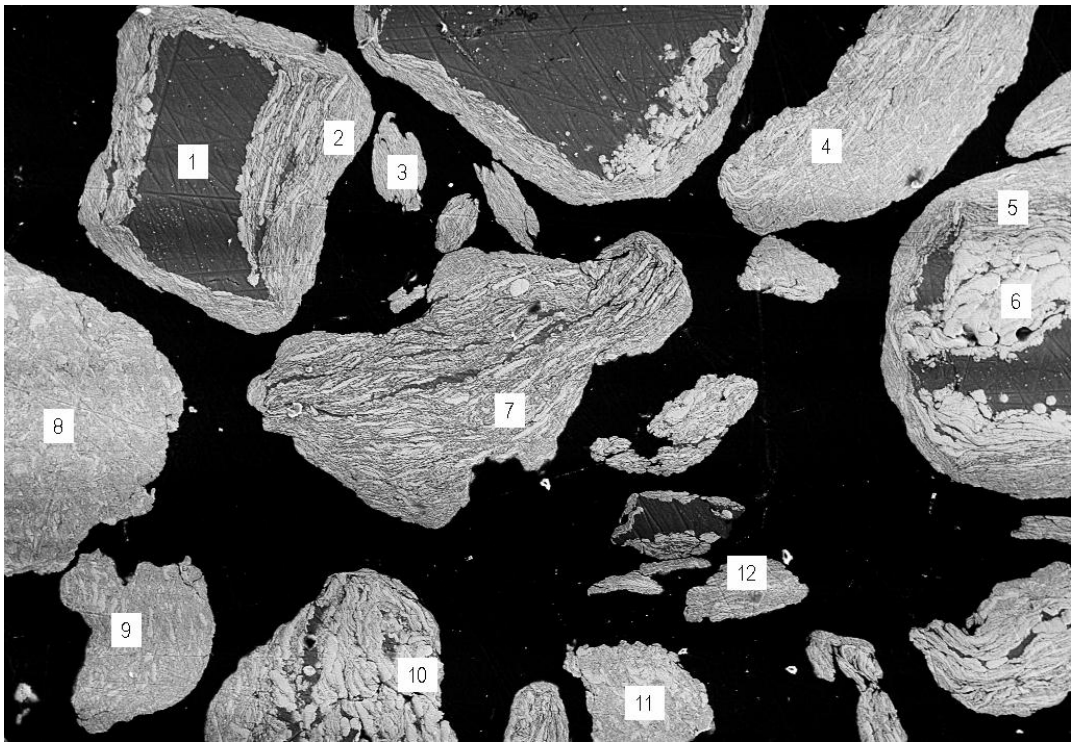

Figure 3.2.1.2.2.1a. SEM micrograph of Ti-Mg powder mixture upon low-energy ball milling for 32h showing unmixed core comprised of dark (100%Mg) particles and heterogeneous layered structure on the surface consisting of mainly lighter (Ti-rich) particles.

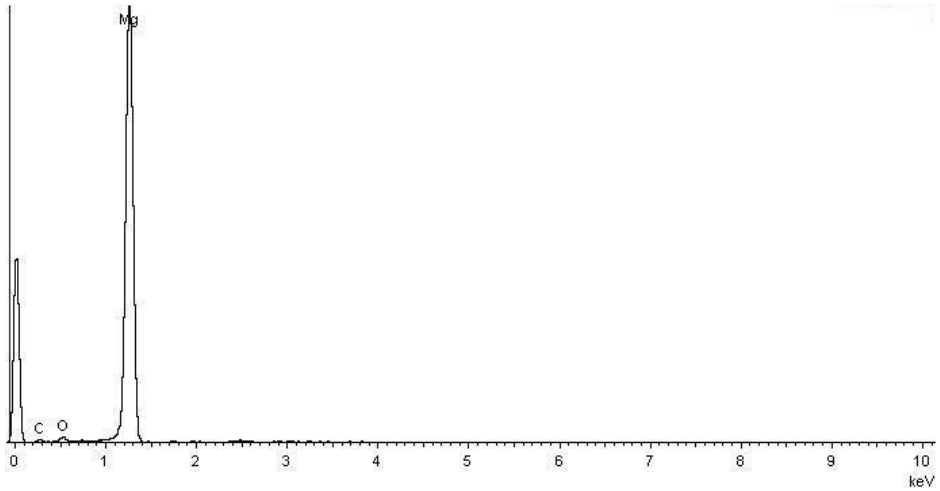

Figure 3.2.1.2.2.1a -1: EDS spectrum from spot 1 which shows a cross-section of milled powder.

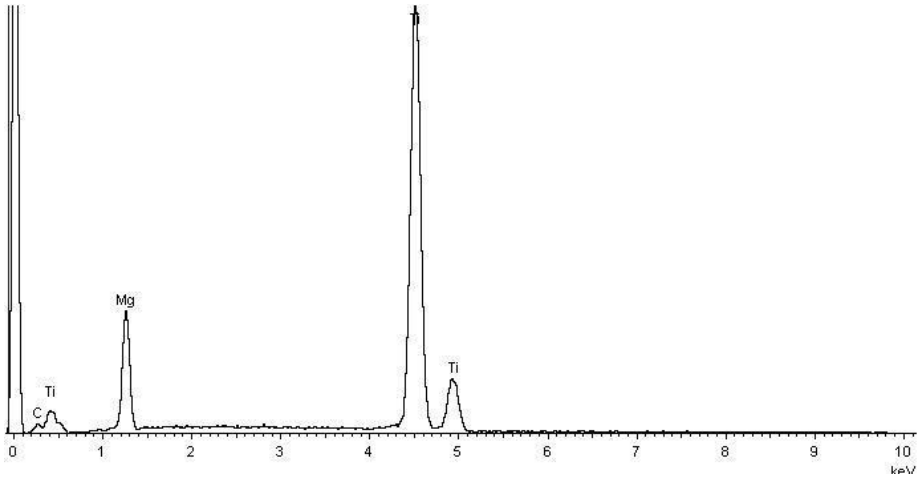

Figure 3.2.1.2.2.1a -2: EDS spectrum from spot 2

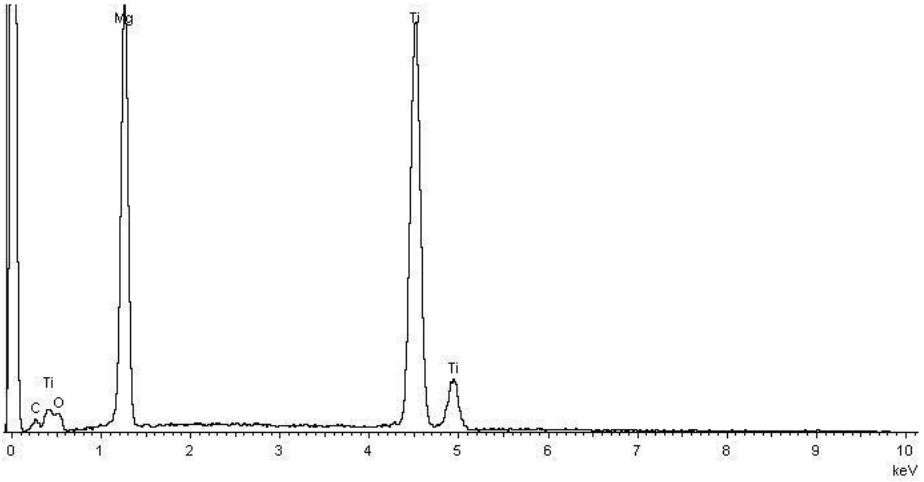

Figure 3.2.1.2.2.1a -9: EDS spectrum from spot 9

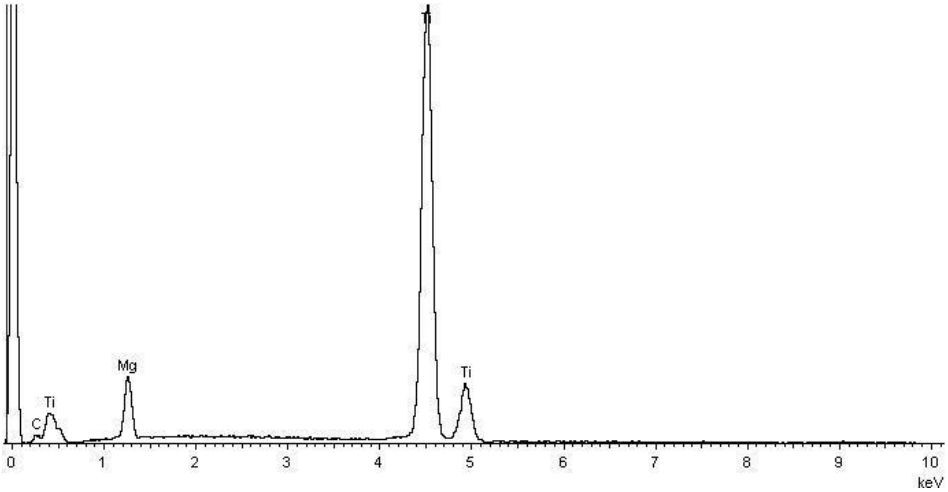

Figure 3.2.1.2.2.1a -12: EDS spectrum from spot 12

Table 3.2.1.2.2.1. SEM-EDS chemistry of different spots in Figure 3.2.1.2.2.1a.

Species	Spot 1	Spot 2	Spot 9	Spot 12
Ti at.%	0	84	63	91
Mg at.%	100	16	37	9

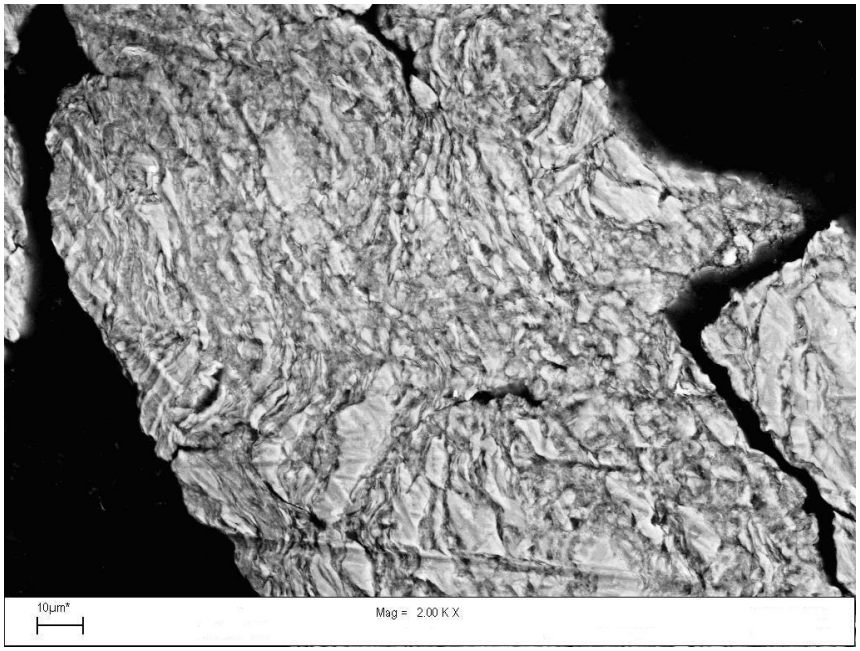

Figure 3.2.1.2.2.2. SEM picture illustrating the fracturing of the surface of the powder particles after 32h low-energy ball milling.

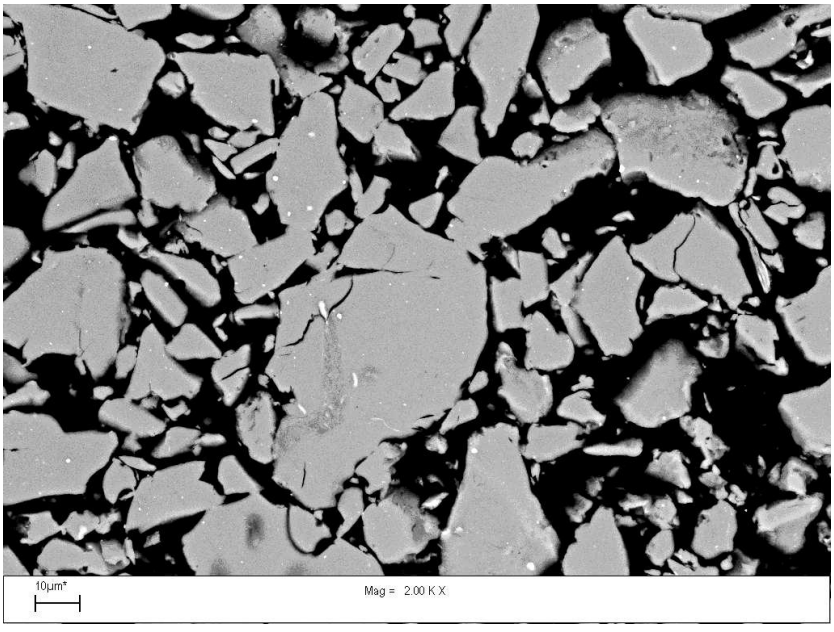

Figure 3.2.1.2.2.3. SEM micrograph of the single phase metastable $Ti_{50}Mg_{50}$ alloy formed after 72h high-energy ball milling.

Table 3.2.1.2.2.2. SEM observations at different milling parameters.

Size (μm)	(rpm	Milling time (hours)					
		4h	8h	16h	24h/32h	48h	72h
Mg chips 300 - 600 Ti < 45	**200**		Agglomerate of non deformed Ti particles in large equi-axed Mg particles.	The amount of Ti particles glued around surface of ductile Mg particles increases.	Plastic deformed Ti particles and formation of a layered structure limited to Mg-rich crown	Refinement of fractured layers by further plastic deformation of particles in the crown.	
	400	Agglomerate of non deformed Ti particles in large equiaxed Mg particles.		Plastic deformed layered structures are formed within the crowns formed around Mg particles.	Fracturing of layered particles (crowns).	Very limited solution in the crown around Mg particles	
Mg < 45 Ti < 45	**200**			Plastic deformation of particles		Homogeneity begins in the layered product	Solid solution not complete
	400	Plastic deformation begins	Plastic deformation proceeds	Formation of layered structure	Refinement of layered structure	Solid solution begins	Solid solution
	800	Plastic deformation of Ti and Mg particles. Formation of layered structure	Deformed particles of Mg and Ti form layered products	Refinement of layered structure and solid solution begins	Solid solution continues	Solid solution	Solid solution

3.2.1.2.3. Yield

The yield of the ball milling process was calculated as the weight ratio between the total powder loaded into the milling chamber and the powder collected at the end of the process. The curves corresponding to the low-energy and the high-energy ball milling are compared in figure 3.2.1.2.3.1. Two important observations were made from the curves of the yield plotted against milling time, i.e. the yield was higher when the starting powders were finer. The yield dropped significantly when the uninterrupted milling time of the finer titanium and magnesium powders was longer than 24h. The same trend was observed in the case of the low-energy ball milling. However, the onset of drop in yield was observed earlier when the magnesium powder particles were larger. These observations are attributed to the fact that the 2 wt.% of stearic acid used as PCA was not efficient in limiting the cold welding and keeping a high surface tension between the powder particles and the wall of the milling chamber. This led to more than half the amount of milled powders adhering to the walls. It was also observed that the transformation and mechanical alloying process was hindered by the cold welding and adhesion of the milled powder on the walls of the jar. The layer formed on the jar walls after 72h milling at 800 rpm is indicative of such case during the alloying process since its (weld) corresponding microstructure is similar to the one observed for the powder milled for just 24h at the same speed. Indeed, two sub-layers were identified within the cold welded powder adhering on the wall of the jar. The inner sub-layer, 0.5 mm thick, that was still in direct contact with the milling balls contained a lot of voids, unlike the outer sub-layer, 1.5 mm thick, which was in contact with the walls of the jar. The first sub-layer, shown in figure 3.2.1.2.3.2, had an homogeneous microstructure of the metastable $Ti_{50}Mg_{50}$, whereas the second shown in figure 3.2.1.2.3.3 had dense well compacted but heterogeneous microstructure identical to the one observed at shorter time high-energy milling (24h) of the fine powders. It follows from figures 3.2.1.2.3.2 and 3.2.1.2.3.4 that the alloying process is hindered once cold welding of the powder on the wall of the jar occurs. Further milling led to a high densification of the heterogeneous cold welded layer but not to any improved mechanical alloying. Mechanical alloying might have occured only inside the jar where fine elemental powder particles are

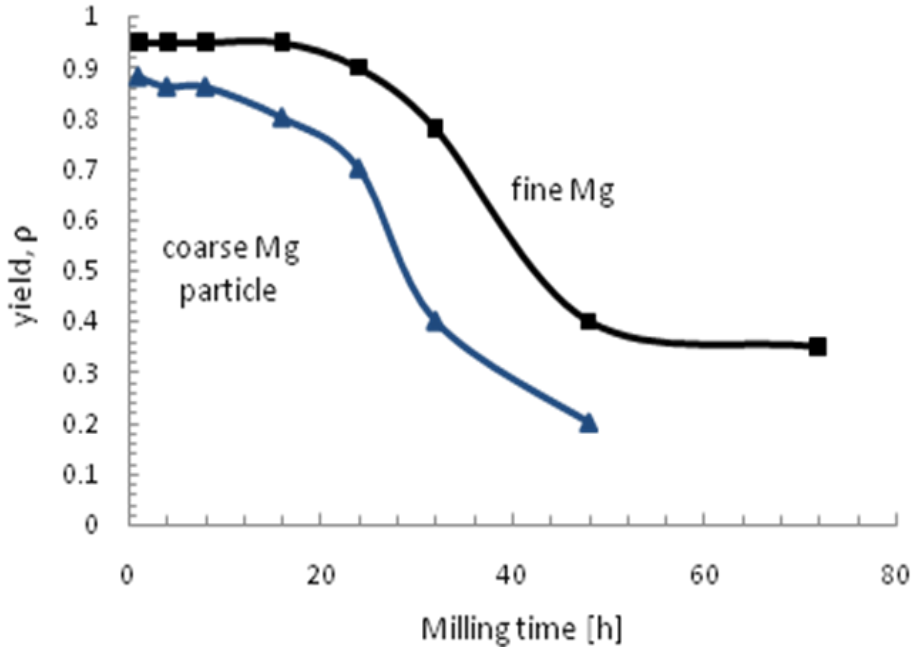

Figure 3.2.1.2.3.1. Yield against milling time plots showing the effects of magnesium particle size.

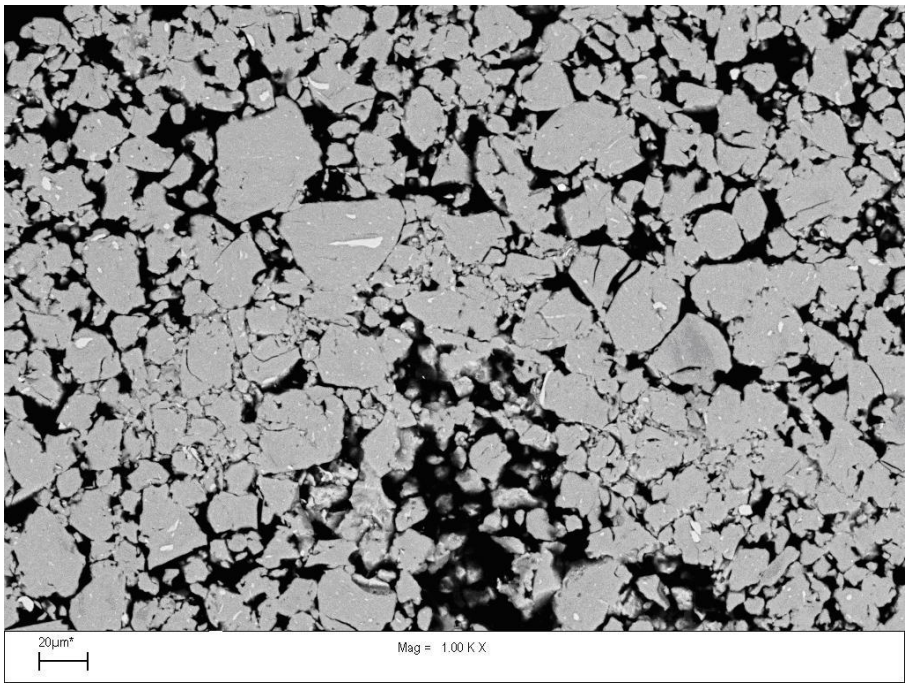

Figure 3.2.1.2.3.2. SEM image of the upper part of the layer of powder adhering on the wall of the jar showing fine sub-layer of homogeneous metastable $Ti_{50}Mg_{50}$ adhering on top of the heterogeneous compact sub-layer after 72h high-energy ball milling.

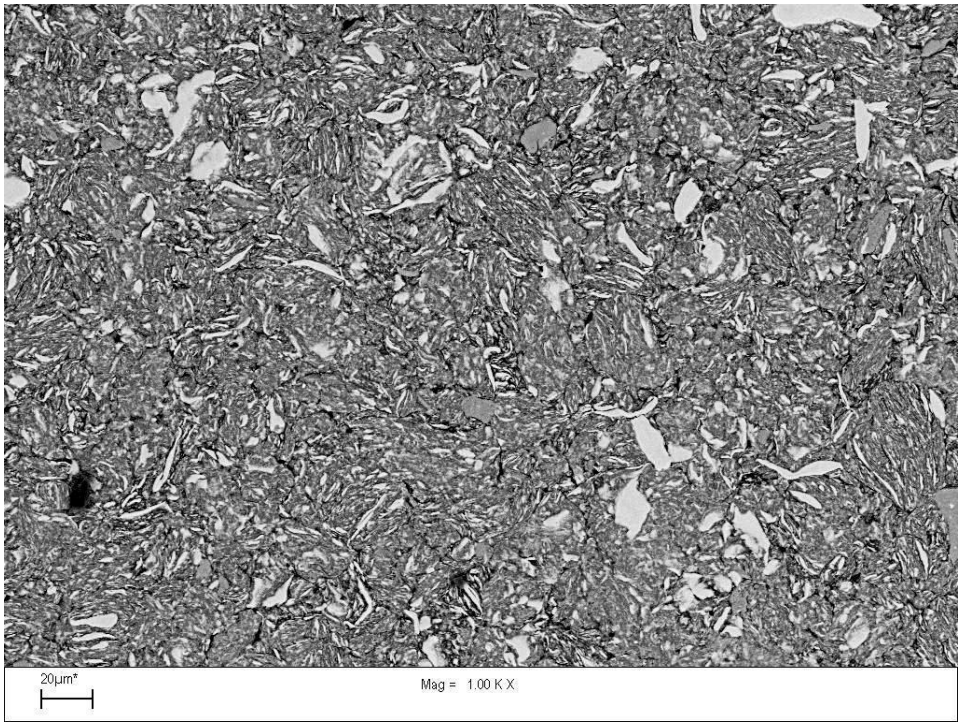

Figure 3.2.1.2.3.3. SEM image of the layer of powder adhering on the wall of the jar showing a dense and compact sub-layer of heterogeneous powder adhering on the wall of the jar after 72h high-energy ball milling

effectively impacted between high speed colliding milling balls.

3.2.1.3. Conclusion

Starting with a raw material containing coarse magnesium powder particles (300 – 600 µm) that are 10 times larger than the titanium particles led to different process steps than those observed in high-energy ball milling of fine (< 45 µm) titanium and magnesium particles. The core of the milled particles starting with coarse Mg remained 100% magnesium. Starting with coarse ductile magnesium powder resulted in significantly lower yield. Based on SEM results, formation of a homogeneous or metastable $Ti_{50}Mg_{50}$ was rather achieved by ball-milling of fine (< 45 µm) powders of elemental titanium and magnesium processed for more than 24h at 400 or 800 rpm. The adhesion of the fine hard titanium particles on the surface of the large ductile

magnesium particles impedes the plastic deformation of the titanium particles, hence the formation of the defaults necessary in mechanical alloying. The yield of the ball milling dropped drastically when the milling time became longer than 24h due to an increase of the total area of the fine powder particles not covered by the PCA. This led to an intense cold welding of powder particles on the walls of the jar. Mechanical alloying process did not progress further inside this cold welded layer. Mechanical alloying only took place inside the jar where fine elemental powder particles are efficiently impacted in between the moving milling balls. Therefore it is observed that the mechanical alloying process was slowed and solid solution of Ti in Mg was difficult to achieve when the starting particle size of the soft Mg was 8 times larger than that of the hard Ti. From the above studies it is inferred that the evolution of the microstructure of Mg–Ti mechanical alloys is process dependent. However, in order to confirm that either homogeneous or metastable $Ti_{50}Mg_{50}$ was achieved by ball-milling, further characterizations based on crystal structure evolution will be carried out in the next subsection.

3.2.2. Effect of milling time and speed on the microstructure and crystal structure of equimolar mixture of elemental Ti and Mg powders

3.2.2.1. Experimental procedure

Elemental titanium powder (99.5% purity) and fine magnesium powder (99.5% purity) were mixed manually to obtain 200 g of powder in the molar ratio 1:1. Stearic acid of approximately 2 wt. % was added to the mixed powders as a process control agent (PCA). The particle size analysis indicated that the starting elemental powders contained 50 wt. % of particles smaller than 27 μm and 90 wt. % of particles smaller than 40 μm. Pure Ti powder was first milled for 4h to form a Ti-coating on the inner surface of the milling chamber and on the surface of the stainless steel balls. This helped prevent contamination of the milled powders by milling medium constituents. The powder mixture was then introduced into the milling chamber together with 2 kg of

the 5 mm diameter Cr-stainless steel balls (0.5 g each) representing a 10:1 ball-to-powder ratio.

Continuous ball milling was conducted at about 20 °C for times varying from 1 to 72h at 400 and 800 rpm. The mechanism of alloying was investigated by analysis of the crystal structure, the lattice strain and crystallite size determined by means of XRD. The XRD analyses were conducted using the Cu Kα radiation, λ=0.15418 nm. The chemistries of the phases formed during ball milling were determined by means of EDS technique. Samples for the SEM analysis were prepared by mounting the powder in a cold resin and then polished to observe their morphologies and distribution inside the cross section of the particles.

3.2.2.2. Results and discussions

3.2.2.2.1. Microstructure evolution of the milled powder particles

The commercial pure Mg and Ti powders used had quasi-spherical cross sections as shown in figure 3.2.2.2.1.1. Titanium particles were spherical (light phase) while Mg particles were irregular (dark phase) in the backscattered electron SEM image. No chemical heterogeneity was observed in the cross sections of the initial powder particles. The shape, size and constituent distributions, and thus the homogeneity of the cross sections of the milled powder particles evolved thereafter as the milling time increased from 1 to 72h. Three major changes could be observed in the morphologies of the particles, in figure 3.2.2.2.1.2, as the milling time increased. Large lamellar structures of fractured Mg and Ti particles were formed at milling times between 4 and 8h. The lamellar structures were refined at intermediate milling times between 16 and 24h. Homogeneous particle distribution starts to occur at these intermediate milling times at both 800 and 400 rpm milling speeds. Comparison between the evolution of microstructures and morphologies in figures 3.2.2.2.1.2 and 3.2.2.2.1.3 shows that the refinement of the lamellar microstructure was faster at higher milling speed (800 rpm) than at 400 rpm. Fully homogeneous microstructures were achieved after 48h milling at 800 rpm whereas milling time of 72h was needed to achieve similar results when milling

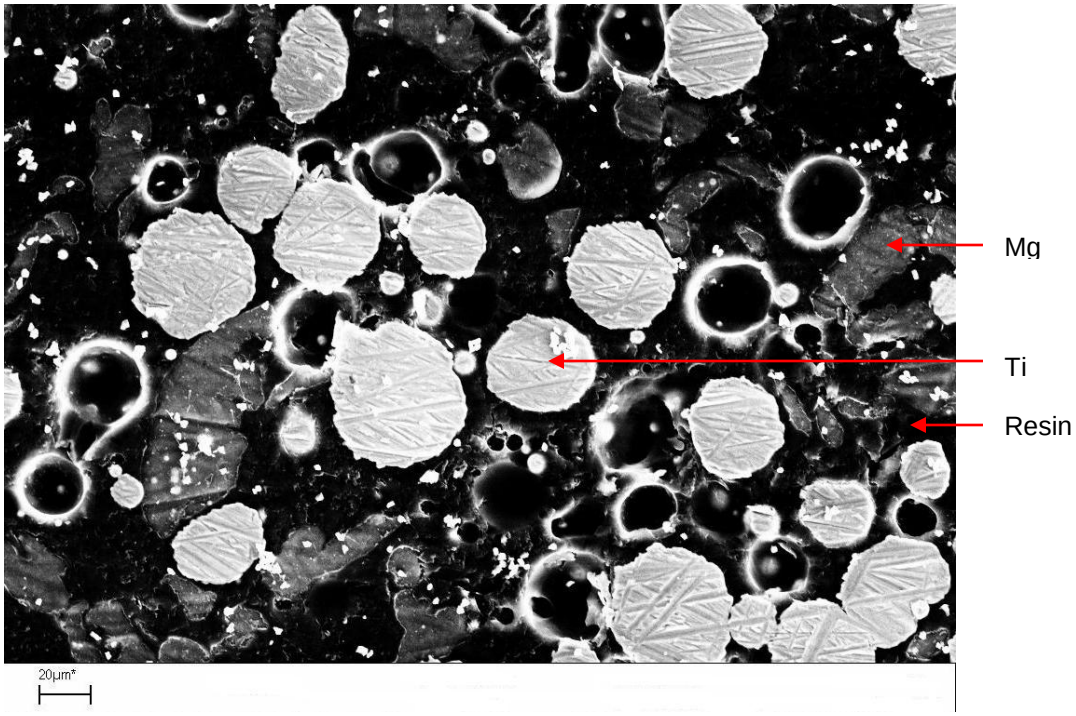

Figure 3.2.2.2.1.1. BSE-SEM of the cross sections of the powders particles before milling. Lighter and grey areas indicate Ti and Mg particles, respectively, while the black areas represent resin.

was conducted at 400 rpm. The localised EDS analysis performed in 30 spots and areas in figure 3.2.2.2.1.2(e) and (f) indicated that the compositions of the phases formed after 48 and 72h milling at 800 rpm ranged between Ti56:Mg44 and Ti50:Mg50. This result seems to confirm the mechanically-induced solid solubili of an equimolar TiMg alloy. The slight loss in magnesium ~3 at.% from the system might have occurred by mechanical drowning during the evacuation stage of the chamber preceding the milling or by a preferential cold welding of Mg onto the surfaces of the milling balls and chamber. From the microstructures in figures 3.2.2.2.1.2 and 3.2.2.2.1.3, it can be seen that milling of Mg and Ti mixtures at 400 rpm by a Simoloyer ball mill yields the same intermediate as well as final products similar to those milled at 800 rpm. However, the kinetics of refinement of the intermediate microstructure and the formation of the solid solution was faster at higher milling speed, which corresponds to the higher impact energy input in the milling process. Asano and his co-workers (2009a,b) found similar trends in Mg–Ti alloys processed in a Fritsch P5 planetary ball mill by varying the specific mass of the milling balls used at a constant milling speed of 200 rpm and for substantially longer milling times. Therefore, microstructurally, the milling process can

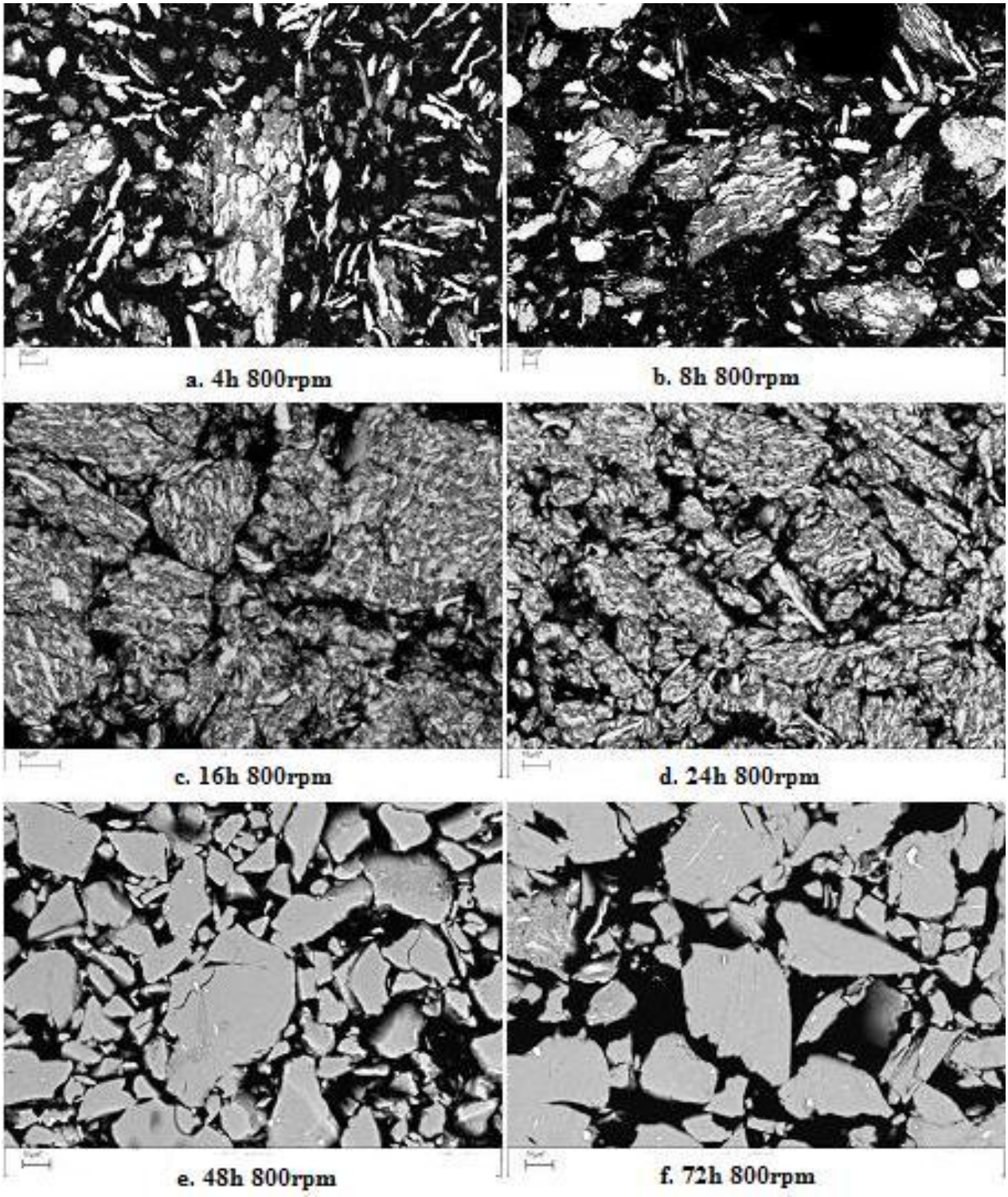

Figure 3.2.2.2.1.2. BSE-SEM pictures a, b, c, d, e and f showing the evolution of the morphology and microstructure of the powder mixture milled for 4h, 8h,16h, 24h, 48h and 72h, respectively at milling speed of 800 rpm. The description of regions as in Figure 3.2.2.2.1.1 with light grey indicating a homogeneous mixture. The scale bar is equal to 10µm.

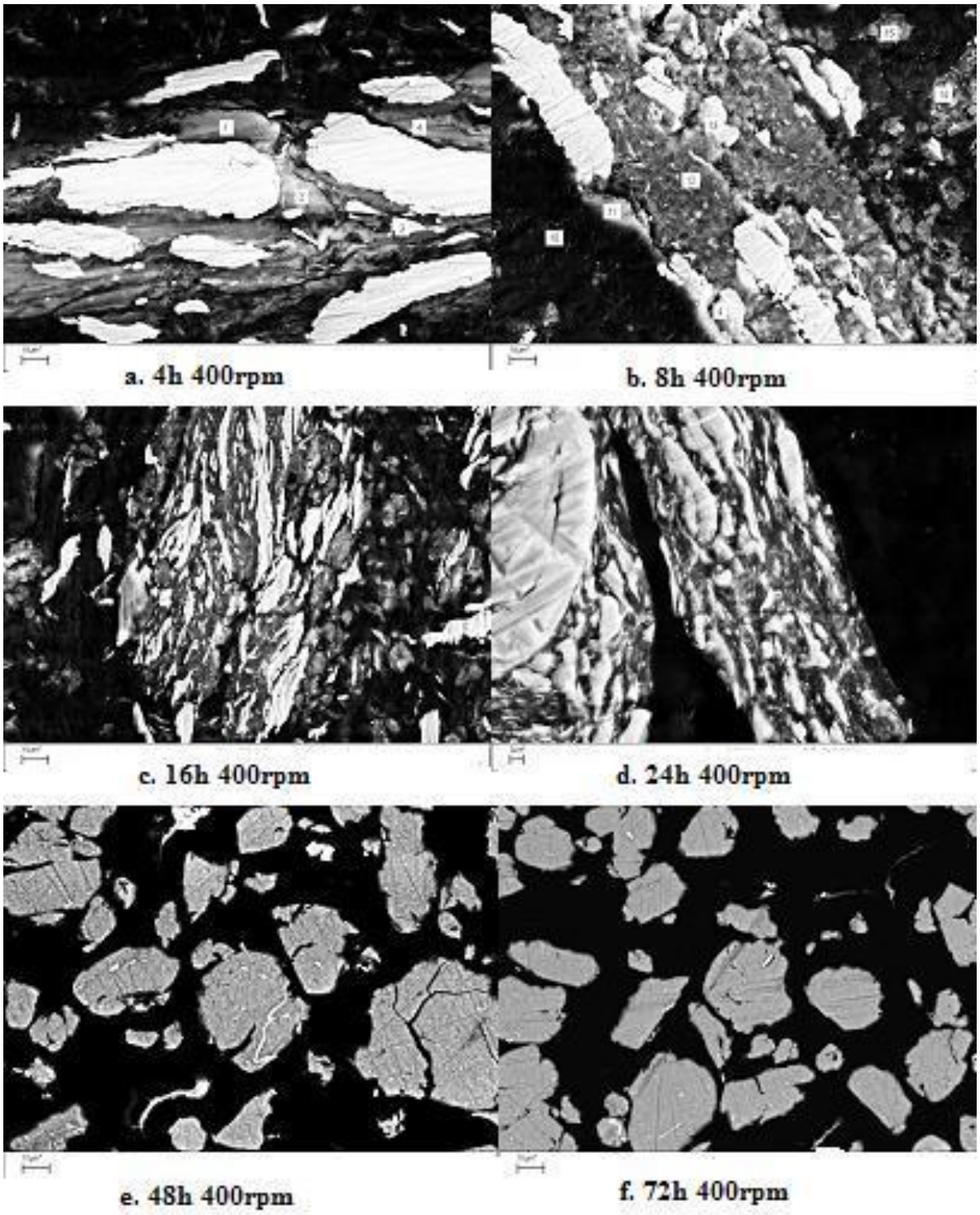

Figure 3.2.2.2.1.3. BSE-SEM pictures a, b, c, d, e and f showing the evolution of the morphology and microstructure of the powder mixture milled for 4h, 8h,16h, 24h, 48h and 72h, respectively at milling speed of 400 rpm. The description of regions as in Figure 3.2.2.2.1.1 with light grey areas indicating a homogeneous mixture. The scale bar is equal to 10µm.

be divided into three stages: at the initial stage, directly reduced Ti and Mg powder particles are cold welded together to form laminated structure. The chemical composition of the composite particles varies significantly within the particles and from particle to particle. Cold welding and fracturing enable powder particles to be always in contact with each other and atomically clean surfaces and with minimized diffusion distance. At the second stage, the laminated structure is further refined as fracture takes place. Thickness of the lamellae is decreased with longer milling times. Although dissolution may have taken place, chemical composition of the powders is still not homogeneous. At the final stage, the lamellae become finer and eventually disappear. A homogenous chemical composition is achieved for all particles resulting in the formation of a new alloy with composition corresponding to the starting powder mixture [Suryanarayana *et al* 1990]. It has now been accepted that the most important reason for the increase in solid solubility is the formation of nanostructures during milling [Suryanarayana *et al* 1990]. The large volume fraction of atoms residing in grain boundaries in these ultrafine-grained materials is expected to enhance diffusion and, consequently, increase the solid solubility. However, since the conclusion on solid solubility cannot be drawn based only on SEM observations, the XRD analyses were carried out in the next subsection.

3.2.2.2.2. Crystal structure and phase analysis

The X-ray diffraction patterns of the initial and milled powders for different durations at 800 rpm and 400 rpm are shown in figures 3.2.2.2.2.1 and 3.2.2.2.2.2, respectively. It is evident from both figures that the XRD peaks of Mg and Ti became short and broader with increased milling due to grain refinement. In addition, the Mg peak intensities decreased more rapidly than those of Ti and most of its peaks shifted slightly to higher angles indicating the modification of the lattice parameters due to plastic deformation. This implies that Mg grains were refined faster and could consequently deform quicker. Our XRD results suggest that Mg crystals were deformed first before any possible dissolution took place. This is supported by the fact that the CRSS values at ambient temperatures are 0.5 MPa for a basal plane slip system in Mg [Tonda and Ando 2002]

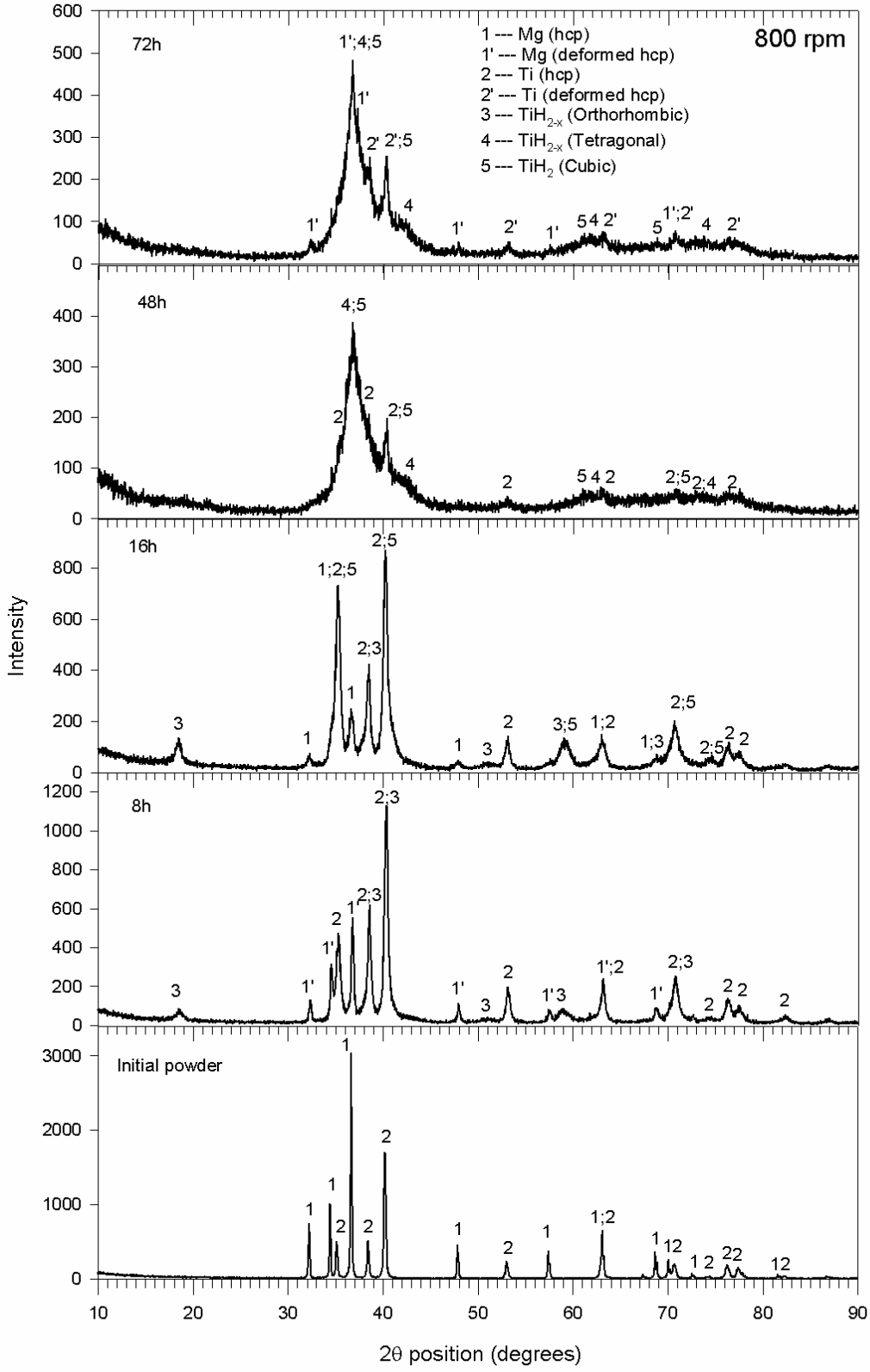

Figure 3.2.2.2.2.1. XRD patterns of Ti-Mg powders milled for various milling times at 800 rpm.

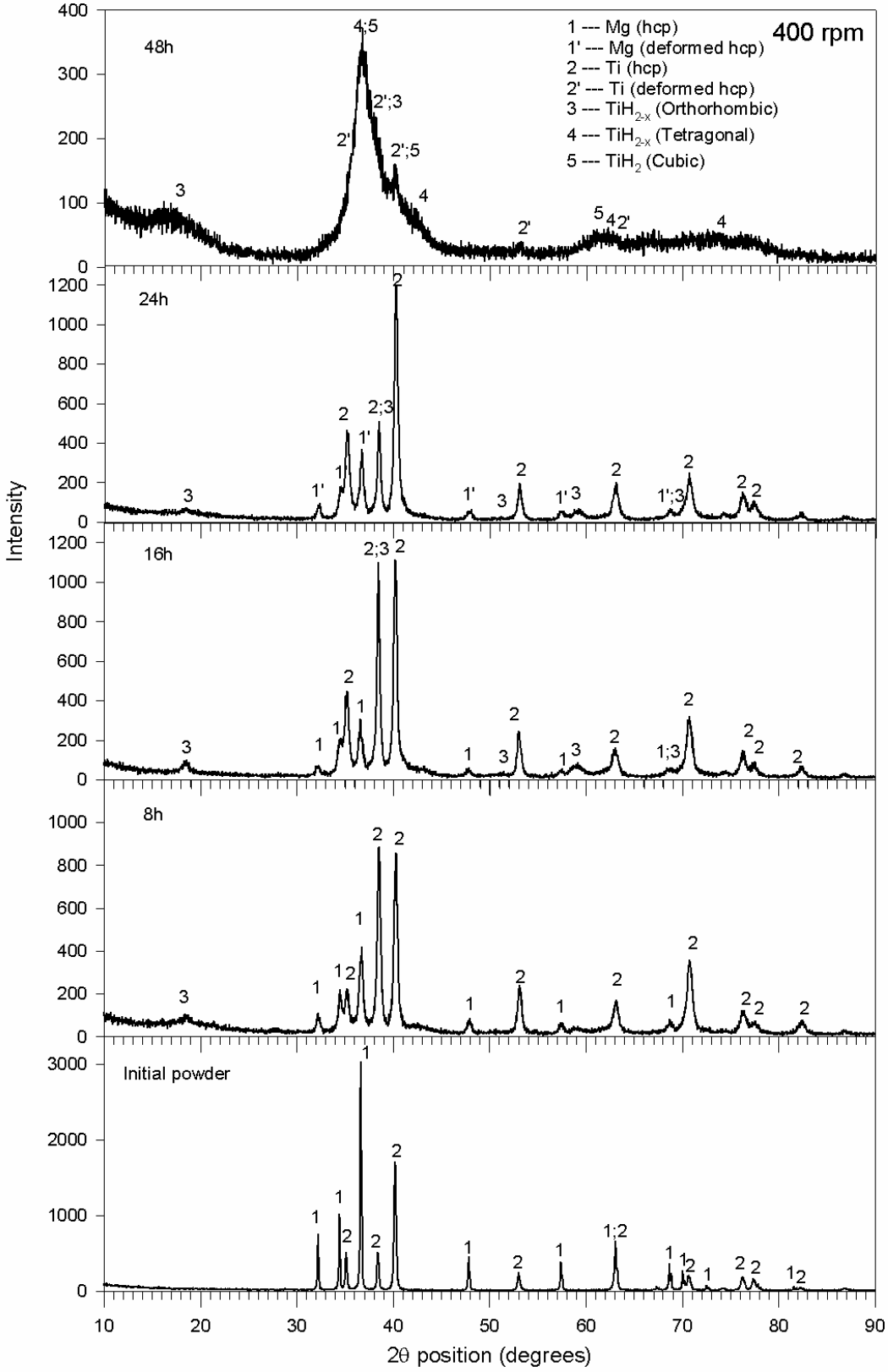

Figure 3.2.2.2.2.2. XRD patterns of Ti-Mg powders milled for various milling times at 400 rpm.

and 140 MPa for a twinning in Ti [Yoo 1981], which justify that Mg crystals could readily deform in the first stages of ball milling compared to Ti crystals. As indicated by the peak intensities of the first three peaks, it is worth noting that the preffered crystal orientation for both metals changed with milling time as was observed previously for pure Ti [Bolokang and Phasha 2010]. After 8 and 16h milling at 800 rpm as well as 8, 16 and 24h at 400 rpm, new peaks corresponding to a structure similar to $Mg(OH)_2$ (brucite) appear more distinctively at 18.5, 51 and 59^o 2θ positions. Initially, formation of this phase was attributed to (i) the reaction between ultrafine Mg powder particles and OH^- ion due to the moisture in the milling chamber or (ii) dissolution of Ti in Mg to form trigonal omega (ω) phase prior to FCC solid solution. The XRD results in figure 3.2.2.2.2.1 suggested that Mg atoms from the metastable FCC phase could also simultaneously have been adsorped into the strained HCP Ti lattice to form a metastable HCP solid solution of Mg in Ti. Such metastable FCC and HCP solid solutions were reported by Asano *et al* [2009a, b] in high titanium systems and by Rousselot *et al* [2008] at lower milling energy and shorter milling times. Furthermore, the XRD patterns of the milled products obtained after milling for 48h at speeds of 800 and 400 rpm were similar, indicating that there was no significant structural difference between the two products formed.The peaks intensities however, were slightly higher in the case of the 72h milled than those obtained after 48h milling, indicating an increase in grain size after 72h milling. This was attributed to cold welding due to inefficient PCA action at longer milling time.

However, after further systematic scrutiny of the XRD patterns, it seems this new phase is neither brucite nor omega Mg-Ti solid solution as we initially thought [Phasha *et al* 2010b, Maweja *et al* 2010] but rather orthorhombic nonstoichiometric titanium hydride (TiH_{2-x}). The mechanism for TiH_{2-x} formation is such that hygrogen protons (H^+) from the deprotonated stearic acid are absorped into some of the fresh thin film surfaces of deformed nanocrystalline Ti crystals [Bolokang and Phasha 2010], and occupy the interstitial tetrahedral sites. As milling continues, more hydrogen gets absorped and consequently the orthorhombic phase transforms to tetragonal TiH_{2-x} phase with *c/a* ratio greater than 1 or even cubic TiH_2, as observed after 48 and 72h. Grinding of

stearic acid (C17H35COOH) in the presence of metal powders induced the deprotonation process which yielded H^+ and stearate ion ($C17H35COO^-$). Usually, PCA is added to help reduce the effect of cold welding by changing the surface energy and by interacting with the particles and forming hard phases [Suryanarayana 2001]. However, systematic characterization of the resulting hard phases is lacking, while they are generally attributed to contamination by impurities. Since Mg hydride could not form at this point because of slow hydration kinetic and smaller formation energy compared to Ti hydrides [Süleyman *et al* 2010], the $C17H35COO^-$ ion will prefer attaching itself on the surface of reactive ultra-fine Mg particles. This results in a softer compound with similar characteristics to those of Mg-stearate, $Mg(C17H35COO)_2$, a metallic soap used in rubber industry, textile goods waterproof as well as pharmaceutical industry as an important lubricant for tablets [Sheikh *et al* 2011, Wang *et al* 2010, Bracconi *et al* 2005]. The brittle TiH_{2-x} particles seem to attach themselves around these softer Mg-based particles. Consequently, the Mg peaks vanished completely after milling more than 16h at 800 rpm. Similar vanishing was observed when milling beyond 24h at speed of 400 rpm as shown in figure 3.2.2.2.2.2. From figure 3.2.2.2.2.1, it is interesting to note that the disappearance of Mg peaks coincides with simultaneous vanishing of orthorhombic phase peaks and emergence of new peaks belonging to a mixture of tetragonal TiH_{2-x} and cubic TiH_2 with lattice parameters a=4.234, c=4.567 and a=4.420 Å, respectively. The XRD patterns for 4h milling at 800 rpm are not shown since they are similar to those after 8h. This implies that the formation of orthorhombic TiH_{2-x} occurred as early as 4h at 800 rpm while it took at least 8h to form the same phase at 400 rpm. However, even after 72h there are still some traces of deformed Mg and Ti HCP crystals.

The possibility of stearic acid serving as a source of contamination was also recently reported on ball milling of Al alloys by Lavernia and co-workers [Zhang 2010] and will be further clarified in the next chapter, wherein each of elemental powders (Mg and Ti) is milled in the presence as well as absence of stearic acid. Unfortunately, attempts to mill Mg and Ti powder mixtures in the absence of PCA were fruitless due to observed severe cold-welding on the grinding media at early stages of milling.

In an attempt to confirm the presence of new phases, the TEM (Transmission electron microscopy) analyses of the milled samples were also conducted under 200 kV in a JEOL TEM. The corresponding indexed electron diffraction patterns are shown in figures 3.2.2.2.2.3 and 3.2.2.2.2.4. Indexing of the electron diffraction rings and the ratios of the ring diameters confirmed the presence of FCC-based phase product formed after milling for 24h, whereas a tetragonal (nearly BCC-like) phase was evident after 48 – 72h milling. The former phase corresponds to the cubic TiH_2 while the latter corresponds to tetragonal TiH_{2-x} phase. However, in both cases the electron diffraction rings were diffused indicating that the products of milled powder consisted of a mixture of very fine crystallites highly strained or even could contain some amount of amorphized material. Deformation twins were observed along the grain boundaries in some particles of powders milled for short time as shown in figure 3.2.2.2.2.5.

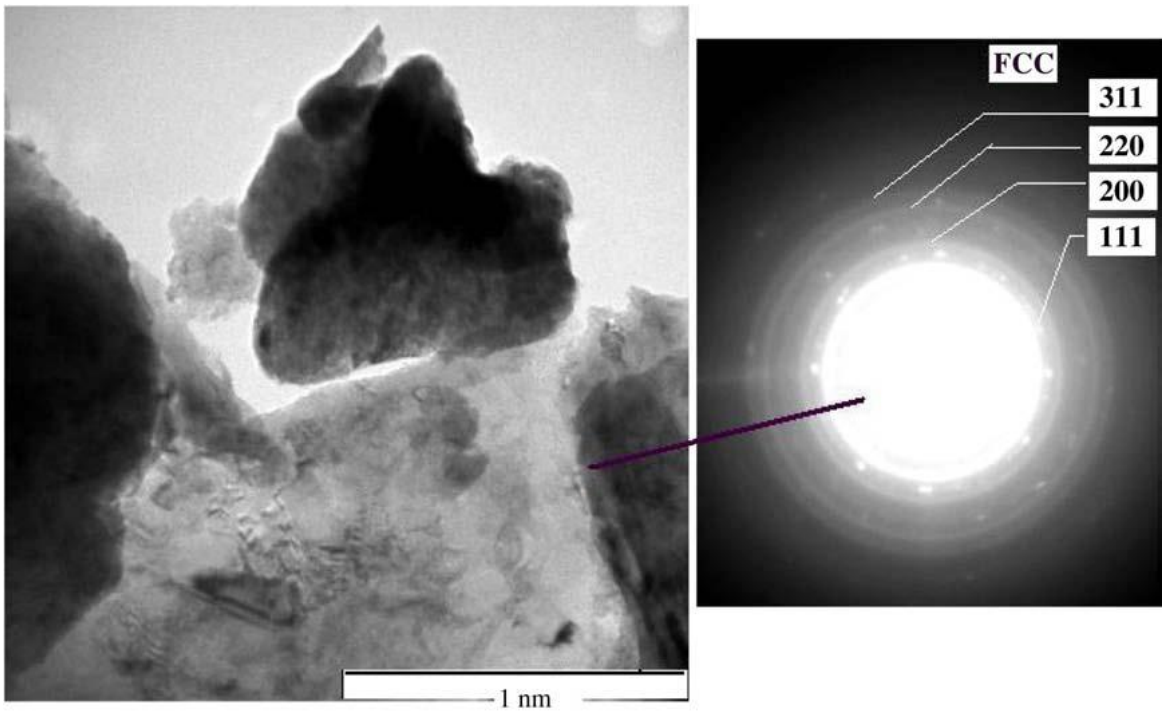

Figure 3.2.2.2.2.3. TEM image and the corresponding SADP illustrating the existence of an FCC-based phase in powders milled for 24h at 800 rpm.

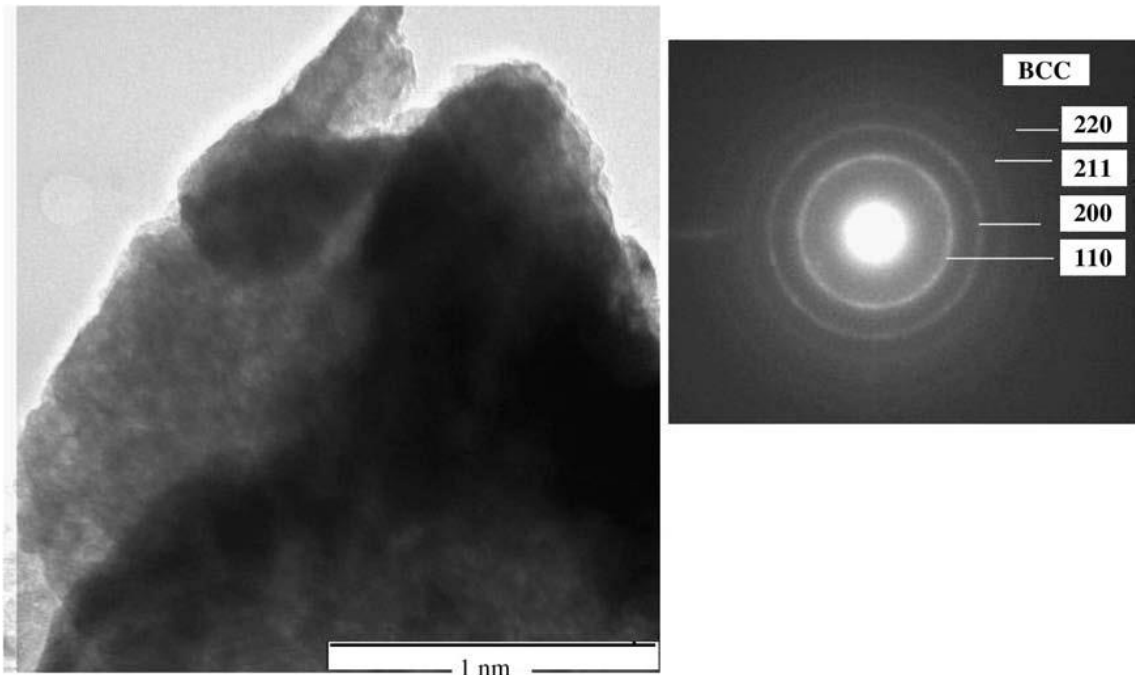

Figure 3.2.2.2.2.4: Typical TEM image of the products milled for 72h at 800 rpm and the corresponding SADP showing the existence of almost BCC matrix.

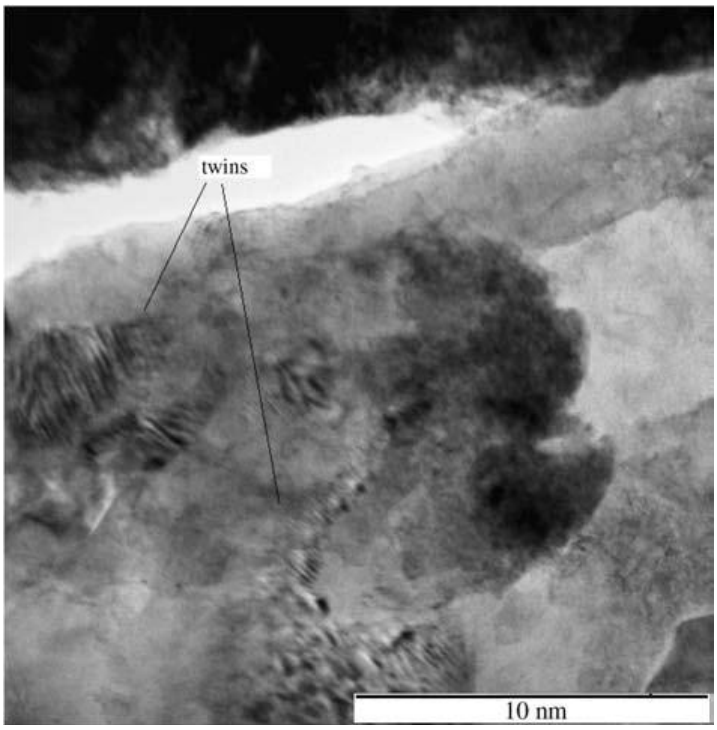

Figure 3.2.2.2.2.5. TEM image showing the twins formed along the boundaries in some areas of the powders milled for 24h at 800 rpm at room temperature.

Twinning would normally be expected as the deformation mode in Ti particles. The twins observed were smaller than 10 nm in both width and length. A more detailed analysis of these twins is still needed to determine the twinning planes, angles and ratios, hence their formation mechanism.

The lattice strains ε of the obtained products increased as the milling time increased at both milling speeds and the trends are schematically illustrated in figure 3.2.2.2.2.6, which shows non-monotonic evolutions. It is noted in this figure that the lattice strains ε of Ti (curve A) and Mg (curve B) increased to local maxima after milling for 4h at 800 rpm or after 8h when milling speed was 400 rpm. The lattice strains decreased after these maxima prior to subsequent increase and decrease occurring at longer milling times.

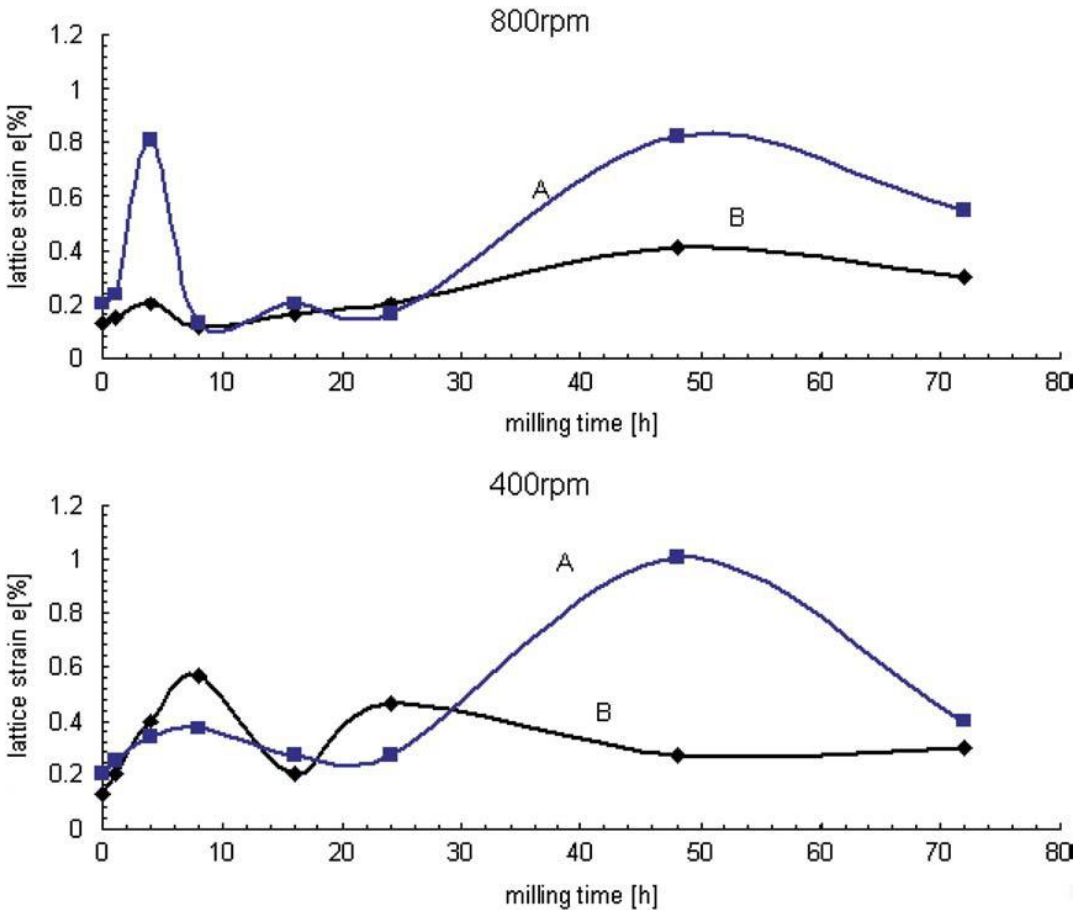

Figure 3.2.2.2.2.6. Evolution of calculated crystal lattice strains of products after milling at 400 rpm and 800 rpm versus milling time. (Curve A=Ti and deformed Ti, Curve B=Mg).

Comparison of these lattice strains to the SEM and TEM results leads to the following remarks on the evolution of the microstructure and crystal structure of the equimolar Mg:Ti mixture during high energy ball milling at 800 rpm:

- Stage 1, the HCP crystal lattices of both magnesium (1) and titanium (2) are deformed, resulting in increased lattice strains in the powders milled for 4h due to grain refinement.

- Stage 2, the deformed Ti crystals adsorbed H^+ from the deprotonated stearic acidis leading to formation of metastable orthorhombic TiH_{2-x} phase (3) which later transformed to a tetragonal TiH_{2-x} (4) or even cubic TiH_2 (5) when stoichiometric amount of H_2 had been adsorbed. The sharp drop in lattice strain in both (curve A) and (curve B) at 8 – 16h milling time in figure 3.2.2.2.2.6, suggests that the lattice strain energy released drove at least partly the protonation of Ti thin film surfaces and either strain relief or cold-welding in the case of Mg crystals. The high recovery or restoration tendency of Mg crystals during ball milling [Grosjean *et al* 2004, Zidoune *et al* 2004] became evident at lower speed as shown by lattice strain fluctuations, more especially between 4 and 24h.

- Stage 3, the undeformed and unprotonated Ti crystals began to deform between 24 and 48h. This lattice deformation led to almost complete protonation after 72h milling. On the other hand, the lattice strain experienced by Mg crystals became almost constant on milling beyond 24h, which implied constant grain size on further milling. Products having similar structures to those achieved after 8h milling at 800 rpm were only formed after 24h milling at 400 rpm.

The crystallite sizes of Ti (curves A) and Mg (curves B) are presented in figure 3.2.2.2.2.7 as milling time increases. It is deduced from these curves that the crystallites of all the phases in the starting materials were refined during the first 4h, followed by cold-welding between 4 and 8h at 800 rpm and between 4 and 16h at 400 rpm. In general the crystallites of both Ti and Mg and those of phases formed during ball milling were finer at lower milling speed (400 rpm) than in the case of 800 rpm until milling time

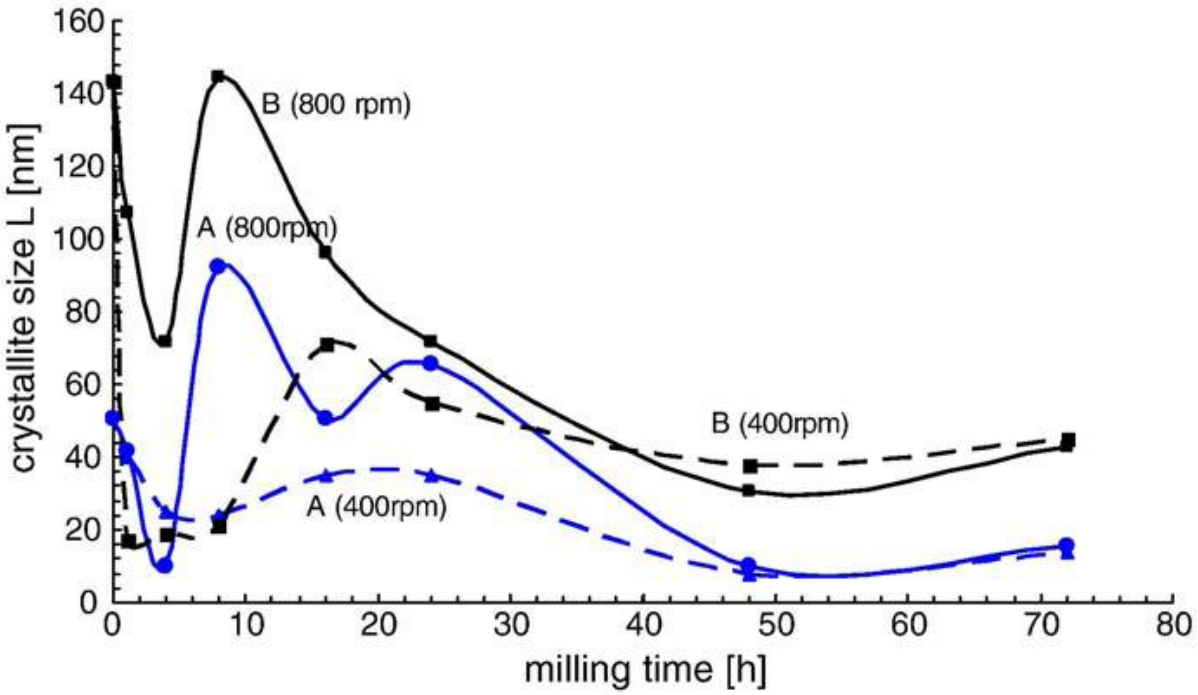

Figure 3.2.2.2.2.7. Crystallite sizes of products formed at various milling times and milling speeds (400 rpm (dashed line) and 800 rpm (solid line)). (Curves A=Ti , Curves B=Mg).

was prolonged for 48h and longer. This is an indication that despite robust mixing, high speed milling also promotes cold-welding. The crystallite sizes of the products were similar in materials milled for more than 48h despite the used speed. Milling beyond 48h did not yield any further decrease in crystallite size, indicating stabilization to about 40 nm and below 20 nm for Mg and titanium hydride crystallite sizes, respectively. Our results for milled Mg are consistent with several ealier findings of Hwang *et al* (2001), Grosjean *et al* (2004) and Zidoune *et al* (2004), who attributed the relatively high limit value of the Mg crystallite size (~40 nm) compared to other ball milled metals to its low melting temperature which facilitates the recovery process rather than the plastic deformation of the material during the milling process. The decrease of the crystallite size was accompanied by the increase of the internal strain associated to the presence of lattice distortion at the grain boundaries and the accentuation of the dislocation density with prolonged milling [Grosjean *et al* 2004, Zidoune *et al* 2004]. Consequently, the larger size of the crystallites formed were attributed to an intense cold welding due to a higher impact energy input which also enhanced the diffusion rates of the hydrogen

proton across the thin-layered surfaces of Ti particles. A summary of the dominant processes taking place during ball milling of Mg and Ti powders is presented in table 3.2.2.2.2.1. It appears from the above observation that the crystal structure of the product obtained by high energy ball milling of equimolar Mg-Ti mixtures depends on the energy input, which is a function of the rotation speed, the mass of the balls and the milling time. This may explain the variety of crystal structures reported in the literature for the Mg-Ti systems and their dependence on milling.

Table 3.2.2.2.2.1. Dominant processes occurring with respect to crystallite size during ball milling of Mg and Ti powders by a Simoloyer.

Milling speed	1-4h	> 4-8h	> 8-16h	> 16-24h	> 24-48h	>48-72h
400 rpm	Grain refinement	Grain refinement	Cold welding, Strain energy release, Formation of metastable TiH_{2-x}	Grain refinement, Formation of metastable TiH_{2-x}	Grain refinement	Cold welding of ultrafine particles. FCC and BCT products
800 rpm	Grain refinement	Cold welding, Strain energy release, Formation of metastable TiH_{2-x}	Grain refinement, Formation of stable TiH_2	Refinement of Mg-rich crystallites. Cold welding of Ti-rich crystallites.	Grain refinement, FCC and BCT products	Cold welding of ultrafine particles. FCC and BCT products

3.2.2.3. Conclusion

Mechanical alloying by means of ball milling is obviously quite complex. The experimental parameters are dependent on each other. However, by using the SEM,

EDS and XRD techniques, it was possible to identify the combined effects of the magnesium powder particle size, the milling speed, milling time and the PCA on the transformation steps, the microstructure, phases in the milled product as well as the overall of the ball milling process. The solid solubility of the 50–50 at.% Mg-Ti by means of high energy ball milling was not achieved using a Simoloyer type high energy ball mill but a nanocrystalline Mg-TiH_{2-x} composite was instead formed. The EDS spot analysis revealed that the chemical composition of the final products milled for 48–72 h varied from Ti56:Mg44 to Ti50:Mg50 which are very close to the initial equimolar composition of the powder mixtures and the targeted Ti50:Mg50, since H atoms could not be detected by the EDS technique. Both XRD and TEM techniques revealed the existence of FCC- and BCC-based products together with traces of HCP Mg and Ti phases in materials milled for 24–48h and 72h, respectively at 800 rpm. The deformed Ti crystals adsorbed H^+ from the deprotonated stearic acids leading to formation of metastable orthorhombic TiH_{2-x} phase (3) which later transformed to a tetragonal TiH_{2-x} (4) or even cubic TiH_2 (5) when stoichiometric amount of H_2 had been absorbed. The sharp drop in lattice strain curves for both Ti and Mg between 8 and 16h milling suggests that the lattice strain energy released drove at least partly the protonation of Ti thin film surfaces and strain relief in the case of Mg crystals due to crystal recovery or restoration. The crystallite sizes of the products formed at higher milling speed were larger than those formed at lower milling speed. However, the kinetics for protonation of Ti crystals was enhanced in powder particles milled at the higher speed. Twins were observed along the grain boundaries in some particles of powders milled for a short time. The twinning observed could be attributed to the deformation of Ti particles. The crystallite boundaries acted as preferential sites for the heterogeneous nucleation of the twins as a result of protonation.

3.2.3. Effect of starting composition on crystal structure evolution during mechanical milling process

3.2.3.1. Experimental procedure

BM experiments were designed and conducted under similar conditions as in section 3.2.2 for atomic compositions $Ti_{80}Mg_{20}$, $Ti_{75}Mg_{25}$, $Ti_{70}Mg_{30}$, $Ti_{50}Mg_{50}$, $Ti_{40}Mg_{60}$ and $Ti_{20}Mg_{80}$. However, since the $Ti_{50}Mg_{50}$ was studied in previous sections, only the remaining compositions will be considered in the current section. Each powder mixture was introduced into the milling chamber together with 2 kg of the 5 mm diameter Cr-stainless steel balls (0.5 g each) representing a 10:1 ball-to-powder ratio. Ball milling was conducted at 20°C and 800 rpm for 16, 24 and 32h for $Ti_{80}Mg_{20}$, $Ti_{75}Mg_{25}$, $Ti_{70}Mg_{30}$ compositions whereas $Ti_{40}Mg_{60}$ and $Ti_{20}Mg_{80}$ starting compositions were milled for 32h at 800 rpm. The mechanism of alloying was investigated by analysis of the crystal structure, the lattice strain and crystallite size determined by means of XRD. The XRD analysis were conducted using the Cu Kα radiation, λ=0.15418 nm.

3.2.3.2. Results and discussions

The XRD patterns of milled powders with atomic compositions $Ti_{80}Mg_{20}$, $Ti_{75}Mg_{25}$, $Ti_{70}Mg_{30}$ representing Ti-rich and $Ti_{40}Mg_{60}$, $Ti_{20}Mg_{80}$ which represents Mg-rich compositions are presented in figures 3.2.3.2.1 to 3.2.3.2.4, respectively. The corresponding crystal structure details are shown in table 3.2.3.2.1. As shown in figure 3.2.3.2.1(a), there is no indication of HCP lattice of Ti or Mg but only the broad peaks of metastable (1) FCC and (2) FCT (face-centered tetragonal) phases are detected after 16h milling. It is clear that the tetragonal lattices are the intermediate phases of FCC structure due to inhomogeneity of the milling process since on continued milling to 24 (b) and 32h (c), only the FCC phase is observed. According to the lattice parameters presented in table 3.2.3.2.1, FCC and FCT phases correspond to $TiH_{1.5}$ with space group Pn-3m (#224) and $TiH_{1.25}$ belonging to space group P-42m (#111) metastable compounds, respectively. The difference in the crystal structure symmetry of the titanium hydrides with different amounts of hydrogen will be presented and discussed in chapter 6. Increasing milling time to 24 and 32h yielded the same product of cubic TiH with space group F-43m (#216) and lattice parameter of 4.307 Å. The absence of Mg peaks further supports our earlier observation that upon milling Ti and Mg powder mixture, the harder Ti particles cluster around the surface of softer Mg particles in a

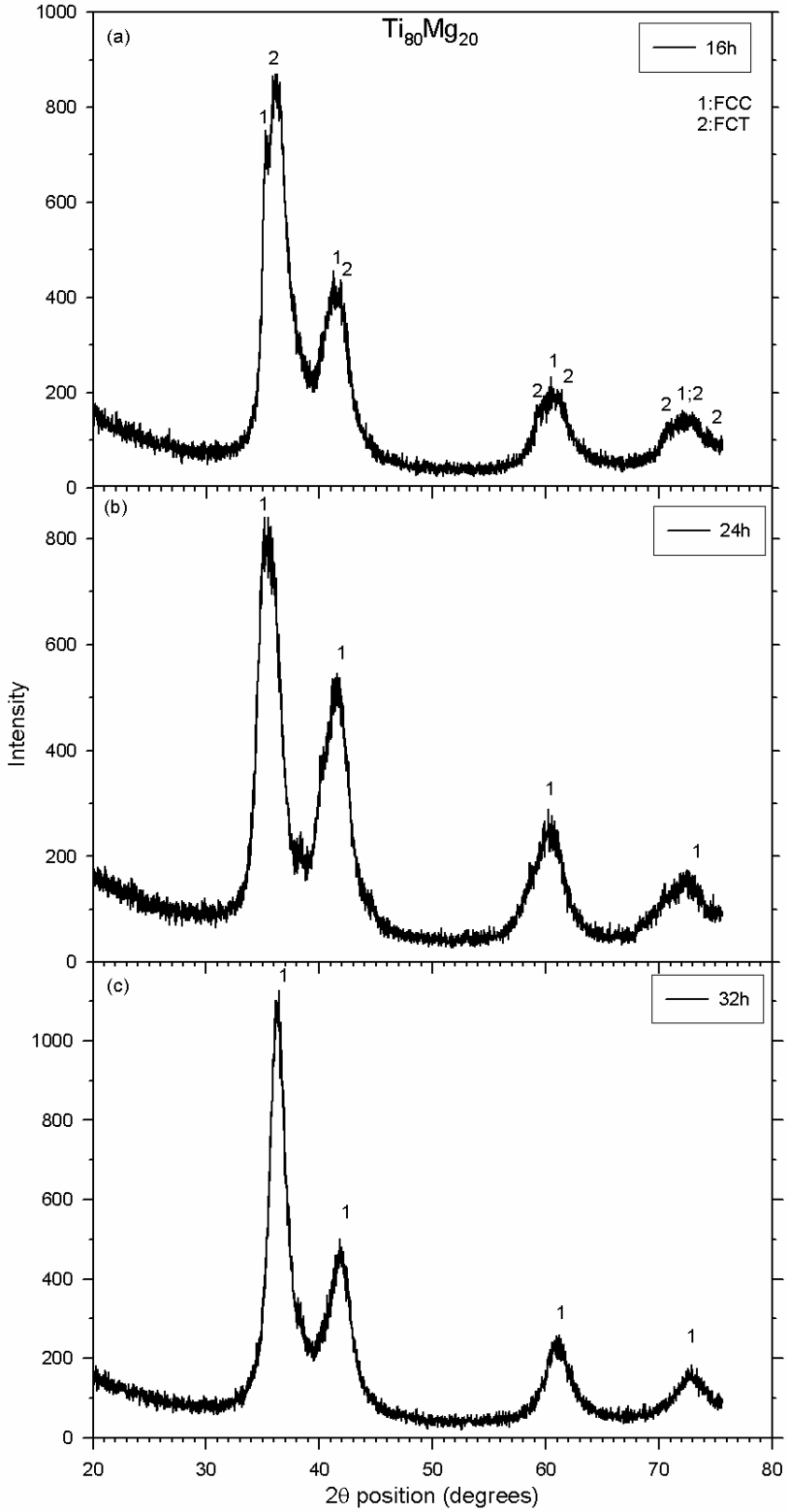

Figure 3.2.3.2.1. XRD patterns of $Ti_{80}Mg_{20}$ atomic composition powder mixture milled for (a) 16h, (b) 24h and (c) 32h at 800 rpm.

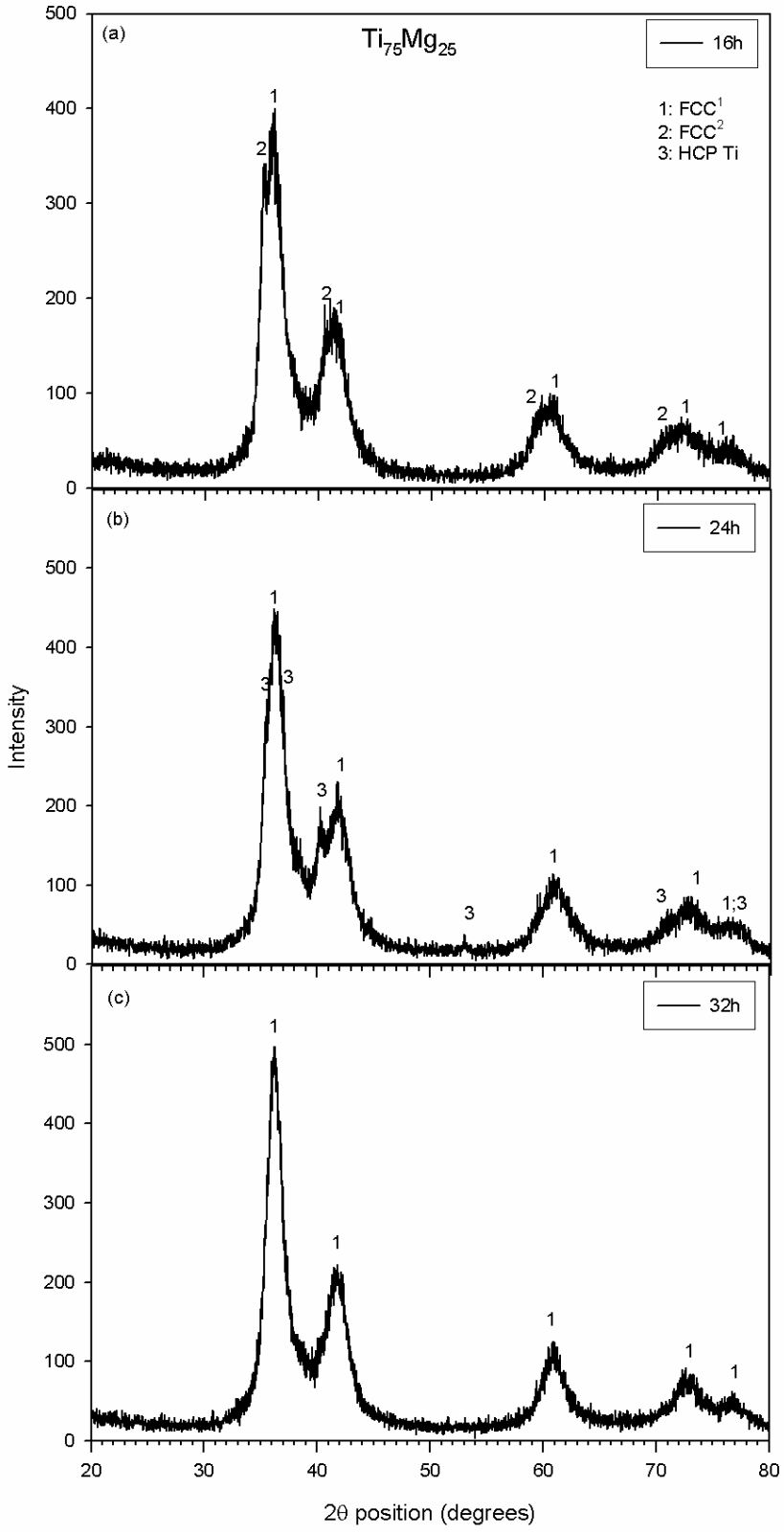

Figure 3.2.3.2.2. XRD patterns of $Ti_{75}Mg_{25}$ atomic composition powder mixture milled for (a) 16h, (b) 24h and (c) 32h at 800 rpm.

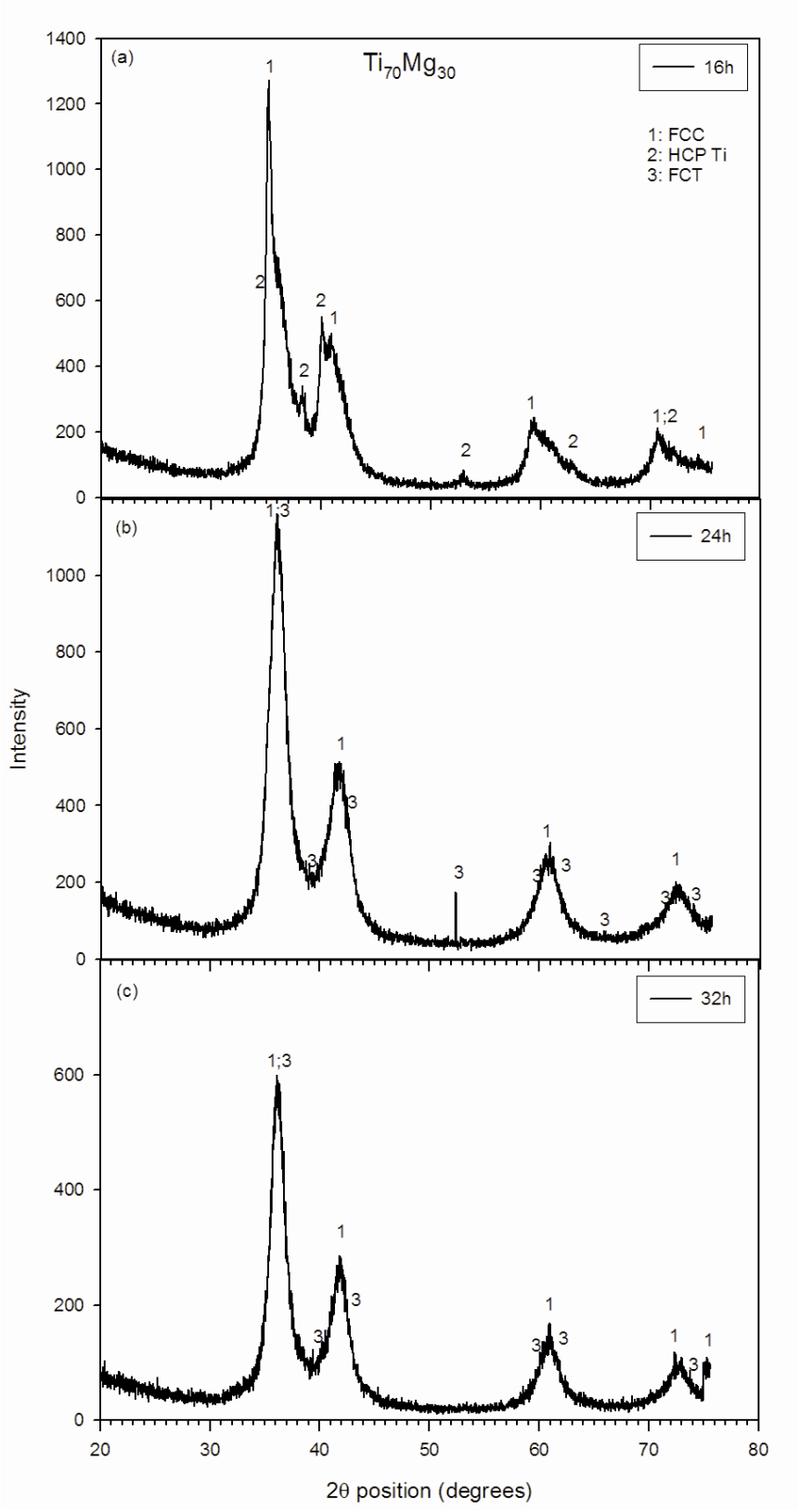

Figure 3.2.3.2.3. XRD patterns of $Ti_{70}Mg_{30}$ atomic composition powder mixture milled for (a) 16h, (b) 24h and (c) 32h at 800 rpm.

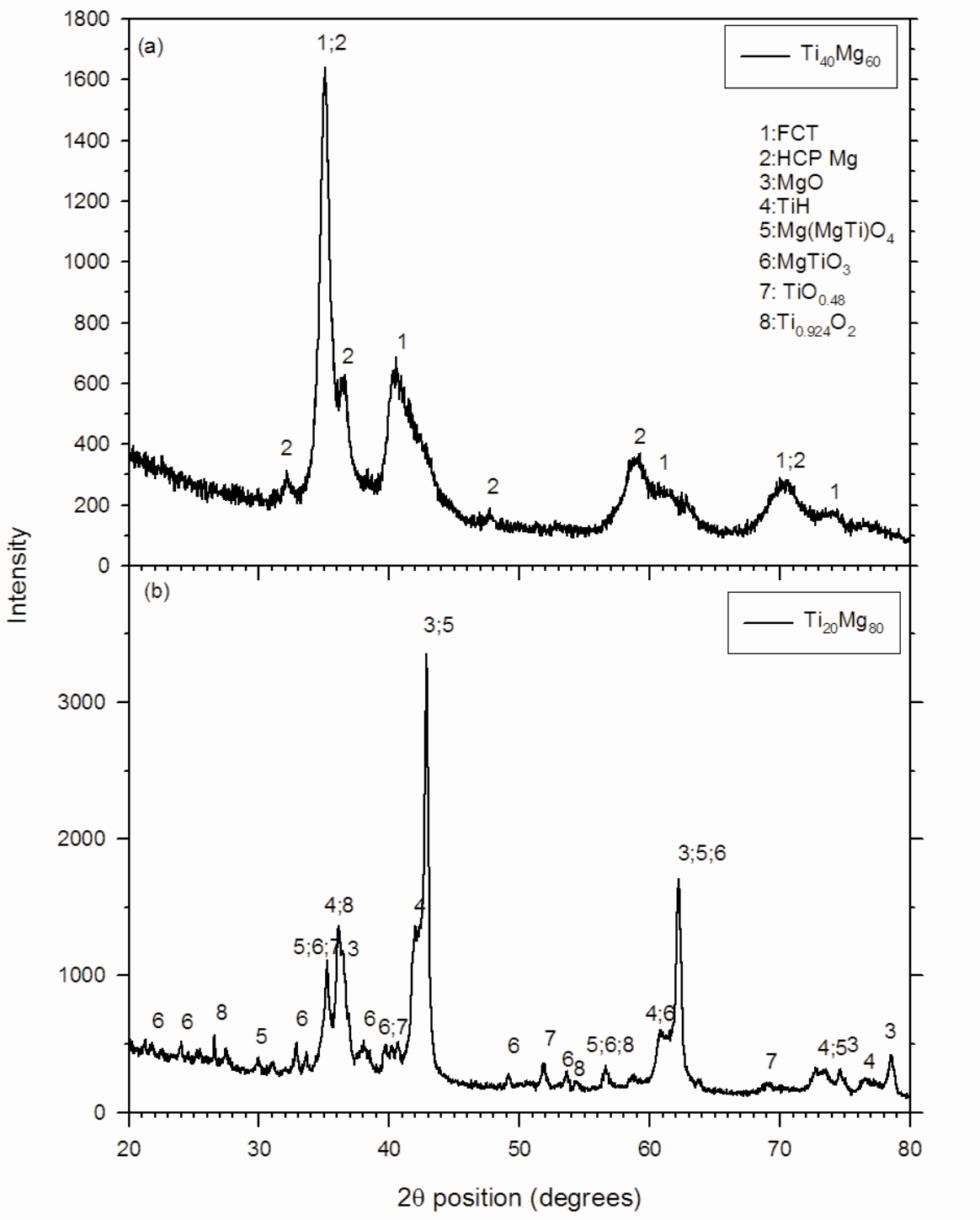

Figure 3.2.3.2.4. XRD patterns of (a) $Ti_{40}Mg_{60}$ and (b) $Ti_{20}Mg_{80}$ atomic composition powder mixtures milled for 32h at 800 rpm.

Table 3.2.3.2.1. Crystal structure details of phases detected by XRD on powders ball milled at 800 rpm.

Sample	$Ti_{80}Mg_{20}$	$Ti_{75}Mg_{25}$	$Ti_{70}Mg_{30}$	$Ti_{40}Mg_{60}$	$Ti_{20}Mg_{80}$
Milling period	XRD detected phases				
16h	**FCC ($TiH_{1.5}$)** Pn-3m (#224) a=4.389 Å **FCT ($TiH_{1.25}$)** P-42m (#111) a=4.271 Å c=4.607 Å	**FCC[1] (TiH)** F-43m (#216) a=4.307 Å **FCC[2] (TiH_2)** Fm-3m (#225) a=4.429 Å	**FCC ($TiH_{1.75}$)** P-43m (#215) a=4.402 Å **HCP (Ti)** $P6_3/mmc$ (#194) a=2.951 Å c=4.685 Å	-	-
24h	**FCC (TiH)** F-43m (#216) a=4.307 Å	**FCC (TiH)** F-43m (#216) a=4.307 Å **HCP (Ti)** $P6_3/mmc$ (#194) a=2.951 Å c=4.685 Å	**FCC (TiH**) F-43m (#216) a=4.307 Å **FCC ($TiH_{1.75}$)** P-43m (#215) a=4.402 Å **FCT ($TiH_{1.25}$)** P-42m (#111) a=4.271 Å c=4.607 Å	-	32h **FCC (MgO)** Fm-3m (#225) a=4.216 Å **FCC (TiH**) F-43m (#216) a=4.307 Å **FCC ($Mg(MgTi)O_4$)** Fd-3m (#227) a=8.440 Å
32h	**FCC (TiH**) F-43m (#216) a=4.307 Å	**FCC (TiH**) F-43m (#216) a=4.307 Å	**FCC (TiH**) F-43m (#216) a=4.307 Å **FCT ($TiH_{1.25}$)** P-42m (#111) a=4.271 Å c=4.607 Å	**FCT ($TiH_{1.924}$)** I4/mmm (#139) a=4.468 Å c=4.400 Å **HCP (Mg)** $P6_3/mmc$ (#194) a=3.209 Å c=5.210 Å	**RHL ($MgTiO_3$)** R-3 (#148) a=5.056 Å c=13.911 Å **HCP ($TiO_{0.48}$)** $P6_3/mmc$ (#194) a=2.970 Å c=4.810 Å **BCT ($Ti_{0.924}O_2$)** P42/mnm (#136) a=4.590 Å c=2.958 Å

core shell manner. In the currect case, the $C17H35COO^-$ ion softened Mg particles are surrounded by brittle titanium hydride particles, hence making it impossible for XRD to detect Mg. Furthermore, the highly protonated brittle Ti particles (TiH_X with $x > 1$) get more attached to Mg particles than the less protonated (TiH_x where $x \leq 1$), hence only TiH is detected on continued milling for 24 and 32h. On the other hand, a different case prevails when the Mg composition is increased to 25 atomic percent (at.%) as shown in Fig. 3.2.3.2.2. Upon milling for 16h, two types of FCC phases with lattice parameters of 4.307 (FCC^1) and 4.429 Å (FCC^2) corresponding to cubic TiH and TiH_2 are detected as shown in figure 3.2.3.2.2(a). It is interesting to note that on further milling to 24h (b), peaks of HCP Ti emerge but disappears again after 32h (c). This behaviour suggests that the particles of untransformed HCP Ti which had been attached to soft Mg particles resurface momentarily during milling process until H^+ becomes available to react with to form TiH. This appearance of Ti peaks indicates that the increased amount of Mg impedes some of the Ti particles from grain refinement and subsequent reaction with available protons, but at the same time the presence of Mg seems to enhance the protonation of nanocrystalline Ti particles.

A similar behaviour is observed upon milling the powder mixture with $Ti_{70}Mg_{30}$ composition for 16h, as presented in figure 3.2.3.2.3(a), wherein FCC $TiH_{1.75}$ and HCP Ti (α) phases were detected from XRD. However, the α Ti phase disappears on further milling for 24h as shown in Fig. 3.2.3.2.3(b), which coincides with the appearance of FCC TiH and FCT $TiH_{1.25}$. The latter two phases persist on increased milling up to 32h as shown in Fig. 3.2.3.2.3(c). As discussed above and observed from figures 3.2.3.2.1, 3.2.3.2.2 and 3.2.3.2.3 as well as in table 3.2.3.2.1, it apparently evident that the increase in Mg composition enhance the protonation of Ti leading to formation of FCC or FCT titanium hydrides. This point is further supported in Fig. 3.2.3.2.4(a), which shows the results of 32h ball milled Mg-rich composition ($Ti_{40}Mg_{60}$) comprised of FCT $TiH_{1.924}$ and HCP Mg. At this composition, the appearance of Mg is attributed to abundancy (high volume fraction) of magnesium powder and inadequate amount of titanium hydride to attach (coat) all Mg particles entirely. However, on milling $Ti_{20}Mg_{80}$ composition for same duration, the powder ignited on exposure to the atmosphere and

formed several kinds of compounds with respective space groups, namely, (3) MgO #225 Fm-3m, (4) TiH, (5) inverse-spinel $Mg((MgTi)O_4)$ #227 Fd-3m, (6) ilmenite-type $MgTiO_3$ #148 R-3, (7) $TiO_{0.48}$ #194 and (8) $Ti_{0.924}O_2$ #136 P42/mnm, as shown in figure 3.2.3.2.4(b) and table 3.2.3.2.1 with corresponding lattice parameters. Although the exact cause of ignition is not known for sure, it is likely to be related to destabilization of Mg or Ti lattice due to presence of stearic acid. This issue will be further investigated in the subsequently chapter.

3.2.3.3. Conclusion

It follows from the current study that starting composition does affect the mechanical alloying kinetics as well as the resultant crystal structure evolution. It is also evident that an increase in Mg impedes some of the Ti particles from grain refinement and subsequent reaction with available protons, but at the same time the presence of Mg seems to enhance the protonation of nanocrystalline Ti particles leading to formation of FCC or FCT titanium hydrides. Additionally, current results further support our earlier observation that upon milling Ti and Mg powder mixture, the harder Ti particles cluster around the surface of softer Mg particles in a core shell manner. In the currect case, the $C17H35COO^-$ ion softened Mg particles which are surrounded by brittle titanium hydride particles, hence making it impossible for XRD to detect the HCP Mg phase. In addition, the highly protonated brittle Ti particles (TiH_x with $x > 1$) get more attached to softer Mg particles than the less protonated (TiH_x where $x \leq 1$). In attempt to further clarify that the absence of HCP Mg peaks from most XRD patterns does not imply complete dissolution in Ti or its protonation, further work on ball milling experiments of pure elemental (Ti and Mg) powders is carried out in the next chapter.

Chapter 4

Effect of milling on the crystal structure of pure elemental Ti and Mg powders

4.1. Introduction

Currently, nanocrystalline (nc, grains sized below 100 nm) metals have captured a great deal of attention due to their improved chemical, physical and mechanical properties compared with that of ultrafine crystalline (ufc, grain sizes ranging from 100 to 500 nm) or microcrystalline (mc, grains sized above 500 nm) metals. For ufc and mc metals, strength is drastically enhanced when grain size is reduced, following the Hall-Petch relationship [Hall 1951, Petch 1953]. Here, the pile-up of dislocations at grain boundaries is envisioned as the key mechanistic process underlying an enhanced resistance to plastic flow from grain refinement; when grain size is relatively large, greater stresses can be concentrated near adjacent grains due to multiple pile-up dislocations, leading to the decrease in yield stress. On the other hand, as grain size is further reduced into nc region, activities of lattice dislocation becomes less significant, providing yield stress deviating from the Hall-Petch relationship [Yamakov *et al* 2002, Gleiter 1995, 2000].

Titanium and its alloys are still in demand in many structural applications; such as in aerospace, automotive and medical industries, due to their low density, high strength-to-weight ratio, and good corrosion resistance. On the other hand, Mg and its alloys continue to be very attractive as the lightest structural materials and have great potential for applications in automotive, aerospace and electronic industries. However, their usage is limited due to some undesirable properties of castings (such as strength, ductility, creep and corrosion resistance) and few fabricating methods besides conventional ingot metallurgy processing. Since grain refinement is generally believed

to have beneficial effect on mechanical properties, fabrication of nc metals and alloys using a powder metallurgical process such as ball milling (BM), which has proven to be an effective processing technique for producing nc metals, has attracted considerable attention in recent years. Moreover, at nano-scale these properties are expected to improve considerably and as such widen application options.

In addition, since it was not clear from the previous chapter whether the absence of HCP Mg peaks from most XRD patterns of milled powder mixtures implies complete dissolution in Ti or that its particles gets surrounded by harder particles of Ti and titanium hydrides. Therefore, in the current chapter, ball milling experiments of pure elemental powders are being carried out in order to understand the deformation path experienced by crystal structure of each metal during ball milling process.

4.2. Experimental procedure

4.2.1. Ball milling of pure Ti powder

4.2.1.1. Introduction

Metastable FCC Ti was obtained by various techniques such as ultrathin films deposited on aluminum substrate [Shechtman *et al* 1994, Van Heerden *et al* 1996, Kim *et al* 1996, Banerjee *et al* 1999], multilayers of nickel [Josell *et al* 1995] and silver [Tepper *et al* 1997], respectively. The lattice parameters of the stabilized FCC Ti varies between 4.15 Å [Kim *et al* 1996] and 4.42Å on Ti-Al alloys [Van Heerden *et al* 1996], respectively. Alternatively, in Ti-Ni and Ti-Ag multilayers the corresponding lattice parameters were 4.40 and 4.34Å respectively [Josell *et al* 1995, Tepper *et al* 1997], while in sputter deposition of Ti-Al-B is 4.21Å [Lofvander *et al* 1995]. So far, the basis for such difference in lattice parameter is not accounted for. Subsequently, different authors using the ball milling process [Chatterjee *et al* 2001a, b, Manna *et al* 2003] later published several articles on the formation of a metastable FCC with varying lattice parameters. In pure Ti, BM does not only reduce the grain size to nanometer level but

also induces solid-state transformation, more especially during intense high energy ball milling (HEBM) [Manna *et al* 2003]. In recent years, an increasing number of reports have been published on solid-state transformation achieved by HEBM in elemental metals [Huang *et al* 1995, Chattopadhyay *et al* 2001, Manna *et al* 2002, 2003, Sort *et al* 2003] as well as in binary solid solutions [Froes *et al* 1995, Ma and Atzmon 1995, Koch and Whittenberger 1996, Suryanarayana *et al* 2001, Maweja *et al* 2010, Phasha *et al* 2010b]. Manna *et al* (2003) reported HCP to FCC allotropic transformation in Ti governed by lattice expansion (negative hydrostatic pressure) as a result of grain refinement or nanocrystallization upon milling. In addition, the lattice expansion was also attributed to formation of NaCl-type TiO, TiN and TiC with lattice parameters 4.293, 4.242 and 4.327 Å respectively, due to high level of contamination during milling process. Despite these reports on HCP to FCC allotropic transition in commercially pure (CP) Ti using BM, systematic studies on HCP to FCC transition mechanism are scarce. However, after observing a similar FCC allotropic phase using TEM on ball milled Zr powder, Manna *et al* (2002) concluded that the stability of FCC phase is not impurity driven. Recently, most researchers have attributed the stability of FCC phase to impurities such as oxygen (O), nitrogen (N) and carbon (C) [Seelam *et al* 2009a, b], even though the sources of these impurities were not clearly identified. Furthermore, Vullum *et al* (2009) obtained FCC with a lattice parameter of 4.10 Å after flushing out hydrogen from titanium hydride by electron beam exposure. However, in addition to unclear underlying transformation mechanism, the basis for such a significant difference in the size of lattice parameter is not known. Hence, in the current chapter, the effect of milling on the crystal structure of pure Ti powder is investigated using XRD. Furthermore, the thermal stability of mechanically induced nanocrystalline metastable phase is studied upon annealing.

4.2.1.2. Experimental procedure

Ball-milling of pure titanium elemental powder (~ 99.5% purity, < 45 μm) was conducted in a Simoloyer CM01-2lm (Zoz GmbH) ball mill under argon atmosphere at milling speed of 800 rpm and ball-to-powder ratio (BPR) of 20:1 for 4, 8, 16, 24 and 30 hours.

The amount of process control agent (PCA), in this case stearic acid, added to the powder mixture was kept constant at 2 weight percent (wt.%). During milling experiments, small samples of approximately 5 grams were taken at the above selected time intervals to study the phase evolution using Phillips PW 1830 X-ray diffraction (XRD) machine fitted with Cu Kα radiation, and 0.02 step size scanned from 20 to 90° (2θ). Furthermore, in order to investigate if the milling interruptions and the presence of PCA have an effect on phase transformation, another Ti powder sample was milled under similar conditions for 24h uninterrupted with and without PCA. The XRD peak broadening was calculated from the full width at half maximum (FWHM) of the most intense Bragg peak. The Scherrer and Williamson-Hall (W-H) methods (mentioned in 2.5.2) were used to determine the average crystallite sizes. The 30 h milled powder was cold pressed in a die using a uniaxial press, at 30 MPa. The resulting powder compact was annealed at 1200°C for 1h in a horizontal tube furnace under argon atmosphere, followed by XRD characterization to identify phases present.

4.2.1.3. Results and discussion

The X-ray patterns of powders milled at 800 rpm for 4, 8, 16, 24 and 30h are shown in figure 4.2.1.3.1. It is evident from figure 4.2.1.3.1 that the diffraction peaks of Ti are slightly displaced towards higher angles and their intensities decreased as the milling duration increases, with exception of the first (100) peak which became stronger with milling. This indicates changes in the crystal structure of Ti due to plastic deformation upon milling and corresponds to combination of lattice contraction as well as grain refinement, as shown in table 4.2.1.3.1. While the peak intensities as well as the order of the first three peaks belonging to (100), (002) and (101) planes change between 4 and 24h [Bolokang and Phasha 2010], the HCP to FCC transformation is only observed after 16h when the average crystallite size is about 50 nm according to Scherrer equation. However, as determined from the *y*-intercept of the straight line graph representing W-H isotropic strain model (ISM) in figure 4.2.1.3.2(c), the crystallite size (D_{WH}) after 16h is below 40 nm when using W-H method. In addition to the determined microstrain from W-H technique, the crystallite sizes obtained using both methods are

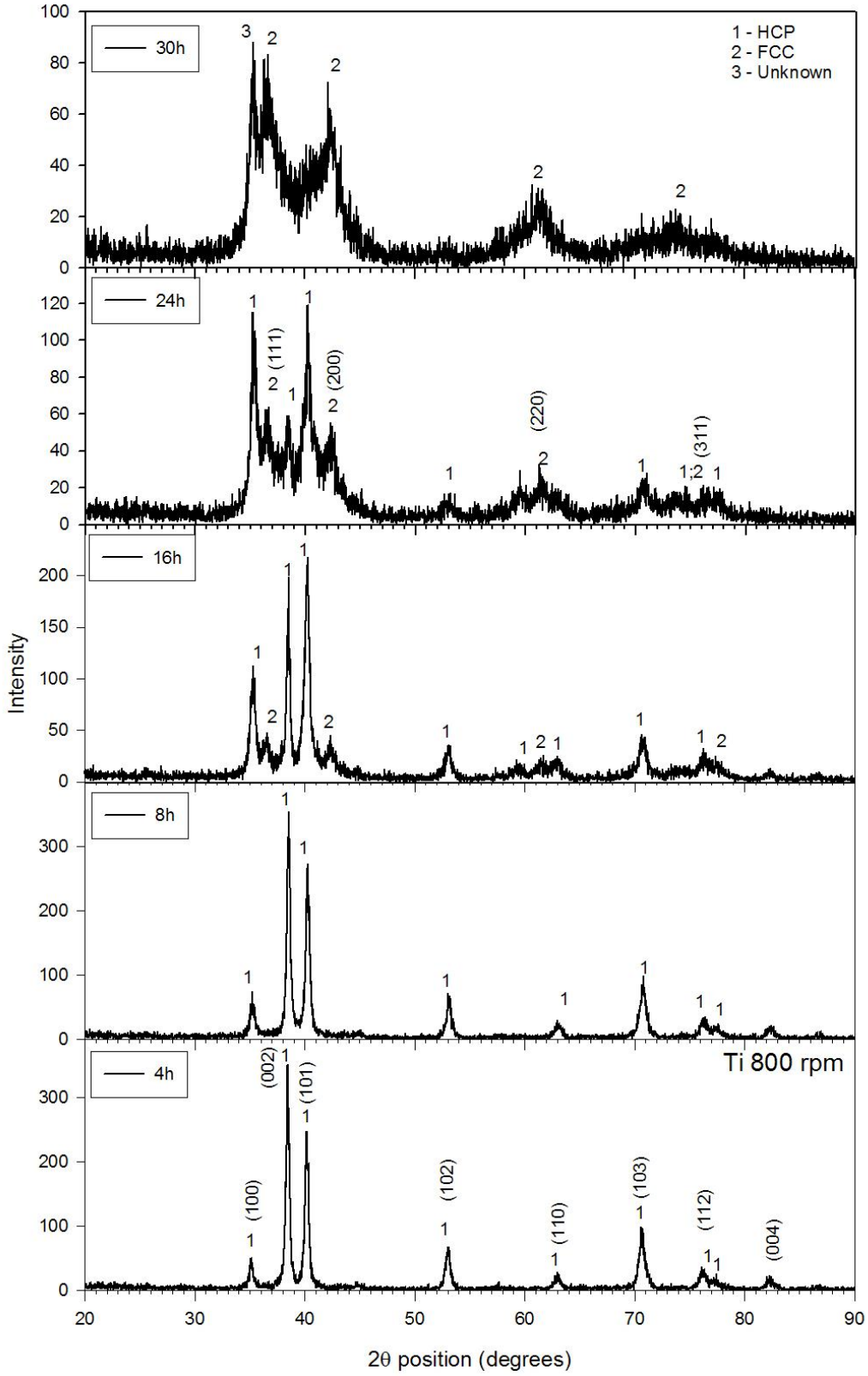

Figure 4.2.1.3.1. XRD patterns of Ti powders milled for 4, 8, 16, 24 and 30 hours.

Table 4.2.1.3.1. XRD crystal structure data for Ti milled powder.

Milling Time (h)	Lattice parameter (Å) a	c	Space group	Crystal Structure
4	2.951	4.685	$P6_3/mmc$ (194)	HCP (100%)
8	2.944	4.678	$P6_3/mmc$ (194)	HCP (100%)
16	2.951 4.262	4.679 -	$P6_3/mmc$ (194) Fm-3m (225)	HCP (80%) FCC (20%)
24	2.944 4.242	4.678 -	$P6_3/mmc$ (194) Fm-3m (225)	HCP (15%) FCC (85%)
30	4.240 Unknown	-	Fm-3m (225) Unknown	FCC (85%) Unknown (15%)

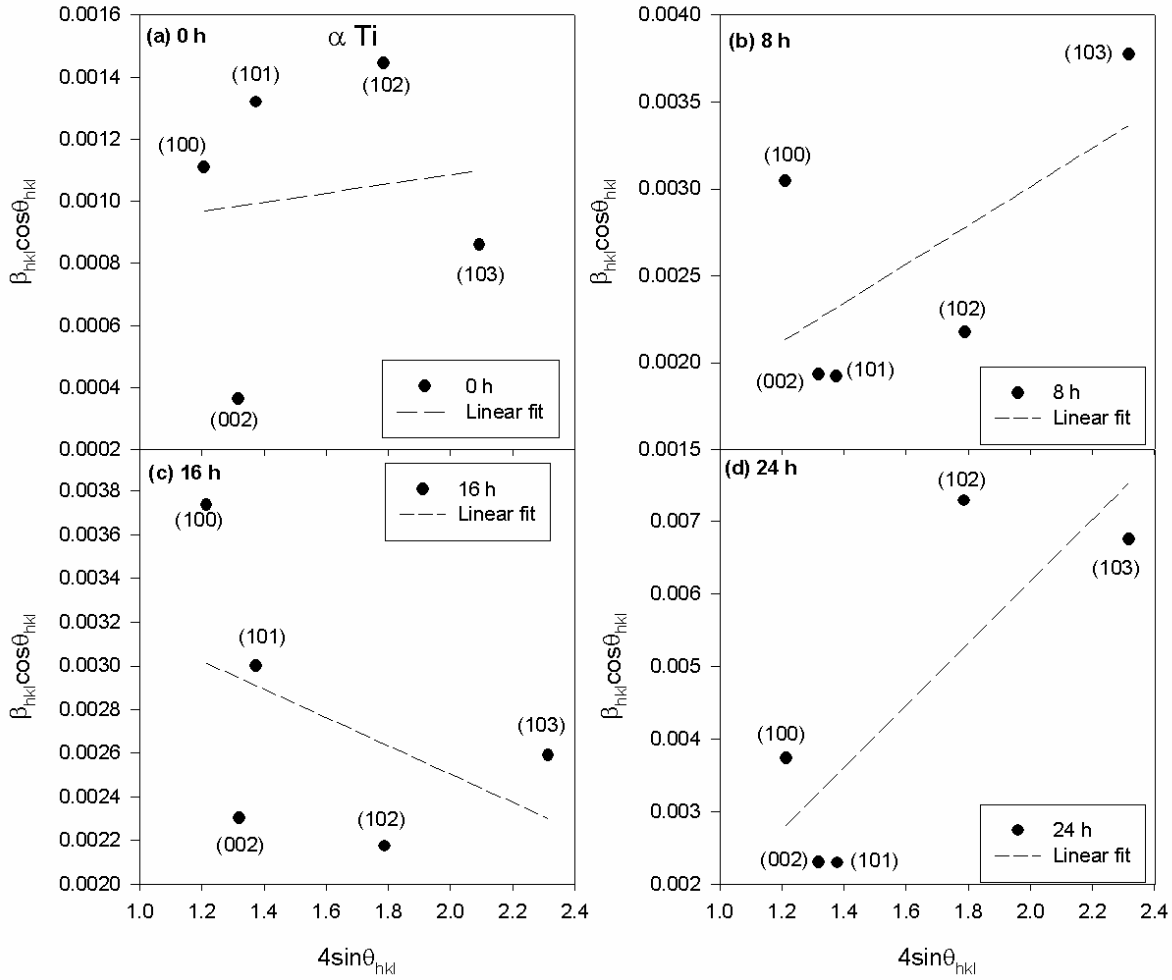

Figure 4.2.1.3.2. Williamson-Hall plots of Ti powder milled for (a) 0 h, (b) 8 h, (c) 16 h and (d) 24 h, assuming uniform deformation. The dashed line represents a linear fit.

presented in figure 4.2.1.3.3(a), while the crystallite sizes (D_S) determined for each plane are shown in figure 4.2.1.3.3(b), all plotted against milling time. It is interesting to note from figure 4.2.1.3.3(a) that the microstrain becomes negative after milling for 16h. This behaviour which corresponds to slightly increased crystallite size along (102) and (103) pyramidal slip planes as shown in figure 4.2.1.3.3(b), is attributed to tension (lattice expansion) due to twinning deformation mode. In general, the (100), (110) prismatic planes as well as the pyramidal planes (101), (102) and (103) show similar behaviour of crystallite size on milling. However, the crystallite size along the (002) basal plane is more affected by milling as indicated by rather rapid reduction after 8h and behaves averagely afterwards. Using both methods for determining D, crystallite sizes were still above the reported critical size of 10 nm [Manna *et al* 2003]. Since the FCC phase was obtained in crystals larger than 10 nm, it clearly follows that not only nanocrystallization or grain refinement to below the critical size of 10 nm induces HCP to FCC transformation in Ti [Dabhade *et al* 2007], but the solid-state transformation could be achieved if the ball impact on the refined nanometer grains is high enough to plastically deform the HCP lattice. Consequently, most of Ti has transformed to FCC with D_S=19 nm after 24h milling, with only about 15% volume fraction of crystals remained in HCP alpha (α) phase. This nanostructured α Ti reaches almost an amorphous state and becomes difficult to detect, hence represented by unknown phase, while the FCC phase reached crystallite size of approximately 12 nm (D_S) when milled further to 30h.

In order to investigate the effect of milling interruptions and presence of PCA, we have shown XRD patterns of Ti powder milled for 24h uninterrupted with PCA, without PCA as well as 6h interval interrupted without PCA in figure 4.2.1.3.4(a), (b) and (c), respectively. For the powder milled for 24h uninterrupted with PCA, the measured lattice parameter of the only detected phase (FCC), was 4.296 Å. Comparing results of Ti milled for 24h in the presence of PCA, interrupted (*a*=4.242 Å) and uninterrupted (*a*=4.296 Å), in figures 4.2.1.3.1 and 4.2.1.3.4(a) respectively, it follows that milling interruption delays either the transformation or H^+ update due to exposure to the atmosphere. Similar results were reported by Lu *et al* (2004) who milled Ti powder with

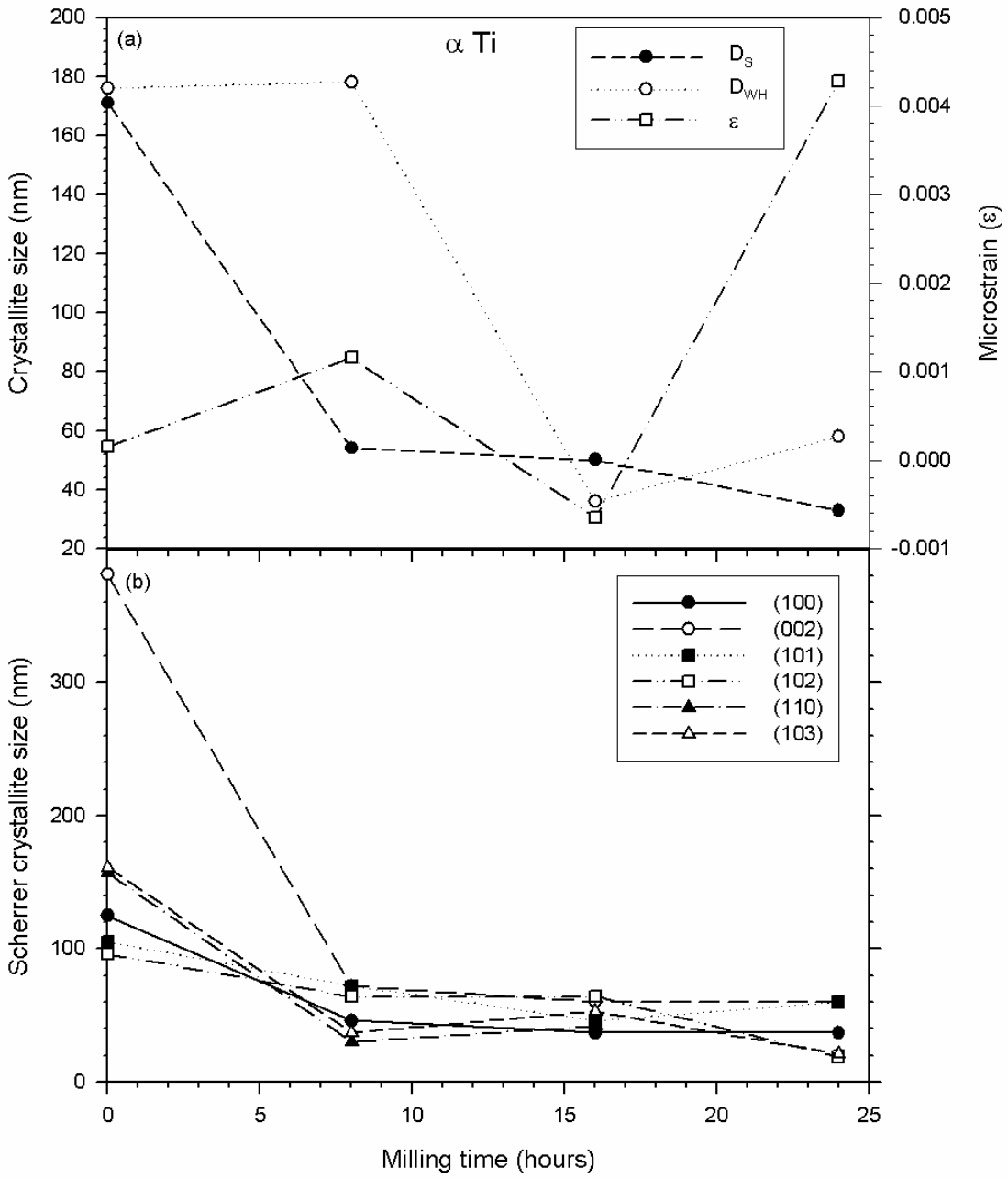

Figure 4.2.1.3.3. (a) Average Scherrer (D_S), W-H (D_{WH}) crystalline sizes and microstrain (ε), (b) Scherrer crystallite size determined on individual (100), (002), (101), (102), (110) and (103) planes of α Ti.

open and closed vial, to obtain a mixture α-Ti$(O,N)_x$, FCC-Ti$(O,N)_y$ and TiO_2. However,when Ti powder was milled in the absence of PCA, no phase transformation was observed for both uninterrupted and interrupted milling cycles as shown in figure 4.2.1.3.4 (b) and (c), respectively. The crystallite sizes corresponding to figure 4.2.1.3.4(a), (b) and (c) determined according to Scherrer formula (W-H method) were

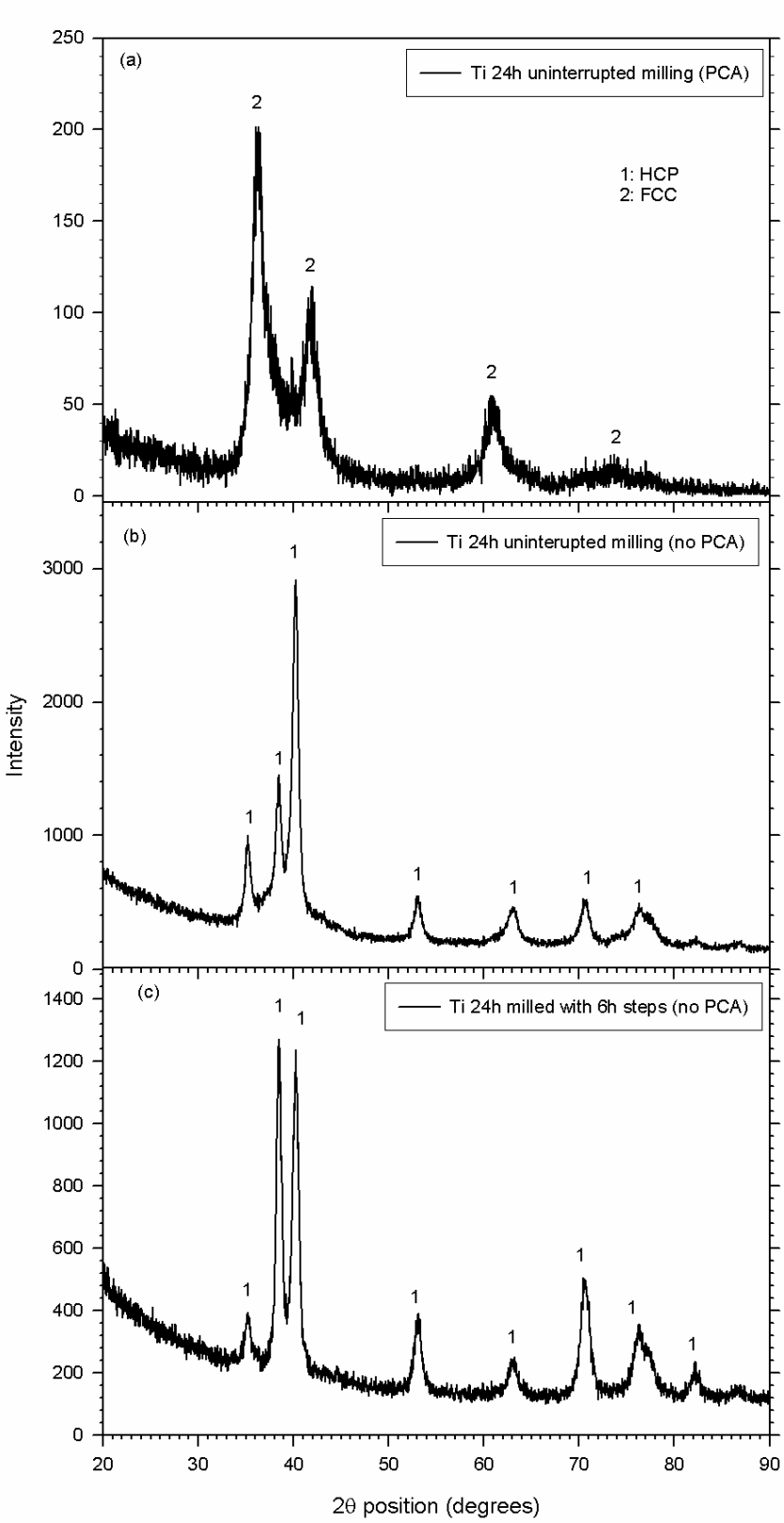

Figure 4.2.1.3.4. XRD pattern of Ti powder milled for 24h (a) uninterrupted with PCA, (b) uninterrupted without PCA and (c) interrupted at 6h intervals with without PCA.

19 (22), 44 (46) and 83 (110) nm, respectively.

The SEM images of unmilled and milled powders presented in figure 4.2.1.3.5 indicate that (i) the precence of PCA promotes rapid grain refinement and reduces cold-welding as shown by change in particle morphology from (a) spherical to (b) a mixture coarse and thin flake-like particles, (ii) the absence of PCA (c) slows grain refinement while (d) milling interruptions promotes cold-welding as indicated by average particle size of less than 100 µm and larger than 100 µm, respectively. As expected, the EDS analysis corresponding to figure 4.2.1.3.5(b) indicates Ti powder bearing high amounts of C and O (~ half the amount of C) at light-grey areas due to presence of stearic acid and almost pure Ti in dark-grey areas. For powders milled in the absence of PCA, small levels of C (less than 5 at.%) are detected. This could be attributed to contamination of milling media from previous milling runs that involved PCA.

Furthermore, the transformation from HCP to FCC in titanium is indeed impurity driven, in agreement with several reports [Manna *et al* 2003, Seelam *et al* 2009a, b]. However, in the current we identified the PCA (stearic acid) as the source of interstitial element (contaminant) that induces this phase transition. In particular, the reaction of nanocrystalline thin flake Ti particles (surcafes) with H^+ (proton) from the stearic acid to form TiH_{2-x} is found to be responsible for this solid-state transition. In support of our results, Zhang *et al* [2010] also reported recently that the stearic acid was the primary source for introducing H and C into cryomilled Al powder.

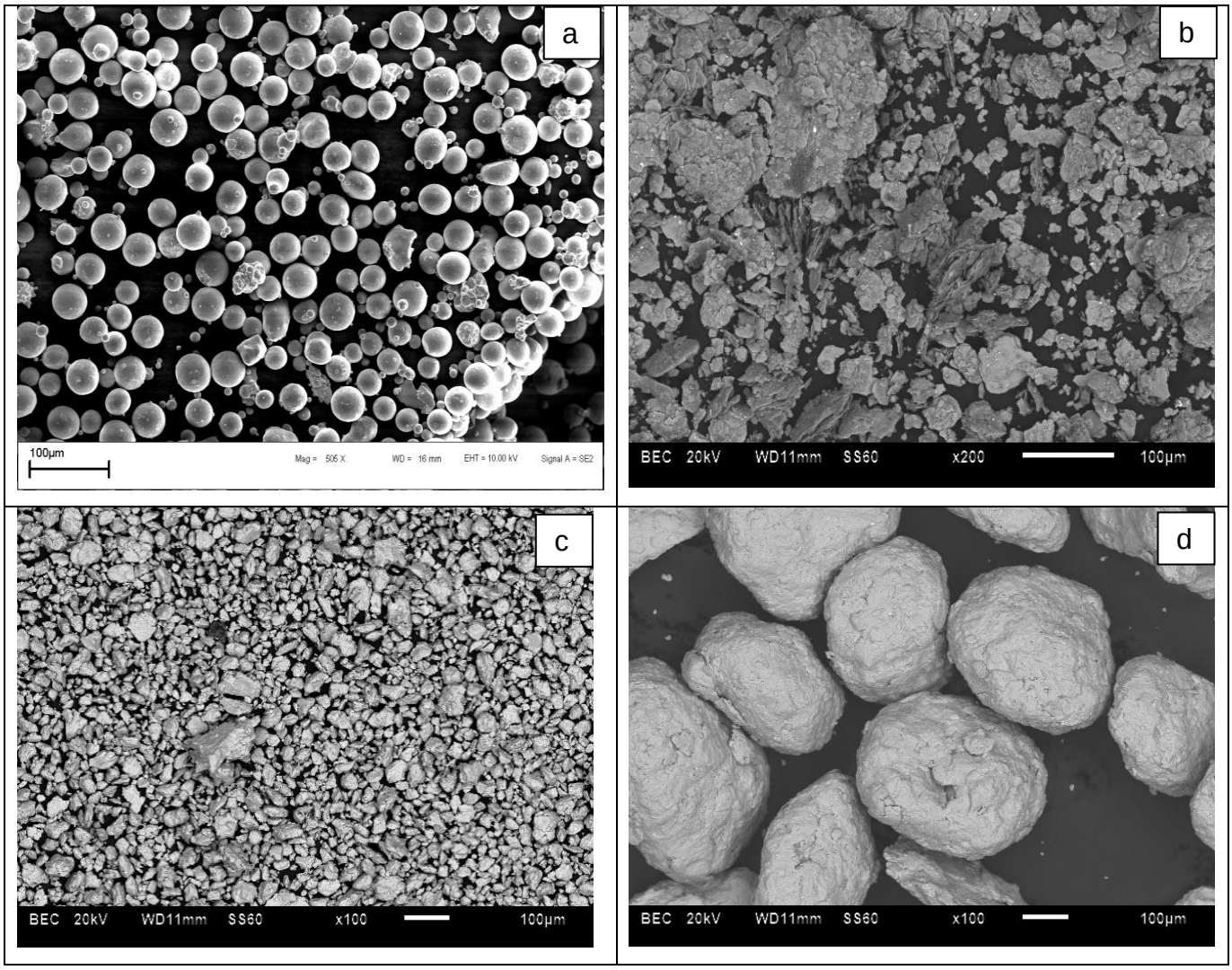

Figure 4.2.1.3.5. SEM images of Ti powder (a) unmilled, (b) 24h milled uninterrupted with PCA, (c) 24h milled uninterrupted without PCA, and 24h milled interrupted at 6h intervals without PCA.

The thermal stability of the metastable FCC phase was investigated by annealing the Ti powder milled for 30h in the presence of PCA. This powder was cold pressed in a die using a uniaxial press at 30 MPa. The resulting powder compact was annealed at 1200^{o}C in a horizontal carbolite tube furnace under continuous argon gas flow for an hour and then furnace cooled. The heating and cooling rates were kept at 20^{o}C/min. Upon cooling to room temperature, the XRD and SEM characterizations were carried out. From the resulting XRD patterns shown in figure 4.2.1.3.6, it is evident that the

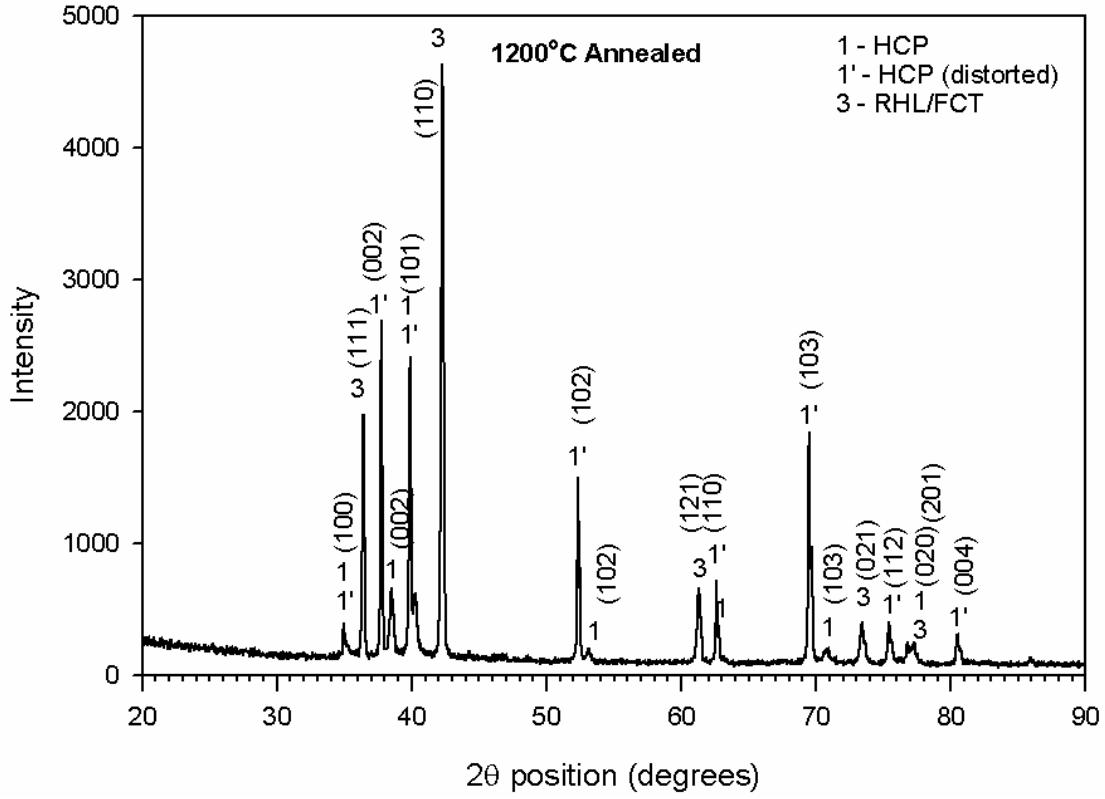

Figure 4.2.1.3.6. XRD patterns of 30 h milled Ti powder compact annealed at 1200^{o}C for an hour.

HCP Ti peaks which had disappeared completely after 30h milling (figure 4.2.1.3.1) reappears alongside the peaks of a new phase after annealing. In addition to the two HCP Ti phases, deformed (7%) and undeformed (8%) represented as 1' and 1 with lattice parameters *a*=2.966 Å, *c*=4.782 Å and *a*=2.951 Å, *c*=4.679 Å, respectively, the XRD detects a new rhombohedral (trigonal) phase (85%) of the $FeO_{0.942}$ type with space group R-3m #166, lattice parameters *a*=*b*=*c*=3.021 Å and α=β=γ=59.992°. It is known from crystallography that the primitive cell of an FCC lattice is RHL when the $\alpha_{RHL}=60^{o}$. This observed RHL (#166 R-3m) has hexagonal representation consisting of lattice parameters *a*=3.0206, *c*=7.4004 Å and *c/a*=2.4500, almost similar to Ti_2C phase with lattice parameters a=3.0736 c=14.8770 Å [Winkler *et al* 2009], in which *c* is doubled. Furthermore, the RHL trigonal phase corresponds to ideal HCP (#194) phase with lattice parameters *a*=3.0206, *c* =4.9336 Å and axial ratio of 1.633, since $c_{RHL}\approx 1.5c_{\alpha}$, and FCT phase with *a*=4.2723, *c*=3.7839 Å and *c/a*=0.885. This type of FCC to RHL

transition is similar to that observed in transition-metal monoxides during their transition from paramagnetic cubic rocksalt (B1) to antiferromagnetic (AFM) rhombohedral structure below Néel temperature (T_N) by way of contracting B1 lattice in the [111] direction [Roth 1958]. Our value of *c/a* ratio (2.4500) is slightly higher than √6=2.4495, which is reported as an indication for B1 lattice contraction in the [111] direction [Eto *et al* 2000]. However, in the current instance, the new phase is attributed to formation of FCT due to dehydrogenation. Therefore, the reappearance of both the α- and distorted α-Ti phase could suggest three possibilities, (i) that the prolonged milling led to hard particles of formed metastable TiH_{2-x} attaching themselves around the fresh surfaces of unprotonated HCP Ti, in a core (α-Ti) - shell (FCC TiH_{2-x}) manner, consequently the core resurfacing on annealing at high temperature, due to higher coefficient of thermal expansion (CTE) of Ti compared to its non-stoichimetric hydride, (ii) the unprotonated α Ti phase dissolved the available C atoms to form a α-solid solution denoted as distorted HCP during annealing while O together with H vapourized, (iii) that annealing led to decomposition of the metasable TiH_{2-x} which led to phase transition from cubic (FCC) to tetrahedral (FCT) lattice as well as α titanium. The latter mechanism seems to be the most favourable as was reported in several recent studies [Sandim *et al* 2005, Kovalev *et al* 2010].

The corresponding SEM images of the annealed powder are presented in figure 4.2.1.3.7 below. As shown in figure 4.2.1.3.7(a), a mixture of small and large grains is observed under low magnification. In addition to the grains of α Ti indicated by black regions, interesting plate-like martensitic features corresponding to the metastable FCT phase are observed in the microstructure at higher magnification, as shown in figure 4.2.1.3.7(b). On average, the EDS measurements conducted on black α-regions detected approximately between 20 and 30 at.% C on phases that did not contain any oxygen, between 10 and 15 at.% C on phases that contained about 25 at% O. Interestingly, the EDS measurements on the grey-platelet areas did not indicate any sign of either O or C but small amounts of Al (< 10 at.%) and V (<0.5 at.%).

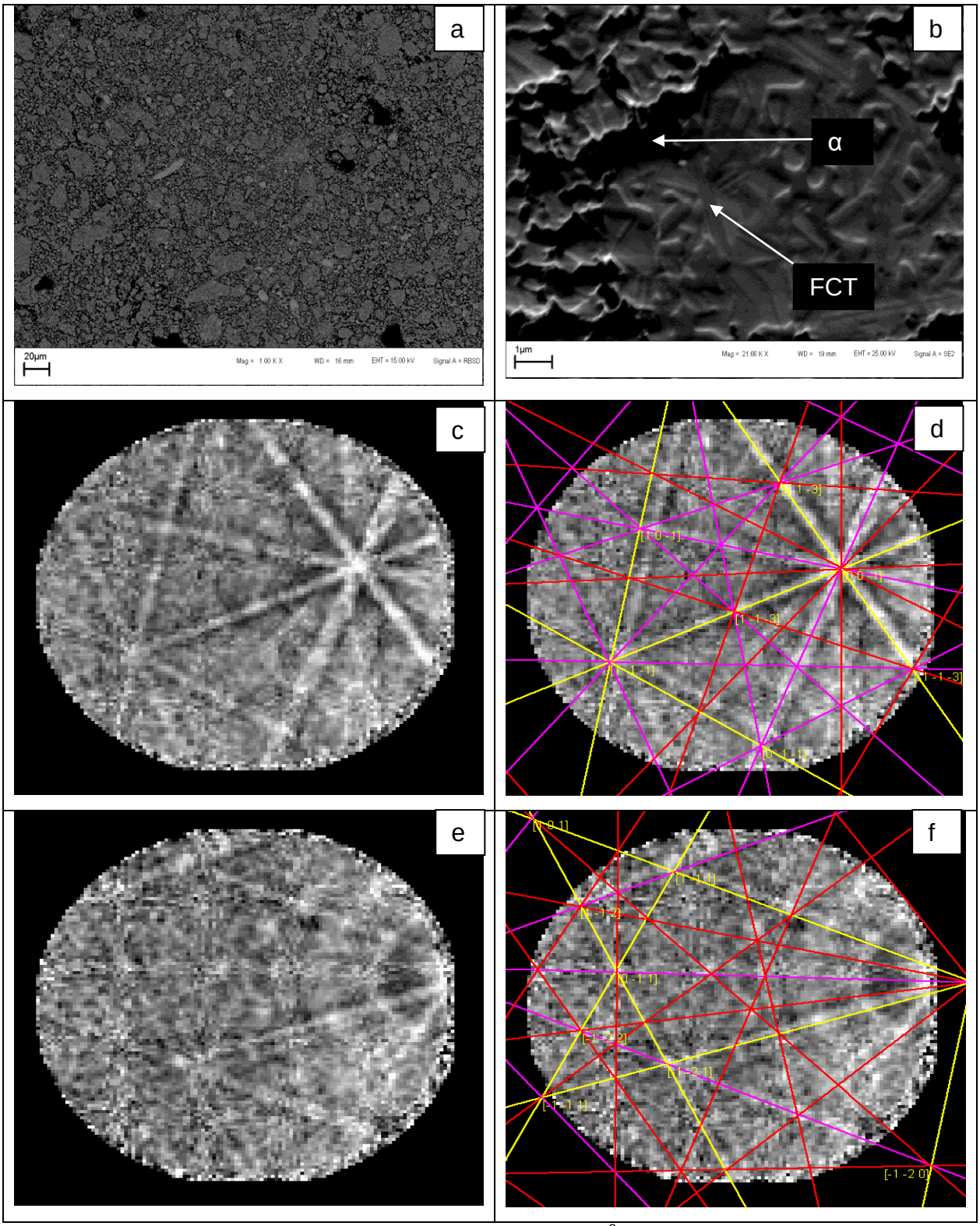

Figure 4.2.1.3.7. SEM images of 30h milled and annealed at 1200^{o}C at (a) lower and (b) higher magnification. The corresponding (c) Collected, (d) indexed EBSP of the FCT phase and (e) collected, (f) indexed EBSP of the α phase.

In an attempt to further identify the phase within the platelets in figure 4.2.1.3.7(b), EBSD analysis was performed at 25 kV with the sample tilted to 70^{o} relative to the incident electron beam. The OXFORD INCA Crystal software was used to solve the characteristic Kikuchi patterns emanating from the sample, thereby allowing for the identification of the different phases present. Figure 4.2.1.3.7(c) shows the collected electron backscattered diffraction pattern (EBSP) of the grey phase which indexed consistently as an FCT phase of Ti with space group I4/mmm #139 was used as the structure model since EDS could not detect H atoms. The simulation of FCT phase in the proper orientation, as determined by the indexing software, is shown in figure 4.2.1.3.7(d) and shows an exact match with the experimental EBSP. Similarly, although a bit faint due to deformation, figure 4.2.1.3.7(e) shows the collected EBSP of the black phase which was indexed as an α phase. The HCP ($P6_3/mmc$ #194) Ti phase was used as the structure model. Figure 4.2.1.3.7(f) shows the exact match between the simulated and experimental image. Our results demonstrate that EBSD technique could be used in conjuction with SEM and XRD to identify the unknown phases.

4.2.1.4. Conclusion

Nanocrystalline Ti powder of about 40 nm crystallite size was produced by ball milling in the presence of PCA for 30h at interrupted intervals. During BM of Ti powder, solid-state transformation from HCP to FCC occurred between 24 and 30h with lattice parameter of ~ 4.240 Å. However, when milling is carried out uninterrupted for 24h, an FCC phase with *a*= 4.296 Å was obtained within powder of about 22 nm crystallite size. Comparing results of Ti milled for 24h in the presence of PCA, interrupted (*a*=4.242 Å) and uninterrupted (*a*=4.296 Å), it follows that milling interruption delays either the transformation or H^{+} uptake due to exposure to the atmosphere. When Ti powder was milled in the absence of PCA, no phase transformation was observed for both uninterrupted and interrupted milling cycles. The average crystallite sizes ranged between 44 and 84 nm for uninterrupted and interrupted milling cycles, respectively. Based on SEM images of unmilled and milled powders the following conclusions were drawn (i) the precence of PCA promotes rapid grain refinement and reduces cold-

welding as shown by change in particle morphology from spherical to a mixture coarse and thin flake-like particles, (ii) the absence of PCA (c) slows grain refinement while (d) milling interruptions promotes cold-welding as indicated by average particle size of less than 100 µm and larger than 100 µm, respectively. Therefore, the transformation from HCP to FCC in titanium is indeed impurity driven, in agreement with several reports. However, in the current study we identified the PCA (stearic acid) as the source of interstitial element (contaminant) that induces this phase transition. In particular, the reaction of nanocrystalline thin flake Ti particles (surcafes) with H^+ (proton) from the stearic acid to form TiH_{2-x} is found to be responsible for this solid-state transition. Upon annealing at 1200^oC, the decomposition of the metasable TiH_{2-x} occurs, leading to phase transition from cubic (FCC) to tetrahedral (FCT) lattice as well as α titanium, as evidenced by XRD and EBSD results. In an attempt to explain the fundamentals governing the solid-state transformation during ball milling, various first-principles calculations of pure Ti in several phase will be carried out in chapter 6.

4.2.2 Ball milling of Mg

4.2.2.1. Introduction

Due to its abundance, low density and low price, magnesium is a very attractive element for light alloys in the automotive and aerospace industries [Polmear 1994]. However, applications of Mg and its alloys is limited because of their high sensitivity to oxidation and their relatively low corrosion resistance. Nonetheless, Mg is able to absorb large quantities of hydrogen (7.6 wt.%) which makes it a particularly interesting element for the elaboration of Mg-based metal hydrides as hydrogen source for fuel cells [Huot *et al* 2001, Orimo and Fujii 2001]. For this reason, Mg and its alloys are considered to be some of the most important candidates for reversible storage materials [Sakintuna *et al* 2007; Jain *et al* 2010]. However, in its microcrystalline form it shows slow sorption kinetics. In addition, other impediments in Mg hydrides include high thermodynamic stability and high reactivity toward air and oxygen which is common with most other lightweight metal hydrides [Zeppelin *et al* 2001]. The high thermodynamic

stability of MgH_2 results in a relatively high desorption enthalpy, which corresponds to an unfavourable desorption temperature (> 300^oC) at 1 bar H_2 [Zeppelin *et al* 2001]. Also, the formation of an oxide layer presents an impenetrable boundary to hydrogen gas molecules [David 2007]. To initiate uptake of hydrogen, the oxide layer must be cracked by activation, which is a long costly process. Even after activation, there is a limited dissociation rate of hydrogen molecules on the metal surface. This is usually improved by a layer of added catalyst, but is also costly. Hydrogenation also depends upon the growth of hydride on the Mg surface. However, this outer layer of the hydride blocks hydrogen from reaching the core or inner unreacted Mg once the layer reaches a thickness of only 100 μm. This means that there is no physical way for Mg to be fully hydrogenated, especially in the microcrystalline form. The solution for these impediments would be to form nanocrystalline magnesium hydride and then a chemical activation. Adjusting the powder size to < 50 μm is thin enough to overcome the hydride blocking issue [Urretavizcaya *et al* 2002]. Hence the recent increased number of research activities that use ball mill process, in which powders are fragmented into very fine particles that are cold welded to form medium sized particles with small grain sizes [Hout *et al* 1999, Gubicza *et al* 2004]. Despite the much improved sorption kinetics of nanocrystalline Mg alloys, most of these studies mill pure Mg under H_2 atmosphere with or without a catalyst [Kwon *et al* 2008; 2010, Song *et al* 2009, David 2007], pure Mg or MgH_2 in the presence of catalyst under argon atmosphere [Song 1995, Song *et al* 1999; Friedrichs *et al* 2006, Amirkhiz *et al* 2011], which makes it difficult to investigate the effect of milling on pure Mg. As a result, only few studies have been reported this far on synthesis of nanocystalline pure Mg by ball milling under inert atmosphere [Zaluska *et al* 1999, Hwang *et al* 2001, Grosjean *et al* 2004, Zidoune *et al* 2004, Gerasimov *et al* 2009, Choi *et al* 2010]. Furthermore, several researchers reported synthesis of HCP, FCC and BCC solid solutions from milling Mg mixed with other metals, although the mechanisms for such formations are still lacking. Similar results were obtained in the previous chapter, hence current focus on the effect of ball milling on pure Mg under argon atmosphere and the corresponding structural evolution.

4.2.2.2. Experimental procedure

Both the ball milling conditions as well as the characterization techniques were similar to those used for pure Ti (4.2.1.2.), although no PCA was added and much longer milling durations (0, 15, 30, 60 and 90h) were introduced due to limited plastic deformation of Mg at room temperature. In addition, milling was also conducted in the presence of stearic acid for 4, 8 and 24h. The fine (< 45μm) magnesium powder (~99.5% purity) was used.

4.2.2.3. Results and discussions

The XRD patterns of Mg powder milled for 0, 15, 30, 60 and 90 h are presented in figure 4.2.2.3.1(a). Figure 4.2.2.3.1(b) shows a magnified XRD patterns between 30 and 40^{o} two theta positions, which indicates clearly that the Mg particles got refined rapidly. The crystallite sizes determined by W-H (figure 4.2.2.3.2) and Scherrer methods, are presented in figure 4.2.2.3.3(a). As shown in figure 4.2.2.3.3(b), which indicates the crystallite sizes (D_S) determined for each plane, a distinctive behaviour of (110) prismatic plane is observed in the Mg powder milled beyond 30h corresponding to significant increase in average crystallite size (D_S) and negative strain. The latter could imply expansion along (110). Even though to a lesser extent, the (102) and (101) pyramidal slip planes also show a similar trend. Conversely, the crystallite size in the (100) prismatic plane and (002) basal plane becomes almost flat when powder was milled more than 30h. These results could be correlated to deformation modes of HCP Mg crystals during ball milling.

In figure 4.2.2.3.4, XRD patterns of Mg powder milled in the presence of PCA are presented. As shown in figure 4.2.2.3.4(a) and (b), besides the change in preferred orientation, shortening and broadening of peaks, there are no structural changes observed between 0 and 8h milling. This behaviour persists even after milling for 24h, although the α-Ti and unknown phase which could be attributed to metastable TiH_{2-x} were depicted, as shown in figure 4.2.2.3.4(c). The presence of these phases seems to suggest that milling Mg in the presence of stearic acid has a tendency or potential to

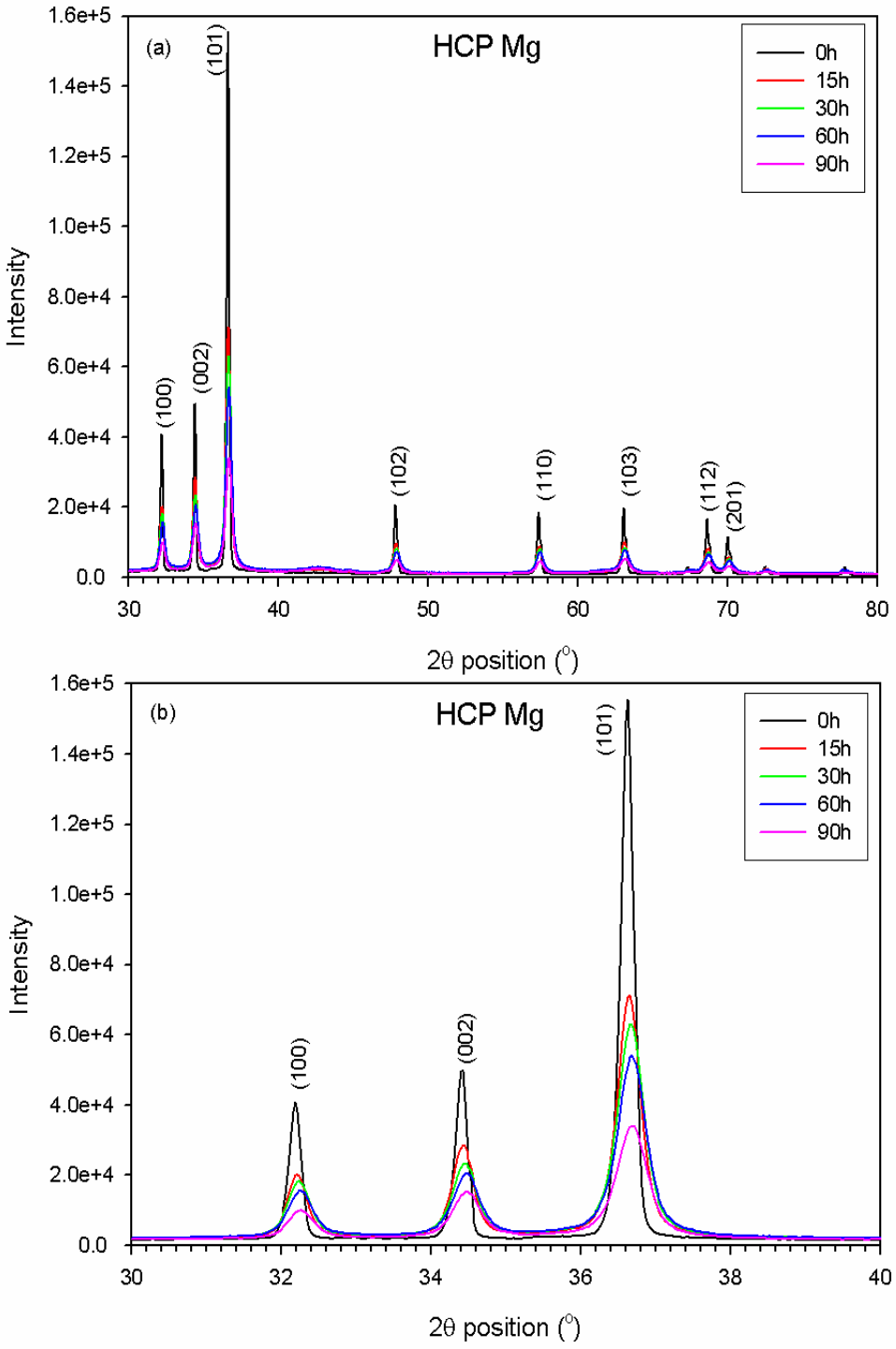

Figure 4.2.2.3.1.(a) XRD patterns of Mg powder milled for 0, 15, 30, 60 and 90 h, (b) magnification of XRD patterns at lower 2θ angles.

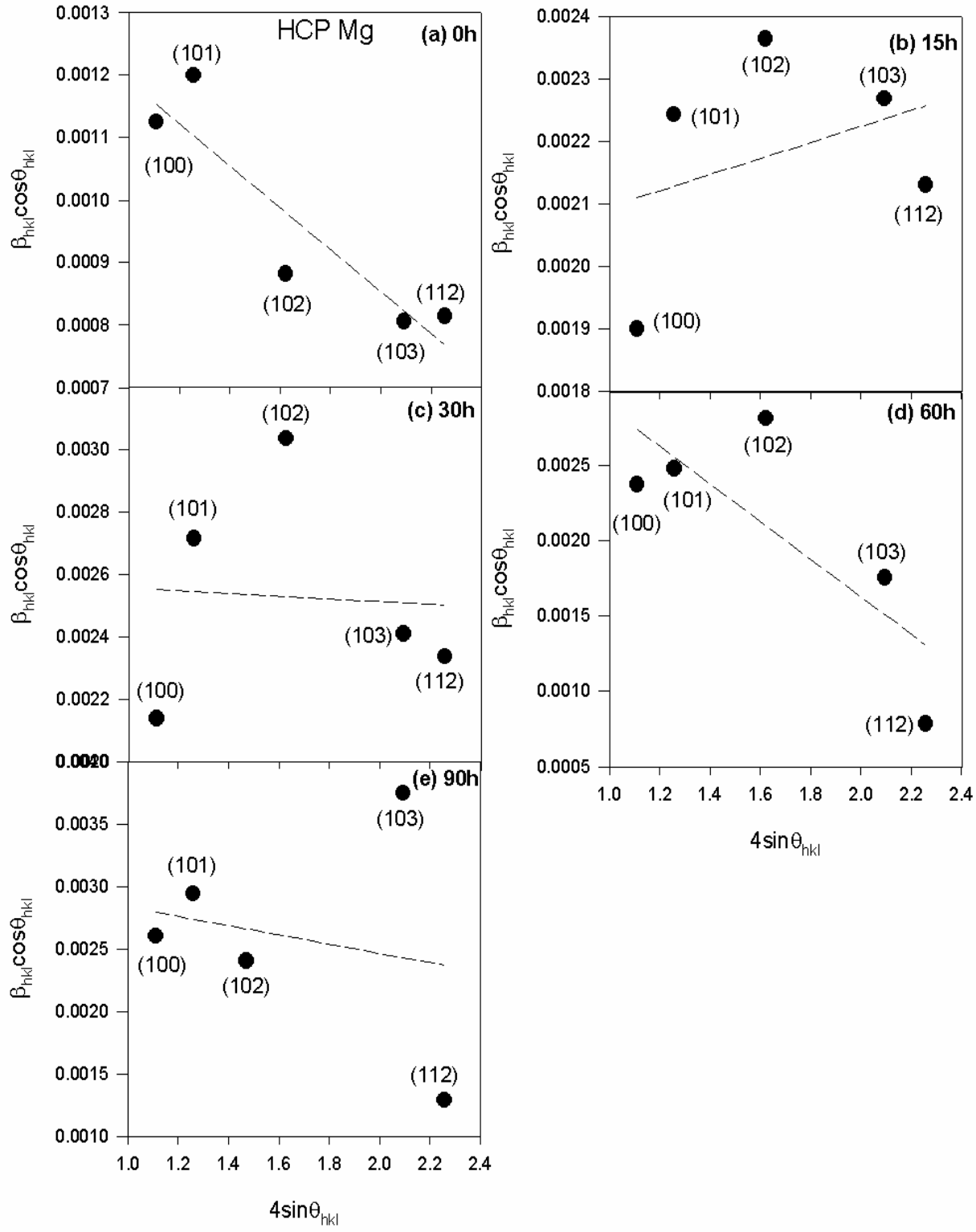

Figure 4.2.2.3.2 Williamson-Hall plots of Mg powder milled for (a) 0 h, (b) 15 h, (c) 30 h, (d) 60 h and (e) 90 h, assuming uniform deformation. The dashed line represents a linear fit.

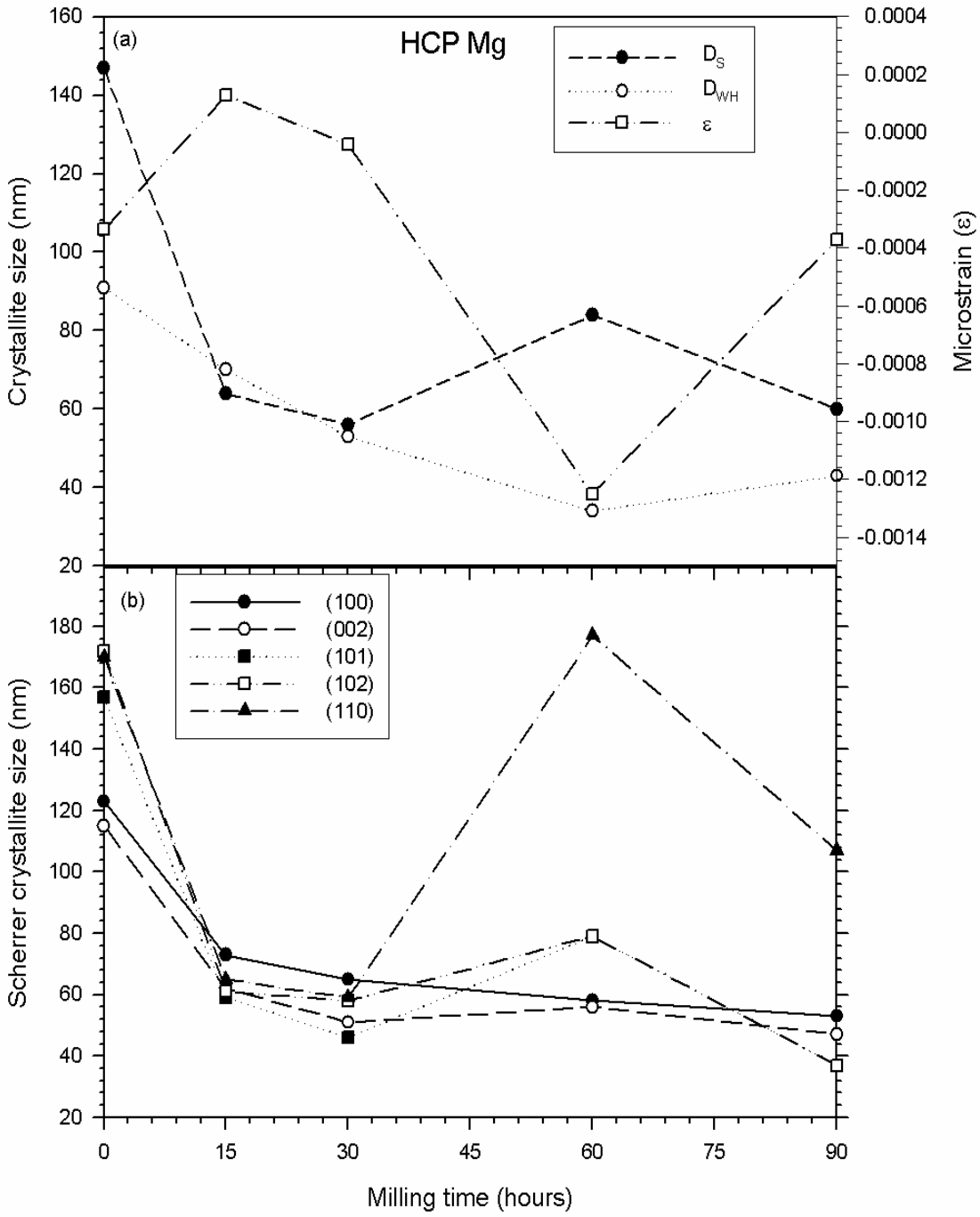

Figure 4.2.2.3.3 (a) Average Scherrer (D_S), W-H (D_{WH}) crystalline sizes and microstrain (ε), (b) Scherrer crystallite size determined on individual (100), (002), (101), (102) and (110) planes of HCP Mg.

clean the severe Ti welds on the surfaces (walls) of the milling media. Again, despite the slower grain refinement (D_S=69 nm) compared to milling in the absence of PCA (D_S<60 nm), no significant structural changes were observed on Mg. At the end of each

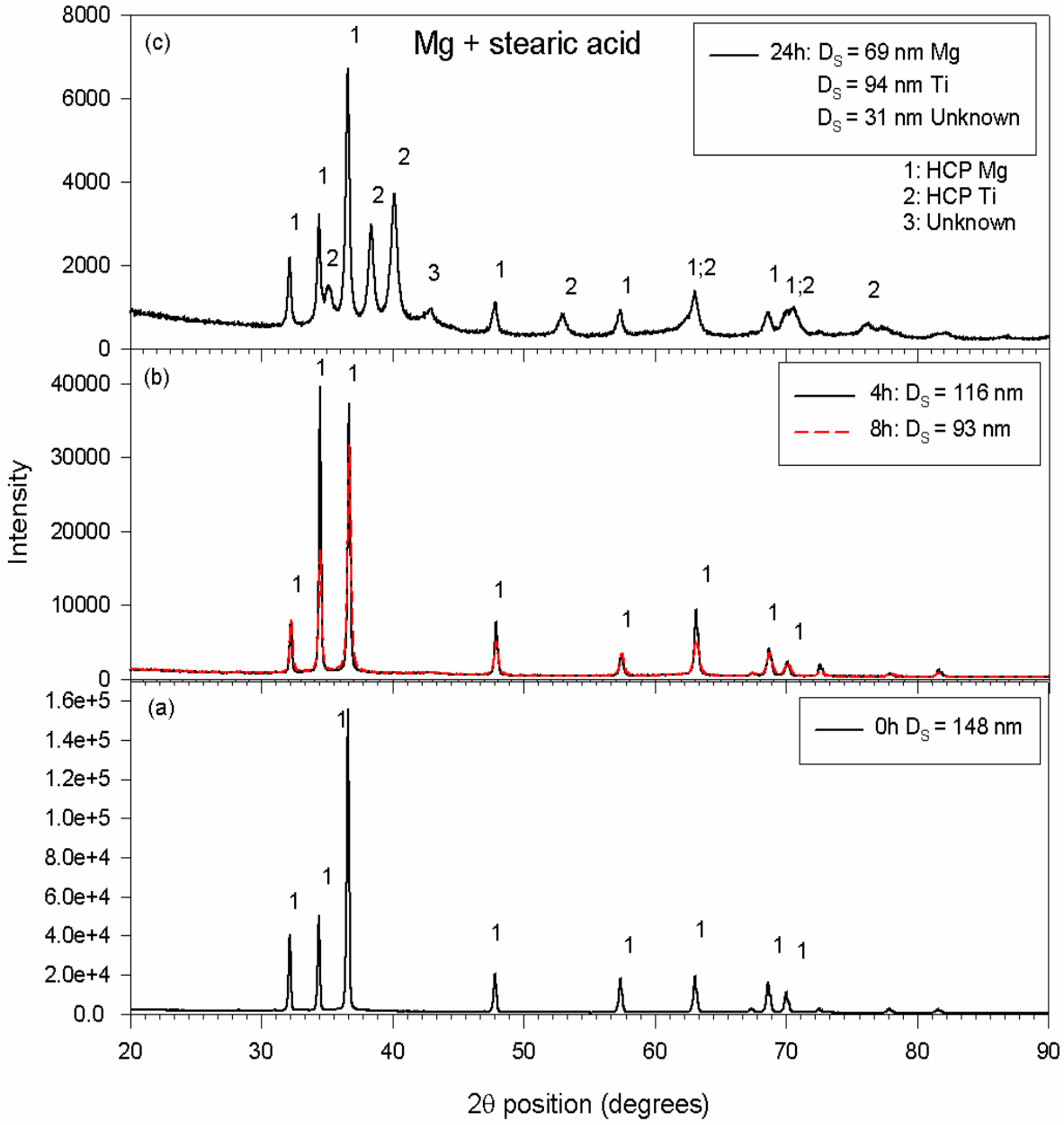

Figure 4.2.2.3.4. XRD patterns of Mg powder (a) unmilled, (b) 4 and 8h, as well as (c) 24h milled. The milling of powder was carried out in the presence of stearic acid (PCA).

milling, some level of cold-welding between Mg particles and the milling vial was observed.

The effects of milling on the particle morphology of Mg powder with or without stearic acid were investigated using SEM, as shown by images in figure 4.2.2.3.5. For unmilled

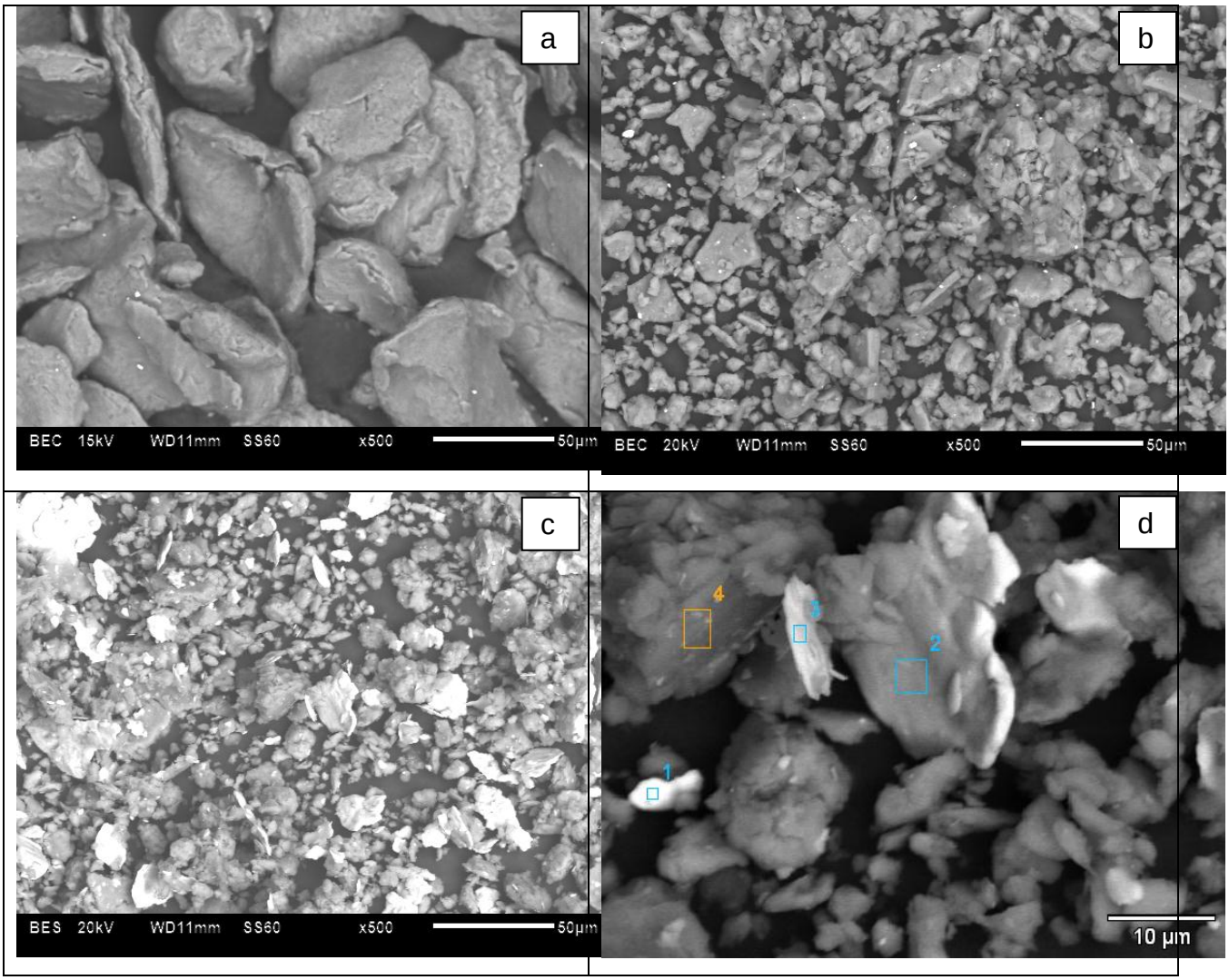

Figure 4.2.2.3.5 SEM images of Mg powder (a) unmilled, (b) 30h milled without PCA, (c) 24h milled with PCA at lower magnification and (d) 24h milled with PCA at higher magnification.

Mg powder, the average particles size is almost 50 µm with an irregular pancake-like shape, as shown in figure 4.2.2.3.5(a). Upon milling with or without PCA, a larger volume fraction of particles was fractured to below 20 µm while other fine particles seem to have cold welded amongst themselves to form coarse particles with average size of 50 µm or less, as shown in figure 4.2.2.3.5(b) and (c) . However, the level of cold welding is less in powder milled in the presence of PCA as evidenced by the average size of less than 30 µm for coarse particles. The EDS spot analyses were carried out on the Mg powder milled in the presence of PCA for 24h, as shown in figure 4.2.2.3.5(d).

The results indicate that, in addition to high levels of C and O due to PCA, the bright spots (1 and 3) are highly contaminated with Ti while grey spots (2 and 4) are mainly comprised of Mg.

4.2.2.2. Conclusion

Mg powder with crystallite size varying between approximately 60 and 40 nm was produced by ball milling in the absence of PCA. However, no solid-state transformation occured even if the powder was milled for 90h. Milling in the presence of PCA for 24h could only yield grains with average D_S = 69 nm, implying a delay in grain refinement compared to milling without PCA. However, when milling was conducted without PCA there was no cold-welding of Mg particles on the walls of milling media but some level of cold-welding was observed in powder milled with PCA. Therefore, current results can be used to suggest a mechanism during ball milling of Ti-Mg mixtures as follows:

During MM, Mg particles get enclosed or covered by harder TiH_{2-x} particles, in a “chewing gum-sand” or “core-shell” manner that is demonstrated clearly by figure 3.2.1.2.2.1(a) spot 1 in the previous chapter and supported by figure 7 in the recent study by Molladavoudi *et al* (2012). These results show that a cross-section of milled powders is vital to confirm mechanical alloying; otherwise the drawn conclusions could be misleading. As a result and in accordance with Hume-Rothery rules, there is no confirmation for solid solution between Ti and Mg induced by MM but only formation of homogeneous nanocrystalline Mg-TiH_{2-x} composite. This is further evidenced by the fact that the crystal structures of either Mg or Ti remained HCP when milling of each metal powder was carried out in the absence of PCA. Moreover, even in the presence of PCA, there is no crystal structural coherency between FCC Ti or TiH_{2-x} and HCP Mg [Badmos and Bhadeshia 1997] which promotes solid solubility.

Chapter 5

Methodology II: *Ab initio* modelling

Computer simulation techniques offer an alternative way of investigating properties of materials (using computers), whereby the simulator builds a model of a real system and explores its behaviour. The mathematical model is physically based with the exploration being done on a computer. In many ways these simulation studies share the same mentality as experimental investigations. However, in a simulation there is absolute control and access to detail, and given enough computer muscle, exact answers for the model.

The fundamental atomistic principles underlying the structural and functional behaviour of materials are astonishingly simple: (a) For most purposes, atomic nuclei can be treated as classical particles with a given mass and positive charge, (b) electrons are particles of spin one half, thus obeying the Pauli exclusion principle, their kinetic behaviour is described by quantum mechanics, and (c) the only relevant interactions are of an electrodynamic nature, in particular, attractions and repulsions governed by Coulomb's law. Based on these fundamental principles it is conceptually possible to explain and predict the wonderful richness of most physical and all chemical properties of matter such as the structure and stability of crystalline phases, the mechanical properties of alloys, the magnetic properties of transition metals and so on. This development in first principle theory has opened up many exciting possibilities for the study of condensed matter since one is now in a position to predict properties of systems which were formerly inaccessible to theory and sometimes experiment.

Common to all atomistic approaches in materials science is the fundamental problem of determining the total energy of a system as a function of the positions of the atoms. Once this energy is known, then essentially all structural, mechanical, thermal and dynamic properties become predictable including crystal structures, defect energies, surface energies, binding energies of atoms, diffusion barriers, and energetics of chemical reactions. Mechanical properties are the main concerns for structural

materials. The classical way of obtaining materials with desired properties is so called 'trial and error', i.e., trying to find the 'formula' of compositions of the materials more or less randomly from combinations of hundreds of chemical species as shown in the periodic table. Being costly both in time and economics, this kind of 'materials design' is obviously not the optimal [Hu *et al* 2006]. With the exponential growth of computer power and the development of efficient algorithms, numerical techniques now can be employed to study many challenging scientific problems that seemed difficult decades ago [Duan 2006]. This brings closer to reality the old dream of materials scientists, of being able to identify the appropriate 'formula' for the desired properties more efficiently, i.e., select the chemical species intentionally according to the target mechanical properties. Among diverse materials modeling methods, *ab initio* techniques based on the electronic structure theory are the most promising. *Ab initio* (first principles) calculations have evolved into a powerful research tool that is widely used in condensed matter theory for the calculation of electronic, magnetic, and structural properties. The method has been remarkably successful in reproducing and /or explaining a wide variety of materials phenomena [Uesugi and Higashi 2005]. Today we can perform calculations of the relevant materials properties faster, more reliably and far cheaper than the actual synthesis and testing.

The state-of-the-art first principles techniques are based on two approaches, namely,

(i) **Hartree-Fock (HF) method** – wherein quantum mechanics equation of Schrödinger is solved to find the exact solution, in exploring the information about the properties of the system. This method could only provide information for simple systems.

(ii) **Density functional theory (DFT)** – instead of solving the complex Schrödinger equation, it is replaced with an equation that is easier to solve, which gives good representation of the exact solution thus provides an opportunity to investigate complex as well as unexplored alloys.

Calculations in this work are performed within the framework of the density functional theory (DFT) [Hohenberg 1964], which states that all ground state properties are functionals of the charge density ρ. Specifically, the total energy E_t is

$$E_t = T[\rho] + U[\rho] + E_{xc}[\rho], \qquad (5.1)$$

where $T[\rho]$ is kinetic energy, $U[\rho]$ the potential field, and $E_{xc}[\rho]$ the exchange-correlation energy. Self-consistent solution of Eq. (5.1) is equivalent to treating the many-body problem of interacting electrons and nuclei by solving a series of one-electron Kohn-Sham (KS) equations [Kohn and Sham 1965]. The final term in Eq. (5.1), the exchange-correlation energy, requires some approximation for this method to be computationally tractable. Unless defined otherwise, the generalised gradient approximation (GGA) functionals [Perdew *et al* 1996] will be used throughout this work, as they provide a better overall description of the electronic subsystem than the local density approximation (LDA) functionals [Perdew *et al* 1992].

The well established *ab initio* simulation software, CASTEP [Segall *et al* 2002], will be employed in the present first-principles calculations. It utilizes the plane-wave basis set to treat valence electrons and pseudopotentials to approximate the potential field of ion cores (including nuclei and tightly bond core electrons) as illustrated in figure 5.1, which is an efficient DFT tool especially suitable for calculations involving necessary geometric optimisation especially for metastable structures. The pseudopotential is an effective potential constructed to replace the atomic all-electron potential such that core states are eliminated and the valence electrons are described by nodeless pseudo-wavefunctions. In this approach only the chemically active valence electrons are dealt with explicitly, while the core electrons are 'frozen', being considered together with the nuclei as rigid non-polarizable ion cores. Using this method, the calculations require the atomic numbers and positions as the only input data to determining the total energy of a crystal structure. These first principles techniques provide a full description of phase stability via heats of formation, electronic structure (band structure, density of states, charge density), magnetism and elasticity of the system. For each phase of interest, the geometry optimization is first performed to find its ground state, as well as to obtain the lattice constants, cohesive energies, bulk moduli, heat of formation, and magnetic

moments. Secondly, the elastic constants are calculated on the basis of the optimized results. The ab initio determined heats of formation can be integrated into thermodynamic modelling packages such as CALPHAD, Thermo-Calc, resulting to significantly more robust thermodynamic predictions. The accuracy and validity of *ab initio* results depend on various selected and tested suitable parameters like **k**-points sampling, smearing width, kinetic cut-off energy, which in addition to convergence criterion, produce reliable and experimentally comparable outputs.

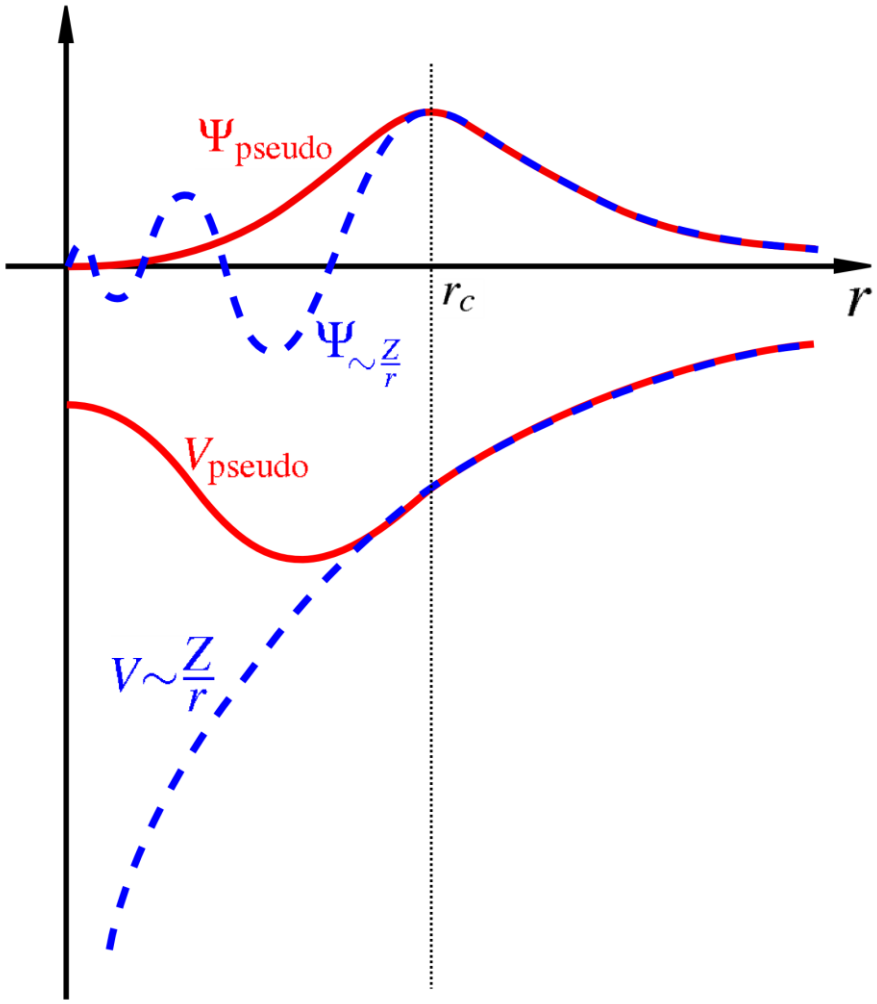

Figure 5.1 Comparison of a wavefunction in the Coulomb potential of the nucleus (blue) to the one in the pseudopotential (red). The real and the pseudowave function and potentials match above a certain cutoff radius r_c [Phillips and Kleinman 1959]

5.1 Density Functional Theory

Density Functional Theory (DFT) focuses on the electronic density of the system $\rho(\mathbf{r})$. In their seminal paper, Hohenberg and Kohn (1964) proved two key theorems.

Theorem 1: The total ground state energy E of an electron system is a unique functional of the electron density, i.e.

$$E = E[\rho] \tag{5.1.1}$$

Theorem 2: This energy functional takes its minimum value E_0 for the correct ground state density $\rho_0(\mathbf{r})$ under variations in the electron density $\rho(\mathbf{r})$ such that the number of electrons is kept fixed, i.e.

$$E_0 \le E[\rho] \tag{5.1.2}$$

for which

$$\int \rho(\mathbf{r}) d\mathbf{r} = N \tag{5.1.3}$$

where N is the number of electrons in the system. The equality in Eq. (5.1.2) occurs if and only if $\rho(\mathbf{r}) = \rho_0(\mathbf{r})$. These two theorems only state that such a functional $E(\rho)$ exists with the variational property given by Eq. (5.1.2). In the following year Kohn and Sham [Kohn and Sham 1965] provided a procedure by which we can approximate the functional and hence solve for the ground state energy and density. They decomposed the energy functional as the sum of three components:

$$E[\rho] = T_0[\rho] + U[\rho] + E_{xc}[\rho] \tag{5.1.4}$$

The first term is the kinetic energy of electrons in a system which has the same density $\rho(\mathbf{r})$ as the real system but in which the electrons are assumed to be non-interacting with the electron-electron interactions turned off. The second term comprises the sum of the usual Hartree Coulomb energy and the electrostatic interaction energy between the electrons and the external potential due to the nuclei i.e.

$$U[\rho] = \int [U_H(\mathbf{r}) + U_{ext}(\mathbf{r})] \rho(\mathbf{r}) d\mathbf{r} \tag{5.1.5}$$

$$U_H(\mathbf{r}) = \int \frac{\rho(\mathbf{r}')}{\mathbf{r}' - \mathbf{r}} d\mathbf{r}' \tag{5.1.6}$$

$$U_{ext}[\rho] = -\sum_{\alpha} \frac{Z_\alpha}{\mathrm{r} - \mathrm{R}_\alpha} \qquad (5.1.7)$$

The third term is the so-called exchange-correlation energy functional, that comprises the sum of the Hartree-Fock exchange energy plus the correlation energy that remains to make the functional Eq. (5.1.4) exact. Thomas-Fermi theory [Thomas 1927, Fermi 1928], had assumed that the non-interacting kinetic energy functional for an inhomogeneous system could be approximated by using the kinetic energy density of a homogeneous free electron gas corresponding to the density $\rho(\mathrm{r})$ at each point in space, namely

$$T_0^{TF}[\rho] = A_s \int \rho(\mathrm{r})^{\frac{5}{3}} d\mathrm{r} \qquad (5.1.8)$$

where $A_s = \frac{3}{10}\left(3\pi^2\right)^{\frac{2}{3}} = 2.871$ atomic units. This approximation failed to describe chemical bonding correctly. Kohn and Sham took the key step of defining the non-interacting kinetic energy functional in the spirit of the original Schrödinger equation:

$$H\Psi_k(\mathrm{r}_1, \mathrm{r}_2, ..., \mathrm{r}_N) = E_k \Psi_k(\mathrm{r}_1, \mathrm{r}_2, ..., \mathrm{r}_N) \qquad (5.1.9)$$

(where the r_1 denotes the coordinates of the 1st electron, r_2 the 2nd electron, and so on, that enter the time-independent Schrödinger equation (Eq. 5.1.9) for the system, where H is the Hamiltonian, i.e., the operator with corresponding eigenvalues E_k and eigenfunctions Ψ_k, whereas k is a point in space), namely

$$T_0[\rho] = \sum_i n_i \int \psi_i^*(\mathrm{r}) \left[-\frac{1}{2}\nabla^2 \right] \psi_i(\mathrm{r}) d\mathrm{r} \qquad (5.1.10)$$

where n_i is the occupation number of state i and $\psi_i(\mathrm{r})$ is an orthonormal set of single-particle wave functions such that

$$\rho(\mathrm{r}) = \sum_{i=1}^{N} |\psi_i(\mathrm{r})|^2 \qquad (5.1.11)$$

The ground state energy is found by minimizing the energy $E[\rho]$ in Eq. (5.1.4) with respect to variations in the electron density $\rho(\mathrm{r})$ ρ(r), given by Eq. (5.1.11), subject to the constraint that the number of particles is conserved through Eq. (5.1.3). Using

variational calculus it may be shown [Kohn and Sham 1965] that the ground state energy can be written

$$E[\rho] = \sum_{i=1}^{N} \varepsilon_i - \frac{1}{2}\iint \frac{\rho(\mathrm{r})\rho(\mathrm{r}')}{\mathrm{r}-\mathrm{r}'} d\mathrm{r}d\mathrm{r}' - \int U_{xc}(\mathrm{r})\rho(\mathrm{r})d\mathrm{r} + E_{xc}[\rho] \quad (5.1.12)$$

where

$$U_{xc}(\mathrm{r}) = \frac{\delta E_{xc}[\rho(\mathrm{r})]}{\delta\rho(\mathrm{r})} \quad (5.1.13)$$

The occupied energy levels ε_i that enter the sum in the first term of Eq. (5.1.12) are the eigenvalues resulting from solving a Schrödinger-like equation for non-interacting particles:

$$\left[-\frac{1}{2}\nabla^2 + U_{eff}(\mathrm{r})\right]\psi_i(\mathrm{r}) = \varepsilon_i\psi_i(\mathrm{r}) \quad (5.1.14)$$

where

$$U_{eff}(\mathrm{r}) = U_{ext}(\mathrm{r}) + U_H(\mathrm{r}) + U_{xc}(\mathrm{r}) \quad (5.1.15)$$

Thus, Kohn and Sham provided a recipe for solving the ground state energy of a many-body electron system within an effective one-electron framework provided the form of the exchange-correlation functional that enters both the Schrödinger equation (5.1.14) and the total energy equation (5.1.12) are known. Thus we now turn to in the next section.

5.2 The Exchange-Correlation Functional

Several different schemes have been developed for obtaining approximate forms for the functional for the exchange-correlation energy. The simplest and yet surprisingly accurate approximation, for non-magnetic systems is to assume that the exchange-correlation energy is dependent only on the local electron density ρ(r) around each volume element dr. This is called the local density approximation (LDA). The local density approximation rests on two basic assumptions: firstly, the exchange and correlation effects come predominantly from the immediate vicinity of the point r, and secondly these exchange and correlation effects do not depend strongly on the variations of the electron density in the vicinity of r. If these two conditions are

reasonably well fulfilled, then the contribution from the volume element $d\mathbf{r}$ would be the same as if this volume element were surrounded by a homogeneous electron density of the constant value $\rho(\mathbf{r})$ within $d\mathbf{r}$. Within LDA the exchange-correlation energy functional is given by:

$$E_{xc}^{LDA}[\rho] = \int \rho(\mathbf{r}) \varepsilon_{xc}[\rho(\mathbf{r})] d\mathbf{r} \qquad (5.2.1)$$

where $\varepsilon_{xc}(\rho(\mathbf{r}))$ is the exchange-correlation energy per particle of a uniform electron gas. This quantity is split into two parts:

$$\varepsilon_{xc}(\rho(\mathbf{r})) = \varepsilon_x(\rho(\mathbf{r})) + \varepsilon_c(\rho(\mathbf{r})) \qquad (5.2.2)$$

The exchange part $\varepsilon_x(\rho(\mathbf{r}))$ can be derived analytically within the Hartree-Fock approximation and can be expressed as

$$\varepsilon_x(\rho(\mathbf{r})) = \left(-\frac{3}{4}\right)\sqrt[3]{\frac{3\rho(\mathbf{r})}{\pi}} \qquad (5.2.3)$$

The correlation part cannot be derived analytically, but can be calculated numerically with high accuracy by means of Monte Carlo simulations [Bloch 1929].

5.2.1 Local density approximation (LDA)

The LDA is generally very successful in predicting structures and ground state properties of materials but some shortcomings are well documented [Hafner 2000]. These concerns in particular: (i) the energies of excited states, in particular the band gaps in semiconductors and insulators are systematically underestimated. This is not surprising since DFT is based on a theorem referring to the ground state only. (ii) Generally, LDA tends to significantly overestimate cohesive energies and underestimate lattice parameters by up to 3%. In solids, the former is thought to occur because the LDA does a poor calculation of the total energy in isolated atoms [Perdew *et al* 1992]. (iii) The incorrect ground state is predicted for some magnetic systems (the most notable example is Fe which is predicted to be hexagonal close packed and non-magnetic instead of body-centered cubic and ferromagnetic) and for strongly correlated systems (e.g. the Mott insulators NiO and La_2CuO_4 are predicted to be metallic in the LDA). (iv) Van der Waals interactions are not appropriately described in the LDA,

although there are some recent suggestions for overcoming this problem [Hult *et al* 1996, Kohn *et al* 1998]. In magnetic systems or in systems where open electronic shells are involved, the local spin density approximation (LSDA) which is the equivalent of the LDA in spin-polarized systems is employed. LSDA basically consists of replacing the exchange-correlation energy density with a spin-polarized expression [Kohanoff and Gidopoulos].

5.2.2 Generalized-gradient approximation (GGA)

During recent years several schemes that go under the generic name of the generalized-gradient approximation (GGA) attempt to provide improvements to LDA by expanding $E_{xc}[\rho]$. The expansion is not a simple Taylor expansion, but tries to find the correct asymptotic behaviour and correct scaling for the usually nonlinear expansion. These enhanced functionals are frequently called nonlocal or gradient corrections, since they depend not only upon density, but also the magnitude of the gradient of the density at a given point. For materials applications, the GGAs proposed by Perdew and co-workers [Perdew *et al* 1992, Perdew 1986, Becke 1988, Perdew and Wang 1992, Perdew *et al* 1996], have been widely used and have proved to be quite successful in correcting some of the deficiencies of the LDA: the overbinding being largely corrected (the GGAs lead to larger lattice constants and lower cohesive energies) [Kresse *et al* 1994] and the correct magnetic ground state is predicted for ferromagnetic Fe [Leung *et al* 1991] and antiferromagnetic Cr and Mn [Asada and Terakura 1993]. However, there are also cases where the GGA overcorrects the deficiencies of the LDA and leads to a large underbinding [Hafner 2000].

The basic idea of GGAs is to express the exchange-correlation energy in the following form:

$$E_{xc}^{GGA}[\rho] = \int \rho(\mathrm{r})\varepsilon_{xc}[\rho(\mathrm{r})]d\mathrm{r} + F_{xc}[\rho(\mathrm{r}), \nabla\rho(\mathrm{r})]d\mathrm{r} \qquad (5.2.2.1)$$

where the function F_{xc} is asked to satisfy a number of formal conditions for the exchange-correlation hole, such as sum rules, long-range decay and so on. Naturally,

not all the formal properties can be enforced at the same time, and this differentiates one functional from another [Kohanoff and Gidopoulos 2003].

The form suggested by Becke (1988) for the exchange part is:

$$E_x^{GGA}\left[\rho_\uparrow,\rho_\downarrow\right]=E_x^{LDA}-\beta\sum_\sigma\int\frac{\rho_\sigma(\mathbf{r})^{\frac{4}{3}}x_\sigma^2}{1+6\beta x_\sigma\sinh^{-1}x_\sigma}d^3\mathbf{r} \qquad (5.2.2.2)$$

where

$$E_x^{LDA}=-C_x\sum_\sigma\int\rho_\sigma^{\frac{4}{3}}(\mathbf{r})d^3\mathbf{r} \qquad (5.2.2.3)$$

$C_x=\frac{3}{2}\left(\frac{3}{4\pi}\right)^{\frac{1}{3}}, x_\sigma=\left|\nabla\rho_\sigma\right|/\rho_\sigma^{\frac{4}{3}}$ and σ denotes either $\uparrow$ or $\downarrow$ electron spin. The constant β is a parameter fitted to obtain the correct exchange energy of noble gas atoms. The GGA improves predicted values of binding and dissociation energies and brings them to within 10 kJ/mol (about 1.0 eV) of experiment [Perdew and Wang 1992].

The following correlation functional as proposed by Perdew and Wang (1992) predicts correlation energies of useful accuracy for an electron gas with slowly varying density:

$$E_c^{GGA}\left[\rho_\uparrow,\rho_\downarrow\right]=\int\rho(\mathbf{r})\varepsilon_c\left(\rho_\uparrow,\rho_\downarrow\right)d^3\mathbf{r}+\int\frac{C_c(\rho)\left|\nabla\rho(\mathbf{r})\right|^2}{de^\Phi\rho(\mathbf{r})^{\frac{4}{3}}}d^3r \qquad (5.2.2.4)$$

where

$$d=2^{\frac{1}{3}}\left[\left(\frac{1+\zeta}{2}\right)^{\frac{5}{3}}+\left(\frac{1-\zeta}{2}\right)^{\frac{5}{3}}\right]^{\frac{1}{2}}, \qquad (5.2.2.5)$$

$$\Phi=0.1929\left[\frac{C_C(\infty)}{C_C(\rho)}\right]\frac{\left|\nabla\rho\right|}{\rho^{7/6}}, \qquad (5.2.2.6)$$

$\zeta=\left(\rho_\uparrow-\rho_\downarrow\right)/\rho$ and $C_C(\rho)$ is a rational polynomial of the density that contains seven fitting parameters.

The correlation energy per particle of the uniform electron gas, $\varepsilon_C\left(\rho_\uparrow,\rho_\downarrow\right)$, is taken from a parameterization by Perdew and Zunger (1981) of the Ceperly-Alder [Ceperly and Alder 1980] Monte Carlo results.

Throughout this thesis we have used the most recent form of GGA due to Perdew-Burke-Ernzerhof (PBE) [Perdew *et al* 1996, 1997]. They write the exchange functional in a form which contains an explicit enhancement factor F_x over the local exchange, namely:

$$E_x^{PBE}\left[\rho_\uparrow,\rho_\downarrow\right]=\int\rho(\mathbf{r})\varepsilon_x^{LDA}\left[\rho(\mathbf{r})\right]F_{xc}(\rho,\xi,s)d\mathbf{r} \qquad (5.2.2.7)$$

where ρ is the local density, ξ is the relative spin polarization, and $s=\left|\nabla\rho(r)/2k_F\rho\right|$ is the dimensionless density gradient. Following [Perdew and Wang 1986] the enhancement factor is written

$$sF_x=\frac{1}{\kappa+s^2\mu}\left(\kappa+s^2\mu+s^2\kappa\mu\right) \qquad (5.2.2.8)$$

where $\mu=\beta\left(\pi^2/3\right)=0.21951$ with $\beta=0.066725$ being related to the second-order gradient expansion [Perdew and Wang 1992]. This form was chosen because it

(i) satisfies the uniform scaling condition,

(ii) recovers the correct uniform electron gas limit because $F_x(0)=1$,

(iii) obeys the spin-scaling relationship,

(iv) recovers the local spin density approximation (LSDA) linear response limit for $s\to 0$, namely $F_x(s)\to 1+\mu s^2$, and

(v) satisfies the local Lieb-Oxford bound [Lieb and Oxford 1981], $\varepsilon_x(\mathbf{r})\geq -1.679\rho(\mathbf{r})^{\frac{4}{3}}$, that is, $F_x(s)\leq 1.804$, for all $\mathbf{r}$, provided that $\kappa\leq 0.804$. PBE chooses the largest allowed value, $\kappa=0.804$.The correlation energy on the other hand is written in the form:

$$E_c^{PBE}\left[\rho_\uparrow,\rho_\downarrow\right]=\int\rho(\mathbf{r})\left[\varepsilon_c^{LDA}(\rho,\zeta)+H(\rho,\zeta,t)\right]d\mathbf{r} \qquad (5.2.2.9)$$

with

$$H\left[\rho,\zeta,t\right]=\gamma\phi^3 In\left\{1+\frac{\beta\gamma^2}{t}\left[\frac{1+At^2}{1+At^2+A^2t^4}\right]\right\} \qquad (5.2.2.10)$$

Here, $t=\left|\nabla\rho(\mathbf{r})\right|/(2\phi k_s\rho)$ is a dimensionless density gradient, $k_s=\left(4k_F/\pi\right)^{\frac{1}{2}}$ is the TF screening wave number and $\phi(\zeta)=\left[(1+\zeta)^{2/3}+(1-\zeta)^{2/3}\right]/2$ is a spin-scaling factor. The

quantity β is the same for the exchange term β=0.066725, and $\gamma = 0.031091$. The function A has the following form:

$$A = \frac{\beta}{\gamma}\left[e^{\varepsilon_c^{LDA}\frac{\rho}{\gamma\phi^3}} - 1 \right]^{-1} \qquad (5.2.2.11)$$

So defined, the correlation term H satisfies the following properties [Kohanoff and Gidopoulos 2003]:

(i) it tends to the correct second-order gradient expansion in the slowly varying (high-density) limit ($t \to 0$),

(ii) it approaches minus the uniform electron gas correlation $-\varepsilon_c^{LDA}$ for rapidly varying densities ($t \to \infty$), thus making the correlation energy vanish (this results from the correlation hole sum rule), and

(iii) it cancels the logarithmic singularity of ε_c^{LDA} in the high-density limit, thus forcing the correlation energy to scale to a constant under uniform scaling of the density.

5.3 Plane-wave Pseudopotential Method

In this section we outline the methodology of solving the Kohn-Sham equation,Eq. (5.1.14), using a plane wave basis and approximating the ion cores with pseudopotentials. We will end with a brief discussion of the commercial software package CASTEP that will be used in subsequent chapters.

5.3.1 Plane-wave Basis Sets

The plane-wave pseudopotential (PWP) method begins by representing the system by a 3-dimensional periodic supercell. This allows Bloch's theorem to simplify the task of solving the Kohn-Sham equation. This is because Bloch's theorem which is based upon the periodicity of the system, reduces the infinite number of one-electron wavefunctions in the real system to only the number of electrons in the chosen supercell. Following Bloch's theorem, the wavefunction can be written as the product of a cell periodic part and a wavelike part:

$$\psi_i(\bar{r}) = \exp(i\bar{k}\cdot\bar{r})\, f_i(\bar{r}) \qquad (5.3.1.1)$$

The first term is the wavelike part and the second term is the cell periodic part of the wavefunction, which can be expressed by expanding it into a finite number of planewaves whose wave vectors are the reciprocal lattice vectors of the crystal,

$$f_i(\bar{r}) = \sum_{\bar{G}} c_i, \bar{G} \exp(i\bar{G}\cdot\bar{r}) \qquad (5.3.1.2)$$

where $\bar{G}$ are the reciprocal lattice vectors. Therefore each electronic wavefunction is written as a sum of plane waves,

$$\psi_i(\bar{r}) = \sum_{\bar{G}} c_{i,\bar{k}+\bar{G}} \exp[i(\bar{k}+\bar{G})\cdot\bar{r}] \qquad (5.3.1.3)$$

The problem of solving the Kohn-Sham equation has now been mapped onto the problem of expressing the wavefunction in terms of an infinite number of reciprocal space vectors for each point $\bar{k}$ within the first Brillouin zone of the periodic cell. For metallic systems a dense set of $\bar{k}$ points is required to define the Fermi surface precisely and to reduce the magnitude of the error in the total energy which may arise due to inadequacy of the $\bar{k}$-point sampling. In principle, a converged electronic potential and total energy can always be obtained provided that the computational time and memory are available to calculate the electronic wave functions at a sufficiently dense set of $\bar{k}$ points [Payne *et al* 1992].

The Fourier series in Eq. (5.3.1.3) is, in principle, infinite. However, the coefficients $c_{i,\bar{k}+\bar{G}}$ are associated with plane waves of kinetic energy $(\hbar^2/2m)\left|\bar{k}+\bar{G}\right|^2$.

The plane waves with a smaller kinetic energy typically play a more important role than those with a very high kinetic energy. The introduction of a plane wave energy cutoff reduces the basis set to a finite size. This kinetic energy cutoff will lead to an error in the total energy of the system but in principle it is possible to make this error arbitrarily small by increasing the size of the basis set by allowing a larger energy cutoff. In principle, the cutoff energy should be increased until the calculated total energy converges within the required tolerance [Payne *et al* 1992].

The main advantage of expanding the electronic wavefunctions in terms of a basis set of plane waves is that the Kohn-Sham equation takes a particularly simple form. Substitution of Equation 5.3.1.3 into the Kohn-Sham equation, (5.1.14), gives

$$\sum_{\bar{G}}\{\frac{\hbar^2}{2m}\left|\bar{k}+\bar{G}\right|^2\delta_{\bar{G}\bar{G}'}+U_{ext}(\bar{G}-\bar{G}')+U_H(\bar{G}-\bar{G}')+U_{xc}(\bar{G}-\bar{G}')\}c_{i,\bar{k}+\bar{G}'}=\varepsilon_i c_{i,\bar{k}+\bar{G}'} \quad (5.3.1.4)$$

We see immediately that the reciprocal space representation of the kinetic energy is diagonal with the various potential contributions being described in terms of their Fourier components. The usual method of solving the plane wave expansion of the Kohn-Sham equation is by diagonalisation of the Hamiltonian matrix whose elements $H_{\bar{k}+\bar{G},\bar{k}+\bar{G}'}$, are given by the terms in curly brackets above. The size of the matrix is determined by the choice of cutoff energy

$$E_c=\frac{\hbar^2}{2m}\left|\bar{k}+\bar{G}_c\right|^2 \quad (5.3.1.5)$$

and will be intractably large for systems that contain both valence and core electrons. This classical problem was solved by advent of the powerful concept of pseudopotentials.

5.3.2 Pseudopotential Approximation

The fundamental idea of pseudopotentials is to replace the real potential, arising from the nuclear charge and the core electrons, with an effective potential, within a core region of radius R_c, as illustrated schematically in Figure 5.1. Certain demands are then placed on this effective potential. It must be such that the valence orbital eigenvalues are the same as those in an all-electron calculation on the atom. It must also preserve the continuity of the wavefunctions and their first derivatives across the core boundary. Finally, integrating the charge in the core region should give the same answer for the pseudo-atom and the all-electron one, that is, the pseudopotential must be *norm-conserving*. A pseudopotential that satisfies these demands will have the same scattering properties, at energies corresponding to valence eigenvalues, as the ionic core it replaces. The self-consistent field equations (Eqs. 5.1.11 and 5.1.14) are carried out only for the valence electrons. Moreover, since the core electrons which do not

influence the properties of the solid phase are removed from the problem, much higher numerical precisions can be achieved. Thus, systems involving heavy atoms are not much more complicated than those with light ones. The phase shift produced by the ionic core is different for each angular momentum component (s, p, d, etc.) of the valence wavefunction. Thus, the scatteringfrom the pseudopotential must be angular momentum dependent. The most general form for a pseudopotential is:

$$V_{NL} = \sum |l_m\rangle V_l \langle l_m|$$ (5.3.2.1)

where $|l_m\rangle$| are spherical harmonics and V_l is the pseudopotential for angular momentum l [Harrison 1980]. A pseudopotential that uses the same potential in each angular momentum channel is called a local pseudopotential. Local pseudopotentials are computationally much more efficient than nonlocal ones. However, only a few elements such as aluminium can be described accurately using local pseudopotentials.

An important recent concept in pseudopotential applications is the degree of *hardness* of a pseudopotential. A pseudopotential is considered *soft* when it requires a small number of Fourier components for its accurate representation and *hard* otherwise. Norm conservation ensures the scattering properties remain correct away from the eigenvalues to linear order in the energy [Gillan 1991] and also ensures that the pseudowavefunction matches the all-electron wavefunction beyond a cutoff radius that defines the core region. Within the core region, the pseudo wavefunction has no nodes and is related to the all-electron wavefunction by the *norm-conservation*: that is, both wavefunctions carry the same charge. These potentials can be made very accurate at the price of having to use a very high energy cutoff. Various schemes have been suggested to improve convergence properties of norm-conserving pseudopotentials [Troullier and Martins 1991]. Despite the best attempts to optimize their performance for the first row elements [Lin *et al* 1993, Rappe *et al* 1991], a more radical approach was required, as suggested by Vanderbilt (1990). This involves relaxing the norm-conserving requirement in order to generate much *softer* pseudopotentials, *ultrasoft pseudopotentials* (USP). In the ultrasoft pseudopotential scheme, the pseudo-wave-functions are allowed to be as *soft* as possible within the core region, so that the cutoff energy can be reduced dramatically. USP have another advantage besides being much *softer* than their norm-conserving counterparts. The generation algorithm guarantees

good scattering properties over a pre-specified energy range, which results in much better transferability and accuracy of the pseudopotentials. This leads to high accuracy and transferability of the potentials, although at a price of computational efficiency. Typically it is found that E_c is about half that for a norm-conserving pseudopotential, which means less than one third as many plane waves are required. As will be shown in chapter 6 and 9, the Ti-Mg ordered and disordered alloys, respectively will be computed using Vanderbilt ultrasoft pseudopotentials whereas Mg-Li disordered alloys will be treated with norm-conserving pseudopotentials in chapter 8.

5.3.3 Grid and Fast-Fourier transforms

Real- and reciprocal-space grids are another key feature of the PWP method. Expressing the wavefunction as an expansion in a finite set of plane waves leads naturally to the idea of a reciprocal-space grid. However, it is advantageous to have a real-space representation too, on the related real-space grid [Segall *et al* 2002]. Fast Fourier transforms (FFT's) are used to transform the data between the two spaces in a highly efficient manner. The direct lattice vectors of the real-space supercell are denoted $\bar{a}_1$, $\bar{a}_2$ and $\bar{a}_3$. The reciprocal lattice vectors $\bar{b}_i$ are defined by the relation $\bar{a}_i \cdot \bar{b}_j = 2\pi\delta_{ij}$,

where $\delta_{ij} = 1$ for $i = j$ but zero otherwise. In practice $\bar{b}_i$ is constructed using

$$\bar{b}_1 = \bar{a}_2 \times \bar{a}_3 / (\bar{a}_1 \cdot \bar{a}_2 \times \bar{a}_3), \qquad (5.3.3.1)$$

$$\bar{b}_2 = \bar{a}_3 \times \bar{a}_1 / (\bar{a}_1 \cdot \bar{a}_2 \times \bar{a}_3), \qquad (5.3.3.2)$$

$$\bar{b}_3 = \bar{a}_1 \times \bar{a}_2 / (\bar{a}_1 \cdot \bar{a}_2 \times \bar{a}_3). \qquad (5.3.3.3)$$

A reciprocal lattice vector $\bar{G}$ is given by

$$\bar{G} = n_1\bar{b}_1 + n_2\bar{b}_2 + n_3\bar{b}_3 \qquad (5.3.3.4)$$

where n_i are integers . A plane wave $\exp(i\bar{G} \cdot \bar{r})$ is commensurate with the supercell, and the set plane waves whose wavevectors are defined by equation 5.3.3.4 above is an orthogonal set [Segall *et al* 2002]. The real-space grid is formed by dividing the

lattice vectors $\bar{a}_1$, $\bar{a}_2$ and $\bar{a}_3$ into N_1, N_2 and N_3 points. A point in the supercell is then denoted

$$(l_1, l_2, l_3)\bar{r} = \frac{l_1}{N_1}\bar{a}_1 + \frac{l_2}{N_2}\bar{a}_2 + \frac{l_3}{N_3}\bar{a}_3, \qquad (5.3.3.5)$$

where the l_i are integers in the range $0 \le l_i \le (N_i - 1)$. The real-space grid can be viewed as the lattice of points for the lattice vectors $\alpha_i = \bar{a}_i / N_i$. The corresponding reciprocal lattice vectors are given by $\beta_i = N_i / \bar{b}_i$ because of the relation $\alpha_i \cdot \beta_j = 2\pi\delta_{ij}$. The vectors β_i are the reciprocal-space supercell vectors. The reciprocal-space grid is the lattice of points for the vectors $\bar{b}_i$. Within the reciprocal-space supercell a point is given by equation 5.3.3.4 with $0 \le n_i \le (N_i - 1)$. In each supercell there are $N_1 N_2 N_3 = N$ points. It can be said that discrete Fourier transforms, or at least plane waves, impose these relationships between the grids. The products $\bar{G} \cdot \bar{r}$ are independent of the supercell dimensions. Although pseudopotentials have reduced the number of plane waves required, that number is still large. FFT's play a role of equal importance because they allow the calculation to scale well with system size.

5.3.4 Advantages of PWP method

The PWP approach has several advantages over other methods, such as those based on localized atomic orbitals. These are:

(i) convergence with respect to the completeness of the basis set is easily checked by extending the cut-off energy (i.e. the highest kinetic energy in the PW basis),

(ii) Fast-Fourier-Transforms (FFT) facilitate the solution of the Poisson equation, and

(iii) forces on atoms and stresses on the unit cell may be calculated directly via the Hellmann-Feynman [Hellmann 1937, Feynman 1939] theorem, without applying Pulay corrections for the site-dependence of the basis set [Pulay 1969].

The main disadvantage is that the chemical insight gained by a description of bonding between localized orbitals is not immediately apparent. However, new codes remove

this deficiency by transforming from the PW description to a localized orbital description once the PWP calculations have converged to the relaxed ground state structure.

5.3.5 CASTEP code

The planewave pseudopotential (PWP) calculations for the solution of the Kohn-Sham equation of Density Functional Theory (DFT) were performed using CASTEP (Cambridge Serial Total Energy Package) [Milman *et al* 2000] with the generalized gradient approximation for the exchange correlation energy functional. CASTEP is a pseudopotential total-energy code which employs special point integration over the Brillouin zone and a plane wave basis for the expansion of the wavefunctions. We used the PBE form of the GGA [Perdew *et al* 1996], which was designed to be more robust and accurate than the original GGA formulation. The total-energy code used, CASTEP, performs a variational solution to the Kohn-Sham equations by using a density mixing scheme [Kresse *et al* 1994] to minimize the total energy and also conjugate gradients to relax the ions under the influence of the Hellmann-Feynman forces. CASTEP uses fast fourier transforms (FFT) to provide an efficient way of transforming various entities (wavefunctions, potentials) from real to reciprocal space and back as well as to reduce the computational cost and memory requirement for operating with the Hamiltonian on the electronic wave functions, a planewave basis for the expansion of the wavefunctions. The convergence of this expansion is controlled by a single parameter, namely the highest frequency at which the series is terminated (conventionally defined as the highest kinetic energy of a plane wave). In this work the summation over the Brillouin zone has been performed with weighted summation over wave vectors generated by Monkhorst-Pack scheme [Monkhorst and Pack 1976], which produces a uniform mesh of k points in reciprocal space. A BFGS-based minimization technique was used for performing geometry optimization, either at ambient conditions or under external stress [Milman *et al* 2000]. The Pulay density of mixing scheme [Payne *et al* 1992] with conjugate gradient solver is applied and pseudopotentials parametrized in the reciprocal space, as implemented in the CASTEP code. An updated iterative (due to the inverse Hessian) is based on the calculated stress tensor and atomic forces.

Ultrasoft pseudopotentials of Vanderbilt form (1990) will be utilized in Ti-Mg system. The above methodology produces very "soft" pseudopotentials which drastically reduce the number of plane waves needed to achieve convergence of the calculated properties. The pseudopotentials were generated using the PBE exchange correlation functional. We used convergence criterion of less than 2 x 10−5 eV on total energy change per atom, 10−3 Å on the displacement of atoms, 0.05 $eVÅ^{-1}$ on the residual forces and 0.1 GPa on the residual bulk stress.

5.3.6 Elasticity

Ab initio calculations enable researchers to determine simple as well as more complex elastic constants. The elastic constants C_{ij} of solids enclose a great deal of important information on their mechanical and dynamical properties. First, the process requires careful choice of the applied deformations (strains) and secondly, calculating the resulting stresses, the elastic constants can be determined. In the present calculations, for each strain pattern, six small strain amplitudes are considered, and the elastic constants can be obtained through the partial differentials of stress and strain. Once all the elastic constants are determined, the mechanical properties can thus be clarified. Nowadays, many experimental techniques are used for the measurement of elastic constants, such as Brillouin scattering, ultrasonic-wave propagation and neutron scattering. While it is very difficult to prepare suitable specimens for many materials the theoretical calculation of elastic constants is also necessary.

For each material, both stress and strain have three tensile and three shear components, giving six components in total. According to the theory of elasticity, 6 x 6 symmetry matrix with 36 elements is thus needed to describe the relationship between stress and strain. The structural symmetry of the crystal makes some of the matrix elements equal and others fixed at zero. For the cubic structures, only three elastic constants, corresponding to C_{11}, C_{12} and C_{44}, are independent. Appling two kinds of strains (ε_1 and ε_4) can give stresses relating to these three elastic coefficients, yielding an efficient method for obtaining elastic constants for the cubic system. This method has been successfully used to study the elastic properties of a range of materials

including metallic systems [Kamran *et al* 2008, 2009]. The mechanical stability criteria of cubic systems as outlined elsewhere [Mehl *et al* 1994, Nye 1985] are given as follows:

$$C_{44} > 0, C_{11} > |C_{12}| \quad \text{and} \quad C_{11} + 2C_{12} > 0 \qquad (5.3.6.1)$$

where C_{11}, C_{12} and C_{44} are the only three independent elastic constants. For the tetragonal and hexagonal structures, there are six elastic constants, corresponding to C_{11}, C_{12}, C_{13}, C_{33}, C_{44}, and C_{66} (for hexagonal crystal, $C_{66} = (C_{11} - C_{12})/2$), are independent. The corresponding mechanical stability criterion for tetragonal crystal reads as

$$C_{44} > 0, C_{66} > 0, , \; C_{11} > |C_{12}| \text{ and } C_{11} + C_{12} - \frac{2C_{13}^2}{C_{33}} > 0 . \qquad (5.3.6.2)$$

For hexagonal crystals, the criterion is

$$C_{11} > 0, C_{44} > 0, C_{66} = \frac{C_{11} - C_{12}}{2} > 0 \text{ and } C_{11} + C_{12} - \frac{2C_{13}^2}{C_{33}} > 0 . \qquad (5.3.6.3)$$

Based on three independent single crystal elastic constants of a cubic crystal, C_{11}, C_{12}, C_{44}, the elastic moduli of polycrystalline material were calculated following averaging schemes of Voigt (upper bound) and Reuss (lower bound) by Hill (1952) as follows:

$$E = \frac{9BG}{3B+G}, \qquad \nu = \frac{E}{2G-1}, \qquad G_V = \left\lfloor \frac{C_{11} - C_{12} + 3C_{44}}{5} \right\rfloor, \qquad G_R = \left\lfloor \frac{C_{44}(C_{11} - C_{12})}{4C_{44} + 3(C_{11} - C_{12})} \right\rfloor,$$

$$G = G_H = \left\lfloor \frac{G_V + G_R}{2} \right\rfloor, \qquad B = \left(\frac{C_{11} + 2C_{12}}{3} \right), \qquad C' = \frac{C_{11} - C_{12}}{2}, \qquad A = \frac{(2C_{44} + C_{12})}{C_{11}}$$

(5.3.6.4)

where E is the Young's modulus, υ Poisson's ratio, G isotropic shear modulus, B bulk modulus, C' tetragonal shear modulus and anisotropic factor A. The Hill average, in general, is selected as the estimation of bulk modulus and shear modulus.

The calculated elastic constants for hexagonal and tetragonal phases allow us to obtain their macroscopic mechanical parameters, namely isotropic bulk (B) and shear moduli (G) in the Voigt (V) approximation as follows:

$$B_V = \frac{2}{9}(C_{11} + C_{12} + 2C_{13} + \frac{1}{2}C_{33}), \qquad (5.3.6.5)$$

$$G_V = \frac{1}{30}(C_{11} + C_{12} + 2C_{33} - 4C_{13} + 12C_{55} + 12C_{66}) . \qquad (5.3.6.6)$$

Similarly, Young's modulus can be calculated by

$$E_x = \frac{[C_{33}(C_{11}+C_{12})-2C_{13}^2](C_{11}-C_{12})}{C_{11}C_{33}-C_{13}^2}, \quad E_z = \frac{[C_{33}(C_{11}+C_{12})-2C_{13}^2]}{C_{11}-C_{12}}. \qquad (5.3.6.7)$$

As given in equation 5.3.6.7 above, E_x represents the Young's modulus along the [100] and [010] directions, whereas E_z on the other hand represents Young's modulus along the [001] direction.

Young's modulus *E* is defined as the ratio between stress and strain and is used to provide a measure of the stiffness of the solid, i.e. the larger the value of *E*, the stiffer the material. Poisson's ratio (υ) refers to the ratio of transverse contraction strain to longitudinal extension strain during stretching, thus reflecting the stability of the crystal against shear. Hence, higher the Poisson's ratio is, the better ductility the crystalline metal has at low temperatures. It is acknowledged that the bulk modulus B_0 is a measure of resistance to volume changed by applied pressure. The elastic anisotropy *A* has an important implication in engineering science since it is highly correlated with the possibility of inducing microcracks in materials [Goumri-Said and Kanoun 2007]. If the material is completely isotropic, the value of *A* will be 1, while values smaller or larger than 1 measure the degree of elastic anisotropy. Thus the macroscopically measurable quantities obtained for materials are the shear modulus *G*, which represents the isotropic response for shearing, Young's modulus *E* corresponding to the stress–strain ratio in the case of tensile forces, bulk modulus B_0, Poisson's ratio υ and the anisotropy constant *A,* which are all important for technological and engineering applications.

Chapter 6

Hypothetical equilibrium ordered Ti-Mg phases

In physical metallurgy, it is known that the more electropositive one element and the more electronegative the other, the greater is the likelihood that they will form an intermetallic compound instead of a substitutional solid solution [Hume-Rothery *et al* 1969]. Furthermore, in accordance with the above, Ti and Mg should be able to form an intermetallic compound since Mg is less electronegative while Ti is more electropositive.

In the present work, first-principles calculations were performed on 34 different intermetallic structures consisting of AB, A_2B, A_3B and A_7B type stoichiometries in the Ti-Mg system. Based on the experimental evidence that so far, crystalline phases obtained by far from equilibrium processes are usually simple structures such as body-centred cubic (BCC), hexagonal-close-packed (HCP) or face-centred-cubic (FCC) comprised of few atoms [Liu 2001]. Generally, a unit cell of an alloy phase containing more atoms frequently corresponds to a larger size than the one comprising fewer atoms, and therefore it probably requires a larger critical radius for nucleation and growth of the phase. It follows from above that the phases with complicated structures require, perhaps, highly sufficient kinetic conditions to nucleate and grow, e.g., need relatively high temperature to enhance the atomic mobility and long time enabling the atoms to arrange themselves into an ordered configuration.

It is also known that subjecting materials to high pressure affects the electronic structure and crystal packing, hence altering their chemical reactivity [Parker *et al* 1996, McMillan 2006, Demazeau 2008, Zeng *et al* 2009]. In some cases it is reported to even induce compound formation between elements that do not bond under ambient conditions [Atou *et al* 1996, Feng *et al* 2008, Kirillova *et al* 2005, Dubrovinskaia *et al* 2005]. Therefore, pressure has become a powerful tool for altering individual atoms and their electronic structure, changing the bonding chemistry, and creating novel materials. This has been demonstrated by the discovery of intermetallic compounds in the incompatible

K-Ni, K-Ag [Atou *et al* 1996], K-Cu [Snider and Badding 2004], Ca-Co [Kirillova *et al* 2005], Fe-Mg [Dubrovinskaia *et al* 2005] and Li-Be [Feng *et al* 2008] systems under high pressures and temperatures. Thus, in the current and next chapters the following are examined:

i. the structural and cohesive properties of a series of ordered hypothetical superstructures of binary Ti-Mg alloys at equilibrium,
ii. the effect of pressure on phase stability and electronic structure of pure metals (Ti, Mg),
iii. martensitic transformation in elemental metals (Ti, Mg),
iv. the effect of pressure on the elastic constants of selected most likely ordered alloys,
v. the effect of pressure on the electronic structure of few selected more likely compounds,

using *ab initio* electronic structure technique, in particular the plane-wave pseudopotentials (PWP) method embodied in the CASTEP total energy package codes.

6.1. *Ab initio* modelling procedure

6.1.1. Hypothetical ordered Ti-Mg intermetallic phases

Our *ab initio* calculations were performed using the well-established total energy code, CASTEP [Segall *et al* 2002]. The CASTEP code is a first principles quantum mechanical programme for performing electronic structure calculations within the Hohenberg-Kohn-Sham density functional theory (DFT) [Hohenberg and Kohn 1964, Kohn and Sham 1965]. It was used within the generalized gradient approximation (GGA) formalism [Perdew and Wang 1992] to describe the electronic exchange-correlation interactions. We used the recent Perdew-Burke-Ernzerhof (PBE) [Perdew *et al* 1996] form of GGA, which was designed to be more robust and accurate density functional formalism and employs the plane-wave basis set to treat valence electrons and pseudopotentials to approximate the potential field of ion cores (including nuclei

and tightly bond core electrons). In CASTEP, maximum plane wave cut-off energy of 500 eV was employed on the following crystal structures chosen in this study since they are comprised of few atoms: seven crystal structures having A_3B or AB_3 composition, i.e., A15, DO_{18}, DO_{19}, DO_{23}, DO_{22}, DO_3, and $L1_2$, five structures with A_2B or AB_2 stoichiometry, i.e., C14, C15, C32, ω, $C11_b$, six structures with AB composition, i.e., B18, B19, B2, B32, B_h and $L1_0$, and finally two FCC (D7) and BCC (B2) superstructures named FCC-SC and BCC-SC with A_7B and $A_{15}B$ stoichimetric compositions, respectively. The more robust Vanderbilt-type ultrasoft pseudopotentials (US) [Vanderbilt 1990] were employed to describe the electron-ion interaction. Geometry optimization was conducted using the Broyden-Fletcher-Goldfarb-Shanno (BFGS) method [Fischer and Almlof 1992]. The integration in the Brillouin zone (BZ) is done on the special k-points determined from the Monkhorst-Pack scheme [Monkhorst and Pack 1976]. The energy cut-off as well as the number of k-points was converged to within 1 meV per atom. With the application of ultrasoft pseudopotentials, the original valence electron configurations are $2p^6 3s^2$ and $3s^2 3p^6 3d^2 4s^2$ for Mg and Ti, respectively. We employed convergence criterion of less than 2×10^{-5} eV on total energy per atom, maximum displacement of 10^{-3} Å, residual forces of 5×10^{-2} eV $Å^{-1}$ and 0.1 GPa on the residual bulk stress. For each phase of interest, the geometry optimization was performed to find its ground state, as well as to obtain the equilibrium structural properties. The hydrostatic pressure of up to 250 GPa was then applied on the optimized structures with lower heat of formation. The elastic properties for each phase at several pressure values were computed from another set of calculations involving stress-strain relation.

6.2. Results and discussion

6.2.1 Equilibrium structural and cohesive properties of ordered hypothetical Ti-Mg phases

Starting from the above structures, crystal structures were first optimized with full relaxation of the cell shape and atomic position. The computed equilibrium parameters

such as lattice constants and heat of formations (ΔH) for the hypothetical crystalline structures of Ti-Mg system, as predicted by the present *ab initio* calculations, are listed in table 6.2.1.1.

6.2.1.1 Heats of formation

In order to evaluate the alloying abilities of the present compounds, we calculated the heat of formation (ΔH) of the alloy according to the relation [Zhang 2009, Sahu 1997, Phasha *et al* 2010a]

$$\Delta H^{Ti_{1-x}Mg_x} = \frac{1}{n} E_{total}^{Ti_{1-x}Mg_x} - \left[(1-x)E_{solid}^{Ti} + xE_{solid}^{Mg}\right] \qquad (6.2.1.1.1)$$

where $E_{total}^{Ti_{1-x}Mg_x}$ is the total energy of the alloy, E_{solid}^{Ti} and E_{solid}^{Mg} are the total energies of the stable structures of elemental Ti and Mg, *n* is the total number of atoms in the superstructure, *x* and *1-x* refer to the fractional concentrations of the constituent elements. If ΔH is negative, the formation of a compound from its elements is usually an exothermic process, while if it is positive, the compound is thermodynamically unstable thus bound to dissociate into elemental entities. Furthermore, the more negative ΔH is, the stronger the alloying ability. The heats of formation plotted in figure 6.2.1.1.1 were calculated relative to alpha (α) Mg and omega (ω) Ti structures, since these phases were predicted to be more stable. We note that the heat of formation curve shown in figure 6.2.1.1.1 makes a parabolic shape comprised of positive ΔH, with its maximum at the equi-atomic concentration, thus confirming the inability of Ti-Mg system to form any intermetallic compound [Massalski 1990, Vermeulen 2009].

For the Ti_3Mg composition, A15, DO_{18} and DO_3 structures have clearly higher formation energies than other four structures, with DO_{18} being the most unstable phase since it has the highest formation energy. There is a strong stability contest amongst DO_{19}, DO_{22} and DO_{23} phases as to which structure is lowest in energy. This competition is revealed by small differences in the formation energies. The $L1_2$ phase remains second to the above three structures in terms of relative stability trend.

Table 6.2.1.1 Predicted structural properties of hypothetical crystal structures for Ti-Mg system with respect to ground-state omega (ω) Ti and HCP Mg phases.

Phase	*Space group (No.)*	*a (Å)*	*c/a*	*V_0 (Å^3/atom)*	*△H (kJ/mol)*
$Ti_{15}Mg$					
BCC-SC	Pm-3m (221)	6.55	1.00	17.53	13.84
Ti_7Mg					
D7 (FCC-SC)	Fm-3m (225)	8.28	1.00	17.76	13.55
Ti_3Mg					
A15	Pm-3n (223)	5.26	1.00	18.17	22.76
DO_{18}	$P6_3/mmc$ (194)	4.60	1.82	19.22	45.38
DO_{19}	$P6_3/mmc$ (194)	5.92	0.80	18.06	15.13
DO_{22}	I4/mmm (139)	4.12	2.06	18.04	15.00
DO_{23}	I4/mmm (139)	4.15	4.04	18.01	15.07
DO_3	Fm-3m (225)	6.61	1.00	18.02	26.27
$L1_2$	Pm-3m (221)	4.16	1.00	18.00	16.03
Ti_2Mg					
C14	$P6_3/mmc$ (194)	5.44	1.67	19.34	28.30
C15	Fd-3m (227)	7.73	1.00	19.24	27.37
$B8_2$	$P6_3/mmc$ (194)	4.71	1.22	18.44	27.74
ω - C6	P-3m1 (164)	4.75	0.59	18.30	25.87
ω - C32	P6/mmm (191)	4.75	0.59	18.32	25.55
TiMg					
B18	$P6_3/mmc$ (194)	4.97	2.41	21.35	26.91
B19	Pmma (51)	4.88 2.87	1.13	19.27	21.47
B2	Pm-3m (221)	3.36	1.00	18.94	26.15
B32	Fd-3m (227)	6.11	1.00	14.26	37.24
$L1_0$	P4/mmm (123)	4.76	0.70	18.98	26.15
B_h	P-6m2 (187)	2.91	1.80	19.19	20.97
$TiMg_2$					
C14	$P6_3/mmc$ (194)	5.66	1.56	20.53	35.21
C15	Fd-3m (227)	7.89	1.00	20.51	36.69
$B8_2$	$P6_3/mmc$ (194)	4.87	1.20	20.01	27.36
ω - C6	P-3m1 (164)	4.89	0.60	20.24	23.65
ω - C32	P6/mmm (191)	4.88	0.60	20.27	23.54
$TiMg_3$					

A15	Pm-3n (223)	5.55	1.00	21.38	34.55
DO_{18}	$P6_3/mmc$ (194)	4.94	1.78	23.20	40.01
DO_{19}	$P6_3/mmc$ (194)	6.20	0.79	20.58	15.70
DO_{22}	I4/mmm (139)	4.90	1.41	20.64	20.84
DO_{23}	I4/mmm (139)	4.45	3.82	21.00	18.44
DO_3	Fm-3m (225)	6.91	1.00	20.63	20.82
$L1_2$	Pm-3m (221	4.35	1.00	20.63	15.67
$TiMg_7$					
D7 (FCC-SC)	Fm-3m (225)	8.88	1.00	21.86	10.27
$TiMg_{15}$					
BCC-SC	Pm-3m (221)	7.10	1.00	22.36	7.10

Focussing on A_2B compounds, the chances of forming a compound with Ti_2Mg stoichiometry are closely contested, with C32 omega phase having slightly higher possibility while C14 has the least. A similar behaviour occurs at $TiMg_2$ composition, in which the Laves phases C14 and C15 are less likely to form than the two omega phases (C6 and C32). Surprisingly, the $B8_2$ structure has nearly the same formation energy in both compositions (Ti_2Mg and $TiMg_2$), although the lattice parameters differ.

At 50-50 concentration, the B19 and B_h structures have the lowest formation energy amongst its competing counterparts. It turns out that the B32 structure has the highest positive heat of formation, followed by B2 and $L1_0$ phases which have equal chance of forming.

For the $TiMg_3$, DO_{19} and $L1_2$ structures have the lowest formation energy, followed by DO_{23} phase. In regard to the metastability of the possible structures, as in the Ti_3Mg case, the DO_{18} and in this case including A15 structure, still has the highest formation energy followed by the DO_{22} and DO_3 structures, which have almost the same formation energy.

Among the predicted energies of all the considered phases, the A_7B and $A_{15}B$ stoichiometric compositions are the most probable compounds to form as indicated by the lowest energy required to overcome the immiscibility barrier.

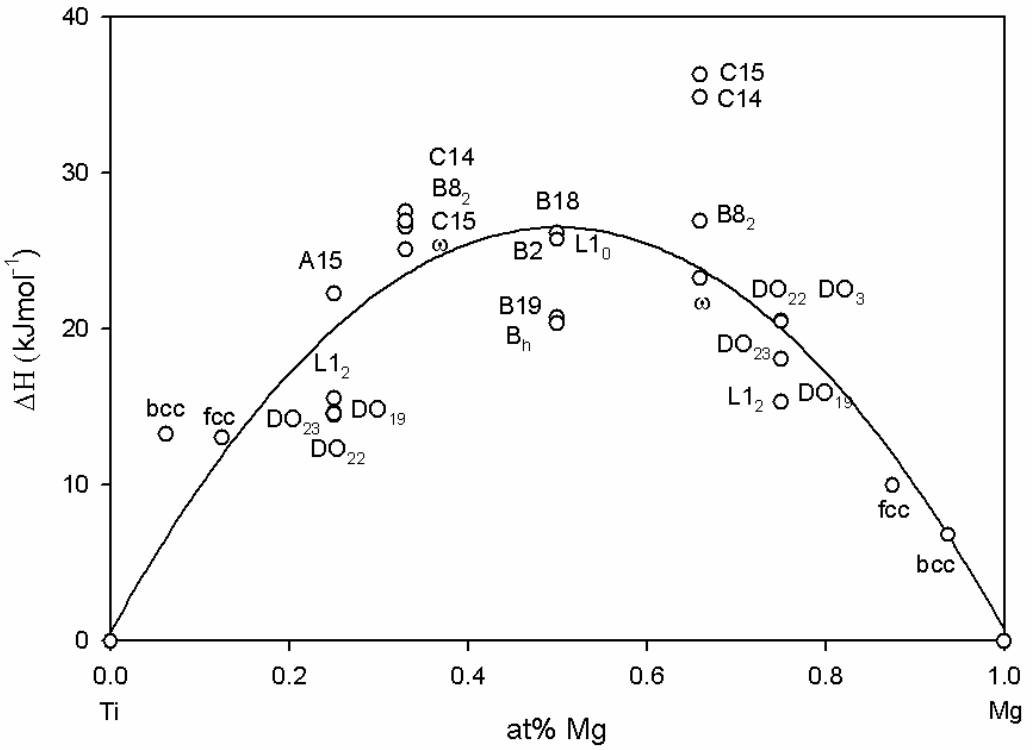

Figure 6.2.1.1.1. Predicted heats of formation for various phases in Ti-Mg system.

6.2.2 Effect of pressure on phase stability and electronic structure of elemental metals (Ti, Mg)

Since high pressure studies of intermetallic phases require Δ*H* to be calculated with respect to the most stable lattice of each metal at that applied pressure, we first carried out high pressure studies on pure metals, which indicate the phase that is most stable at a particular pressure depending on their atomic energies. Furthermore, from the free-energy against pressure curves, we can observe phase transition occurrence where energy curves cross one another. In addition, the effect of pressure on electronic structure of pure metals will also be investigated. Therefore, the effect of pressure on phase stability and elastic properties of promising hypothetical Ti-Mg intermetallic phases will be presented in the next chapter.

6.2.2.1 Effect of hydrostatic pressure on phase stability of elemental Ti and Mg crystals

The *ab initio* calculations were carried out on omega (ω-C6 and -C32), alpha (α), FCC, rhombohedral (RHL) and BCC phases for Ti while HCP, FCC and BCC structures were considered for pure Mg. For each phase, the geometry optimization was performed to find its ground state, as well as to obtain the equilibrium structural properties. Subsequently, the hydrostatic pressure of up to 200 and 300 GPa for Ti and Mg, respectively, was applied on the optimized structures to track any change in preferred phase stability. The results of geometry optimized Ti in five crystal structures are presented in table 6.2.2.1.1. Our predicted lattice parameters of optimized phases are very close to experimental results [Manna *et al* 2003; Phasha *et al* 2010c, Vullum *et al* 2009, Massalski 1990] as well as other theoretical results [Wang *et al* 2004, Ghosh and Asta 2005] using VASP (Vienna ab initio simulation package) [Kresse and Furthmuller 1996]. To check the accuracy of our results, we compared HCP, FCC and BCC phases to other calculated results [Wang *et al* 2004, Ghosh and Asta 2005] and found an excellent agreement. Our results predict the ω (omega) phase to be the ground-state structure of Ti at 0K and P=0 GPa, in support of other previously reported *ab initio* results [Jomard *et al* 1998, Ahuja *et al* 1993, Greeff *et al* 2001, Kutepov and Kutepova 2003]. The stability of the omega phase is also evident from the temperature-pressure phase diagram of Ti [Hennig *et al* 2005]. This enhanced stability is more pronounced between 100 and 200 GPa, where the highly dense ω phase is much more stable, as shown in figure 6.2.2.1.1(a). For the ω phase, current results show no sign of phase transition up to 200 GPa, except for the distinct anomalous behaviour in all Ti phases between 80 and 100 GPa. However, the stability of alpha (α) phase is surpassed by that of the FCC lattice at approximately 100 GPa, hence the occurrence of a possible α → FCC transition. At the same time the atomic energy of RHL (#166 R-3m) phase is being almost equal to that of FCC phase, although slightly more stable than the FCC above 100 GPa, suggesting a further FCC → RHL transition. Although it is known from crystallography that the primitive cell of an FCC lattice is RHL when the $\alpha_{RHL}= 60^{o}$, we experimentally obtained RHL phase with a lattice parameter of 3.0206 Å and $\alpha_{RHL}= 59.992^{o}$ after sintering at 1200^{o}C for an hour, a ball milled Ti powder which had transformed to an FCC or FCT phase with *a* = 4.240 Å (equivalent to RHL lattice with *a*=2.9981, *c*=7.3439 Å and *c/a*=2.4495) due to protonation process [Phasha *et al*

Table 6.2.2.1.1. Geometry optimized structural properties of Ti in various phases. For comparison, experimental and other theoretical results are shown in square brackets and parentheses, respectively. PUC denotes primitive unit cell while CUC denotes conventional unit cell.

Phase	**Lattice constant (Å)**	**Space group**	**c/a ratio**	**Total Energy (eV/atom)**	**ΔE_{wrtHCP} (meV/atom)**
ω-C6	a=4.5789, c=2.8338	P-3m1 (#164)	0.6188	-1603.1319	-6
ω-C32	a=4.5844, c=2.8288	P6/mmm (#191)	0.6171	-1603.1320	-6
	[a=4.625][a], [c=2.813][a]		0.6082[a]		
α	a=2.9409, c=4.6471	$P6_3/mmc$ (#194)	1.5802	-1603.1258	0
	[a=2.951][b], [c=4.685][b]		1.5876[b]		
	[a=2.9506][a], [c=4.6835][a]		1.5873[a]		
	(a=2.929)(c), (c=4.628)(c)		1.5801(c)		
	(a=2.9229)(d), (a=4.6271)(d)		1.5830(d)		
RHL (PUC)	a=2.9072, α=60.063º	R-3m (#166)		-1603.0658	60
(CUC)	a= 2.9099, c=7.1177		2.4460		
	[a=3.0206][b], [α=59.992º]				
	[a=3.0206][b], [c=7.3994]		2.4496[b]		
FCC	a=4.1127	Fm-3m (#225)	1.00	-1603.0657	60
	[4.350][e]				
	[4.240][b]				
	[4.272][b]				
	[4.10][f]				
	(4.099)(c)				
	(4.0963)(d)				
BCC	a=3.2563	Im-3m (#229)	1.00	-1603.0085	117
	[3.3065][a]				
	(3.241)(c)				
	(3.2398)(d)				

[a]Massalski 1990, [b]Phasha *et al* 2010c, [c]Wang *et al* 2004, [d]Ghosh and Asta 2005,[e]Manna *et al* 2003
[f]Vullum *et al* 2009

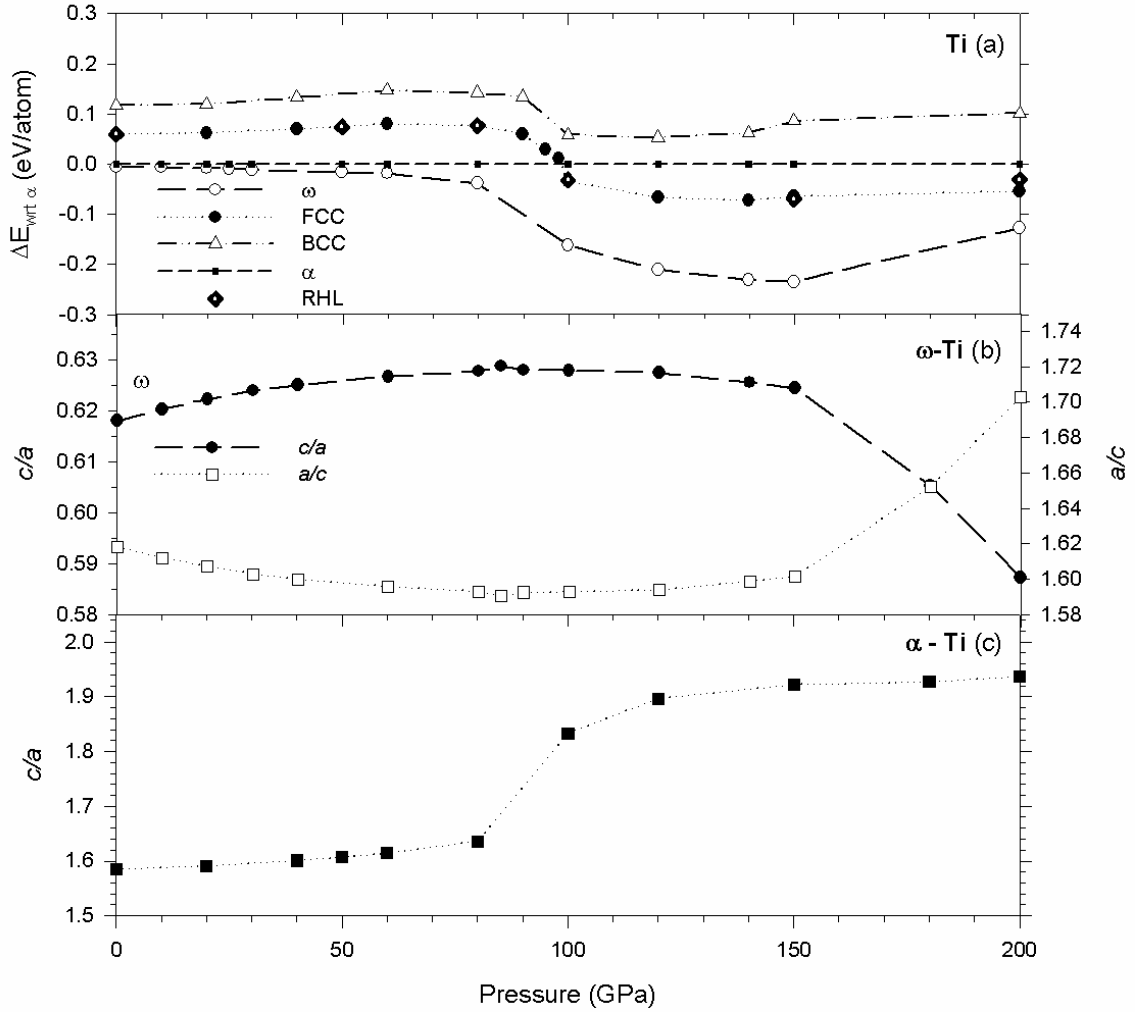

Figure 6.2.2.1.1. The upper panel (a) shows the atomic energy differences of ω, FCC, BCC, RHL(trigonal) Ti phases with respect to α phase represented by horizontal dashed line. The *c/a* axial ratio variation of ω and α alpha phases at various pressures are shown in the middle (b) and bottom (c) panels, respectively.

2010c]. The slight deviation of α_{RHL}angle to below 60^o is an indication of a transition away from the FCC structure. The experimentally observed RHL (#166 R-3m) phase upon sintering corresponds to RHL phase with *a*=3.0206, *c*=7.3994 Å and *c/a*=2.4496 as listed in table 6.2.2.1.1, which is very close to FCC phase with *a*=4.2723 Å (with trigonal primitive cell consisting of *a*=3.021 Å, *c*=7.400 Å, *c/a*=2.4495). Therefore the

lattice expansion during sintering could be attributed to further dissolution of impurities into a more stable Ti-based compound since the pristine FCC Ti phase with *a*=4.1127 Å consists of RHL primitive cell with *a*=2.9083, *c*=7.1239 Å and *c/a*=2.4498. This possible FCC → RHL transition is similar to that noted in transition-metal monoxides during their transition from paramagnetic FCC rocksalt (B1) to antiferromagnetic (AFM) rhombohedral structure below Néel temperature (T_N), by way of contracting B1 lattice in the [111] direction [Roth 1958]. Our value of √6=2.4495 corresponds to *c/a* ratio of RHL given by 1/tan22.208^o constructed from α phase at ideal *c/a*=1.633. Hence the current structural energy difference results predict preferred stability of RHL above 100 GPa. This atomic distortion leading to RHL phase seems to occur just above the metastable FCC phase when $\alpha_{RHL} < 60^o$. In the case of the FCC→RHL transition, the FCC lattice undergoes compression along the [111] direction, thus decreasing the angle of its primitive RHL to below 60^o.

Since no significant difference between the energy of C32 and C6 omega phases under applied hydrostatic pressure was noticed, only the results of C32 are presented. Despite the appearance of anomalies above 80 GPa in figure 6.2.2.1.1(a), neither α → ω nor ω → α transition is reflected by the total atomic energies up to 200 GPa. The trends of *c/a* and *a/c* axial ratios versus pressure for ω phase are shown in figure 6.2.2.1.1 (b). It is interesting to note that *c/a* increases with pressure and reaches a maximum of 0.6288 at 85 GPa and decreases gradually past the ideal *c/a*=√⅜=0.6124 for ω phase up to 200 GPa, while *a/c* ratio shows the opposite trend with minimum of 1.5903 equal to *c/a* of optimized α phase. In addition, such maximum and minimum correspond to the start of anomalies observed in figure 6.2.2.1.1(a). In figure 6.2.2.1.1(c), the plot of *c/a* ratio against pressure for an α phase is shown, which also indicates anomalous behaviour between 80 and 100 GPa. Such behaviour originates from unexpected sudden increase in the *c*-axis and sharp decrease in *a*-axis of the α phase, as shown clearly in figure 6.2.2.1.2(a) and (b). The *c/a* increases gradually until 1.633, thereafter increases sharply up to approximately 1.85, then increases gradually to 1.94 where it levels off. It is also worth noting that the *a/c* behaviour of the ω phase between 90 and 200 GPa in figure 6.2.2.1.1(b) is similar to that of the α phase between 0 and 90 GPa. Although not

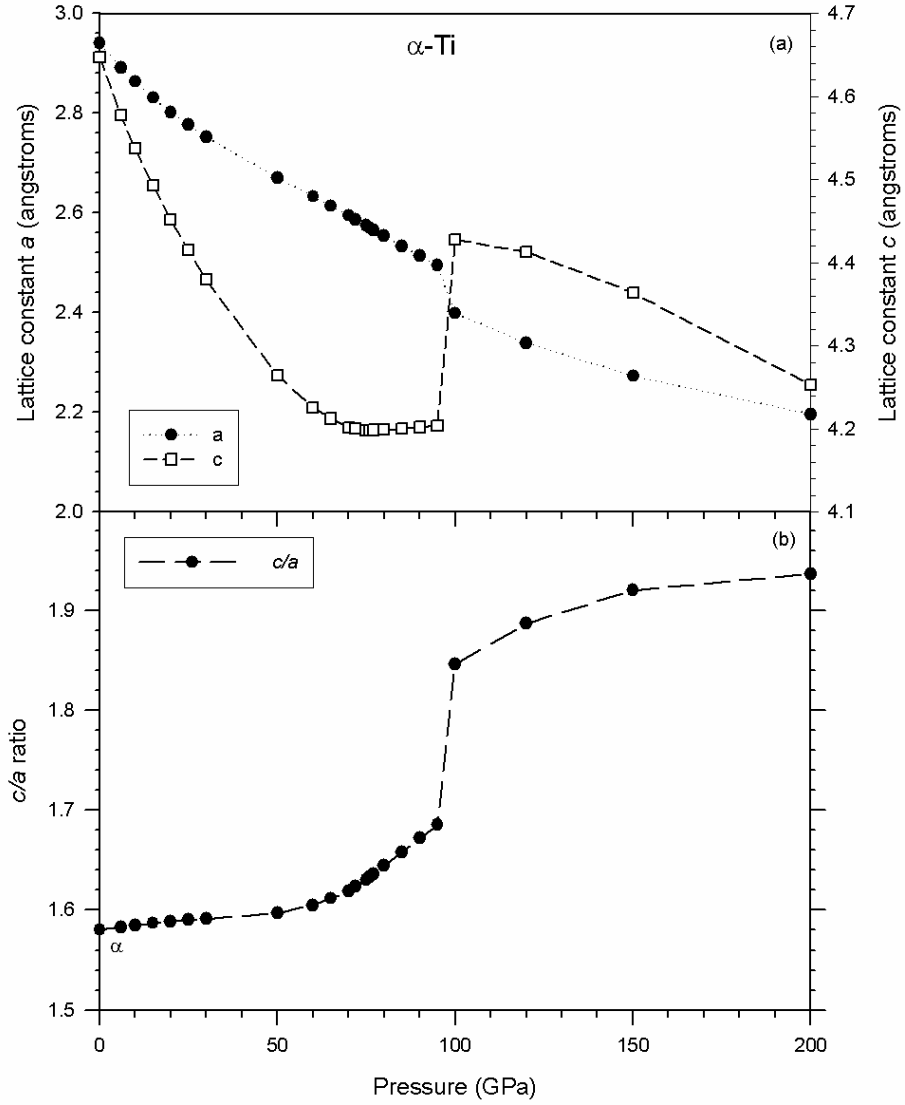

Figure 6.2.2.1.2. The upper panel (a) indicates the variation of lattice parameters *a* and *c* of α Ti with pressure, while the lower panel (b) shows the corresponding variation of *c/a* axial ratio with pressure.

validated, it is tempting to think of possible implications of this similarity as follows: by applying 90 GPa hydrostatically to the ω phase would result in the equilibrium α phase. Similar *c/a* trends in α and ω Ti were recently reported for pressures up to 90 GPa [Jona and Marcus 2005], although the authors associated this behaviour to the α → ω transition between 50 and 70 GPa while the ω → α transition is predicted above this pressure range. It is emphasized here that the amount of hydrostatic pressure leading to sharp increase in *c/a* ratio is not equivalent to mechanical pressure but the *c/a* ratio is

an indication of what is required to displace atoms in order to induce deformation slip in pure Ti.

In figure 6.2.2.1.3(a), the HCP lattice with lattice parameters a= 3.1995 and c=5.1780 Å is predicted to be the ground-state phase for magnesium, followed by FCC and BCC phases with lattice parameters 4.5219 and 3.5807 Å, respectively. The atomic energies difference of HCP, FCC and BCC Mg lattices and the *c/a* axial ratio of the HCP phase are plotted against pressure in figure 6.2.2.1.3(a) and (b), respectively, while the $(c/a)/(c/a)_0$ ratio against V/V_0 is shown in (c).

According to *c/a* ratio-pressure plot in figure 6.2.2.1.3(b), subjecting HCP Mg lattice to pressure of ~ 4-6 GPa leads to compression of the *a-axis* more than the *c-axis*, hence the maximum *c/a* ratio at 6 GPa, thus rendering *c-axis* incompressible in this pressure range. Upon further loading the *c-axis* softens, hence the decrease in the axial ratio. The observed anomalous behaviour of *c/a* in the pressure range of interest corresponds to V/V_0 values of between 0.90 and 0.88 as indicated in figure 6.2.2.1.3(c) by a $(c/a)/(c/a)_0$ maximum. A similar anomalous change in figure 6.2.2.1.3(c) was reported experimentally much earlier [Clendenen and Drickamer 1964, Perez-Albuerne *et al* 1966], especially above $V/V_0=0.90$ (7 GPa). The authors ascribed the peculiar shape of *c/a* curve between ~ 7 to 12 GPa to the unusual features of incompressible *c* axis in this pressure range. At 25 GPa, the *c/a* ratio is equal to that at equilibrium while it reaches a minimum at 50 GPa with $V/V_0=0.60$. Furthermore, the observed crossing of free-energy difference curves in figure 6.2.2.1.3(a) seems to coincide with *c/a* minimum around 50 GPa in figure 6.2.2.1.3(b). It is interesting to note that in literature HCP Mg is reported to transform to BCC at this pressure [Moriarty and McMahan 1982, McMahan and Moriarty 1983, Olijnyk and Holzapfel 1985, Wentzovitch and Cohen 1988]. It may consequently be summarised from our results that the Mg HCP→BCC transformation at 50 GPa occurs via the *c*-lattice compression.

Furthermore, if *c/a* axial ratio is considered to show phase transition, our results suggest further BCC→HCP transition above 80 GPa. Another striking feature is observed at 60 GPa corresponding to $V/V_0 = 0.57$, where we note the exchange in phase stability

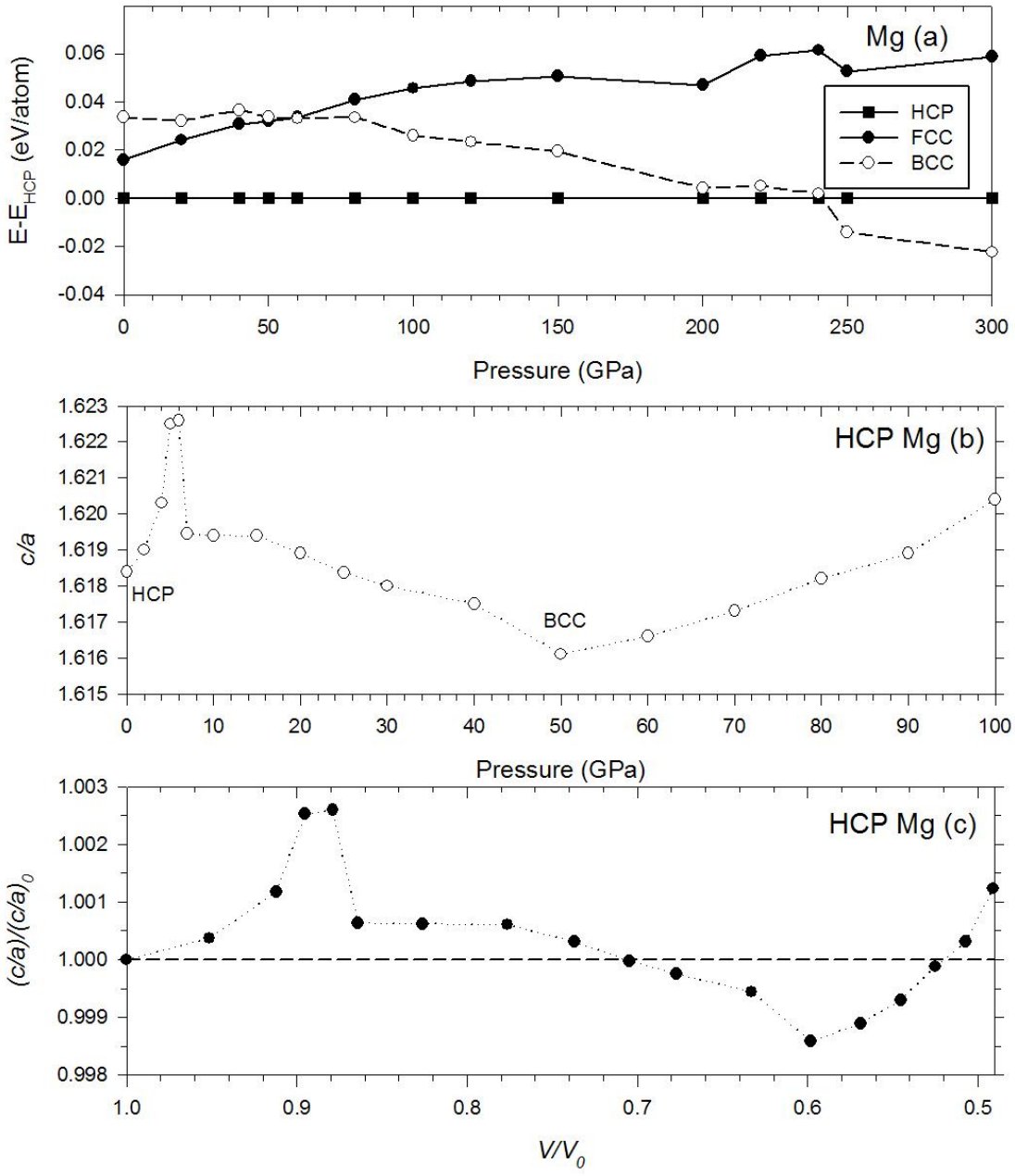

Figure 6.2.2.1.3. The upper panel (a) presents the energy difference of FCC, BCC Mg lattices, plotted against pressure ranging from 0 to 300 GPa with respect to HCP phase represented by horizontal dashed line. The *c/a* axial ratio variation of HCP Mg phase at various pressures is shown in the middle panel (b) while the $(c/a)/(c/a)_0$ ratio against V/V_0 in the bottom panels (c).

between FCC and BCC phases, as shown by the crossing of their free-energy curves in 6.2.2.1.3(a). As a result, BCC lattice became second to HCP in stability over FCC, as opposed to the stability trend below 50 GPa. Although predicted at different pressures

and V/V_0 volume change, similar type of behaviour in Mg was reported earlier and most recently by other authors using different first-principles techniques: the generalized pseudopotential theory (GPT) and the linear-muffin-tin orbitals (LMTO) [McMahan and Moriarty 1983], perturbative local pseudopotential theory (PLPT) [Perdew *et al* 2000] and local pseudopotential theory (LPT) [Chavarria 2005]. Even if not discussed, results by McMahan and Moriarty indicated FCC→BCC free-energy crossing transition slightly below and above V/V_0 = 0.80 using GPT and LMTO, respectively, while it also occurred just below 0.80 for both results computed from local pseudopotentials (PLPT and LPT). However, in the current study the energetic HCP→ BCC phase transition could only be obtained at 250 GPa (V/V_0=0.36), just after another anomaly between 200 and 240 GPa. Using GPT and LMTO McMahan and Moriarty reported HCP→BCC pressure-induced phase transition at 50 (V/V_0 = 0.58) and 57 GPa (V/V_0 = 0.56), respectively, whereas it occurred at 44.6 GPa for LPT [Chavarria 2005] and at 137 GPa for PLPT [Perdew *et al* 2000]. However, in agreement with Chavarria and Perdew *et al*, we do not observe any sign of further BCC→FCC transition up to 300 GPa reaching V/V_0 value of 0.34. Conversely, McMahan and co-workers articulated further transition at V/V_0 = 0.24 and 0.40 predicted by GPT and LMTO methods, respectively.

Figure 6.2.2.1.4 presents plots of *a* and *c* versus pressure for (a) HCP Mg and (b) ω Ti. In figure 6.2.2.1.4(a), both lattice parameters vary smoothly with pressure. However, on focussing at pressures below 20 GPa, as shown in the insert, we notice that the *c* axis depicts some strange features indicated by arrows between 4 and 7 GPa. The observed behaviour was also reported by Clendenen and Drickamer (1964). Interestingly, the lattice constants of ω Ti seem to follow a similar trend to those of Mg, where the *a-axis* varies smoothly with pressure while the *c-axis* behaves in an unexpected manner between 100 and 250 GPa. This striking behaviour is more pronounced in Ti at 250 GPa. Thus, from current results, the anomalous change in *c/a* ratio at applied pressures could be linked to a change in preferred crystal (principal) deformation mode prior to any possible pressure-induced solid-state phase transition. We will later explore the basis for the observed anomalies at high pressures in both elemental metals from electronic structure point of view. In figure 6.2.2.1.5, it is shown that HCP Mg has higher

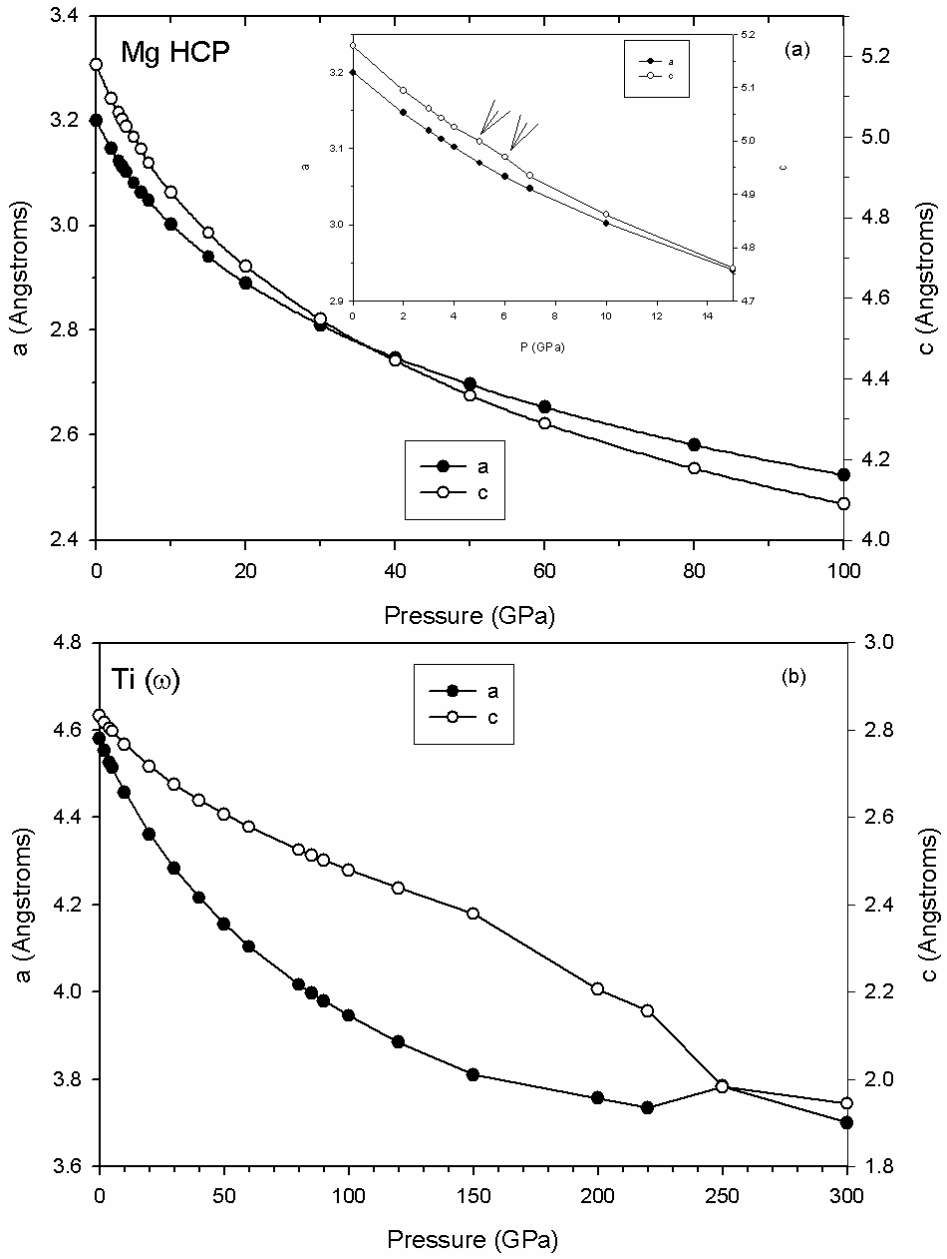

Figure 6.2.2.1.4. The variation of *a* and *c* lattice parameters with pressure for (a) HCP Mg and (b) ω Ti. The insert shows magnification at low pressures.

atomic size than ω Ti at 0 GPa as indicated by atomic volume. Furthermore, the former has high compressibility compared to the latter, particularly below 100 GPa after which their respective atomic volumes are almost equal. Therefore at pressures above 100 GPa, the two metals have similar atomic sizes due to early drastic decrease in the lattice volume of Mg. The observed sharp decrease in atomic size difference may

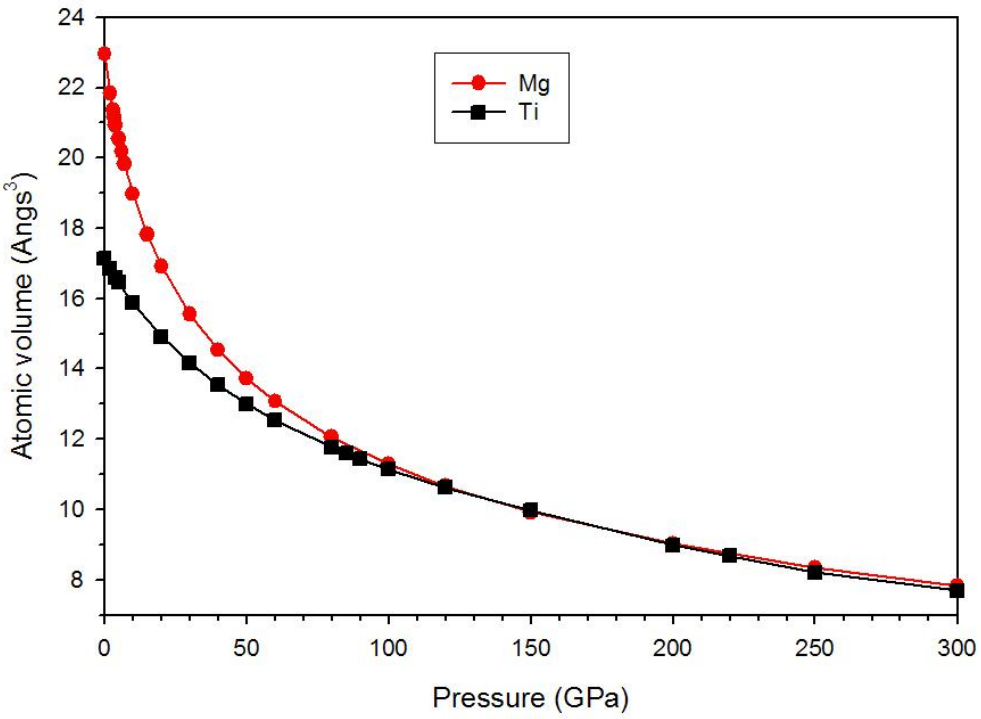

Figure 6.2.2.1.5. Equations of state of ground-state structures of Mg (HCP) and Ti (ω) elements.

increase the possibility of extending solid-solution of Mg and Ti at high-pressure conditions, provided their respective crystal structures are similar.

6.2.2.2 Effect of pressure on the electronic structure of elemental Ti and Mg phases

Similar to the heats of formation and elastic constants, the electronic structure in the form of density of states (DOS) can be used to investigate the stability of pure metals as well as metal alloys. The DOS discussions below rely mainly on the shape of the DOS curves near the Fermi level (E_F), which divides the lower energy states (valence-band) and higher energy states (conduction-band). Since the effect of pressure on materials is known to bring about modifications in the physical and chemical properties [McMillan 2006, Chandra 2007], it is thus of great importance to study the electronic structural changes due to compression. These results might provide insights on how this happens within energy bands of individual elements. The DOS will also indicate if large changes in the outer electron shells, under extreme densification conditions, can promote alloying in immiscible systems.

6.2.2.2.1 Total density of states (TDOS)

In figure 6.2.2.2.1.1, we display the total density of states (TDOS) curves for Ti in (a) ω, (b) α, (c) FCC and (d) BCC lattices at equilibrium as well as at various high pressures. The left part of the DOS corresponds to the bonding states whereas the right part corresponds to non-bonding states. The anti-bonding states are located well above the Fermi level and are not shown in the plots.

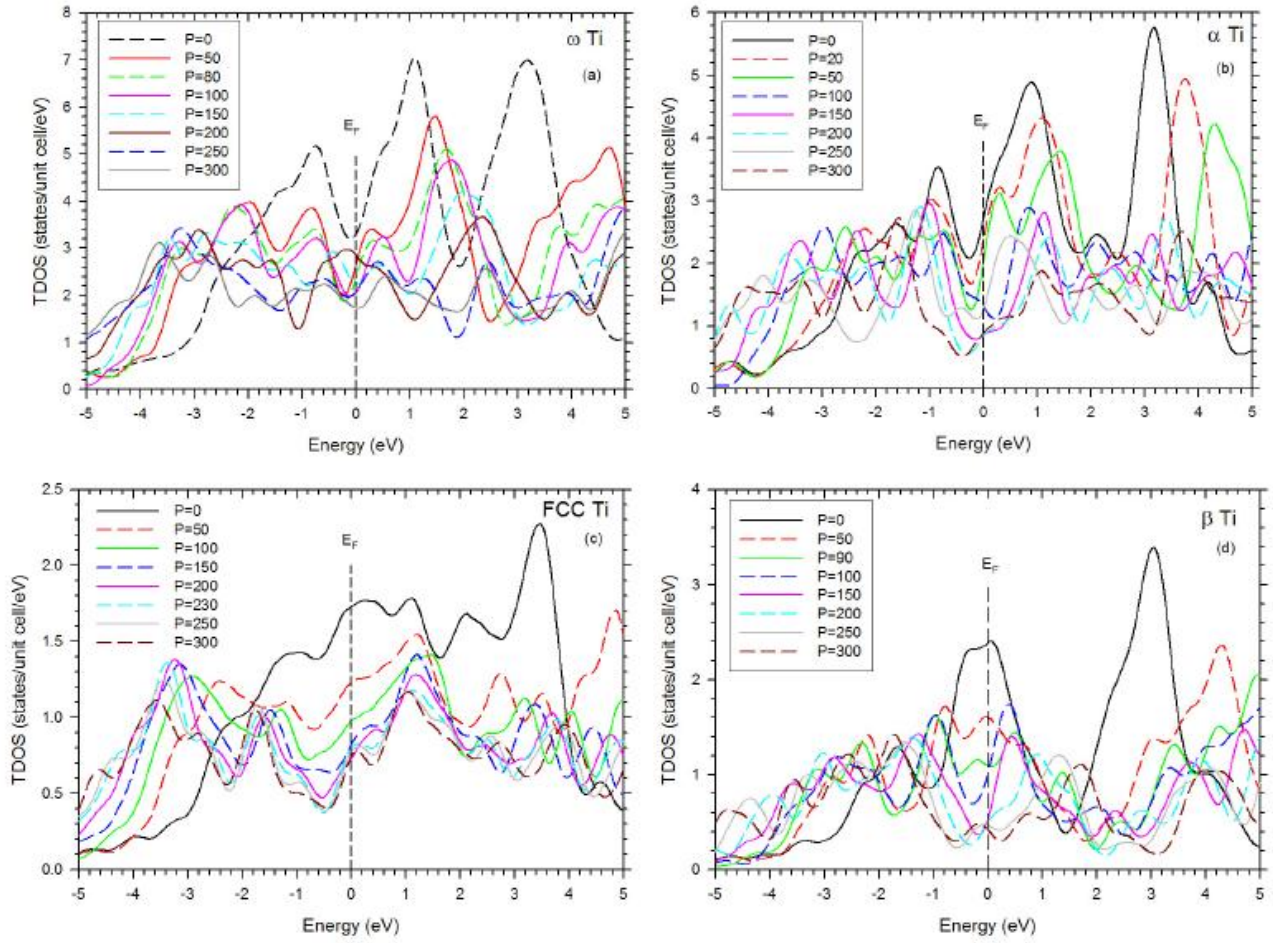

Figure 6.2.2.2.1.1. The TDOS plots for Ti in (a) omega, (b) alpha, (c) FCC and (d) beta (β) crystal structures at various pressures of up to 300 GPa.

As expected, at zero pressure and temperature the E_F lies in a dip (pseudo-gap) of the DOS of the omega (ω) phase, suggesting this phase to be the most stable among other

considered phases. It however cuts through a shoulder of a rising peak in the alpha (α) phase, showing some level of instability, as is the case for FCC and BCC structures. With pressures below 100 GPa, no significant stability changes in the DOS behaviour are observed, except for the BCC phase which seems to become metastable at around 90 GPa. The overall TDOS curves lower around the E_F with increasing pressure. Beyond this pressure, other than omega, no other phase seems to be stable. Besides stability, Ti in all four phases shows a near-free-electron (NFE) metal behaviour.

Among TDOS plots shown in figure 6.2.2.2.1.2 for (a) HCP, (b) FCC and (c) BCC Mg phases, the E_F cuts almost through the pseudo-gap in the BCC lattice at 0 GPa as opposed to the expected ground-state HCP phase. The Fermi level cuts on a shoulder of a rising peak and at the tip of the peak for HCP and FCC phases, respectively. However, a closer look at lower pressures as shown in subsequent figure 6.2.2.2.1.3 for HCP, reveals tendency to stabilize around 10 to 15 GPa. Our results suggest that the experimental observed HCP ground-state structure corresponds to lattice compressed between 10 and 15 GPa at 0K. The DOS behaviour between 20 and 250 GPa in BCC and HCP lattices is almost similar despite lowering of pseudogap towards horizontal energy axis. However, distinct changes are observed in FCC lattice above 20 GPa, where E_F shifts from cutting through a peak to cutting through a dropping peak closer to the pseudo-gap. There seems to exist a weakly pronounced stability of FCC lattice at P=60 GPa. Although we do not see any sign of the BCC stability at high pressures, the presence of a pseudo-gap in the DOS with Fermi level residing close to the minimum remains a prominent feature in the plots of both Mg and Ti. It is slightly above E_F in FCC and slightly below E_F in HCP phase. In particular at P=0, all Mg phases also show NFE metal behaviour.

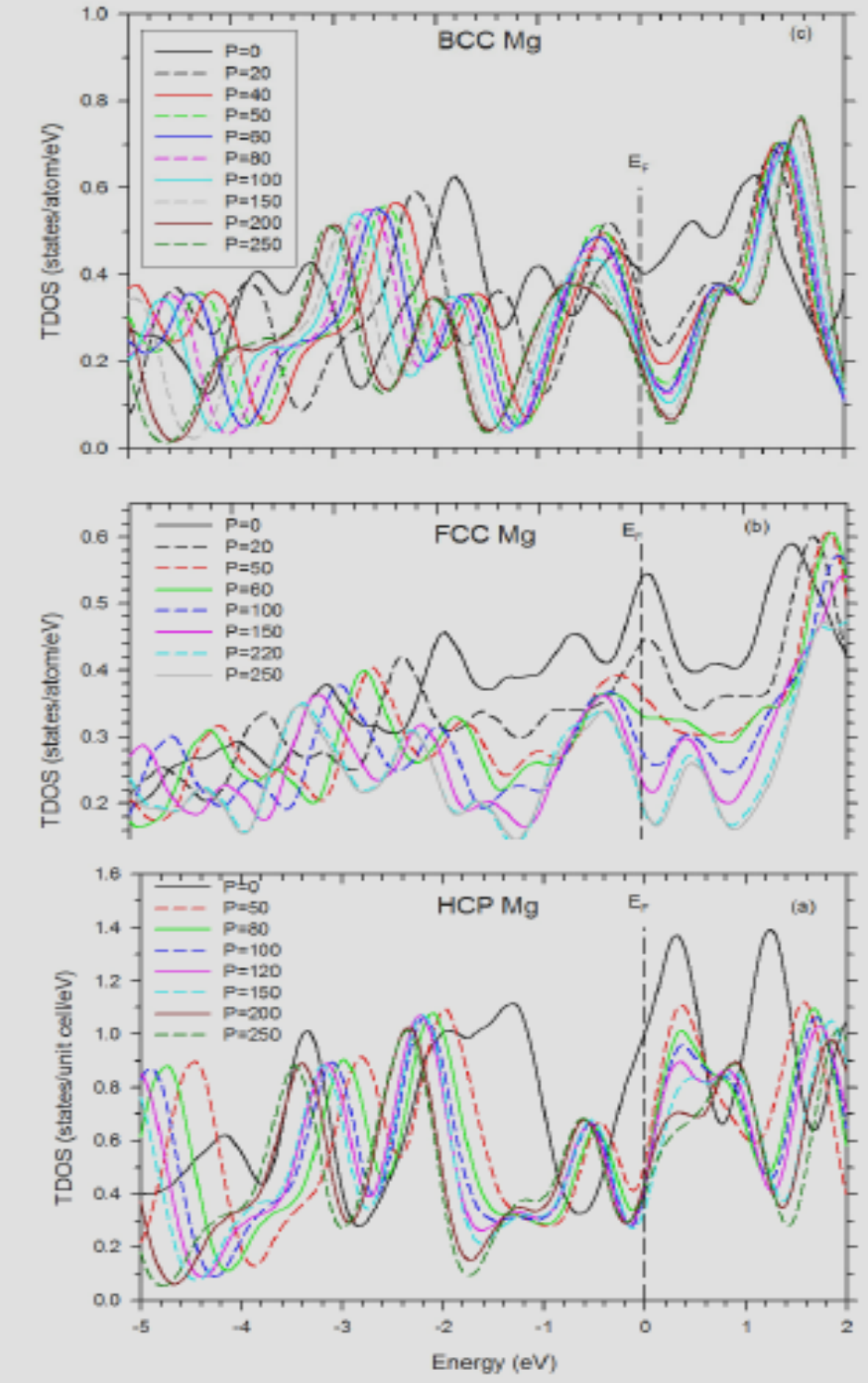

Figure 6.2.2.2.1.2. The TDOS plots for Mg in (a) HCP, (b) FCC and (c) BCC phases at pressure values varying between 0 and 250 GPa.

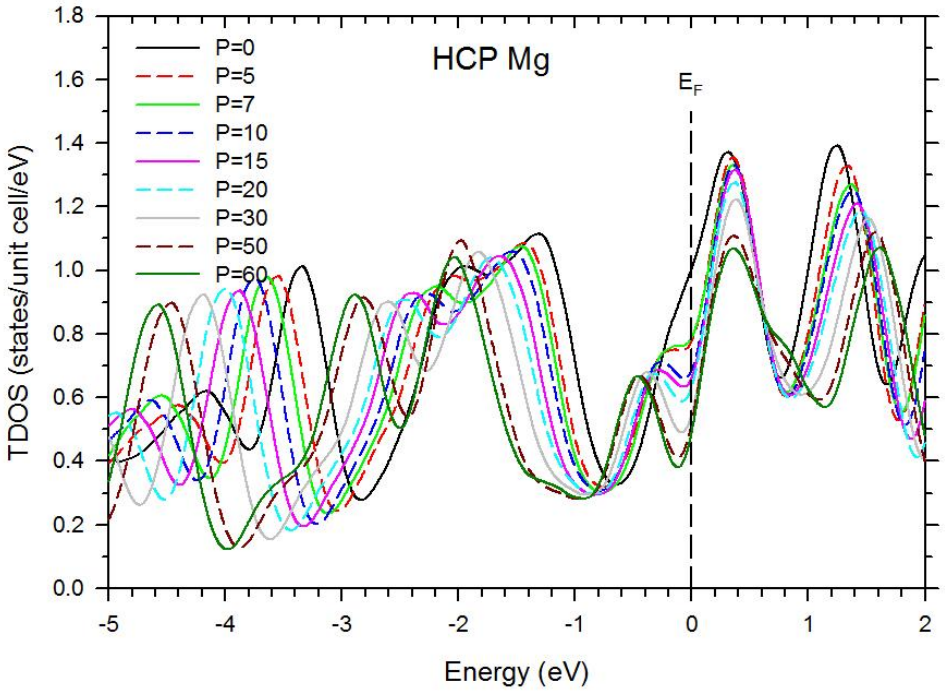

Figure 6.2.2.2.1.3. The TDOS curves for Mg in HCP lattice at lower pressures.

6.2.2.2.2 Partial density of states (PDOS)

The partial densities of states (PDOS) curves of most stable elemental phases in the pressure range 0-300 and 0-250 GPa for (a) Ti and (b) Mg, respectively, are displayed in figure 6.2.2.2.2.1. It appears from these PDOS plots that the electron configurations of individual elements tend to deviate from the initial ideal $2p^6 3s^2$ and $3p^6 4s^2 3d^2$ for Mg and Ti, respectively, during geometrical optimization. However, on applying pressure the situation improves towards attaining the ideal case. It is not yet clear if this electronic behaviour could be attributed to the unrestricted movement of electrons belonging to the valence outer most shells in NFE metals since the total number of valence electrons remains 8 and 12 for Mg and Ti, respectively.

In the case of omega Ti at equilibrium, we observe a slight difference in orbital population between the three atoms in a unit cell. As shown in figure 6.2.2.2.2.1(a), two Ti atoms represented as 2 and 3 have equal orbital filling somehow different from the other Ti atom represented as 1. The electrons belonging to $4s^2$ are distributed in 3*s*, 3*p*-

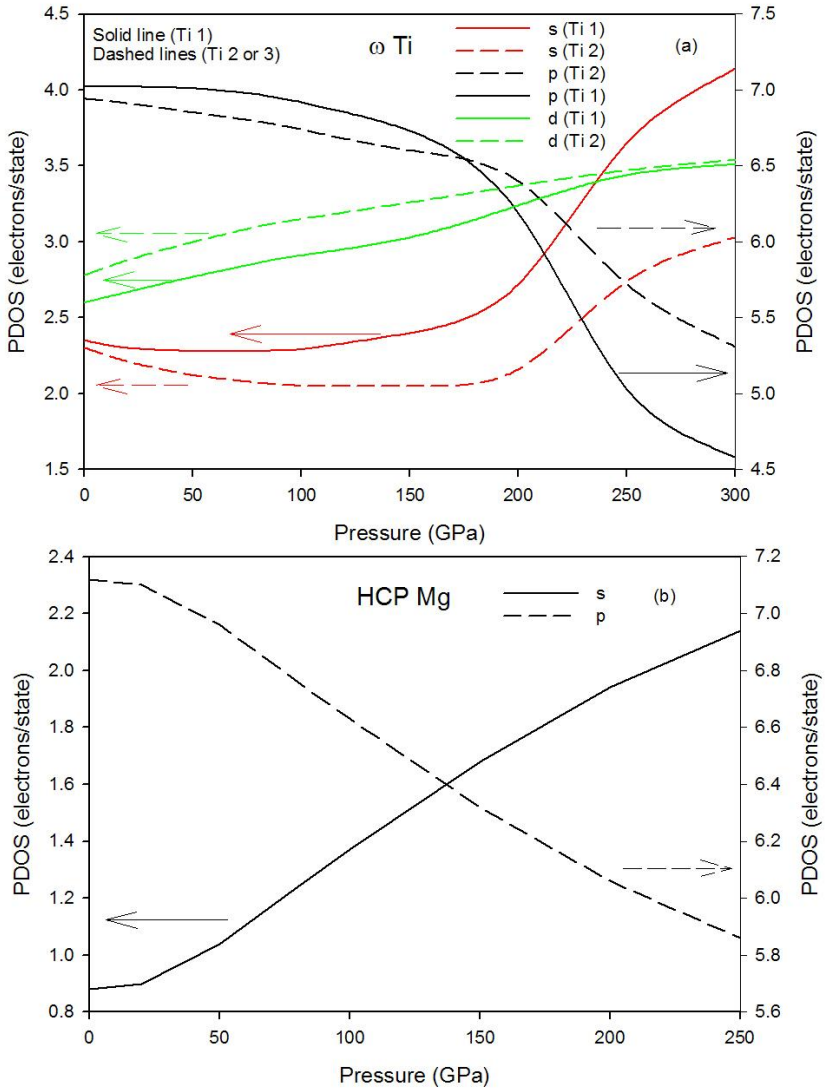

Figure 6.2.2.2.2.1. Partial density of states (PDOS) of (a) omega Ti and (b) HCP Mg at pressure range 0 to 300 and 250, respectively.

and 3*d*-states. With increasing pressure, although quantities differ noticeably, the changes within states follow similar path. It is worth noting that *p*→*d* electron transfer is evident below for pressures below 200 GPa since the number of electrons occupying *s*-orbital is nearly constant while starting at 250 GPa, the *d*-orbital electron occupation which increased gradually with pressure is almost equal in all Ti atoms. On the other hand, the *p*→*s* electron transfer is evident in Ti with further increase in pressure as indicated by coinciding decrease and increase rates in *p* and *s* orbital fillings, respectively. These changes became rapid between 200 and 250 GPa. It is in this

pressure range where Ti attains its ideal electronic structure, with *p*-electrons being six or below. Strangely, despite what happens in the *s* and *p* states, the electrons in the *d*-state seem to increase at an almost constant rate. Nonetheless, as shown for pressures below 250 GPa, it makes sense to think of possible ***s→d*** hybridization in the transition metal, where the electron population in the *p*-state is more than its maximum capacity of six. Hence, the increase in electrons in the *d*-state may well be understood as contribution due to *s*-electrons as indicated by red dashed lines.

As shown by the HCP Mg PDOS plot in figure 6.2.2.2.2.1(b), at equilibrium some of the 3*s* electrons are clouded around 2*p*-state (orbital). Hence at high pressure we observe ***p→s*** electron transfer, attaining ideal $2p^6 3s^2$ electron configuration at 200 GPa. Hence, the HCP→BCC phase transition commencing above 200 GPa could be linked to ***p→s*** hybridization after obtaining the ideal $2p^6 3s^2$ electron configuration. As shown by the free-energy difference curves in figure 6.2.2.1.3(a), this transition is only obtained at 250 GPa, which is exactly 50 GPa above ideal electronic structure attainment, in accordance with experimental observations.

6.2.3 Martensitic phase transformation in pure metals (Ti and Mg) through shearing and shuffling mechanisms

It is well known that the group IVB metals (Ti, Zr and Hf) all have the HCP (α) crystal structure at room temperature and zero pressure. At high temperature and zero pressure they transform to the BCC phase before the melting temperature is reached [Aguayo *et al* 2002]. Since the transformation is first order, diffusionless and the resultant lattice distortion can mostly be described by a shear with almost no volume changes, it is thus called martensitic transformation. In addition to tremendous scientific and technological interest, displacive or diffusionless phase transformations of martensitic type play a fundamental role in shape memory materials with numerous applications of so-called smart intelligent materials. The elementary mechanisms involved in such displacive transformations are essentially shear deformations and shuffling of atomic planes [Paidar 2008]. The displacive nature of the transition requires

the unit cell of the parent lattice to distort continuously into the unit cell of the daughter lattice. Such a change produces orientation relations between the two phases: certain vectors and planes in the parent phase will be parallel to unique vectors and planes in the daughter phase [Trinkle PhD dissertation 2003]. When the pressure is increased at room temperature, a crystallographic phase transition into another more open hexagonal phase called omega (ω) is observed. This pressure-induced phase transformation in pure Ti has received extensive experimental as well as theoretical attention due to its significant implications in aerospace industry because the ω phase formation lowers toughness and ductility [Conrad 1981, Sikka *et al* 1982]. However, the onset pressure as well as the transformation mechanism for the α→ω phase transition in Ti and other group IVB metals varies greatly; hence the continuing controversy between experiments and theoretical calculations.

In this subsection, for purposes of better theoretical understanding of martensitic transformation, we present the transformation mechanisms in Ti and Mg for α→β and α→FCC martensitic type transformation as well as the controversial α→ω transformation. We consider atomic plane shuffling and shearing as elementary processes that are simultaneously activated during phase transformation.

6.2.3.1 Burgers path: HCP to BCC

The crystallographic relations in the HCP→BCC martensitic transformation was originally proposed by Burgers (1934) for Zr as follows:

$(110)_\beta||(0001)_\alpha$, $[111]_\beta||[11\text{-}20]_\alpha$

where the parentheses and square brackets represents atomic plane and direction, respectively. The parallel orientation relation of the atomic planes in HCP and BCC phases are shown by red spheres in figure 6.2.3.1.1(a) and (b). The energetic and corresponding deformation paths during α→β phase transformation in Ti are presented in figure 6.2.3.1.2(a), (b), and (c). The distortion of the α phase towards the β phase involves simultaneous shearing and shuffling of B-layer atoms (⅔ ⅓ ½) or (⅔ ⅓ ¾) with respect to atoms on the A-layer (0 0 0) or (⅓ ⅔ ¼) from (⅔ ⅓ ½) to (1 ½ ½), which led

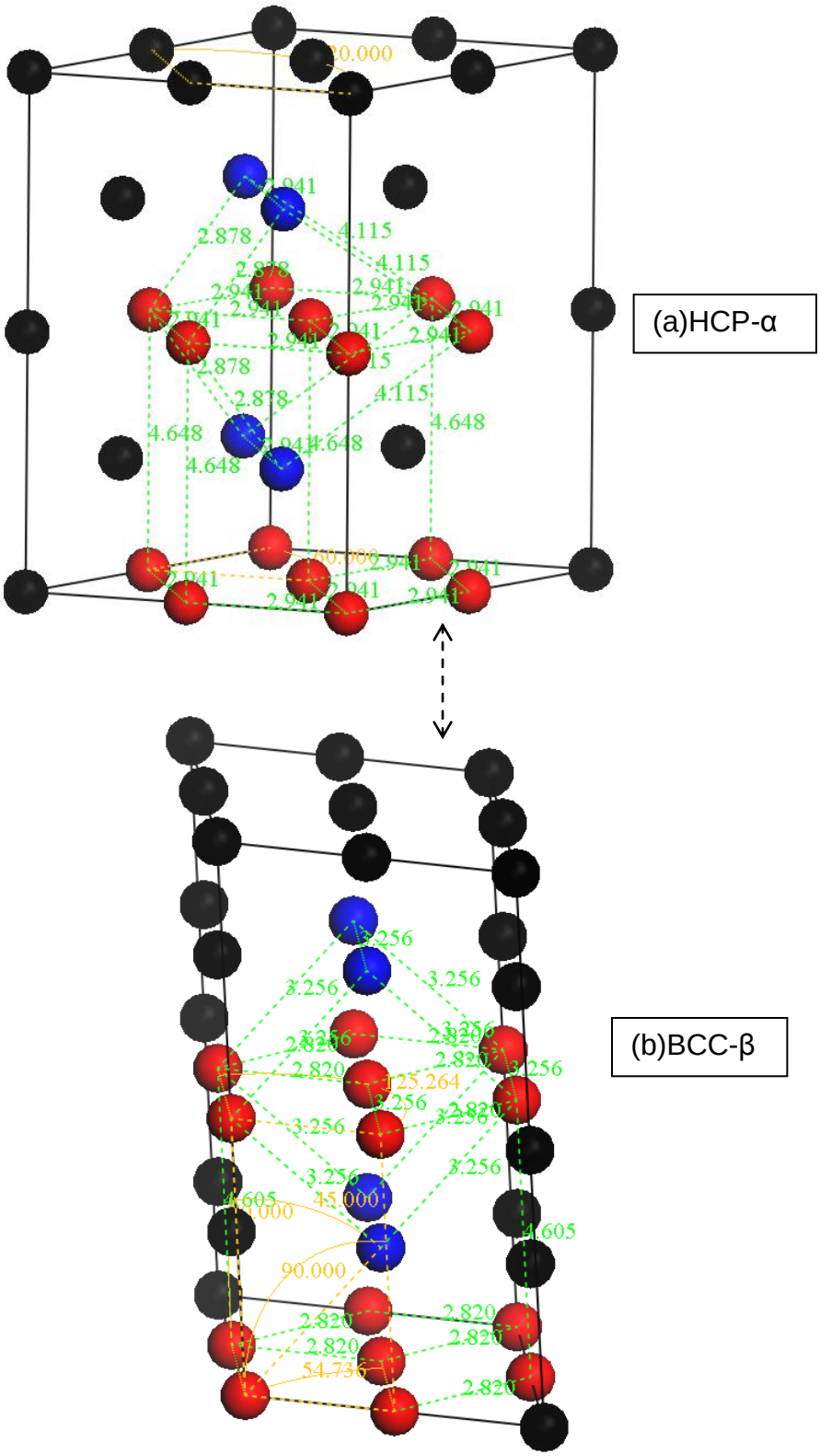

Figure 6.2.3.1.1. Crystallographic relationship between α and constructed β lattices at (a) low-temperature α and (b) high-temperature β Ti phases.

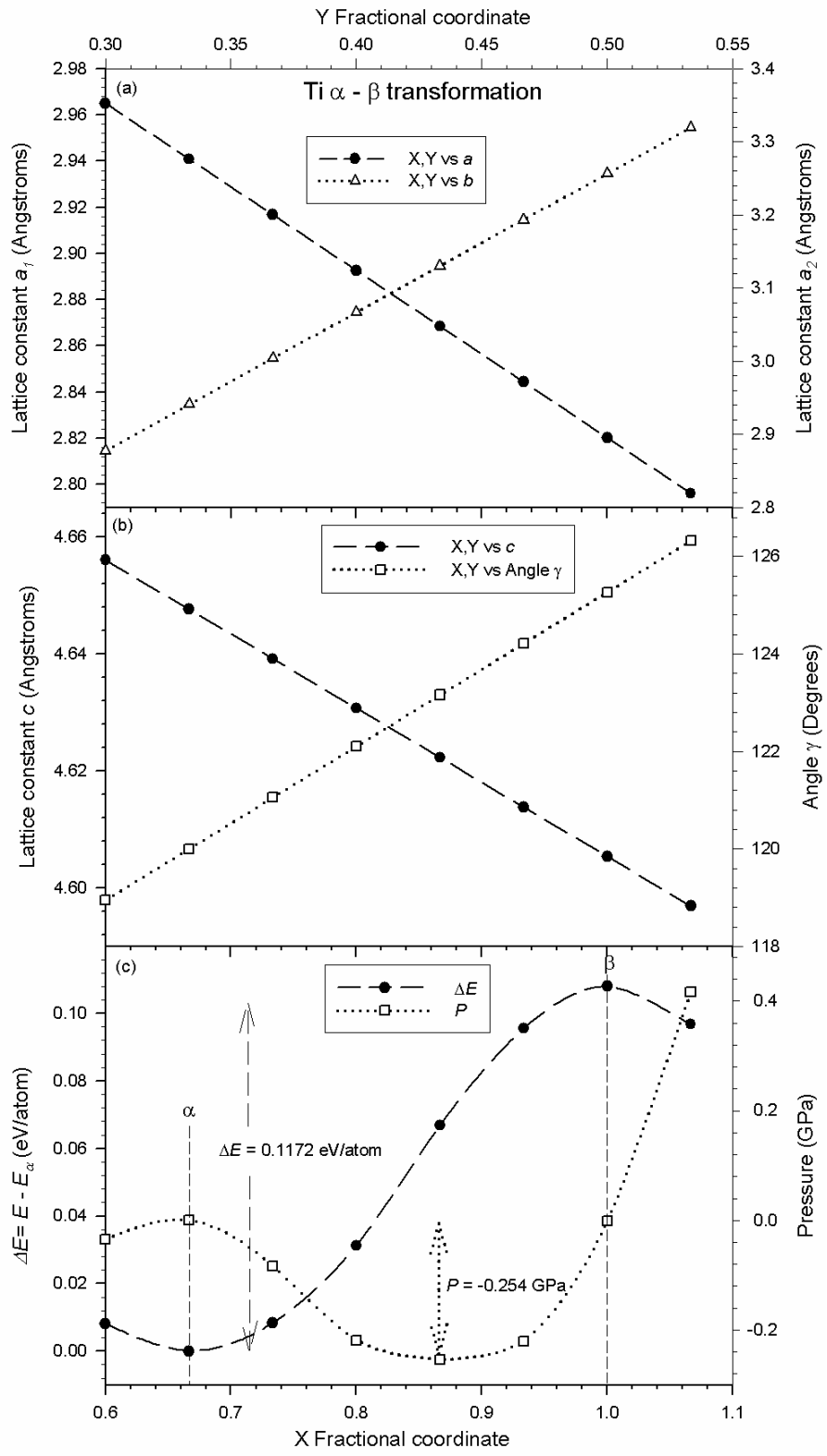

Figure 6.2.3.1.2. Illustration of Ti α→β phase transformation shown by lattice parameters (a) a_1 and a_2, (b) c and γ angle, as well as (c) change (ΔE) and required stress (P) plotted against atomic fractional coordinates corresponding to lattice deformation.

to change in lattice parameters (*a, b, c*) from 2.941 to 2.820 and 3.256 Å, *c/a* (1.580 to 1.633) and *c/b* (1.580 to √2) axial ratio, *γ* angle (120^o to 126.264^o) , *x* (⅔ to 1) and *y* (⅓ to ½) atomic fractional coordinates (since the *z* atomic coordinates remain unchanged at ½) at β phase. Contrary to Miller conventional cell of α phase in which basal axes a_1, a_2 and a_3 are equal, on deformation towards β phase only $a_1=a_3\neq a_2$. The resulting lattice parameter a_1 and a_2 of the distorted HCP lattice are plotted against the corresponding *x* and *y* atomic coordinates in figure 6.2.3.1.2(a), while lattice parameter *c* and *γ* angle are also plotted against the same *x*-axis in figure 6.2.3.1.2(b). Energy difference (Δ*E*) between distorted and undistorted α phase is calculated with respect to the ground state α phase and the required stress (*P*) are also plotted against *x* and *y* atomic coordinates in figure 6.2.3.1.2(c). At BCC, as shown in figure 6.2.3.1.1(b), the corresponding lattice parameters of BCC and distorted HCP lattices are related by following expressions:

$a_1 = a_3 = a_{BCC\ primitive\ cell}$,

$a_2 = a_{BCC\ conventional\ unit\ cell}$

$c = \sqrt{2} \times a_2$, and $c = 1.633 \times a_1$.

Therefore the average *c/a* ratio for distorted HCP at BCC is equal to 1.56 and hence some HCP metals such as Ti, Zr, Hf with lower *c/a* prefers to slip prismatically to BCC phase at high temperatures. As shown in figure 6.2.3.1.2(a) and (b), the phase transformation from α→β is accompanied by decrease in lattice parameters a_1, a_2 and *c*, and increase in a_2 and *γ* angle. The intermediate phase along this path is orthorhombic with space group Cmcm #63. The calculated energy barrier of 0.1172 eV/atom and required shear stress (δ) of -254 MPa are determined from the maximum and minimum, respectively, of the curves presented in figure 6.2.3.1.2(c). The observed curvature trends resembles those reported by Šob *et al* (2004), who used *ab initio* calculations to predict strength of cubic crystals.The negative value of the required shear stress (δ) indicates that the deformation is thermally activated. Since the magnitute of the shear stress (δ) is known, therefore the minimum shear stress (τ) required to initiate plastic deformation or prismatic slip (CRSS) can be determined using the equation

$$\tau = \sigma \cos\theta \cos\eta \qquad 6.2.3.1.1$$

where θ is the angle between applied force and slip direction while η is the angle

between the applied force and the slip plane normal **N**. Thus the CRSS for α→β transition is equal to 106 MPa for θ = 42.005^{o}, η = 55.889^{o}, with Schmid factor m = cosθcosη= 0.416. Although it is for the first time that *ab initio* calculations of such mechanical properties is carried out, our predicted results are in excellent agreement with experimental data of 240 MPa for ultimate tensile strength (yield tensile strength 170 – 310 MPa) [Elias *et al* 2008] and prismatic slip CRSS ranging between 86 and 127 MPa [Gong and Wilkinson 2011]. Our established solid-solid phase transformation mechanism is almost similar to that reported by Johnson and Carter (2008), Liu and Johnson (2009), for iron as well as that of Caspersen and Carter (2005) for lithium.

Following a similar procedure, the HCP→BCC transformation path for Mg was established, as presented in figure 6.2.3.1.3. This transformation path is almost similar to the theoretical model proposed by Wentzcovitch and Cohen (1988), although they only accounted for c = 1.633 x a_1 at BCC but not for c = √2 x a_2. We found the calculated energy barrier to be equal to 0.0278 eV/atom and required shear stress (δ) of -96 MPa, as shown in in figure 6.2.3.1.3(c). Thus, using equation 6.2.3.1.1 above, the CRSS for prismatic slip in pure Mg is equal to 40 MPa when θ = 41.725^{o}, η = 56.105^{o} and m = 0.4162. Our predicted value of CRSS for prismatic slip is in excellent agreement to 39 and 50 MPa reported by Ward Flynn *et al* (1961) and Reed-Hilland and Robertson (1957) as reviewed by Hutchinson and Barnett (2010).

In an attempt to clarify the *c/a* minima observed in figure 6.2.2.1.3(b) and (c) for Mg under hydrostatic pressure, we present and compare the change in energy and pressure in figure 6.2.3.1.4(a) and (b) for the HCP→BCC transformation path at 0, 20 and 50 GPa. It is evident from figure 6.2.3.1.4(a) that due to small increase in *c/a* ratio which led to larger shear stress, the energy barrier for HCP→BCC transition is slightly higher at 20 GPa compared to 0 GPa. However, the energy slope as well as the energy barrier becomes lower at 50 GPa. This behaviour could be attributed to a decrease in *c/a* ratio since the required shear stress is even higher than at 0 and 20 GPa. It is therefore clear that a decrease in *c/a* ratio reduces the energy barrier for HCP→BCC in Mg, although the necessary deformation stress for prismatic slip system rises with an

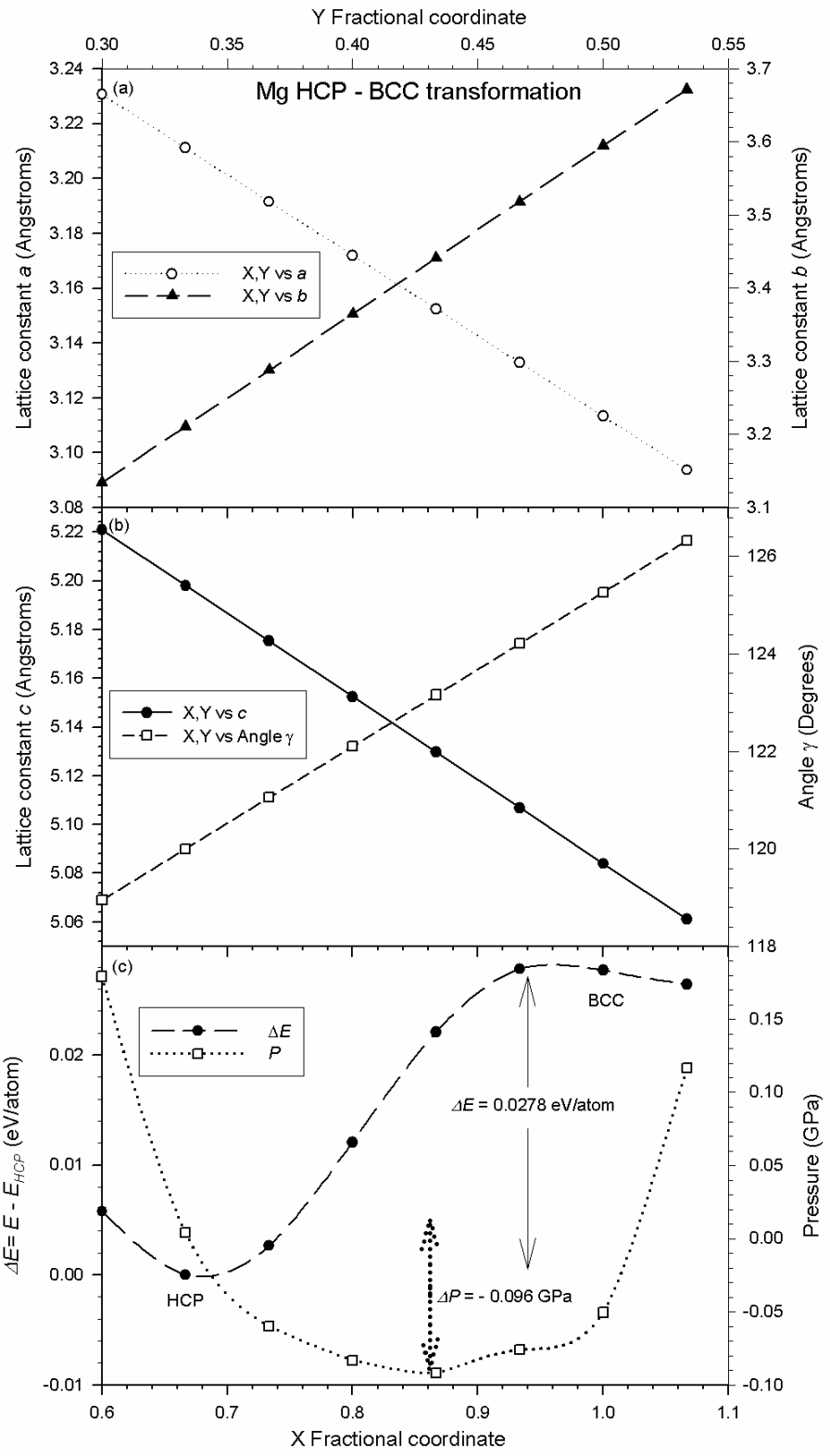

Figure 6.2.3.1.3. Illustration of Mg α→β phase transformation shown by lattice parameters (a) a_1 and a_2, (b) c and γ angle, as well as (c) change (ΔE) and required stress (P) plotted against atomic fractional coordinates corresponding to lattice deformation.

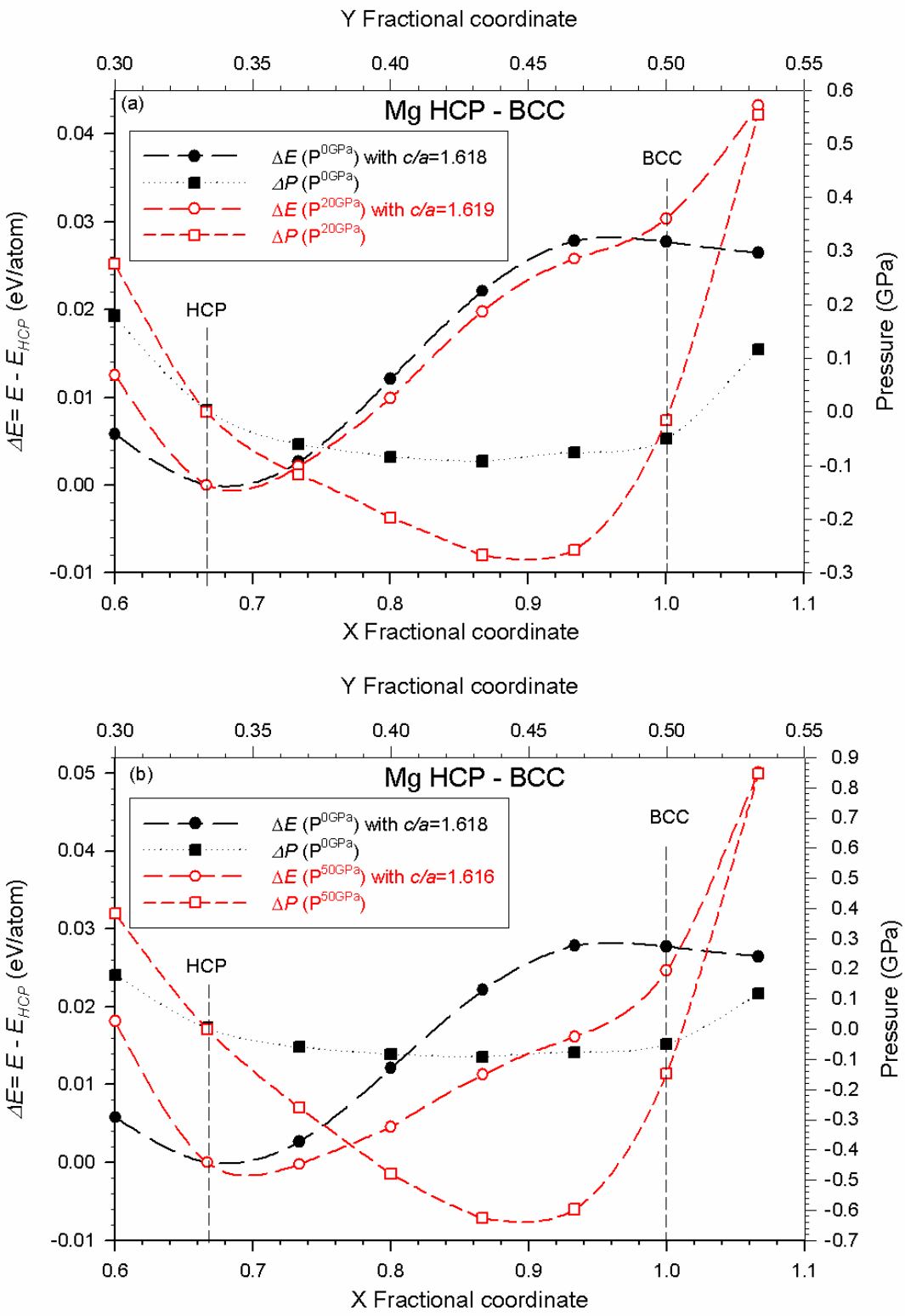

Figure 6.2.3.1.4. Comparison of change in energy and pressure for Mg α→β transition under hydrostatic pressure of (a) 0, 20 GPa and (b) 0, 50 GPa.

increase in hydrostatic pressure. Current results imply that the HCP→BCC phase transition in Mg under hydrostatic pressure corresponding to minimum *c/a* ratio is stress-assisted activated instead of being only energy driven (MEP).

6.2.3.2 Wassermann path: HCP to FCC

It is well known that upon cooling, cobalt undergoes a polymorphous transformation form FCC to HCP. The temperature corresponding to the equilibrium between the high-temperature FCC and low-temperature HCP phases in cobalt is about 417^{o}C [Hess and Barrett 1952]. The orientational relationships at the diffusionless FCC to HCP transition are

$(111)_{FCC}||(0001)_{HCP}$, $[110]_{FCC}||[11\text{-}20]_{HCP}$

as determined by Wassermann (1932) using X-ray technique. The parallel orientation relation of the atomic planes in α and FCC phases are shown by red spheres in figure 6.2.3.2.1(a) and (b). The energetic and corresponding deformation paths during α→FCC phase transformation in Ti are presented in figure 6.2.3.2.2(a), (b), and (c). The distortion of the α phase towards the FCC phase also involves simultaneous shearing and shuffling of B-layer atoms of α phase (⅔ ⅓ ½) or (⅔ ⅓ ¾) with respect to atoms on the A-layer (0 0 0) or (⅓ ⅔ ¼) from (⅔ ⅓ ½) to (1 ½ ½), which led to change in lattice parameters (*a* and *c*) from 2.941 to 2.908 Å and 4.647 to 5.037 Å respectively, *c/a* (1.580 to √3), β angle (90^{o} to 106.779^{o}) , *x* (⅔ to 1) and *y* (⅓ to ½) atomic fractional coordinates (since the *z* atomic coordinates remain unchanged at 1/2) at FCC lattice. Similar to Miller conventional cell of α phase, on transformation towards FCC phase, all the basal axes remain equal ($a_1=a_2=a_3$). The resulting lattice parameters *a* and *c* of the distorted HCP lattice are plotted against the corresponding *x* and *y* atomic coordinates in figure 6.2.3.2.2(a), while *c/a* and β angle are also plotted against the same *x*-axis in figure 6.2.3.2.2(b). Energy difference (Δ*E*) between distorted and undistorted α phase is calculated with respect to the ground state α phase as well as the required stress (*P*) are also plotted against *x* and *y* atomic coordinates in figure 6.2.3.2.2(c). At FCC, as shown in figure 6.2.3.2.1(b), the corresponding lattice parameters of FCC and distorted α lattices are related by following expressions:

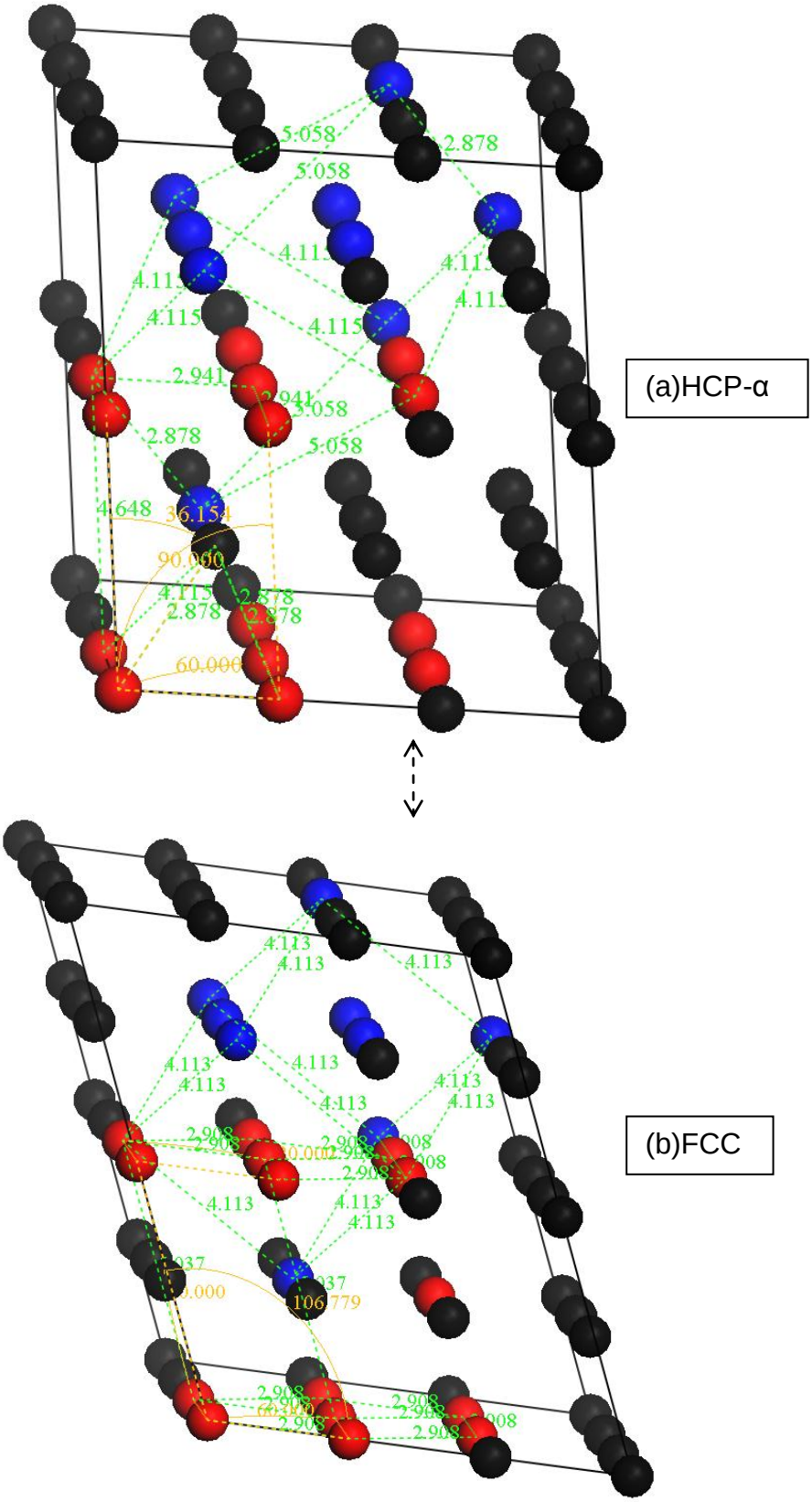

Figure 6.2.3.2.1. Crystallographic relationship between α and constructed FCC lattices at (a) low-temperature α and (b) FCC metastable Ti phases.

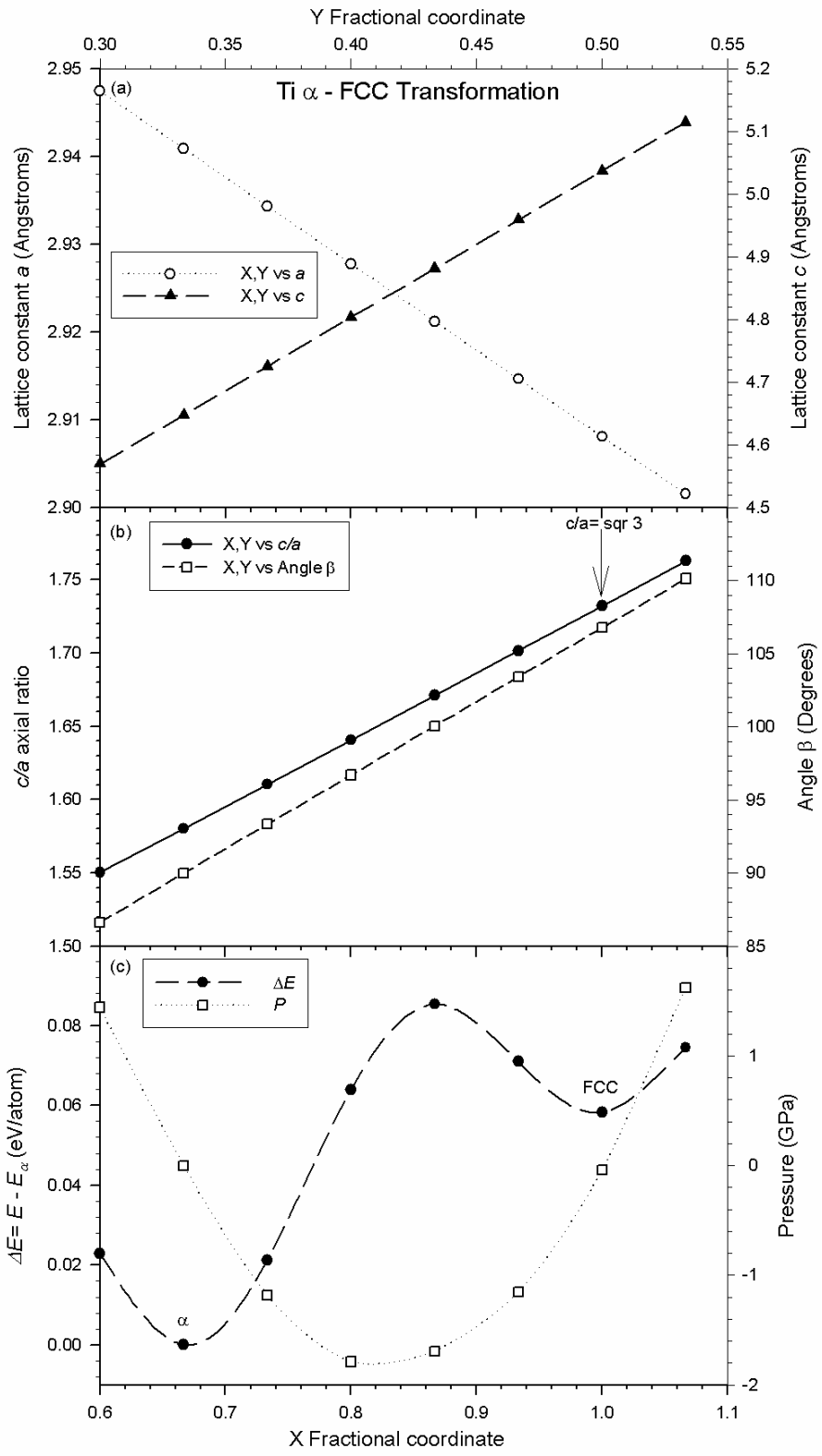

Figure 6.2.3.2.2. Illustration of Ti α→FCC phase transformation shown by lattice parameters (a) *a* and *c*, (b) *c/a* and β angle, as well as (c) change (Δ*E*) and required stress (P) plotted against atomic fractional coordinates corresponding to lattice deformation.

$a_1 = a_2 = a_3 = a_{FCC\ primitive\ cell}$,

$c_\alpha = \sqrt{3} \times a_\alpha$ (α refers to distorted phase).

Consequently, HCP metals with larger *c/a* ratio such as Co, Mg are reported to deform via basal slip sytem [Yoo 1981]. As shown in figure 6.2.3.2.2(a) and (b), the Ti phase transformation from α→FCC is accompanied by equal decrease in lattice parameters a_1, a_2 and a_3 along basal plane and increase in *c* and β angle. Although the energy difference between α and FCC is equal to 60 meV/atom comparable to 65 and 70 meV/atom reported by Chakraborty *et al* (2011) and Paxton *et al* (1990), the calculated energy barrier of 0.0881 eV/atom while the required shear stress (δ) of -1794 MPa determined from the maximum and minimum, respectively, are presented in figure 6.2.3.2.2(c). Again, the negative value of the required shear stress (δ) indicates the athermal dislocation mechanism. The intermediate phase along this path is monoclinic with space group C2/m #12 .Using equation 6.2.3.1.1, the CRSS for basal slip in pure Ti is equal to 658 MPa when $\theta = 43.368^o$, $\eta = 59.717^o$ and m = 0.3666. In spite of smaller energy barrier for basal slip in Ti accompanied by τ = 658 MPa, our predictions suggest the easiest deformation to be via prismatic slip as indicated by smaller CRSS value of 106 MPa.

In order to clarify the transition around the proposed α→FCC transition at 100 GPa for Ti as shown in figures 6.2.2.1.1 and 6.2.2.1.2, we present in figure 6.2.3.2.3(a)-(b) the comparison of change in energy and pressure for Ti α→FCC transition under hydrostatic pressure of 0, 50 and 100 GPa. It is evident from figure 6.2.3.2.3(a) that at 50 GPa there is small increase in *c/a* ratio from 1.58 to 1.60 and significant increase in shear stress to about -6 GPa, which led to less steep energy favourable barrier compared to 0 GPa. However, upon applying 100 GPa, the FCC phase becomes energetically more stable than α phase with *c/a* = 1.85, accompanied by pressure barrier of about -8 GPa. This behaviour implies that an increase in *c/a* favours the basal deformation slip and MEP (minimum energy path) for α→FCC transition, in accordance with our ealier observation in figures 6.2.2.1.1 and 6.2.2.1.2.

Following a similar approach, the HCP→FCC transformation path for Mg was

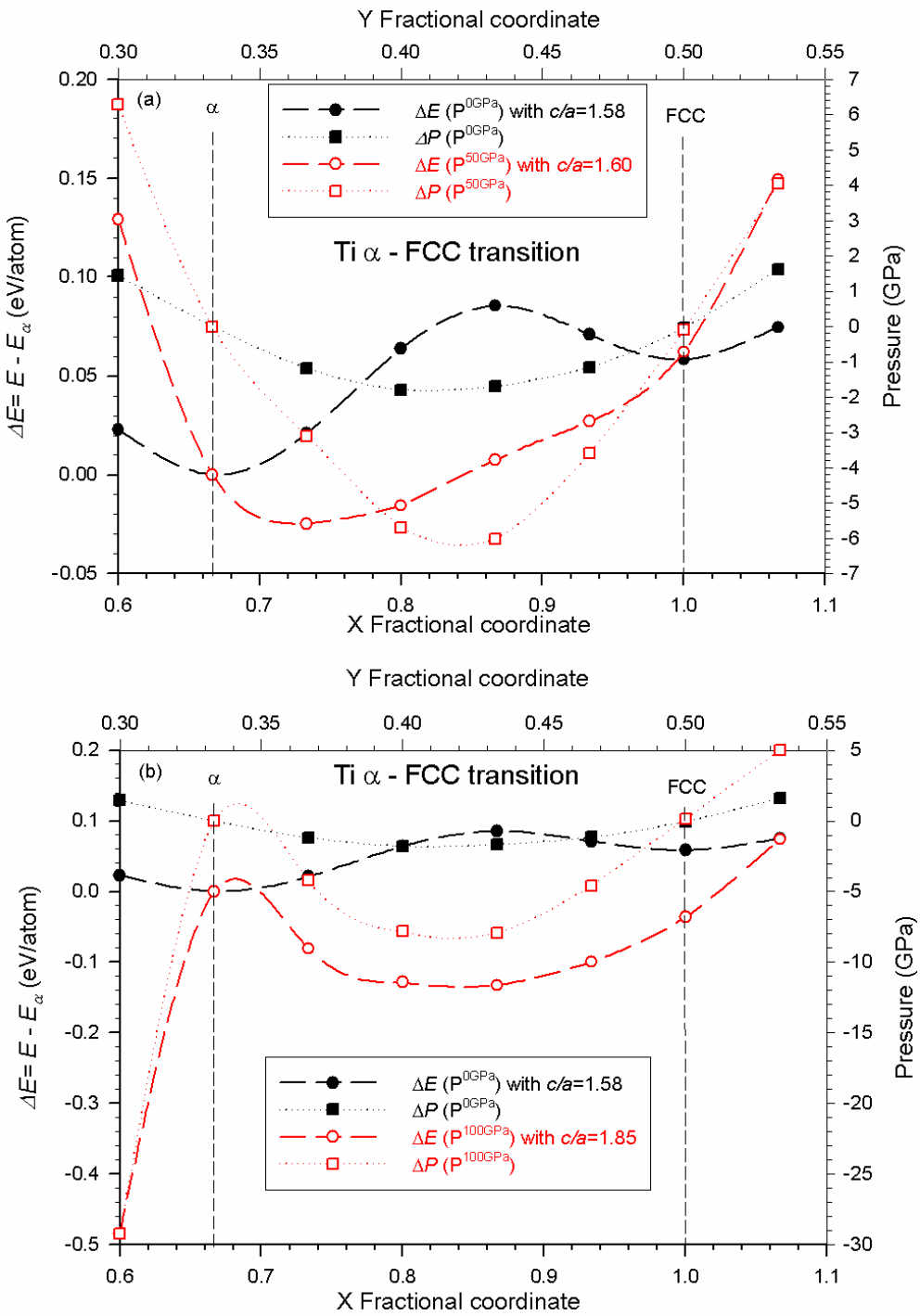

Figure 6.2.3.2.3. Comparison of change in energy and pressure for Ti α→FCC transition under hydrostatic pressure of (a) 0, 50 GPa and (b) 0, 100 GPa.

established, as presented in figure 6.2.3.2.4. We found the calculated energy barrier to be equal to 0.0237eV/atom and the required shear stress (δ) of -331 MPa, as shown in

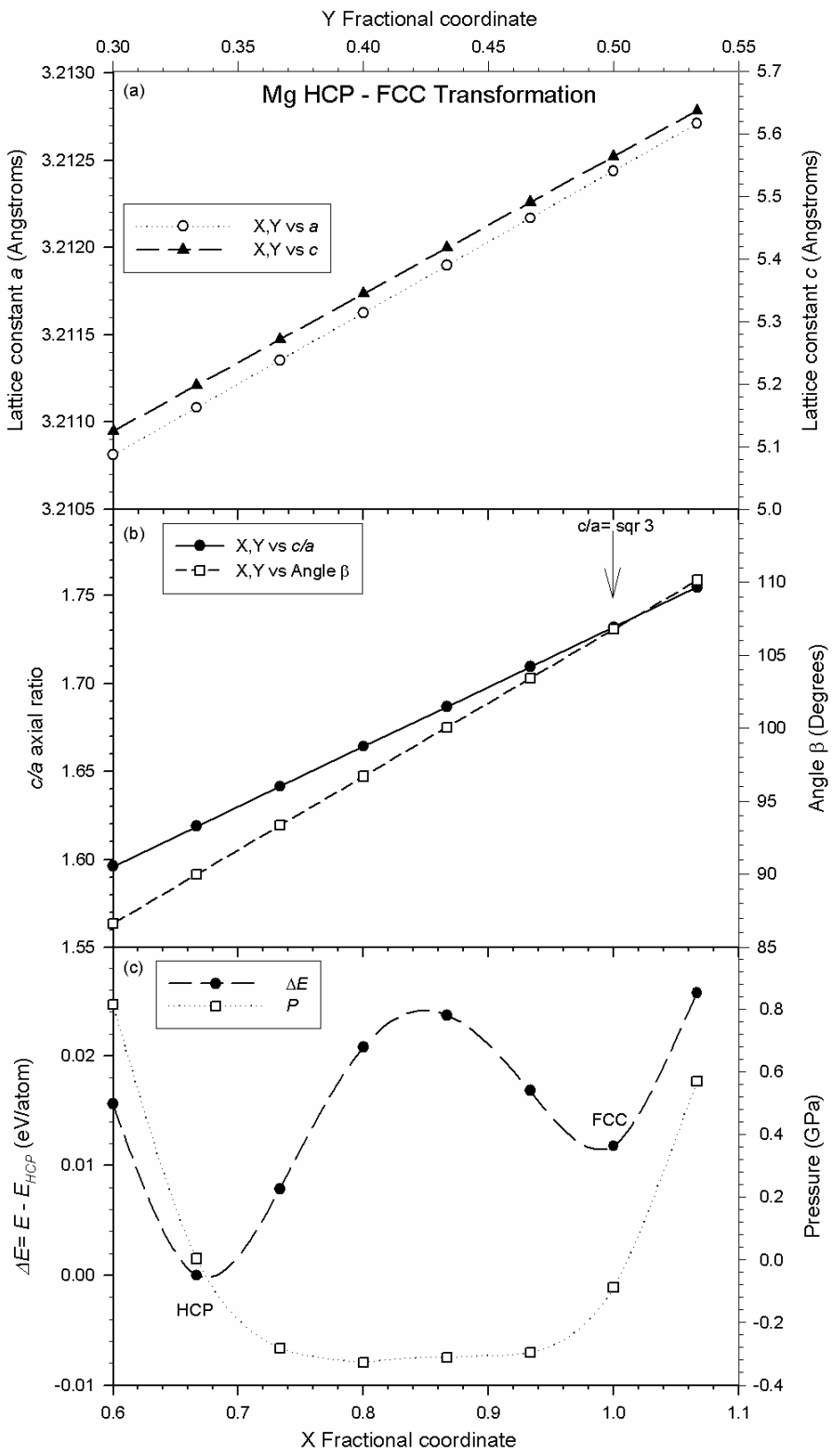

Figure 6.2.3.2.4. Illustration of Mg α→FCC phase transformation shown by lattice parameters (a) *a* and *c*, (b) *c/a* and β angle, as well as (c) change (Δ*E*) and required stress (P) plotted against atomic fractional coordinates corresponding to lattice deformation.

figure 6.2.3.2.4(c). Thus, using equation 6.2.2.1.1, the CRSS for basal slip in pure Mg is equal to 121 MPa when $\theta = 42.907^{o}$, $\eta = 60.092^{o}$ and m = 0.3652. Our predicted value of CRSS for basal slip is very high compared to recent experimental studies of Mg single crystals conducted between 4 and 295K, which reported values in the range 1 - 1.5 MPa [Bhattacharya and Niewczas 2011]. Despite the lower energy barrier or minimum energy path (MEP) for HCP→FCC compared to HCP→BCC in Mg, the CRSS for basal slip in Mg is much larger than that required for prismatic slip. Therefore we predict that the easiest slip in pure Mg to be via prismatic, in support of few earlier experimental results [Ward Flynn *et al* 1961, Ahmadieh *et al* 1965, Tyson 1967], although for deformations carried out above 450K. Due to the reactive nature of Mg, it is likely that the presence of impuries might have led to so many experimental studies which found basal slip to be the dominant deformation mechanism [Yoo *et al* 2002, Agnew *et al* 2001, Munroe *et al* 1997, Couret and Caillard 1985, Hauser *et al* 1956]. Furthermore, in accordance with our predictions on favourable prismatic slip involving decrease in *c*-axis, it is well documented in literature that non-basal deformation modes in Mg include ⟨a⟩-type slip on prism planes [Ward Flynn *et al* 1961, Reed-Hilland and Robertson 1957, Hauser *et al* 1956] as well as twinning on (10-11), (10-13) and (30-34) obtained during compression of single crystals along the *c*-axis [Reed-Hilland and Robertson 1957, Kelley and Hosford 1968, Yoshinaga *et al* 1973].

6.2.3.3 Silcock path: α to ω

It was Frost *et al* (1954) who first encountered the ω phase in aged BCC Ti-Cr alloys that were unexpectedly brittle. The ω phase in elemental Ti and Zr under static pressure was later discovered by Jamieson (1963), who confirmed the results using in situ x-ray diffraction. However, for Ti, hydrostatic pressure studies revealed a range of different onset transformation pressures (2 to 9 GPa) and a large hysteresis in the α to ω transformation [Jayaraman *et al* 1963, Zilbershtein *et al* 1973, Vohra *et al* 1977]. So far, most studies believe the source for onset pressure differences to be impurities in the sample [Zilbershtein *et al* 1973, Vohra *et al* 1977, Sikka *et al* 1982, Greef *et al* 2001, Hennig *et al* 2005,]. Zilbershtein *et al* showed that the pressure at which the transition

occurred depended on whether the sample was continuously loaded or held at a constant pressure: 6 and 4.7 GPa, respectively. On the other hand, Errandonea *et al* (2005) recently conducted static compression tests in a variety of pressure-transmitting-media (PTM) and consequently attributed the scattering of the onset pressures to the variation in the non-hydrostatic conditions in different experiments. Usikov and Zilbershtein (1973) were the first to measure the orientation relations by x-ray examination of the retained ω phase after the release of applied pressure. However, up to now, the few proposed transformation mechanisms for α → ω are still debatable [Silcock 1958, Usikov and Zilbershtein 1973, Trinkle *et al* 2003].

In the current study, we found it difficult to crystallographically link the ω phase observed by Frost *et al* (refered as usual ω) with the α Ti phase. Consequently, the possible relation is established when the usual ω phase shown in figure 6.2.3.3.1(a) is modified to the newly proposed ω shown in in figure 6.2.3.3.1(b) and (c), corresponding to 3 atoms and 1 atom per unit cell, respectively. The space group and lattice parameters of the optimized usual ω phase and the pressure induced new ω phase (figure 6.2.3.3.1(a) and (b)) are the same but the main difference is the positions of the two atoms located not at the origin. For the usual ω phase the atomic positions for the three atoms are (0 0 0), (⅓ ⅔ ½), (⅔ ⅓ ½) while in the proposed new ω phase the atomic positions are (0 0 0), (⅓ ⅔ 0), (⅔ ⅓ 0) with second and third atomic positions equivalent to (⅓ ⅔ 1), (⅔ ⅓ 1). Geometry optimization of the new ω phase yields *a*=4.729, *c*=2.740 Å, *c/a*=0.579 and theoretical density of 4.496 g/cm^3. Based on single-point energy calculations, this phase requires overall pressure of about 4.303 GPa in order to maintain lattice parameter of usual ω phase (*a*=4.584, *c*=2.829 Å, *c/a*=0.617 and theoretical density of 4.634 g/cm^3), comprised of -9.440 and 5.971 GPa X,Y and Z stress tensors corresponding to compression along basal axis and *c*-axis expansion, respectively. The energy differences between the α and the optimized as well as the pressure-induced new ω lattice are 0.3638 and 0.4024 eV/atom, respectively. Thus, following the proposed ω phase, it is clear that the ground-state structure of Ti is α which when subjected to unhydrostatic pressure of 4.303 GPa transforms to new ω phase.

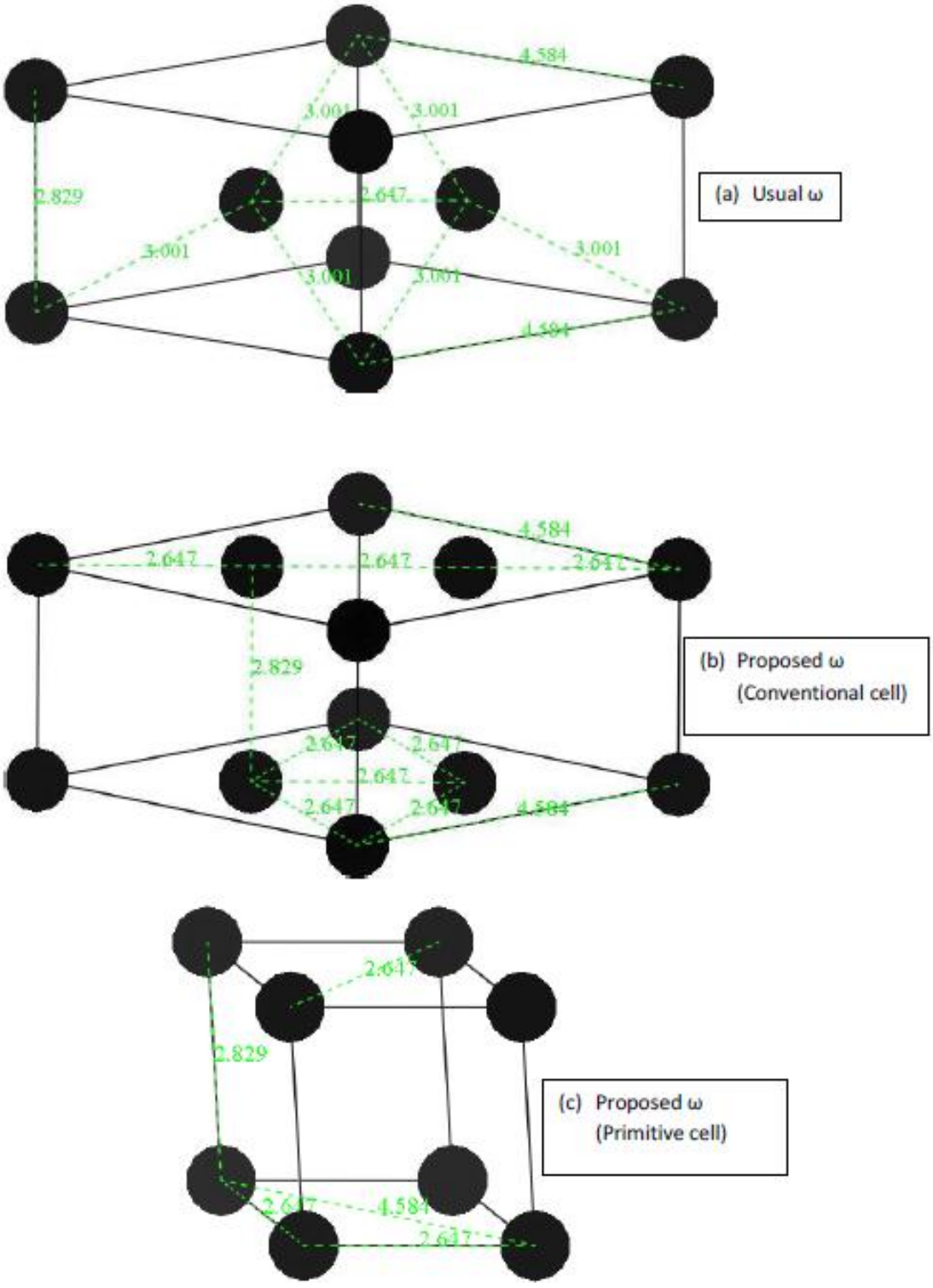

Figure 6.2.3.3.1. The crystal structures of Ti (a) usual ω, (b) conventional proposed ω and (c) primitive proposed ω, phases.

Using the above proposed modification, in figure 6.2.3.3.2 we show a model of compressed α suprecell leading to new ω phase (constructed in red dotted lines). As a result, we propose the orientation relation:

$(0001)_\alpha||(0001)_\omega$, $[11\text{-}20]_\alpha||[21\text{-}30]_\omega$ indicated by blue dotted lines compared to

$(0001)_\alpha||(01\text{-}11)_\omega$, $[11\text{-}20]_\alpha||[10\text{-}11]_\omega$ and

$(0001)_\alpha||(1\text{-}210)_\omega$, $[11\text{-}20]_\alpha||[0001]_\omega$

reported by Usikov and Zilbershtein (1973) and Gray *et al* (1993), respectively. For the pressure driven α → ω phase transition, the deformation involves simultaneous shearing and shuffling of B-layer atoms (⅔ ⅓ ½) with respect to atoms on the A-layer (0 0 0) from (⅔ ⅓ ½) to (1 0 ½), which led to change in lattice parameters (*a* and *c*) from 2.941 to 2.647Å and 4.647 to 5.658 Å respectively, *c/a* (1.58 to 2.14), *x* (⅔ to 1) and *y* (⅓ to 0) atomic fractional coordinates (since the *z* atomic coordinates remain unchanged at ½) at ω lattice. Our model suggests that α → ω phase transition involves compression of basal axes and expansion of *c*-axis.

The resulting lattice parameters *a* and *c* of the distorted HCP lattice are plotted against the corresponding *x* and *y* atomic coordinates in figure 6.2.3.3.3(a), while *c/a* is also plotted against the same *x*-axis in figure 6.2.3.3.3(b). Energy difference (Δ*E*) between distorted and undistorted α phase is calculated with respect to the ground state α phase as well as the required stress (*P*) are also plotted against *x* and *y* atomic coordinates in figure 6.2.3.3.3(c). At ω phase, as shown in figure 6.2.3.3.2, the corresponding lattice parameters of ω and distorted HCP lattices are related by following expressions:

$a_1 = a_2 = a_3$ = 2.647 Å = nearest neighbour distance (NN) in ω phase

$c_\alpha = 2 \times c_\omega$ = 5.658 Å and $(c/a)_\alpha$=2.14 (α refers to distorted),

while a_ω = 4.584 Å = distance perpendicular to [11-20] on the basal plane of distorted α phase.

The calculated energy barrier of 0.4024 eV/atom and the required shear stress (δ) of 5.036 GPa determined from the maximum and minimum, respectively, are presented in figure 6.2.3.3.3(c).

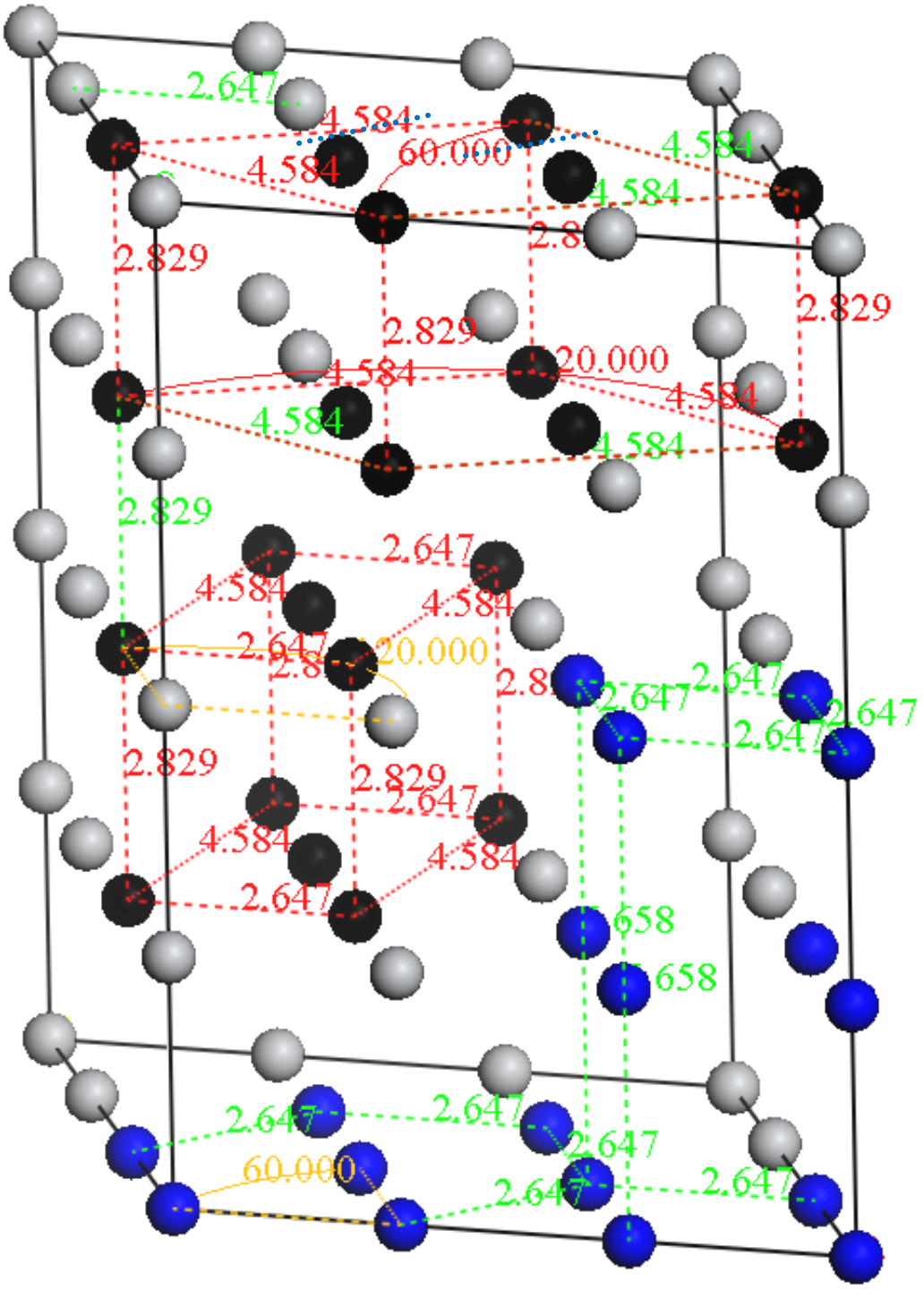

Figure 6.2.3.3.2. A supercell model of compressed α Ti phase leading to the new ω phase constructed in red dotted lines.

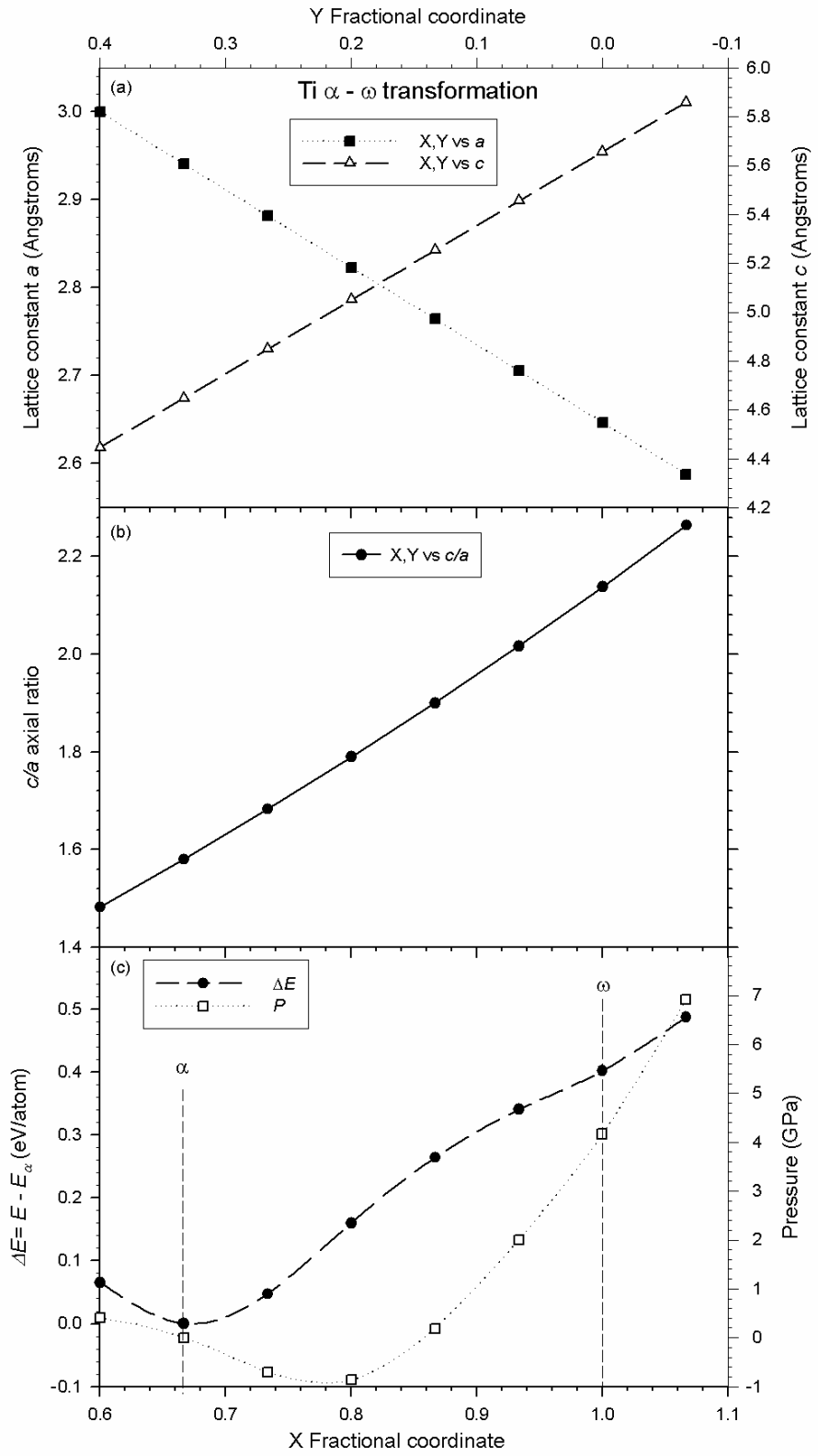

Figure 6.2.3.3.3. Illustration of Ti α→ω phase transformation shown by lattice parameters (a) *a* and *c*, (b) *c/a* as well as (c) change (Δ*E*) and required stress (P) plotted against atomic fractional coordinates corresponding to lattice deformation.

The intermediate phases prior and beyond ω along this α→ ω path are all orthorhombic with space group Cmcm #63 in accordance with experimental results [Akahama *et al* 2001, Vohra and Spencer 2001], similar to that found in α→β path. It seems the first part of the transition path, indicated by negative stress reaching minimum at fractional coordinates X=0.8 and Y=0.2 and lattice parameter a being equal to the atomic diameter of Ti, corresponds to thermally activated dislocation. Beyond this point, the basal axes (nearest neighbour distance) becomes less than the atomic diameter of Ti, hence stress induced deformation begins. Moreover, when the contribution due to expansion is subtracted, the resulting shear stress (δ) amounts to 4.167 GPa, which falls within the range of reported onset transition pressure. The positive value of the required shear stress (δ) indicates the compressive dislocation mechanism. Using equation 6.2.2.1.1, the CRSS for complete α→ω transition in pure Ti is equal to 2.079 GPa when θ = 43.096^{o}, η = 46.904^{o} and m = 0.4989. In addition, our α→ω path is in agreement with Silcock pathway though with slight change in the shuffling distance as follows: in each α stacking plane, three out of six atoms shuffle by 0.764 Å along $[11\text{-}20]_{\alpha}$, while the other three shuffle in the opposite direction $[\text{-}1\text{-}120]_{\alpha}$. The shuffling distance is given by the expression:

$$D_{shuffle} = \tfrac{1}{3}(NN_{\omega} \times \cos 30^{o}) \qquad (6.2.3.3.1)$$

where NN_{ω} is the nearest-neighbour distance in ω, which is equal to 2.647 in our case.

In an attempt to understand the transition around the proposed α→FCC transition around 100 GPa for Ti as shown in figures 6.2.2.1.1 and 6.2.2.1.2, we present in figure 6.2.3.3.4(a)-(b) the comparison of change in energy and pressure for Ti α→ω transition under hydrostatic pressure of 0, 50 and 100 GPa. It is evident from figure 6.2.3.3.4(a) that at 50 GPa the small increase in *c/a* is accompanied by significant increase in shear stress from -0.8688 GPa to about -7 GPa and slight decrease in energy barrier corresponding to atomic fractional coordinates of X=0.8 and Y=0.2. Although the stress is almost zero at ω, the change in energy has increased in comparison to 0 GPa. However, upon applying 100 GPa as shown in 6.2.3.3.4(b), both the energy barrier and stress becomes less but still not yet stable than α phase. This result further supports our earlier proposition that there is α→FCC transition around 100 GPa for Ti as shown in

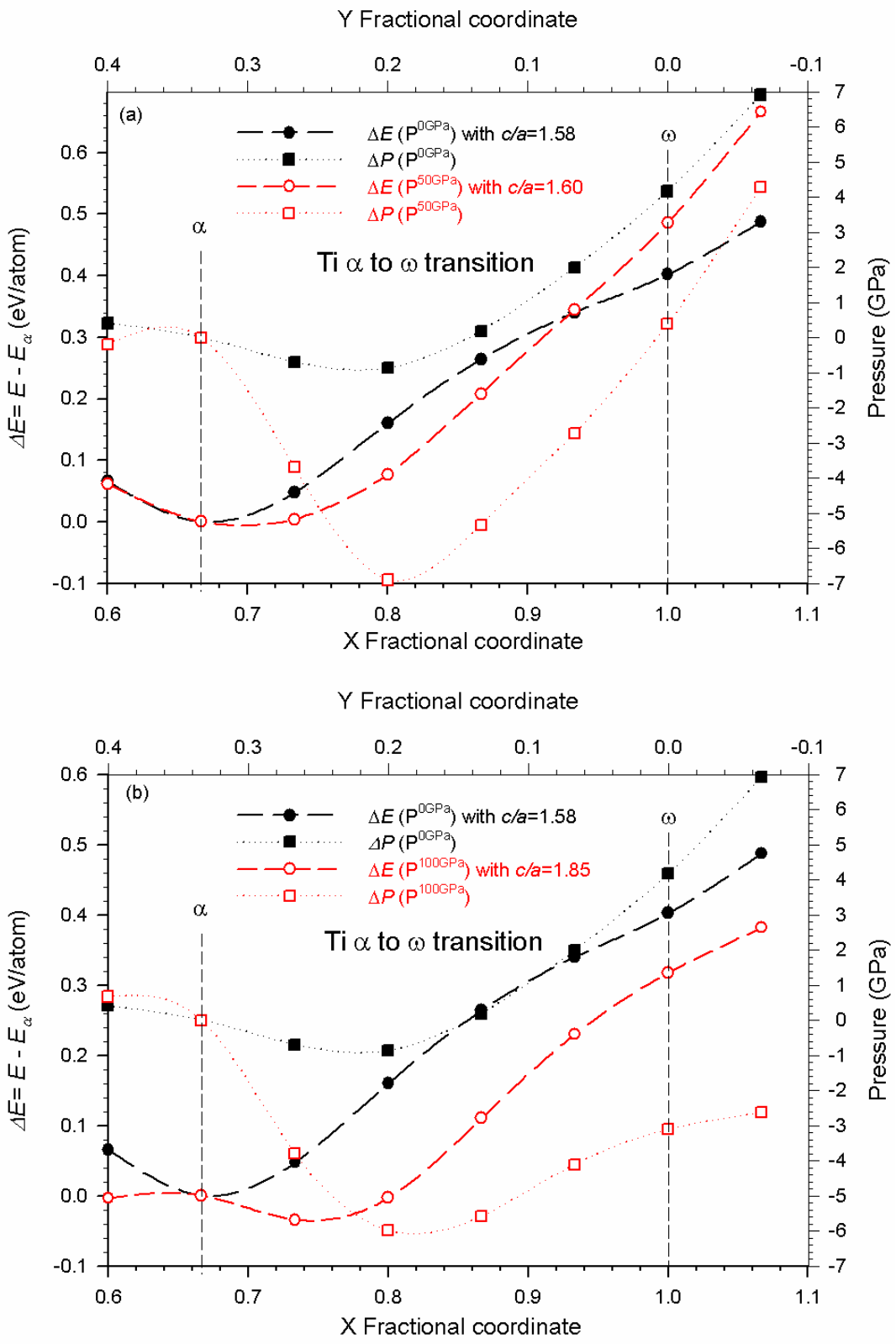

Figure 6.2.3.3.4. Comparison of change in energy and pressure for Ti α→ω transition under hydrostatic pressure of (a) 0, 50 GPa and (b) 0, 100 GPa.

figures 6.2.2.1.1 and 6.2.2.1.2.

6.3. Conclusion

The calculated heats of formation for the hypothetical ordered Ti-Mg phases are positive with maximum at the equi-atomic concentration, thus confirming the inability of Ti-Mg system to form any intermetallic compound.

Our optimization results predict the ω (omega) phase to be the ground-state structure of Ti at 0K and P=0 GPa, in support of other previously reported *ab initio* results. However for the ω phase, current results show no sign of phase transition up to 200 GPa, except for the distinct anomalous behaviour in all Ti phases between 80 and 100 GPa. Since the stability of the alpha (α) phase is surpassed by that of the FCC lattice at about 100 GPa, therefore this anomaly which corresponds with the sudden sharp rise of the *c/a* ratio is attributed to the α → FCC phase transition which involved basal slip. Almost in the same pressure range, the atomic energy of the RHL (#166 R-3m) phase is almost equal to that of FCC phase, although slightly more stable than the FCC above 100 GPa, suggesting a possible further FCC → RHL transition.

Similarly, the crossing of total energy difference curves between FCC and BCC lattices was also observed at 50 GPa for Mg. However, in this case the crossing coincides with the minimum *c/a* around 50 GPa. It is interesting to note that in literature HCP Mg is reported to transform to BCC at this pressure. It may consequently be surmised from our results that the Mg HCP→BCC transition at 50 GPa is *c/a* driven due to a rapid *c*-lattice compression over the *a*-axis owed to the pressure-induced primastic deformation slip. Thus, from current results, the change in *c/a* ratio at applied pressures could be linked to a change in preferred deformation mode prior to any possible phase transition.

As expected, at 0 K and 0 GPa, the E_F lies in a dip (pseudo-gap) of the DOS of the omega (ω) Ti phase, suggesting this phase to be the most stable among other considered phases. It however, cuts through a shoulder of a rising peak in the alpha (α)

phase, showing some level of instability, as is the case for FCC and BCC structures. With pressures below 100 GPa, no significant stability changes in the DOS behaviour are observed, except for the BCC phase which seems to become metastable at around 90 GPa.

Surprisingly, the TDOS plots for Mg indicated the E_F cutting almost at the pseudo-gap in the BCC lattice at 0 GPa as opposed to the expected ground-state HCP phase in which it cuts on a shoulder of a rising peak. A closer look at lower pressures on HCP phase revealed a tendency to stabilize around 10 to 15 GPa. The PDOS for Ti indicates that starting at 250 GPa and above, the *d*-orbital electron occupation which increased gradually with pressure is almost equal in all Ti atoms. On the other hand, the ***p***→***s*** electron transfer is evident in Ti with increase in pressure as indicated by coinciding decrease and increase rates in *p* and *s* orbital fillings, respectively. These changes became rapid between 200 and 250 GPa. Nonetheless, as shown for pressures below 250 GPa, it is sensible to think of possible ***s***→***d*** hybridization in the transition metal. Similarly, the ***p***→***s*** electron transfer is observed at high pressures for Mg, attaining ideal $2p^6 3s^2$ electron configuration at 200 GPa. However, the ***p***→***s*** hybridization that could be linked to HCP→BCC phase transition appears to commence above 200 GPa. Based on free-energy difference curves, this transition is only obtained at 250 GPa, which is exactly 50 GPa above ideal electronic structure, in accordance with experimental observations.

In spite of smaller energy barrier for basal slip in both metals, our proposed martensitic transformation (MT) model predicts that elemental Ti and Mg prefer to deform via prismatic slip as indicated by lower shear stress as well as CRSS values compared to those calculated for basal slip. Current results therefore indicate that the deformation in HCP metals occur via stress-assisted activation as opposed to being solely energy driven (MEP). The proposed (MT) paths for Ti reveal that an increase in *c/a* favours the MEP (minimum energy path) for α→FCC transition observed around 100 GPa. In addition, a new ω Ti phase which is less stable than the α phase at 0 GPa is proposed. Based on this phase, α→ω deformation path, yielding the onset transition pressure of 4.167 GPa is established.

Chapter 7

High pressure effect on ordered Ti-Mg phases

In this chapter, the effect of hydrostatic pressure on the phase stability, elastic and electronic properties of hypothetical ordered Ti-Mg phases is investigated. The positive heat of formation indicates a tendency of the system towards phase segregation, and the negative towards alloying. At zero pressure, the heats of formation predicted for hypothetical ordered phases of Ti-Mg system have positive values, as shown in figure 6.2.1.1.1, thus confirming the immiscibility of the two metals (Ti and Mg) under equilibrium conditions, and in agreement with experiments [Massalski 1990].

7.1 Effect of pressure on phase stability of Ti-Mg intermetallic phases

In figures 7.1.1 to 7.1.4, the heats of formation for few selected hypothetical Ti-Mg intermetallic compounds with lower formation energy values are plotted against high pressures. The formation energies were calculated using two approaches, namely, with respect to (wrt)

(i) the most stable phase (lowest energy) of each metal element at that applied pressure.
(ii) pressure-induced deformation slip or allotropic phase according to anomalous *c/a* axial ratio.

Applying high pressures, our theoretical calculations predict that the heats of formation for ordered phases of Ti-rich Ti_3Mg composition change sign from positive to negative at about 80GPa with respect to *c/a*, as shown in figure 7.1.1(a), while the same could only be achieved at 200 GPa and above with respect to energetically most stable lattice (see figure 7.1.1(b)). It follows from above that if at 80 GPa, in agreement with high pressure experimental studies [Ahuja *et al* 2004], Ti metal transforms to BCC as illustrated by *c/a*

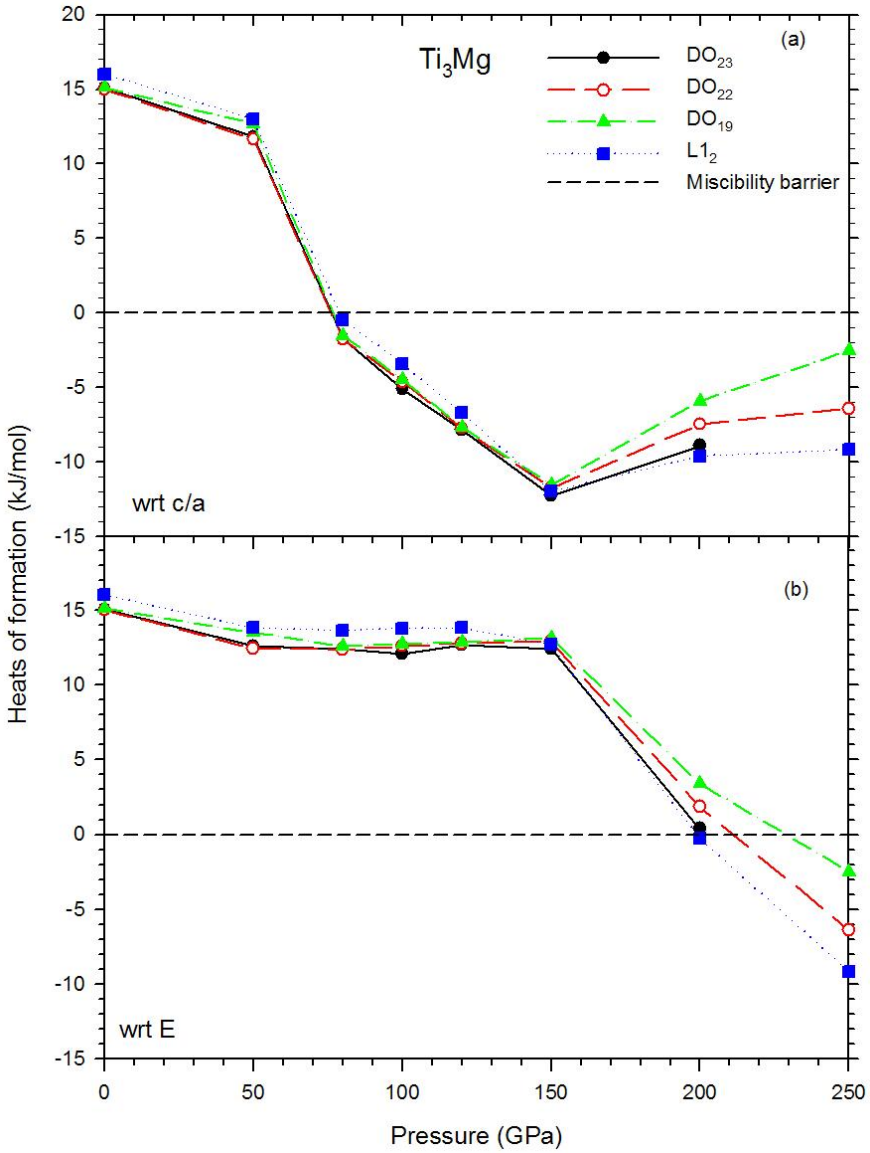

Figure 7.1.1. Formation energies (H_f) of Ti_3Mg-based compounds at various pressures. The top panel (a) shows the H_f calculated with respect to energy of stability according to *c/a* axial ratio, whereas in the lower panel (b) H_f calculated with respect to energy of stable lattice as determined from phase stability energy curves.

behaviour, then the possibility of forming an alloy increases when reacting with also compressed BCC Mg as indicated by transition towards negative heats of formation. Furthermore, it makes sense to think of Ti beginning to transform at about 90 GPa since its bulk modulus is approximated at 110 GPa, hence dislocation of atoms could start below 110 GPa. However, with respect to energetic phase stability the likelihood to form an alloy could only be realised at pressures above 200 GPa where HCP Mg transforms

to BCC and later α Ti to FCC. In figure 7.1.2, the H_f curves of Ti_2Mg and $TiMg_2$-based compounds plotted against pressure are presented. As shown in the top panel (a) the heats of formation of C15 structure started by increasing with pressure until 50 GPa with respect to *c/a* (represented by open squares) and 120 GPa with respect to most stable lattices (denoted by filled squares). Beyond the above mentioned pressures the formation energies decreased sharply towards miscibility barrier line but never crossed it.

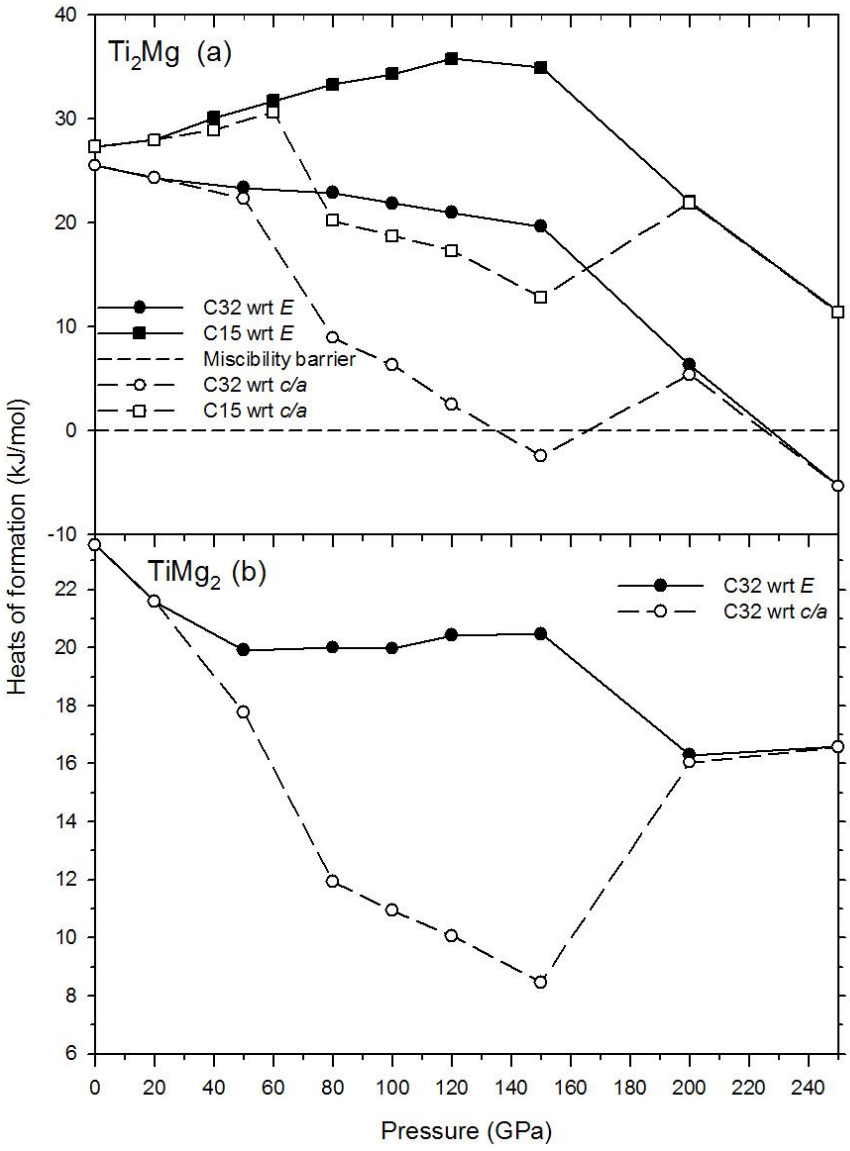

Figure 7.1.2. Formation energies of C15 and C32 phases of Ti_2Mg stoichiometry in the (a) top panel and C32 of $TiMg_2$ composition in the (b) lower panel. Open symbols represent H_f with respect to *c/a* while filled symbols represent H_f with respect to energy (*E*) of stable lattice.

On the other hand, C32 phase followed a similar trend as in C15 but its H_f began by decreasing in the afore mentioned pressure range. Furthermore, the miscibility barrier was crossed at 150 GPa with respect to *c/a* and at 250 GPa in both approaches. A similar behaviour as in the case of C32 with Ti_2Mg was observed in C32 phase with $TiMg_2$ stoichiometry shown in the lower panel (b). However, the energy drop were much sharper than in (a), although the formability state was never reached in this instance.

At 50:50 composition presented in figure 7.1.3, the transition of the most likely B_h and B2 structures towards forming could only be obtained at 250 GPa with respect to elemental lattices with lowest energy (FCC Ti and BCC Mg) , while the B19 phase remains unstable with positive heats of formation of about 3.5 kJ/mol. On the other hand, with respect to *c/a* axial ratio the formability of both structures can be achieved at 150 GPa, after which they become unstable again and follow the trend as followed by the same structures with respect to lattice stability.

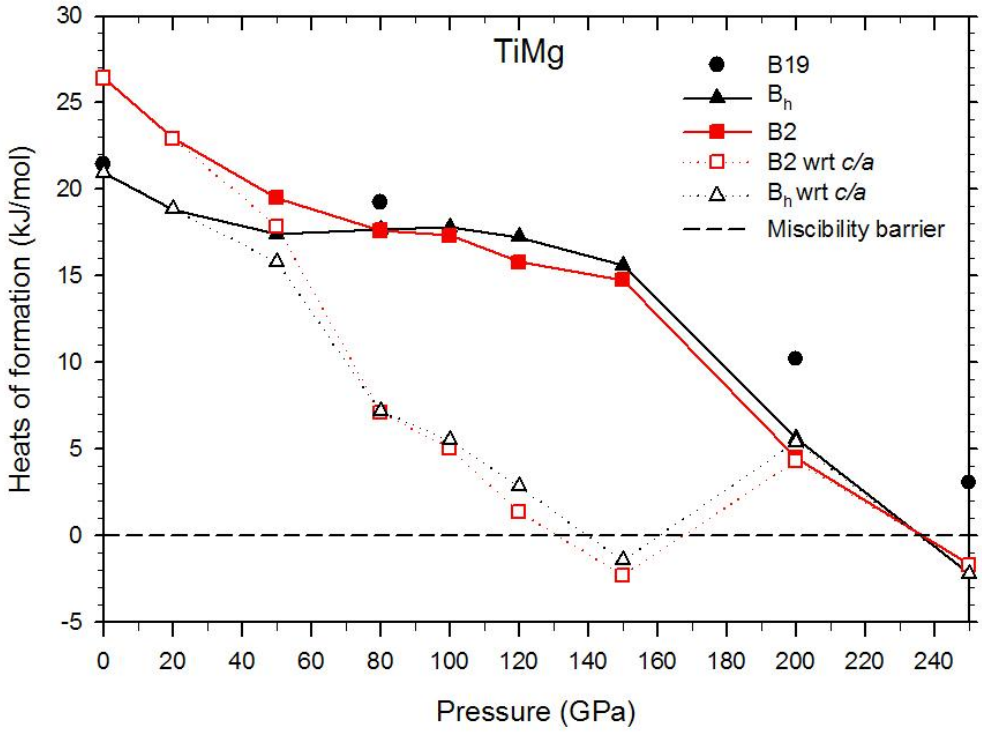

Figure 7.1.3. Formation energies of B19, B2 and B_h structures at equimolar (50:50) TiMg composition. The closed triangles represent the heats of formation of B_h phase with respect to elements with lowest energy, while open triangles represent formation energy calculated from elemental energy of the lattice that is stable according to *c/a* ratio.

A similar behaviour as in figure 7.1.3 is also noticed in figure 7.1.4 for the Mg-rich $TiMg_3$ composition, in which possibility of forming with respect to *c/a* was found above 100 GPa for $L1_2$ and DO_{19} phases while DO_3 remains unstable, but this was lost at much higher pressures between 150 and 200 GPa, as shown in the upper panel (a). However, formability could not be obtained until at 250 GPa pressure at least for DO_{19} phase, with respect to stable lattices presented in the lower panel (b).

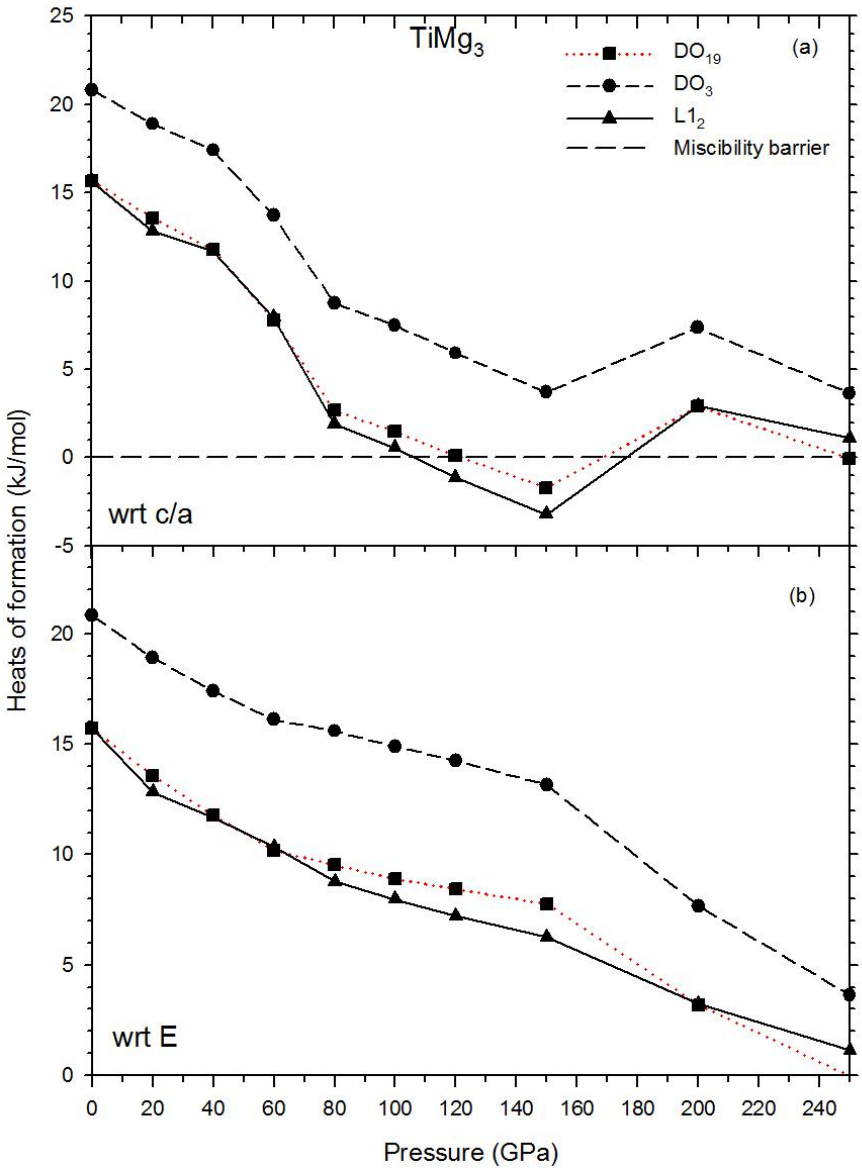

Figure 7.1.4. Formation energies of $TiMg_3$-based compounds at various pressure values. The top panel shows the results calculated with respect to elemental stability due to *c/a* axial ratio, whereas in the lower panel elemental stability is due to energy.

For A_7B and $A_{15}B$-based Ti-Mg compounds, the immiscibility barrier could not be overcome up to 120 GPa with respect to most stable lattices, as shown in table 7.1.1. Owing to high number of atoms involved, which makes computations expensive, calculations for pressures above 120 GPa were not performed. However, it is clear that the H_f of Ti-rich compounds rise with increase in pressure while the opposite holds for Mg-rich alloys.

Table 7.1.1. Predicted heats of formation for A_7B and $A_{15}B$-based Ti-Mg compounds at high pressure.

Pressure (GPa)	Heats of formation (kJ/mol)			
	Ti_7Mg	$TiMg_7$	$Ti_{15}Mg$	$TiMg_{15}$
P=0	13.55	10.27	13.84	7.10
P=80	15.65	8.29		
P=120	18.83	8.12	24.39	5.20

In summary, the region where a sharp energy drop crosses miscibility barrier line indicates that, already at 0K, there is a transition from the tendency towards phase separation between Ti and Mg at zero pressure to the tendency towards alloying at higher pressures, with respect to *c/a* axial ratio. Nonetheless, both approaches (with respect to stable lattice and *c/a*) indicate that forming an alloy from metal elements that are immiscible under equilibrium conditions require either a basal slip or structural change from HCP to FCC in the case of Ti and HCP to BCC or prismatic slip for Mg. Hence, it emerged from the current study that the necessary phase alteration can be obtained by applying high pressure in the region of 100 GPa for most structures. Thus, due to the entropy contribution, the observed miscibility behaviour could be expected to accelerate further at elevated temperatures [Dubrovinskaia *et al* 2005].

7.2 Effect of pressure on elastic properties of Ti-Mg intermetallic phases

In the current chapter, predicted elastic constants will be used to investigate the mechanical stability of few selected hypothetical compounds belonging to Ti-Mg system.

Furthermore, the response of these elastic constants to high pressure will also be studied. However, for the purpose of our study, high pressures elasticity of only simple cubic structures, comprised of few atoms, will be considered since they require less computational resources than complex ones. In this chapter, we will only present elastic properties of considered Ti-Mg hypothetical alloys.

According to our calculations, if the considered Ti-Mg hypothetical intermetallic compounds were to be successfully synthesized, they would have had the elastic properties as listed in table 7.2.1. As shown in table 7.2.1, all the elastic constants of equilibrium Ti-Mg structures, with exception of $TiMg_3$ $L1_2$ cubic phase, obey the corresponding cubic, tetragonal and hexagonal stability conditions as defined in equation 5.3.6.1, 5.3.6.2 and 5.3.6.3, respectively. This is an indication that all of them are mechanically stable. The stability can also be confirmed by providing Poisson's ratio, whose value is usually between -1 and 0.5, corresponding to the lower and upper limits where the materials do not change their shapes. In addition to C_{11} being lower than C_{12} leading to negative tetragonal shear modulus (C'), the instability of $L1_2$ phase with $TiMg_3$ composition is further confirmed by Poisson's ratio value of 0.51 which is greater than the upper limit as well as the negative value of Young's modulus. The bulk modulus increases with Ti concentration, while for stable compounds the Poisson's ratio is low at extreme ends but reaches maximum at 50:50 composition whereas at the same time G is minimum for B_h phase. In general, Ti-rich compounds have higher G than Mg-rich side. Since B_0 is a measure of resistance to volume changed by applied pressure, and shear modulus G, a measure of resistance to reversible deformations upon shear stress, that is, materials with high bulk or shear modulus are likely to be hard materials. Therefore, in order to predict the brittle and ductile behaviour of solids, Pugh proposed the ratio of the bulk modulus (B) to shear modulus (G) to predict the ductility or brittleness of polycrystalline phases [Pugh 1954]. A high (B/G) value is associated with ductility whereas a low value is related to brittleness. The critical value which separates ductile and brittle materials is about 1.75. Following table 7.2.1, besides the $TiMg_3$ compounds with B/G below the critical value, all considered Ti-Mg compounds are ductile as indicated by their B/G value above 1.75.

Table 7.2.1. Predicted elastic properties of Ti-Mg based hypothetical compounds.

Phase	***C_{11}* (GPa)**	***C_{12}* (GPa)**	***C_{44}* (GPa)**	***C_{13}* (GPa)**	***C_{33}* (GPa)**	***$C'=(C_{11}-C_{12})/2$* (GPa)**	***B* (GPa)**	***E* (GPa)**	***G* (GPa)**	υ	***B/G***
Ti_3Mg											
$L1_2$	131	58	51			36	82	95	45	0.31	1.82
DO_{19}	146	53	39	60	138	46	86	113 101	42	0.22 0.30	2.05
DO_{22}	129	70	52	63	137	30	87	84 97	44	0.41 0.32	1.98
Ti_2Mg						42					
C15	124	41	31				69	103	34	0.25	2.03
C32	139	41	41	50	138	49	78	117 110	44	0.19 0.28	1.77
TiMg						6					
B2	78	66	73				70	16	29	0.46	2.41
B_h	113	68	11	23	152	22	67	72 146	22	0.58 0.13	3.04
$TiMg_2$						24					
C15	88	41	23				56	62	23	0.32	2.43
C32	114	33	19	26	109	40	56	102 100	30	0.18 0.17	1.87
$TiMg_3$						-1					
$L1_2$	50	52	52				51	-2	15	0.51	3.40
DO_{19}	102	31	31	18	115	36	50	91 110	36	0.29 0.13	1.39
DO_{22}	112	-1	55	42	70	56	51	78 38	32	- 0.30 0.38	1.59
DO_3	68	43	55			12	51	36	31	0.38	1.64

The calculated high pressure dependence elastic properties of simple cubic phases are presented in table 7.2.2. Following this table, it is evident that the stability at 50:50 and for Ti-rich phases increases with pressure as indicated by rising shear moduli, C_{44} and C'.

Table 7.2.2 Variation of elastic constants with pressure in cubic $L1_2$, C15 and B2 Ti-Mg phases.

Phase	C_{11} (GPa)	C_{12} (GPa)	C_{44} (GPa)	C' (GPa)	B (GPa)	E (GPa)	G (GPa)	υ	B/G
Ti_3Mg ($L1_2$)									
P=0	131	58	51	36	82	95	45	0.31	1.82
P=100	448	330	159	59	369	169	107	0.42	3.45
P=150	564	455	189	54	492	158	115	0.45	4.28
P=250	807	718	254	44	748	131	129	0.47	5.80
Ti_2Mg (C15)									
P=0	124	41	31	42	69	103	34	0.25	2.03
P=80	458	227	92	116	304	308	101	0.33	3.01
P=100	534	274	105	130	360	348	114	0.34	3.16
P=250	1002	621	172	190	748	527	179	0.38	4.18
TiMg (B2)									
P=0	78	66	73	6	70	16	29	0.46	2.41
P=50	252	217	106	18	229	51	53	0.46	4.32
P=100	414	337	141	39	363	112	84	0.45	4.32
P=150	530	475	153	28	493	81	78	0.47	6.32
P=250	781	703	205	39	729	114	107	0.47	6.81
$TiMg_2$ (C15)									
P=0	88	41	23	23	56	62	23	0.32	2.43
P=100	312	367	8	-27	349	-84	5	0.54	69.8
P=250	644	752	-112	-54	716	-166	-84	0.54	
$TiMg_3$ ($L1_2$)									
P=0	50	52	52	-1	51	-2	15	0.51	3.40
P=80	265	311	174	-23	296	-70	12	0.54	24.67
P=100	310	370	192	-30	350	-93	2	0.54	175
P=150	408	512	218	-52	477	-161	-46	0.56	
P=250	601	772	220	-86	715	-267	-209	0.56	

It is also clear from values of *B/G* ratio that the ductility is also improving as a function of pressure, as again shown by increasing Poisson's ratio. In addition, the bulk and Young's moduli as well as the Posson's ratio also increase with pressure. Furthermore, in addition to *B/G,* Poisson's ratio is also correlated with ductility of crystalline alloys and could also be utilized as the first screening tool to predict ductility.

In cubic Mg-rich compounds below 50 at.% Ti, conversely, the stability is negatively affected (suffers) by increase in pressure. This is indicated by continuous declining shear moduli *C'* and *G* in addition to Poisson's ratio larger than 0.5, since C_{44} increases for $L1_2$ $TiMg_3$ but decreases in C15 $TiMg_2$. It is also apparent that the only Ti-Mg compound that behaves isotropically is C15 structure with $TiMg_2$ composition, since all shear moduli C_{44} , *C'* and G are equal.

7.3 Effect of pressure on electronic structure of Ti-Mg intermetallic phases

7.3.1. Total density of states (TDOS)

The TDOS for $L1_2$ structures of Ti_3Mg (top panel) and $TiMg_3$ (lower panel) compounds at different pressures are presented in figure 7.3.1.1. For both compounds, the pseudo-gap is above the Fermi level (E_F) in the conduction band (CB) and the E_F cuts the DOS on the shoulder of a dropping peak of the valence band (VB) at P=0. However, a clear distinct behaviour is observed when the structures are subjected to high pressure. In the top panel (Ti_3Mg), the E_F shifts towards the pseudo-gap with increasing pressure and eventually falls in the dip at 100 GPa. In addition to the falling DOS, beyond 100 GPa the E_F is positioned above the pseudo-gap, which is now shifted in the VB. On the other hand, the pseudo-gap shifts to the right (higher energies) with increasing pressure and the two main peaks are thus split further in the lower panel. The E_F continued to cut the DOS closely to the peak. It could be concluded that high pressure continues to de-stabilize the $L1_2$ phase of $TiMg_3$ as opposed to possible stability achieved in Ti_3Mg.

In figure 7.3.1.2, the TDOS for C15 and C32 Ti_2Mg phases are presented in the top and lower panels, respectively. At equilibrium, the total DOS shapes for both structures appears almost similar, with E_F cutting the top of the main peak but in C15 the DOS drops flat at about 4 eV. In addition to shifting the energy where DOS falls to zero from 4 eV to 5 eV, the pressure of 40 GPa on C15 Ti_2Mg structure splits the main DOS peak

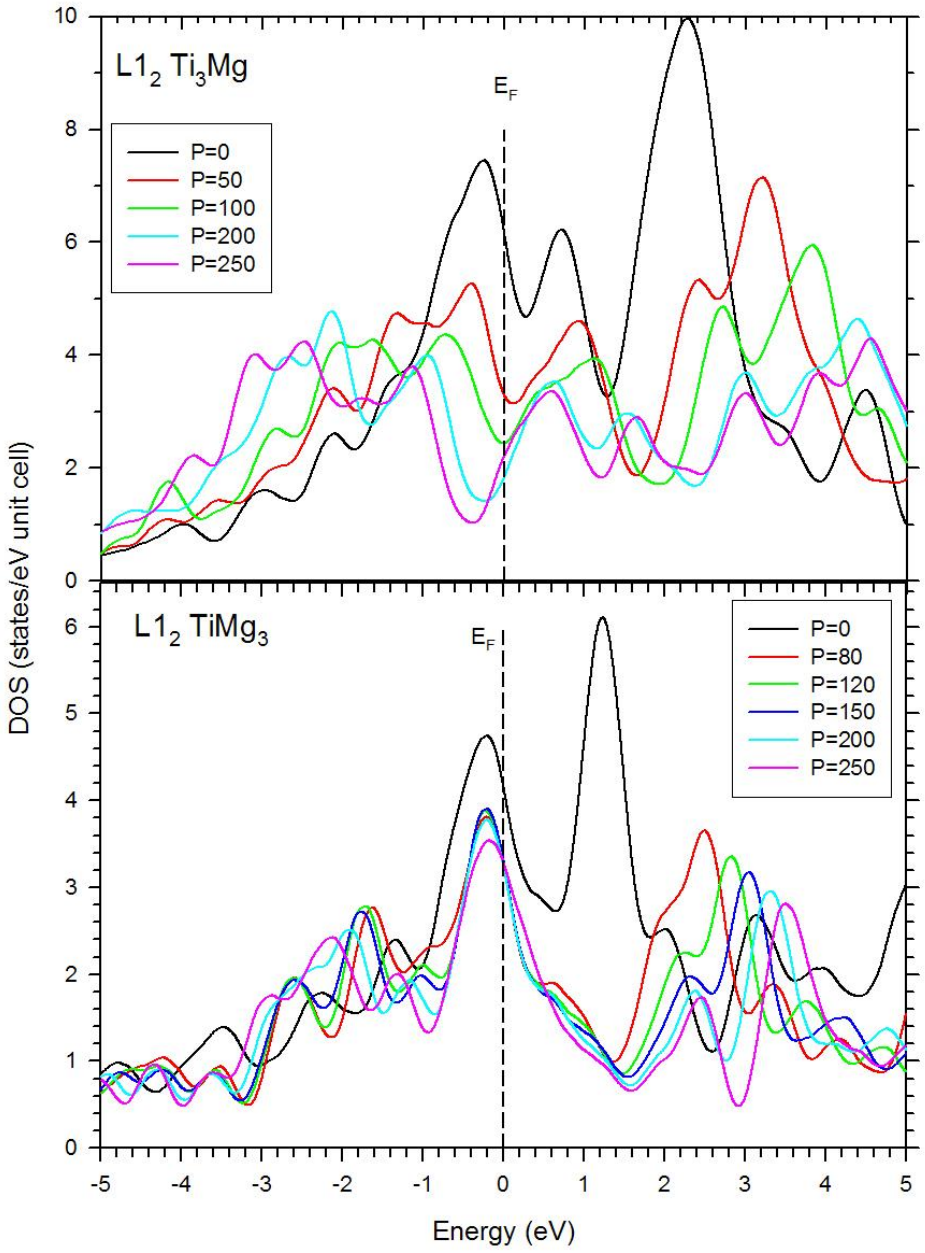

Figure 7.3.1.1. The TDOS curves for $L1_2$ structures of Ti_3Mg (top panel) and $TiMg_3$ (lower panel) at different pressures.

at E_F into two and E_F cuts exactly on a dip separating them. In first-principles calculations, this behaviour is correlated to phase stability. Although occurring at lower DOS, a similar trend also prevailed at much higher pressures. The behaviour of the DOS for C32 phase at high pressures, as shown in the lower panel, somehow closely resembles that of C15 but quite slowly. As an example, the DOS behaviour at 50 GPa in

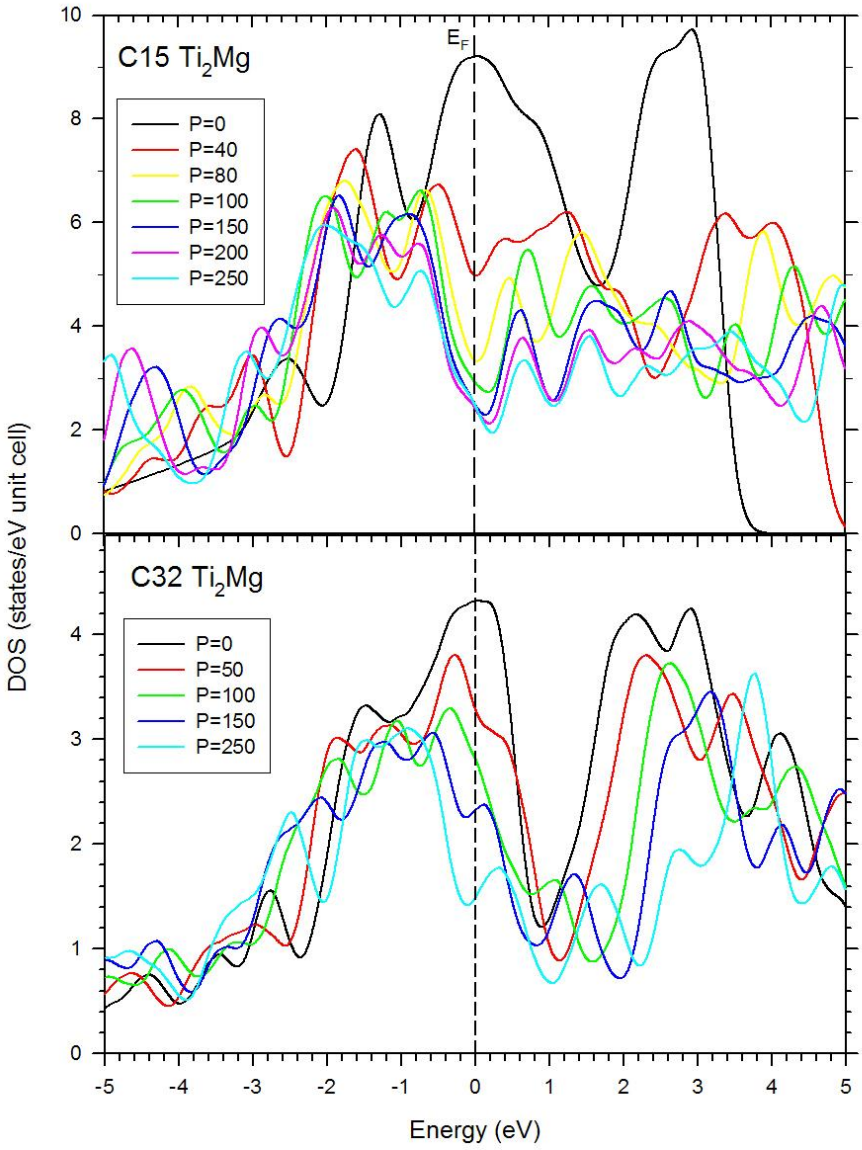

Figure 7.3.1.2. The TDOS curves for C15 and C32 Ti_2Mg structures at different pressures are presented in the top and lower panels, respectively.

C32 phase is almost common to that of C15 at 0 GPa, while that at 250 GPa is very similar to C15 phase at 50 GPa.

The TDOS for 50:50 TiMg alloy are shown in figure 7.2.1.3. In the top panel, the DOS for B2 structure are shown, in which at 0 GPa the Fermi level (E_F) cuts the total DOS on the shoulder of a dropping peak in the valence band (VB), much closer to the pseudo-gap. With increasing pressure the highest peak of B2 phase in the conduction band

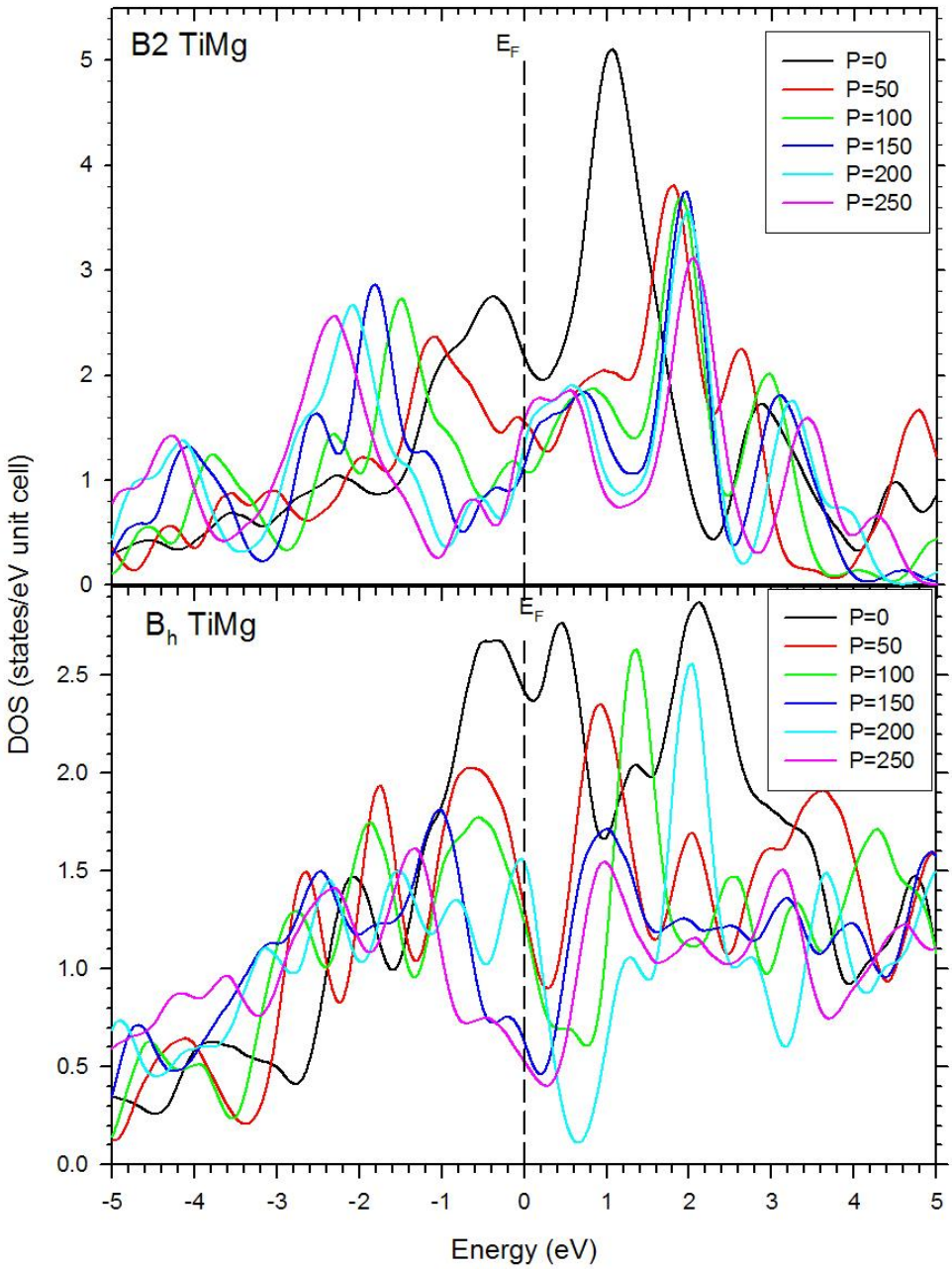

Figure 7.2.1.3. Total density of states curves for B2 and B_h structures of TiMg at different pressures.

(CB) shifts to the right while that in the VB shifts to the left towards the core shell. However, in both bands the pseudo-gap (minima) drops towards empty states (energy axis) with increasing pressure. For B_h structure, the Fermi level cuts almost between two intense peaks at 0 GPa, which got split as a result of applying high pressure. At high pressures, these peaks are much further apart. However, at 150 GPa a unique behaviour is observed, at which the E_F dissects a single sharp peak into two halves.

7.3.2. Partial density of states (PDOS)

As shown in figures 7.3.2.1 to 7.3.2.4 for Ti_3Mg ($L1_2$), $TiMg_3$ ($L1_2$), B_2 and B_h TiMg, respectively, an apparent electron transfer from Mg to Ti due to pressure seems to favour $L1_2$ Ti_3Mg stability whereas the opposite favours instability of $L1_2$ $TiMg_3$ phase, in agreement with heats of formation, elasticity, and DOS stability trends. The elemental TDOS behaviour for both Ti and Mg in B2 are similar to that in $L1_2$ Ti_3Mg, while for B_h is common to that in $L1_2$ $TiMg_3$ structure. The overall decrease in electrons per state in Mg is influenced by its *p*-electrons while an increase is due to *s*- electron filling. On the

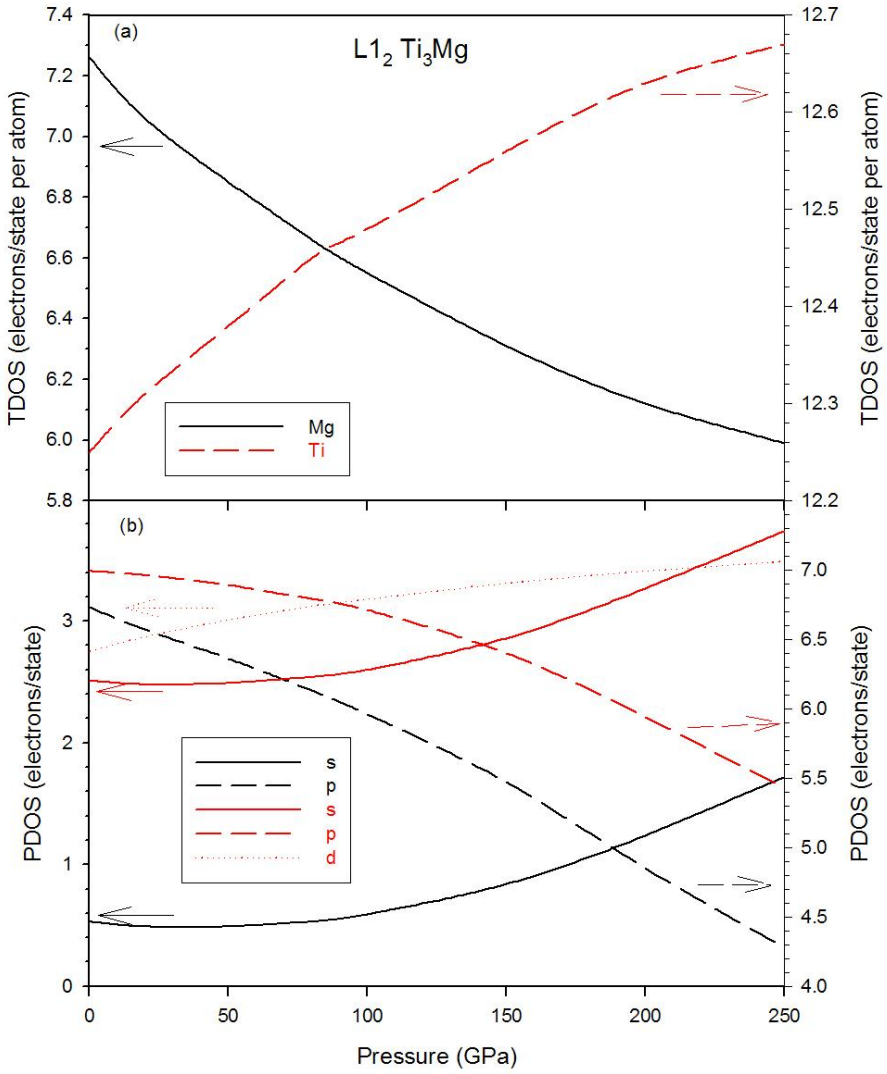

Figure 7.3.2.1. PDOS curves indicating electronic contributions by individual elements in $L1_2$ Ti_3Mg.

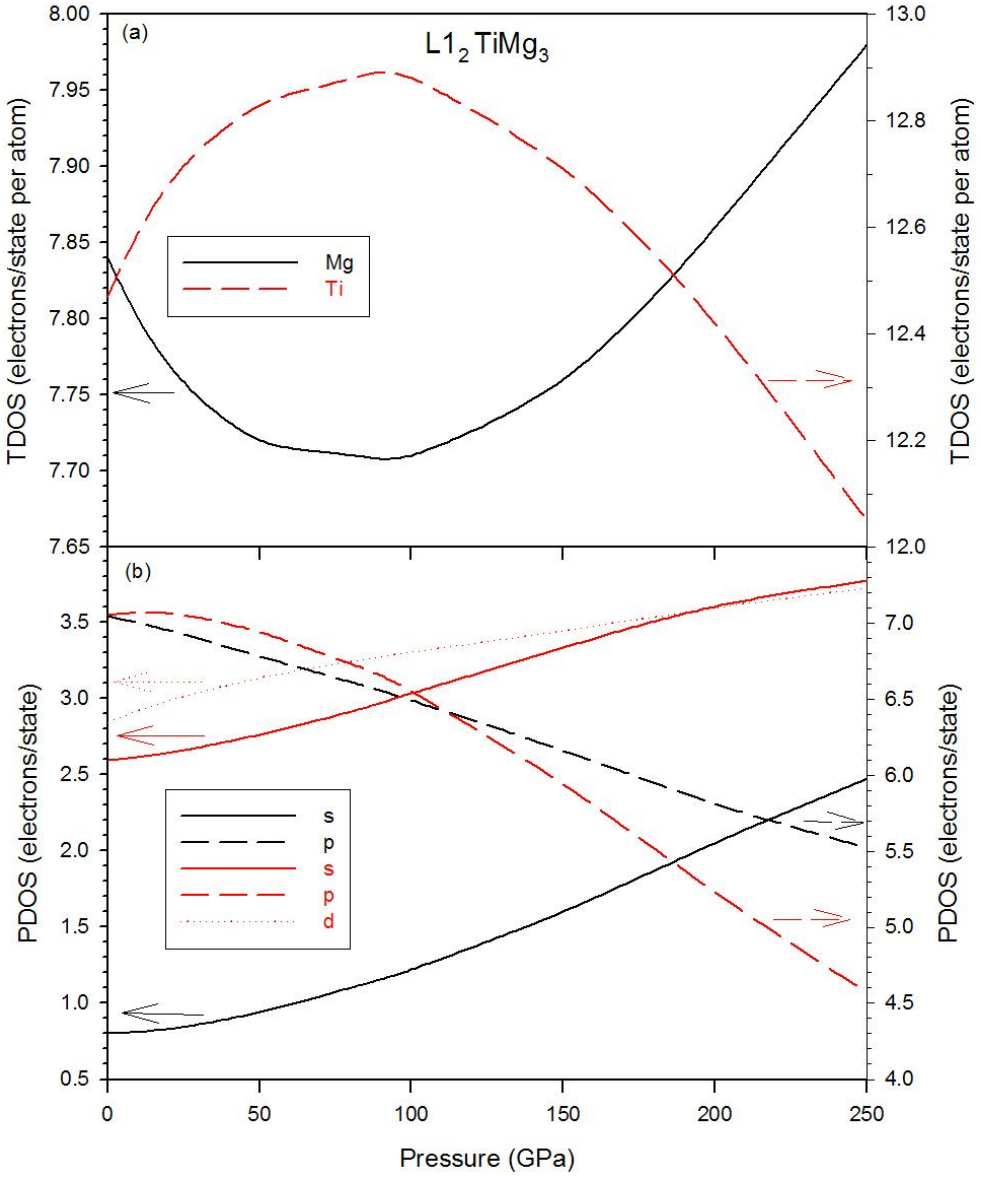

Figure 7.3.2.2. PDOS curves indicating electronic contributions by individual elements in $L1_2$ $TiMg_3$.

other hand, an increase in the total electrons of Ti is due to contribution of *s*- and *d*-orbital filling while a decrease is due to drop in *d*-electrons with increasing pressure.

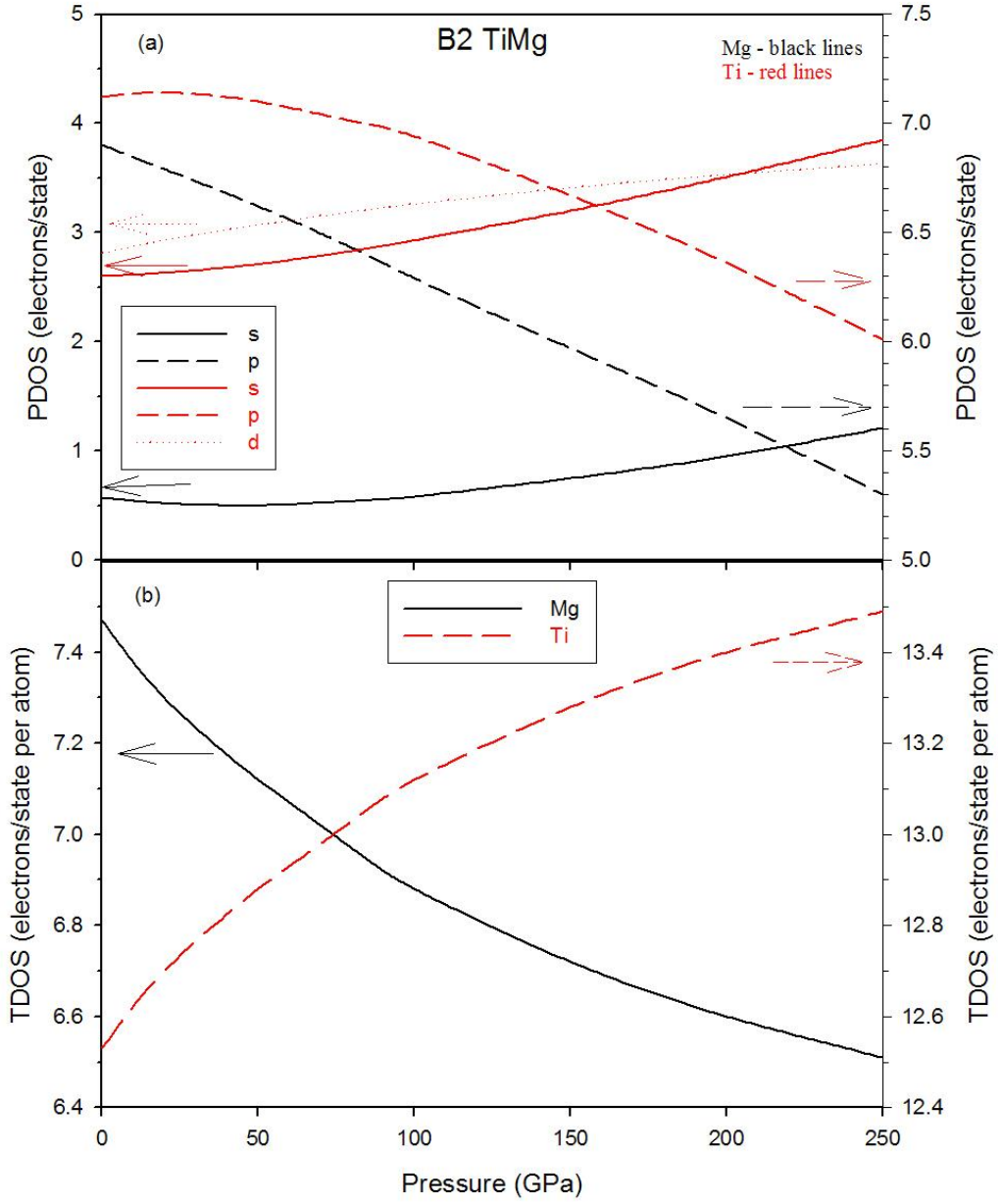

Figure 7.3.2.3. PDOS curves indicating electronic contributions by individual elements in B2 TiMg compound.

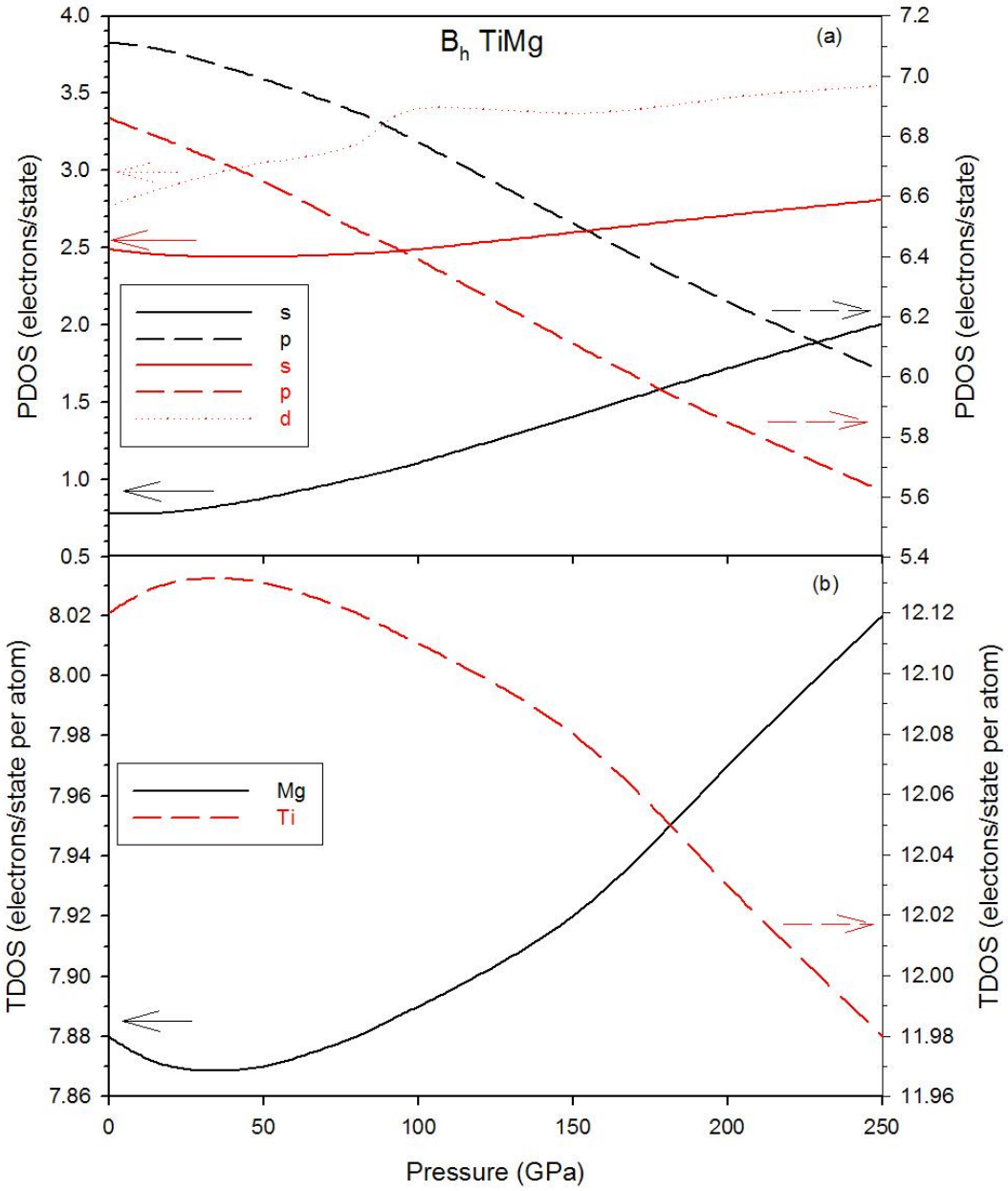

Figure 7.3.2.4. PDOS curves indicating electronic contributions by individual elements in B_h TiMg compound.

7.4 Conclusion

In summary, using calculated heats of formation, elasticity and DOS, it has been possible to show that $L1_2$ $TiMg_3$ could not form even at as high pressure as 250 GPa. Generally, it is evident that at high pressures Mg tends to donate electrons to Ti ($L1_2$

Ti_3Mg and B2 TiMg) while for $L1_2$ $TiMg_3$ and B_h TiMg this only happens in the range 0-100 and 0-50 GPa, respectively. Above this range, the behaviour takes the opposite route, hence the difficulty in electronic structure stability. A decrease in electrons with increasing pressure is noted in the *p*-orbital of Mg while an increase is associated with *s*-orbital behaviour. Thus in general, the DOS for formable alloys are characteristic of a strong hybridization between *d*-states of Ti, which act as an electron acceptor and *s*-states of Mg, which act as an electron donor. In compounds where this electron transfer does not occur, it is apparently difficult to stabilize them or for them to cross the miscibility barrier. Therefore, since the estimated pressure (in literature) that could build-up during ball milling due to the impact forces exerted by the grinding medium on the powders is limited to less than 10 GPa [Maurice and Courtney 1990], our predictions suggest that no intermetallic Ti-Mg phase could form by this process.

Chapter 8

Solid solutions: pseudo-atom approach of disordered Mg_{100-x}-Li_x alloys as a test case

"Combining one metal with another leads to a range of alloys with properties superior to each individual end member. Since the Bronze and Iron Ages, the quest for new metallic alloys through various chemical and metastable quenching paths has played a crucial role in the advancement of civilizations. The most common type of alloy is a substitutional crystalline solid solution in which atoms of one element randomly substitute for atoms of another element in a crystal structure." [Zeng *et al* 2009]

8.1. Mg-Li system: a test case for pseudo-atom approach for random alloys

8.1.1. Introduction

Currently, the development of Mg alloys with desirable physical and mechanical properties with remarkable weight saving applications remains a challenge. If the development of these alloys follows a path similar to Al alloys, using traditional trial and error methods and techniques, it would require a similar level of effort of many years. Fortunately, parallel to the development in solid-state physics, where computational physics has developed into a respected branch of scientific investigation after classical experiment and theory; atomistic modeling and simulation has become a maturing tool in materials science and particularly for the investigation of the mechanical properties of materials. Several developments in the recent past have made the atomistic approach increasingly more attractive [Li *et al* 2003]. As a result, *ab initio* density functional theory (DFT) methods provide an opportunity to drastically accelerate materials research by efficiently predicting new phases and accurately describing their ground states [Uesugi

and Higashi 2005]. Despite massive experimental efforts dedicated to binary Mg-Li alloys in the past [Grube *et al* 1934, Hume-Rothery *et al* 1945, Barett and Trautz 1948, Jackson *et al* 1949, Freeth and Raynor 1953, Levinson 1955, Jones and Hogg 1956, Herbstein and Averbach 1956a, b, Mashkovetz and Puchkov 1965, Kelley and Hosford 1968, Lynch, and Edwards 1970, Chakravorty 1994, Furui *et al* 2005, Chang *et al* 2006, Bialobrzeski *et al* 2007, Wu *et al* 2009; 2010, Pezda 2009, Meng *et al* 2009, Qu *et al* 2010], only few investigations has been carried out in the last few decades via various theoretical methods [Hafner 1976, Punz and Hafner 1987, Vaks and Trefilov 1988, Salo and Kokko 1993, Rajput *et al* 1993, Korzhavyi *et al* 1995, Sahu 1997].

Recently, *ab initio* calculations have concentrated on gaining a detailed knowledge of the electronic structure of materials and its effects on microscopic and macroscopic behaviours [Ducastelle 1991, Turchi 1995]. Considering these simulation advantages, the theoretical *ab initio* studies on Mg-Li system have received much attention in recent years [Uesugi *et al* 2000, 2001, Anusionwu 2002, Counts *et al* 2008, 2009, Phasha *et al* 2010a, Liang and Gong 2010, Taylor *et al* 2010]. The work by Uesugi *et al* focused only on HCP Mg_7Li alloy (#194 $P6_3/mmc$) in which the γ=120° angle was also varied in attempt to stabilize it but the symmetry deviated from that of HCP [Uesugi *et al* 2000; 2001]. On the other hand, Counts *et al* recently determined the mechanical properties of B2 (#221 Pm-3m) type Mg-Li alloys spanning the entire concentration range using the supercell approach [Counts *et al* 2008, 2009]. More recently, several researchers reported phase stability of ordered binary Mg-Li alloys in HCP, FCC, BCC lattices using different *ab initio* simulation packages [Phasha *et al* 2010a, Liang and Gong 2010, Taylor *et al* 2010].

Despite such immense efforts dedicated at understanding fundamental properties of Mg-Li alloys in the last decade, the above theoretical investigations were carried out on intermetallic phases rather than on solid solutions (random alloys). Furthermore, to study small additions of Mg and Li to pure Li and Mg metals respectively, by applying current theoretical methods on ordered phases requires large supercells containing many atoms thus making these calculations computationally expensive. Although a

comparison of energy between HCP-, FCC- and BCC-based intermetallic compounds could give a reasonable picture about phase stability, the mechanical properties thereof could be different from those of random alloys since they depend strongly on crystal structure and corresponding symmetry. Our aim is to use Mg-Li system to show and develop an *ab initio* approach that can accurately predict phase stability and mechanical properties of solid solutions (random alloys) spanning the entire concentration range and generating results that are comparable to experiment while maintaining both correct crystal structure and symmetry. As result, in the current study, we propose a new approach which allows systematic investigation of random alloys spanning the entire composition range in HCP, FCC and BCC lattices. In this method, only the atomic composition including very small additions is altered while both the crystal lattice and symmetry are maintained. This approach for disordered alloys is applied to Mg-Li system as a test case, since there is sufficient experimental data for validation. In the next chapter the approach will be extended to Ti-Mg system where experimental information is not equally abundant.

8.1.2. Methodology

8.1.2.1. Background

In this work, a random solid solution with BCC, FCC and HCP crystal structures are represented by a model shown in figure 8.1.2.1.1 (a), (b) and (c), respectively. Ideally using this model, Mg-Li solid solution may be formed when an atom of Mg or Li occupy randomly any position in the crystal, thus only changing the composition. Thus by maintaining correct symmetry and crystal structure as reported in experimental data [Massalski 1992], the composition can be varied by representing atoms as a fractional composition, $A_{100-x}B_x$. This type of pseudo alloy atom was earlier proposed by Tanigawa and Doyama using perturbation theory pseudopotentials on Cs-K and Cs-Rb disordered alloys [Tanigawa and Doyama 1972, 1973], and later applied to study Li-Mg solid solutions by Hafner [Hafner 1976]. However, despite linear variation of lattice constant with composition, the calculated heats of solution were all positive in Cs-K and Cs-Rb

systems that are known to have complete miscibility. Similarly results were reported by Iñiguez *et al* (1981, 1982), who studied theory of heats of formation and volume of formation in several homovalent disordered solid alloys formed by two alkali metals and two alkali-earth metals using the hybrid density functional pseudopotential (DFP) method. Using the improved perturbation theory in the pseudopotential, Vaks and Trefilov (1988) investigated the effect of proximity of the Fermi surface (FS) to a singularity in the electron state density (SDS) on atomic properties of a nearly free-electron metal. They further illustrated the character of the small distances between the FS and BZ (Brillouin zone) face dependence of atomic properties by model calculations for disordered $Li_{1-x}Mg_x$ alloys in the BCC, FCC and HCP structures. On the other hand, Madelung energy and other thermodynamic properties of random Li-Mg metallic alloys in the conventional single-site coherent

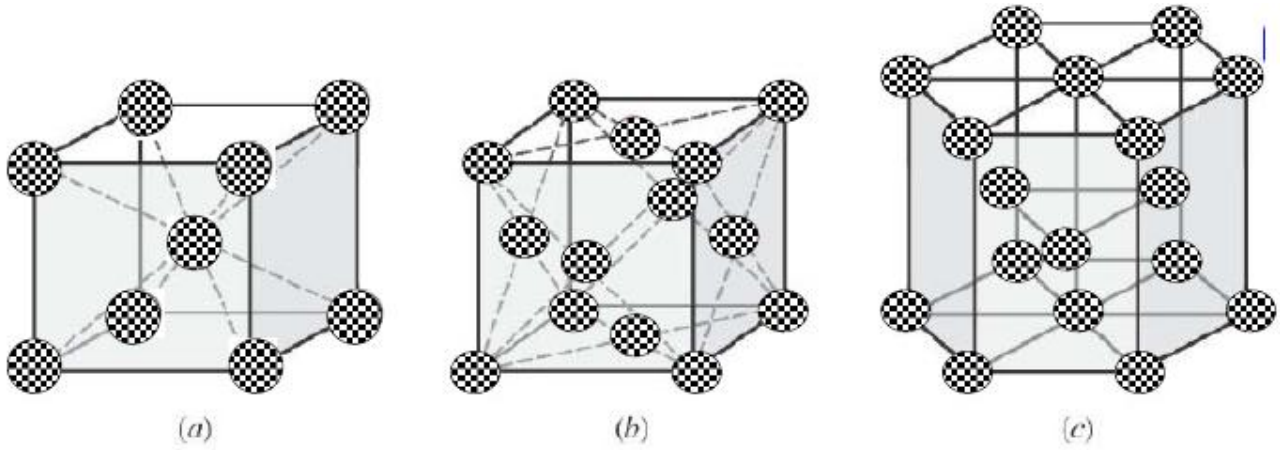

Figure 8.1.2.1.1 Representation of (a) BCC, (b) FCC and (c) HCP pseudo-binary solid solutions ($A_{1-x}B_x$) comprised of pseudo atoms. Every atom consists of the overall fractional composition of the solid solution.

potential approximation (CPA) were studied by Korzhavyi *et al* (1995). Contrary to the above methods, the current proposed approach seeks to use density functional theory formalism to mimic structural (equilibrium lattice constants, cohesive energy, heats of formation) and elastic properties of random Mg-Li alloys in the HCP (#194), FCC (#225) and BCC (#229 structures with space group $P6_3/mmc$ (#194), Fm-3m (#225) and Im-3m (#229), respectively.

8.1.2.2. Computational procedure

Current *ab initio* calculations were performed using the well-established total energy code, CASTEP [Segall *et al* 2002], which has been described in details in preceding two chapters. Geometry optimization calculations were carried out using cut-off energy of 500 eV and k-points of 19x19x10 for HCP and 18x18x18 for FCC and BCC phases. Choice of denser k-points did not yield any significant difference. In this case, the hard norm-conserving pseudopotentials of Kleinman-Bylander (1982) were employed to describe the electron-ion interaction. Hence very dense k-points were used. We employed convergence criterion of less than 5 x 10^{-6} eV on total energy per atom, maximum displacement of 5x10^{-4} Å, residual forces of 3 x 10^{-2} eV $Å^{-1}$ and 0.02 GPa on the residual bulk stress. For each crystal structure, the geometry optimization was performed to obtain the equilibrium structural properties, from which the elastic constants were computed as described below.

8.1.2.3. Numerical details

8.1.2.3.1. Cohesive and formation energy

The cohesive (binding) of the pure elements and pseudo element or solid solution ($A_{1-x}B_x$) alloy was computed according to the relation [Sahu 1997, Zhang *et al* 2009]

$$E_{coh}^{A} = \frac{1}{n} E_{tot}^{solid} - E_{tot}^{atom} \qquad (8.1.2.3.1.1)$$

where E_{tot}^{solid} is the total energy of the element (Mg and Li) or pseudo element ($Mg_{100-x}Li_x$) in their ground-state crystal structures and E_{tot}^{atom} is the total energy of free atom (Mg and Li) or pseudo-atom ($Mg_{100-x}Li_x$), respectively. The fractions indicate the total number of atoms of constituent species in the unit cell, usually referred to as fractional composition. Energy of a free atom is calculated by creating a supercell (P1 symmetry) with lattice parameter a=10 Å and placing an atom or pseudo atom at the center.

On the other hand, the formation energy, ΔH, of the disordered solid solution is computed according to the relation:

$$\Delta H = E_{coh}^{Mg_{100-x}Li_x} - [(1-x)E_{coh}^{Mg} + xE_{coh}^{Li}] \qquad (8.1.2.3.1.2)$$

where E_{coh}^{Mg} and E_{coh}^{Li} are the cohesive energies of elemental Mg and Li in their respective ground-state crystal structures. The fractional (atomic) composition of element B is represented by x. It thus follows from the above expressions (8.1.2.3.1.1) and (8.1.2.3.1.2), that the formation enthalpy of a solid solution depends on the cohesive energy of materials.

8.1.2.3.2. Elasticity

The stress-strain relation may be used to distinguish the elastic and plastic regimes of solid materials [Ghosh and Olson 2002]. The elastic moduli are the fundamental physical parameters which establish the stress-strain relation in the elastic regime. For an isotropic polycrystalline solid, the two independent elastic parameters are the bulk modulus (*B*) and the shear modulus (*G*). On the other hand, the resistance of solids to plastic or permanent deformation is governed by dislocation motion and may be expressed via the yield stress or mechanical hardness. The hardening mechanism in alloys, which arises from disturbances in the lattice caused by the solute atoms in the matrix, is often described by the classical Labusch-Nabarro model [Labusch 1972, Nabarro 1977]. Furthermore, the ratio of *B* to *G* is used to describe the brittleness and ductility of metal. High (low) *B/G* ratio corresponds to ductile (brittle) material. Of importance in metallurgy is how the solute atoms affect the elastic properties of α Mg.

Further details on elastic properties of solid crystals are given in chapter 5 (5.3.6). The anisotropy for hexagonal crystal is calculated as follows:

$$A_1 = 2C_{44}/C_{11} - C_{12} = C_{44}/C_{66},\ A_2 = C_{33}/C_{11},\ A_3 = C_{12}/C_{13} \qquad (8.1.2.3.2.1)$$

For an elastically isotropic hexagonal crystal, the three anisotropy ratios (A_1, A_2 and A_3) must be simultaneously equal to unity [Olijnyk and Jephcoat 2000].

8.1.3. Results and discussions

8.1.3.1. Structural properties

In figure 8.1.3.1.1, the predicted equilibrium (T= 0K, P= 0 GPa) lattice parameters of HCP $Mg_{100-x}Li_x$ solid solutions, the corresponding theoretical densities (ρ) as well as the lattice parameters of cubic-based counterparts, all plotted against Li atomic composition, are presented in (a), (b) and (c), respectively. As expected, the norm-conserving pseudopotentials have underestimated the lattice parameters of pure Li more than those of Mg and as a result a slightly higher density is predicted [Hafner 2000]. Despite the underestimation, an interesting trend of lattice parameter *a* and *c* with Li variation is noticed, as shown in figure 8.1.3.1.1(a). First, the lattice parameter *c* (indicated by empty circles) decreased with Li addition as expected, but only up to 15 at.%. On the other hand, the lattice parameter *a* surprisingly increased with introduction of Li for up to the same concentration, 15 at.%. This anomalous behaviour of lattice parameter *a* resulted in a decrease in *c/a* ratio reaching a minimum at 15 at.% Li, as shown in figure 8.1.3.1.1(b). However, the established trends for *c/a* ratio within this concentration range leading to high temperature HCP→BCC phase transition is in excellent agreement with theoretical [Vaks and Trefilov 1988] and experimental results [Hauser *et al* 1956, Agnew *et al* 2002, Becerra and Pekguleryuz 2008]. In the work of Vaks and Trefilov, the minimum was observed at Li concentrations between 60 and 70 at.%. Although Mg HCP→BCC transition on Li addition has been a subject of research for many years [Hauser *et al* 1956, Kelley and Hosford 1968, Vaks and Trefilov 1988, Agnew *et al* 2002, Kral *et al* 2007, Becerra and Pekguleryuz 2008], it is for the time that this phenomena is presented with such accuracy using theoretical methods. This behaviour of a decrease in the axial ratio (*c/a*) as a function of Li content which led to activation of prismatic <a> slip was earlier observed by Hauser *et al* (1956), but explained by Agnew *et al* (2002) for the improved ductility at maximum solid-solubility limit of 15 at.% Li while Kelley and Hosford (1968) reported the lowering degree of anisotropy. Furthermore, the α region of Mg-Li system was more recently investigated by Becerra and Pekguleryuz (2008), who also concluded that the addition of

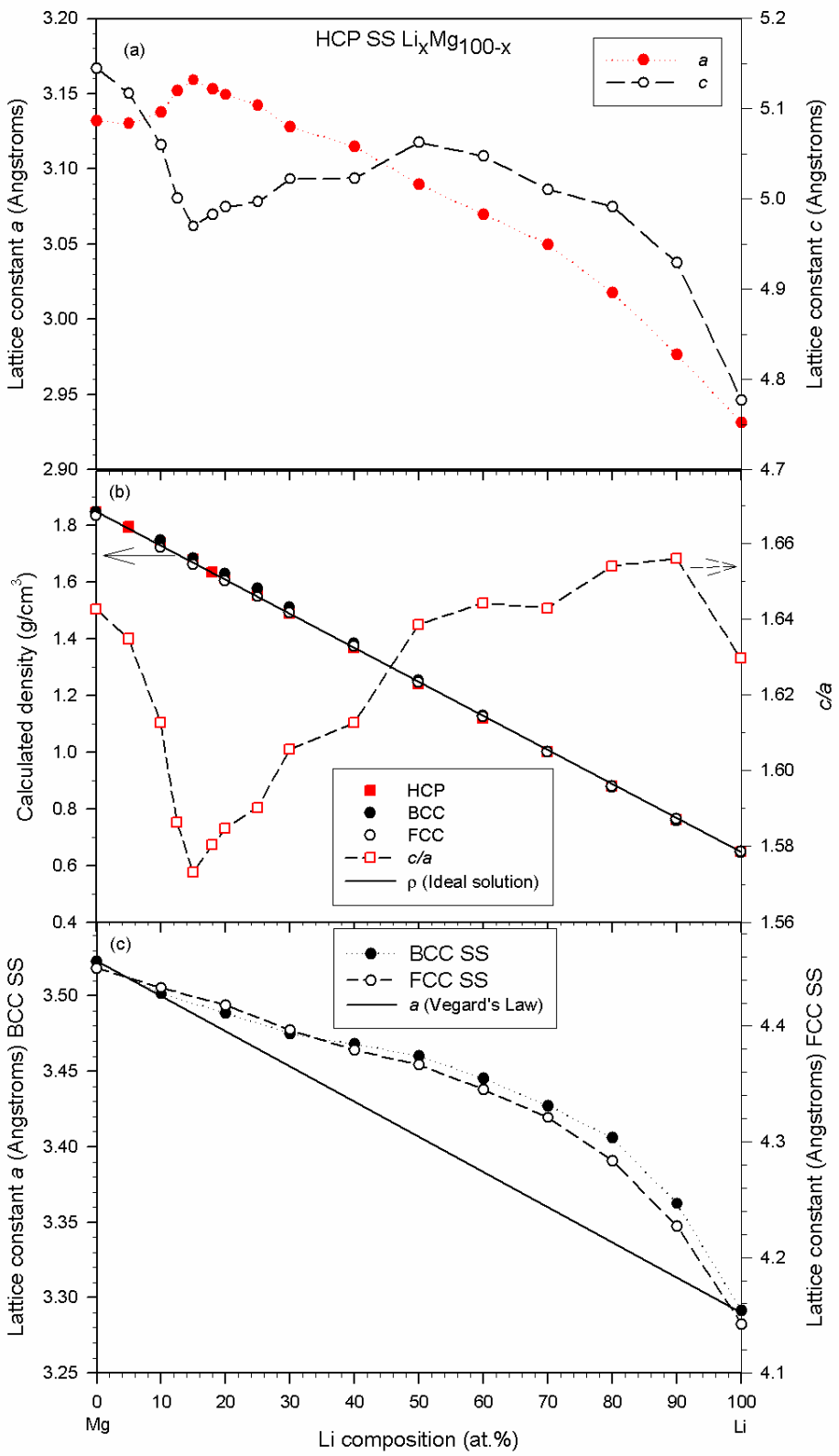

Figure 8.1.3.1.1. (a) Lattice parameters for HCP $Mg_{100-x}Li_x$, (b) corresponding c/a ratio and theoretical density, (c) lattice parameters for cubic $Mg_{100-x}Li_x$ solid solutions.

monovalent Li decreased the axial ratio of Mg from 1.624 to 1.6068 due to the decrease in electron per atom ratio. This further indicates that the axial ratio is an important factor influencing the formability of HCP metals. However, above the 15 at.% Li composition the behaviour normalizes as lattice parameter *a* decreased monotonically while *c* increased gradually until 50:50 composition, after which it rapidly decreased. As shown in figure 8.1.3.1.1(b), the corresponding *c/a* ratio increased sharply and equalled that of pure Mg at 50:50 composition, before exceeding it at Li-rich compositions. Contrary to the observed changes in lattice parameters of HCP $Mg_{100-x}Li_x$ solid solutions in figure 8.1.3.1.1(a), the change in the theoretical density with Li concentration remained linear for all phases as shown in figure 8.1.3.1.1(b). The linear change of theoretical density with variation of Li content is in accordance with experimental results [Gasior *et al* 1998, Bialobrzeski *et al* 2007]. For the lattice parameters of cubic-based $Mg_{100-x}Li_x$ solid solutions, as shown in figure 8.1.3.1.1(c), a positive deviation from Vegard's law (1921) is noticed with increasing Li composition. Nonetheless, simple alloys are expected to follow Vegard's law for the volumes, that is, the volume per atom in the disordered A_xB_{1-x} alloys can be expressed as:

$$\Omega_x = x\Omega_A + (1-x)\Omega_B \qquad (8.1.3.1.1)$$

However, King (1966), after taking into account that the size of an atom is dictated by its environment, calculated the *effective atomic volume* (Ω^*_A) occupied by a solute in different solvents from reported values of lattice parameters of several substitutional solid solutions as follows:

$$\Omega_x = x\Omega^*_A + (1-x)\Omega_B \qquad (8.1.3.1.2)$$

This approach has been used elsewhere to study lattice parameter and volume changes on disordering of ordered phases [Cahn 1999, Bhatia and Cahn 2005] as well as on cubic intermetallic compounds [Bhatia *et al* 1996, 1998, Coreño-Alonso 2004, 2006].

Our lattice parameter variation of BCC $Mg_{100-x}Li_x$ solid solutions are in agreement with earlier experimental results of Levinson (1955), Herbstein and Averbach (1956a, b) at least up to 50:50 composition. However, there exists a discrepancy beyond this composition, which is attributed to underestimated lattice of Li with the choice of

pseudopotentials. The deviation is smaller for Li compositions below 30 at.% for both FCC and BCC solid solutions whereas it is largest at 70 and 80 at.% for FCC and BCC solid solutions, respectively.

8.1.3.2. Phase stability

The calculated binding energy, structural energy difference with respect to HCP lattice and heats of formation of HCP, FCC and BCC $Mg_{100-x}Li_x$ solid solutions are plotted against Li composition in figure 8.1.3.2.1(a), (b) and (c), respectively. As shown in figure 8.1.3.2.1(a), the binding energy decreases rapidly with Li composition and makes a sudden dip at 50:50 composition. However, there is a slight smooth increase in binding energy at compositions above 50 at.% Li. In terms of the structural energy difference, as presented in figure 8.1.3.2.1(b), both pure elements are most stable in HCP structure although difference in atomic energies of the three phases is very large for Mg compared to very little energy difference for Li. In addition, the phase stability trend is similar: HCP-FCC-BCC. However, on Li addition, the energy difference between HCP and FCC lattice widens until reaching maximum at 15 at.% Li while at the same time that between HCP and BCC narrows. Even though after 15 at.% Li composition, the HCP-FCC energy difference begin to reduce, it is still larger than that between HCP and BCC lattices. Between 15 and 30 at.% Li, HCP-BCC energy difference decreases rapidly until BCC lattice becomes more stable at 30 at.% Li. This behaviour is in accordance with experimental observations that 30 at.% (11 wt.%) Li is required to induce a crucial HCP to BCC structural transition [Jackson *et al* 1949, Freeth and Raynor 1953, Massalski 1992]. The superiority of BCC solid solution continues up to just below 60 at.% Li, after which the FCC becomes more stable until 90 at.% Li. The stability of FCC in this region, especially at extremely low temperatures, is in agreement with other predictions [Hafner 1976, Punz and Hafner 1987, Phasha *et al* 2010a].

Furthermore, it was in this region that BCC to HCP martensitic transformation in Li-Mg alloys is reported [Barett and Trautz 1948, Punz and Hafner 1987]. As shown in figure 8.1.3.2.1(c), the enthalpy of mixing for the most stable phase is plotted against variation

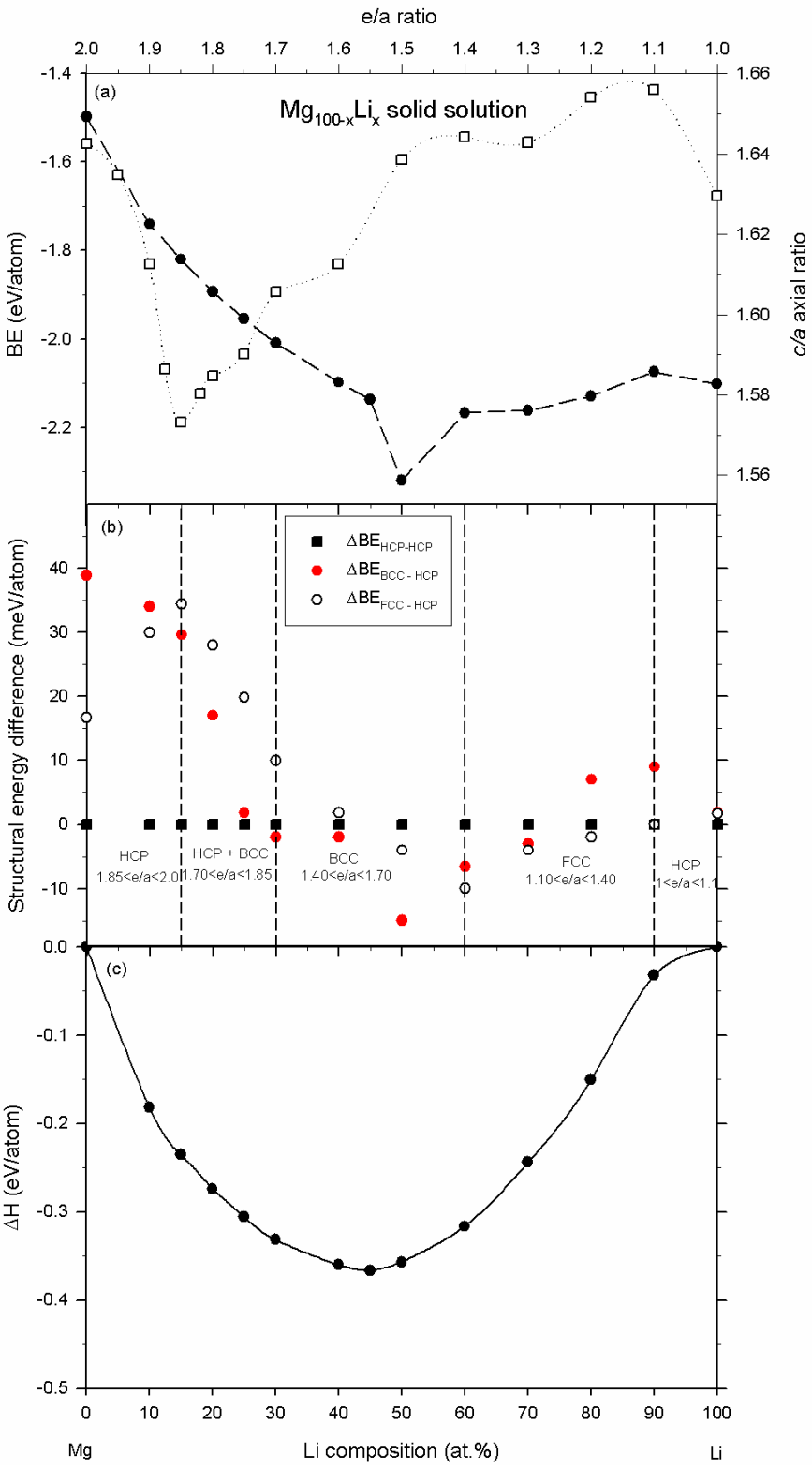

Figure 8.1.3.2.1. The calculated (a) binding energy for $Mg_{100-x}Li_x$, (b) structural energy difference with respect to HCP lattice and (c) heats of formation at equilibrium. The plotted binding and formation energy were calculated from the most stable phase at every composition.

in Li composition. Current results show minimum at 45 at.% Li, in agreement with calculations of Hafner (1976) and very close to the evaluations of Saunders (1990), Nayeb-Hashemi *et al* (1984) and those determined for liquid alloys [Mashkovetz and Puchkov 1965, Anusionwu 2002]. In general, our results have been able to mimic reliable phase stability regions leading to HCP-BCC-FCC-HCP trend for $Mg_{100-x}Li_x$ solid solutions and are comparable to experiments and other theoretical results, especially the Jones-type analysis [Phasha *et al* 2010a].

It follows from these results that the possible reason for finding positive mixing enthalpy for systems that have complete solubility lies in the equation used. In almost all these studies, the equation for calculating the heat of formation for ordered intermetallics phases is used. On the contrary, if equation (8.1.2.3.1.2) is employed in such random systems, the correct heats of solution could be obtained.

8.1.3.3. Elastic properties

The elastic constants C_{11}, C_{12}, C_{13} and C_{33} of HCP and C_{11}, C_{12} of cubic $Mg_{100-x}Li_x$ solid solutions are plotted against Li concentration in figure 8.1.3.3.1(a) and (b), respectively. Since the elastic constant C_{44} in both the HCP and cubic structures is directly linked to mechanical stability of crystals, it will be presented later in figure 8.1.3.3.2 and discussed later. As shown by filled and empty spheres in figure 8.1.3.3.1(a), the trends of C_{11} and C_{12} elastic constants, respectively, of HCP solid solutions are opposite to each other on addition of Li. Within the 15 at.% Li concentration range, C_{11} increases while C_{12} decreases, thus increasing mechanical stability of HCP phase. This behaviour correlates to the anomaly of lattice parameter *a* and *c* observed in figure 8.1.3.1.1(a). Although C_{11} begins to decrease while C_{12} increases beyond this point, the trends are not reasonably smooth as evidenced by the fluctuations. On the other hand, the variations of elastic constants C_{13} and C_{33} are smooth and closely resembling the behaviour of C_{12} and C_{11}, respectively. As for cubic phases in figure 8.1.3.3.1(b), the C_{11} (filled spheres) of BCC solid solutions up to 20 at.% Li remains lower than C_{12} (empty spheres) and thus confirming its instability in this region, except for strange behaviour at

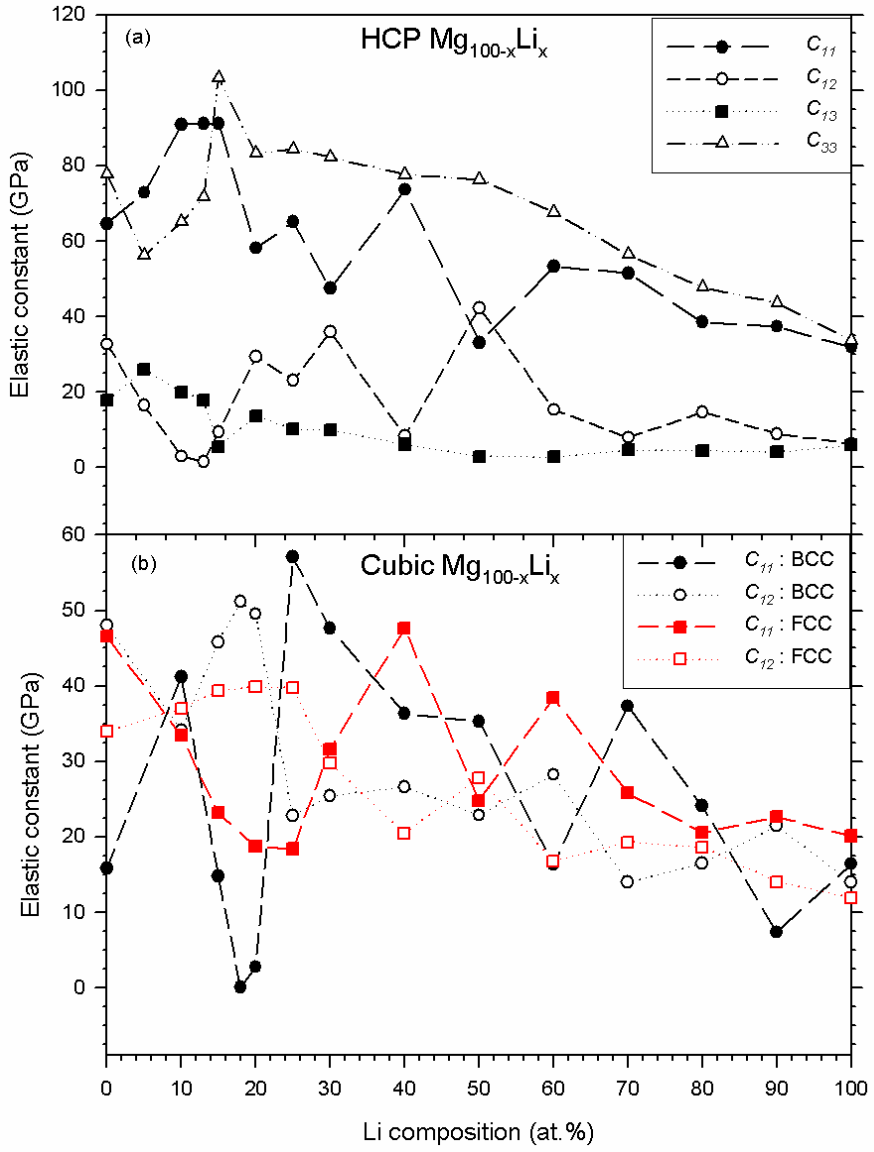

Figure 8.1.3.3.1. Calculated elastic constants C_{11}, C_{12}, C_{13} and C_{33} for (a) HCP and C_{11}, C_{12} for (b) cubic (FCC and BCC) phases of $Mg_{100-x}Li_x$ solid solutions.

10 at.% Li. However, above this composition the changes take an opposite turn, where C_{11} becomes larger than C_{12}, which is indicative of mechanical stability, with exception of 60 and 90 at.% Li compositions. The elastic constants of FCC solid solutions, represented by filled (C_{11}) and empty (C_{12}) squares, show a smooth behaviour similar to C_{12} and C_{11}, respectively, of HCP until up to 25 at.% Li. Within this concentration range the mechanical instability of FCC phase prevails since C_{11} elastic constant is smaller than C_{12}. At 30 at.% Li the C_{11} and C_{12} are almost equal but start to fluctuate between

this composition and below 60 at.% Li . However, as from 60 at.% up to 100% Li, the mechanical stability of FCC phase is maintained as evidenced by elastic constant C_{11} being greater than C_{12}. As described previously, the mechanical instability can be depicted by the following elastic moduli becoming negative: tetragonal, trigonal shear modulus (C', C_{44}), Young's modulus (E); and Poisson's ratio (υ) higher than 0.5. In figure 8.1.3.3.2, the predicted mechanical stability moduli (C', C_{44}, E and C_{66} for HCP) for (a) BCC, (b) FCC and (c) HCP $Mg_{100-x}Li_x$ solid solutions are presented. As shown in figure 8.1.3.3.2(a), the C' of BCC solid solutions is negative below 25, at 60 and 90 at.% Li, implying mechanical instability at such compositions. Except at 10 at.% Li composition, it is interesting to note that regions where C' is positive correlate with concentrations at which BCC solid solutions are either very close or more stable than either HCP counterparts (refer to Fig. 8.1.3.2.1(b)). It is also worth noting that the elastic constant C_{44} remains positive on Li variation whereas E follows a trend similar to that of C'. Trends similar to those of BCC are observed for FCC $Mg_{100-x}Li_x$ solid solutions. However, the mechanical instability of FCC-based solutions indicated by negative C' and E are noted below 30 and at 50 at.% Li.

In BCC solid solutions, the elastic constant C_{44} remains positive on Li variation whereas E follows a trend similar to that of C'. Consequently, FCC solid solutions are mechanically stable at 40 and between 60 and 100 at.% Li, as shown in figure 8.1.3.3.2(b). It thus follows from these elastic moduli results that C' is much more reliable compared to C_{44} in predicting the mechanical stability of cubic crystals. In figure 8.1.3.3.2(c), the changes of C_{44}, $E_{[100]}$ and C_{66} shear moduli for HCP solid solutions are similar while those of C' and $E_{[001]}$ also follow identical path on addition of Li. The mechanical stability of HCP solutions increased below 20 at.% Li as shown by , $E_{[100]}$ and C_{66} and reached maximum at 15 at.% Li after which it depreciated and recovered at 40 at.% Li. However, according to $E_{[100]}$ and C_{66}, the HCP solid solutions only become mechanically unstable at 50:50 composition while C_{44} indicates the instability at 60 at.% Li while C' and $E_{[001]}$ remain positive throughout Li addition. It is quite interesting to note that the minima and maxima reported by Vaks and Trefilov (1988) for elastic moduli C_{44} and C' in HCP, FCC and BCC $Mg_{100-x}Li_x$ solid solutions correlate with compositions

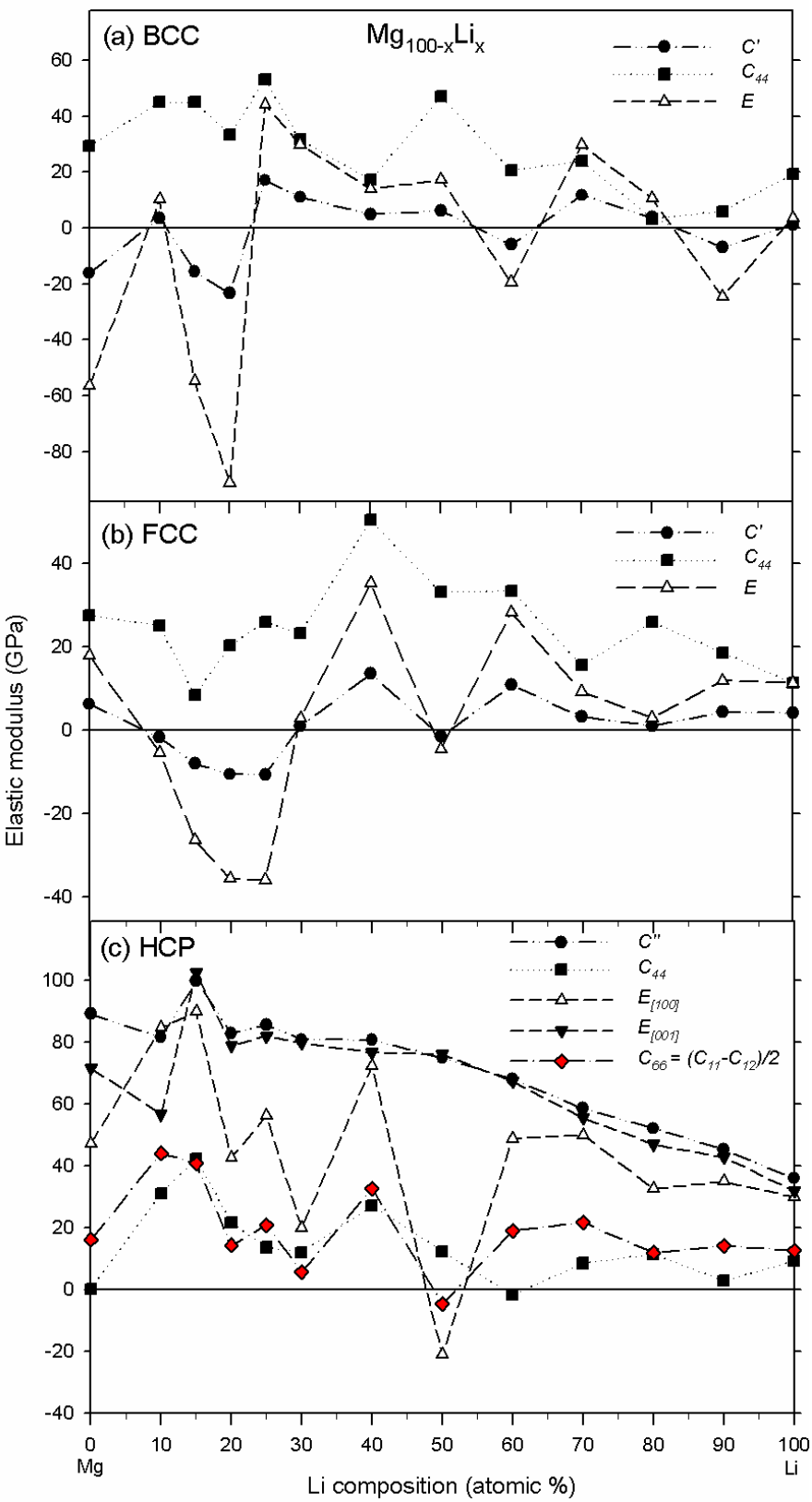

Figure 8.1.3.3.2. The predicted mechanical stability moduli *C'*, C_{44} and *E* for (a) BCC, (b) FCC and (c) HCP $Mg_{100-x}Li_x$ solid solutions.

showing mechanical instability and stability, respectively, in the current work.

In an attempt to further clarify the issue of mechanical stability of $Mg_{100-x}Li_x$ solid solutions, the calculated Poisson's ratio for BCC, FCC and HCP lattices is presented in figure 8.1.3.3.3. Despite the discrepancy at 10 at.% Li, the BCC-based solid solutions show Poisson's ratio (υ) values above 0.5 up to 20 at.% Li and at 60 and 90 at.% Li, which is an indication of mechanical instability. On the other hand, mechanical stability is predicted between 20 and 60 at.% Li and again at 70 and 80 at.% Li. Such stability behaviour correlates with that observed for *C'* and *E* in figure 8.1.3.3.2(a). The same applies for FCC $Mg_{100-x}Li_x$ solid solutions. Futhermore, while the trend of $\upsilon_{[100]}$ correlates with behavior of C_{44} and C_{66} shear moduli for HCP solid solutions in figure 8.1.3.3.2(c) and even more with $E_{[100]}$, the $\upsilon_{[001]}$ corresponds to the behaviour of *C'* and $E_{[001]}$ on Li addition. The predicted mechanical stability profiles using Poisson's ratio resembles those observed in figure 8.1.3.3.2. Other mechanical properties of interest, namely, the bulk modulus (*B*), Pugh's ductility/brittles measure (*B/G*) and isotropic shear modulus (*G*) of HCP, FCC, BCC $Mg_{100-x}Li_x$ solid solutions are presented in figure 8.1.3.3.4(a), (b) and (c), respectively.

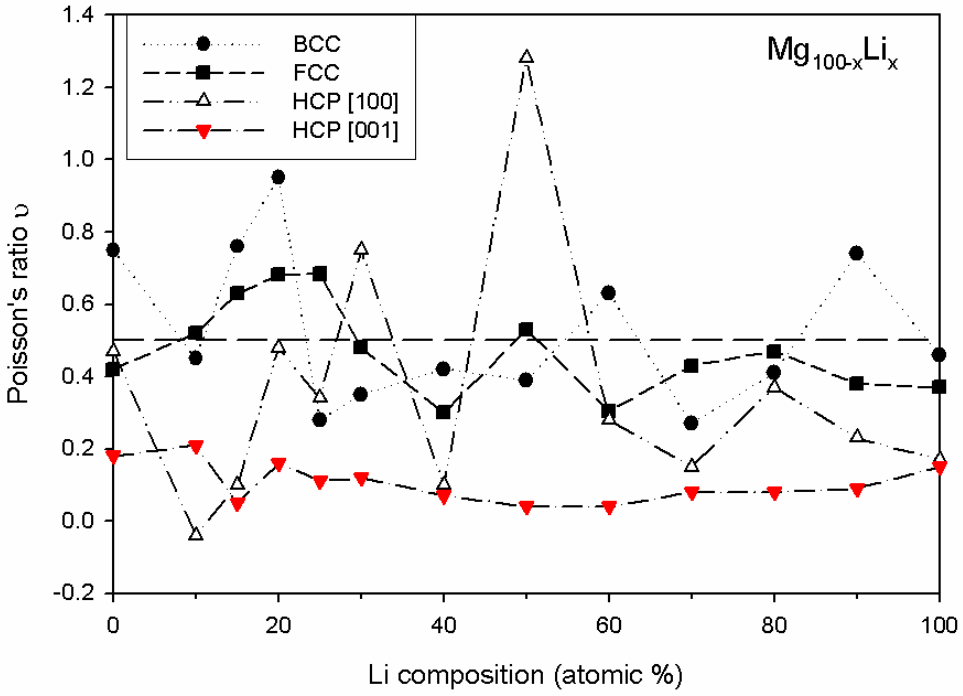

Figure 8.1.3.3.3. The calculated Poisson's ratio (υ) for HCP, FCC and BCC $Mg_{100-x}Li_x$ solid solutions at equilibrium.

As shown in figure 8.1.3.3.4(a), *B* decreases monotonically with increase in Li composition despite the structure-type, in excellent agreement with almost all previous calculations. In the Mg-rich region, the bulk modulus seems to soften more for FCC solid solutions while it gets slightly harder between 25 and 30 at.% Li for BCC solid solutions. In general, the FCC Mg-Li alloys are more ductile above 25 at.% Li composition as shown by *B/G* ratio being above the critical value of 1.75, in figure 8.1.3.3.4(b). On contrary, the BCC and HCP Mg-Li alloys tend to be brittle with exception for 40 and 80 at.% Li composition in the former and 30 and 60 at.% Li composition in the latter. In addition, the isotropic shear modulus (*G*) correlates with mechanical stability on Li addition, as shown in figure 8.1.3.3.4(c). This conclusion emanates from the values of (*G*), which are negative for compositions which were found to be mechanically unstable in figures 8.1.3.3.2 and 8.1.3.3.3 and *vice-versa*.

Lastly, the elastic anisotropy factor (*A*) for HCP lattice according to Olijnyk and Jephcoat (2000) and for cubic lattice using Zener's model are presented in figure 8.1.3.3.5(a) and (b), respectively. The solid horizontal line represents isotropic material (A=1). As shown in figure 8.1.3.3.5(a) and in excellent agreement with experimental observations by Kelley and Hosford (1968), the anisotropic factors A_2 and A_3 decrease on adding Li up to 15 at.% in HCP lattice, after which they remain positive and reach three maxima at 30, 60 and 80 at.% Li compositions. On contrary, A_1 continues to increase with higher Li concentration until reaching its maximum value at 30 at.% Li. However, all anisotropic factors are closer to unity at 40 at.% Li and only A_2 remains so between 60 and 100 at.% Li. While the BCC Mg-Li alloys are almost isotropic between 25 and 30 at.% as well as between 70 and 90 at.% Li, the anisotropic factor of FCC counterparts is closer to unity between 15 and 25 at.% Li as well as at 40, 60, 70, 90 and 100 at.% Li, as shown in figure 8.1.3.3.5(b). All other compositions indicate large anisotropy.

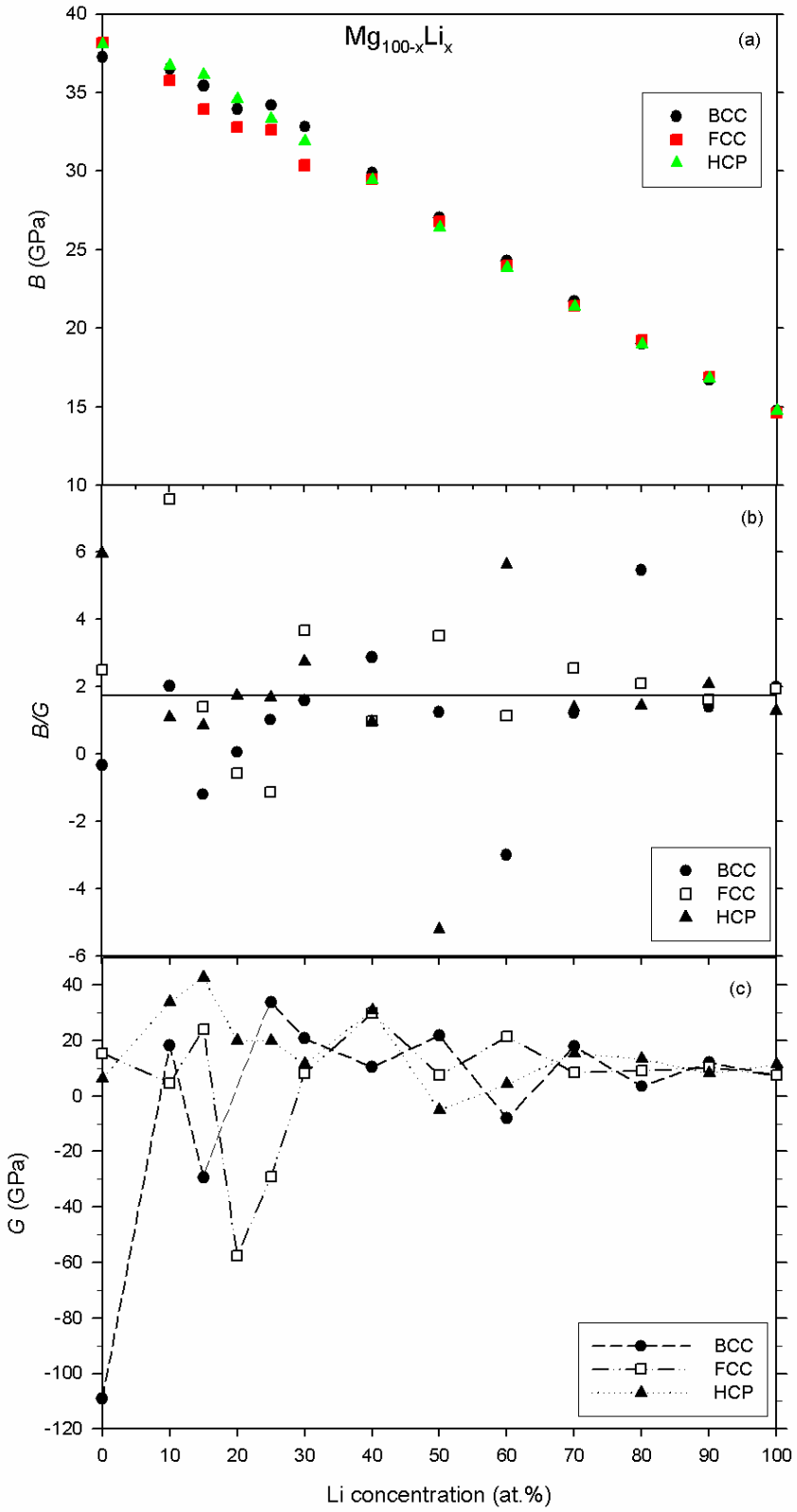

Figure 8.1.3.3.4. The calculated (a) bulk modulus (*B*), (b) *B/G* ratio and (c) isotropic shear modulus (G) for HCP, FCC and BCC $Mg_{100-x}Li_x$ solid solutions.

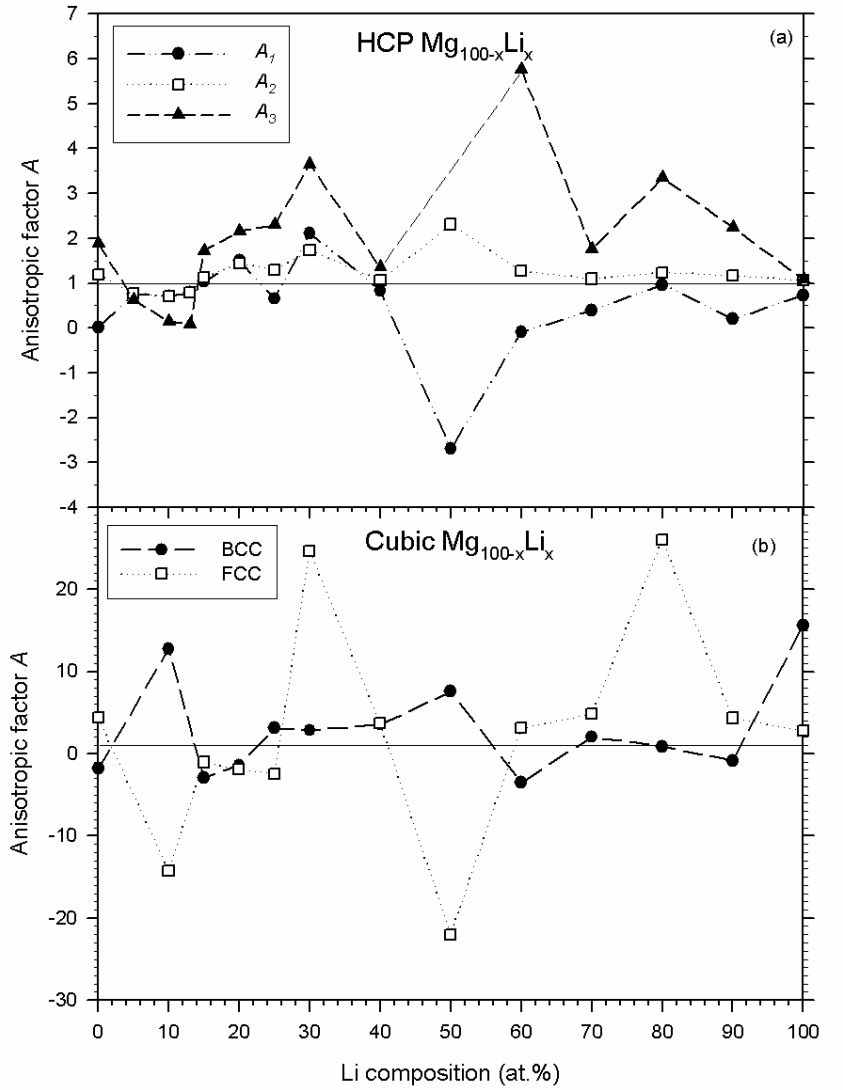

Figure 8.1.3.3.5. Elastic anisotropy of (a) HCP- and (b) cubic-based structures of $Mg_{100-x}Li_x$ solid solutions.

8.1.4. Conclusions

In summary, a DFT-based model for predicting phase stability and elastic properties of binary random alloys is proposed. The current model is applied on binary Mg-Li system as a test study. The predicted phase stability trends at 0K resemble those observed experimentally in Mg-Li phase diagram, more especially at lower temperatures. Furthermore, the mechanical properties of random binary Mg-Li alloys spanning the entire composition range were predicted for the first time using DFT-based calculations

and were found to be in excellent agreement with earlier experiments. The proposed model for random alloys is not only accurate but also less computationally expensive compared to traditional supercell approach. Following correct prediction of structural, cohesive as well as mechanical properties of binary Mg-Li alloys, this approach will enable researchers to study other properties such as surface properties of disordered binary Mg-Li alloys with ease. Therefore the use of correct crystal structure and symmetry to represent the experimental solid solution is a crucial benchmark. The current approach does not only predict correct structural parameters but it is also computationally and time efficient.

Chapter 9

Prediction of Equilibrium and Non-equilibrium Ti-Mg Solid Solutions

9.1 Ti-Mg system

Although the Ti-Mg system shows a solid solubility of less than 2 atomic percent (2 at.%) of each metal into another at equilibrium, recent studies indicated extended solid solubility of up to 45 at.% and 50 at.% using far-from equilibrium processes such as physical-vapor-deposition (PVD) [Zheng *et al* 1997] and mechanical milling (MM) [Asano *et al* 2009, Rousselot *et al* 2008], respectively. In such studies, the compositions were randomly selected with no particular mechanical property drive, except density and crystal structure. Recently, HCP, FCC and BCC solid solutions of Ti-Mg system have been synthesized using MM, although the emphasis was on their potential use in hydrogen storage [Asano *et al* 2007 to 2009, Maweja *et al* 2010, Phasha *et al* 2010b]. In the current work, we employ the *ab initio* technique to predict the possible alloying mechanism, preferred metastable crystal structures, resulting mechanical properties at various compositions, from which the compositions possessing interesting properties could be selected and experimented on.

9.1.1. Objective

The objective of this chapter is to investigate formation of HCP, FCC and BCC solid solutions with compositions spanning the entire concentration range (0-100%) of Ti and Mg under equilibrium and non-equilibrium conditions. The results will be useful in determining the extended solid solubility limit. This study is also carried out in order to generate data on effects of composition variation on the lattice parameter(s), phase stability and mechanical properties. Such parameters should indicate which

compositions are thermodynamically feasible and which are unlikely. In addition, the elastic constants calculations will be carried out on the optimized crystal structures. It will then be possible to predict which compositions and corresponding crystal structures possess attractive mechanical properties derived from calculated elastic constants.

9.2. Ti-Mg solid solutions under equilibrium conditions using USP

9.2.1. Computational procedure

The *ab initio* modelling work was carried out as described in the previous chapter (Chapter 8), for both structure optimization and elastic constants calculations. However, the more robust Vanderbilt-type ultrasoft pseudopotentials (USP) [Vanderbilt 1990] were employed to describe the electron-ion interaction. Current calculations were performed on HCP (space group # 194 $P6_3/mmc$), FCC (space group # 225 Fm-3m) and BCC (space group # 229 Im-3m) phases for pure Ti and Mg as well as their solid solutions spanning the entire composition range. The calculations were performed using 11 x 11 x 6 and 12 x 12 x 12 Monkhorst-Pack k-point grid for HCP and cubic phases, respectively. The energy cut-off of 500 eV as well as the number of k-points were converged to within 2 meV per atom. For each phase of interest, the geometry optimization is first performed to find its ground state, as well as to obtain the equilibrium structural properties. Furthermore, elastic properties of each alloy composition in HCP, FCC and BCC phases were computed from another set of calculations involving stress-strain relation. A similar procedure as in the previous chapter was followed in determining the properties of disordered Ti-Mg alloys.

9.2.2. Results and discussions

9.2.2.1. Phase stability

In figure 9.2.2.1.1, the predicted equilibrium (T= 0K, P= 0 GPa) lattice parameters of cubic and hexagonal Ti-Mg solid solutions as well as their corresponding densities (ρ)

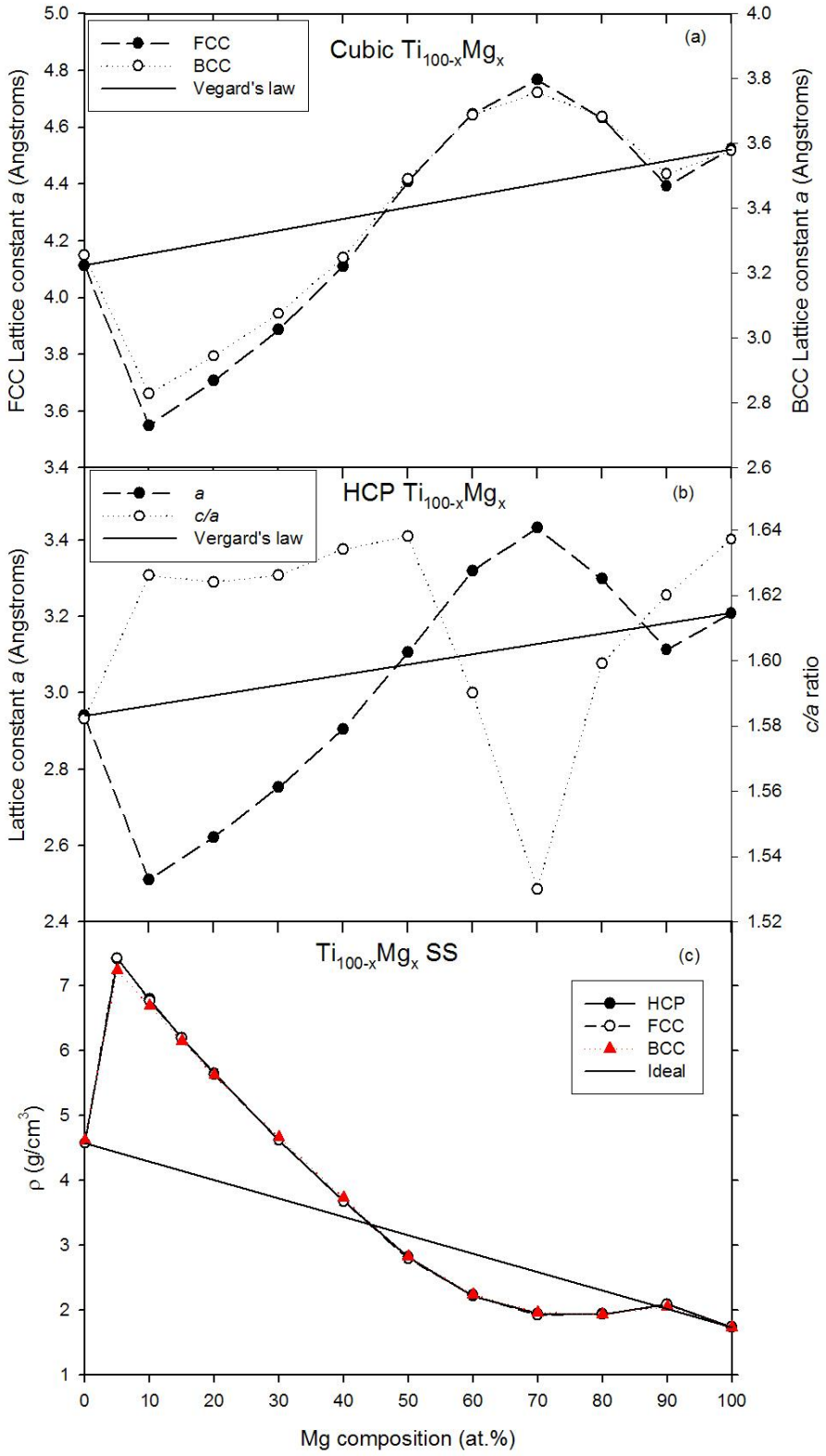

Figure 9.2.2.1.1. Predicted structural properties, (a) lattice parameters for cubic (b) lattice parameters for HCP and (c) theoretical density, for $Ti_{100-x}Mg_x$ ss solid solutions at equilibrium.

plotted against Mg atomic composition are presented in (a), (b) and (c), respectively. Unexpectedly, the lattice parameter variation is not linear with increasing Mg content in all three crystal structures, as expected for ideal solid solutions. It is clear from (a) and (b) of this figure that common to other equilibrium binary alloy combinations, an appreciable deviation from Vegard's law (indicated by solid lines) is observed; however in this case it is quite significant. The deviation is strongly negative below 40% and positive between 50 and 90 at.% Mg. However, in terms of calculated density the deviation takes the opposite trend, as shown in (c). The anomaly in the above composition ranges corresponds to densities of solid solutions being higher than the densities of pure elements, and the lattice parameters of solid solution being smaller or larger than that of the constituent pure Mg and Ti elements.

The calculated binding energy and heats of formation of HCP, FCC and BCC solid solutions (ss) are plotted against Mg composition in figure 9.2.2.1.2(a) and (c) while the structural energy differences with respect to HCP ss are presented in figure 9.2.2.1.2(b). As shown in figure 9.2.2.1.2(a), an anomalous behaviour is observed in Ti-rich side where there is a sharp decrease in binding energy on introduction of 5 at.% Mg. However, this drop gradually decreases with further increase in Mg content until it equals that of pure Ti at 50 at.% Mg. Above equi-atomic composition, the situation normalizes as expected, i.e. the cohesive energy of the solid solution lies almost linearly between those of constituent pure elements. On the other hand, the difference in structural energy indicates HCP stability dominance over a wide range of compositions except for between 55 and 65 at.% Mg where BCC is most stable, as shown in figure 9.2.2.1.2(b). Furthermore, FCC phase seems to be metastable very close to pure elemental compositions, as observed at 10 and 90 at.% Mg. A similar trend as in (a) for binding energy is also observed in (c) for heats of formation, although the energy is higher by almost a half. These results appear to suggest that the formability of the alloy depends strongly on its cohesion ability. In addition, it is clear that above 60 at.% Mg the formation energy becomes positive implying miscibility gap in this composition range. This issue of phase stability will be further strenghtened in the next sub-section (9.2.2.2) using mechanical stability results derived from calculated elastic constants.

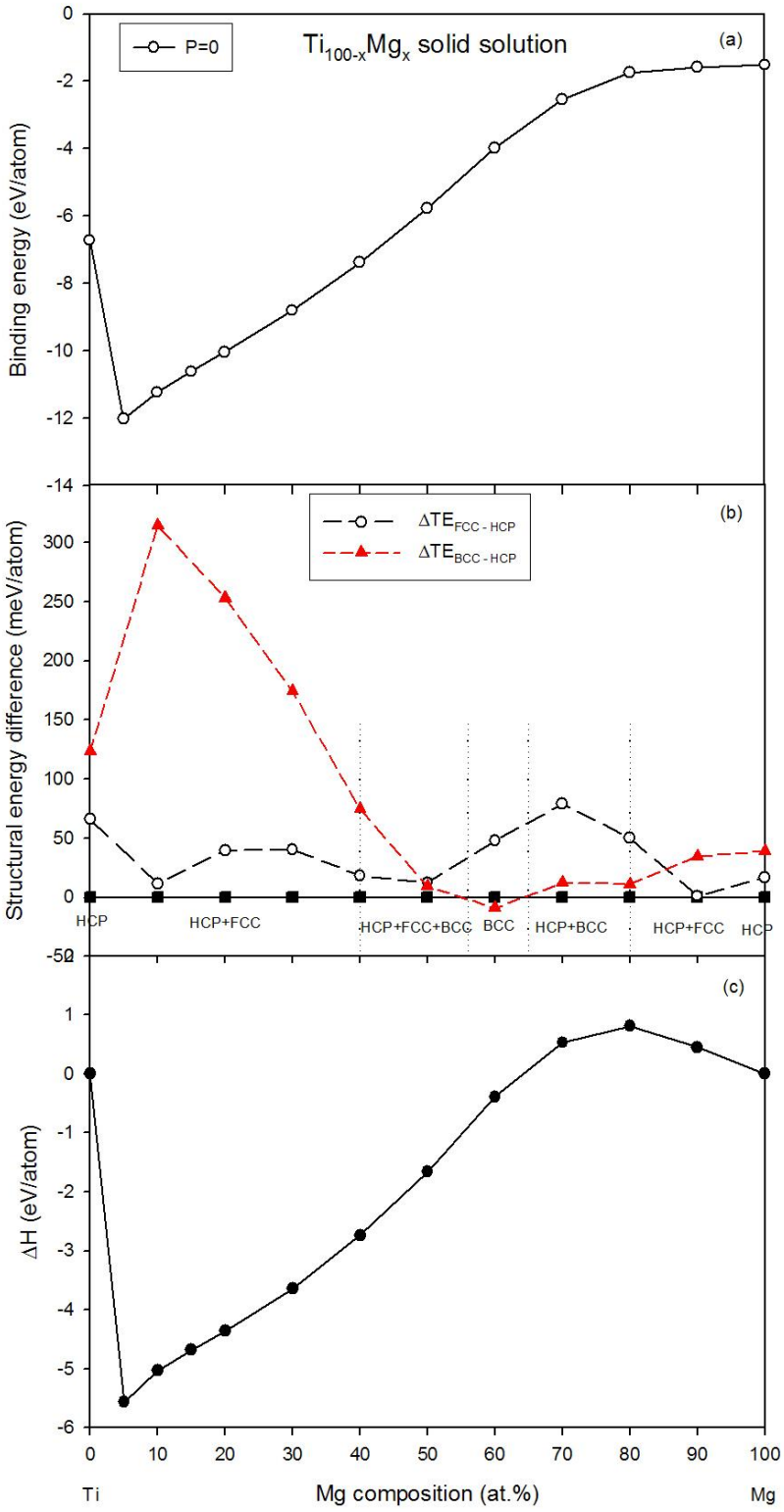

Figure 9.2.2.1.2. The calculated (a) binding energy, (b) structural energy difference with respect to HCP lattice and (c) heats of formation, at equilibrium for $Ti_{100-x}Mg_x$ solid solutions,. The plotted binding and formation energy were calculated from the most stable phase at every composition of interest.

9.2.2.2. Elastic properties

In figures 9.2.2.2.1, 9.2.2.2.2 and 9.2.2.2.3, as derived from expressions in the previous chapter, the bulk modulus (*B*), Young's modulus (*E*), Poisson's ratio (υ), *B/G* of HCP, FCC and BCC Ti-Mg system in various compositions are presented. As described previously in mechanical stability criterion, the mechanical instability can be indicated by the following elastic moduli if negative: tetragonal, trigonal shear moduli (*C'*, C_{44}), Young's modulus (*E*) and Poisson's ratio (υ) higher than 0.5. It is evident from figure 9.2.2.2.1(a) that *B* and *E* of HCP solid solution increases abruptly on Mg addition, reaching maximum values at 10 at.% Mg. These values decreases gradually with increasing Mg amount until at about 40-50 at.%, where they are just below those of pure Ti. Above this composition the bulk modulus and $E_{[001]}$ decrease almost linearly, whereas *E* in [100] direction soften drastically to a negative value (indicating crystal structure instability). This anomalous behaviour occurs between 50 and 70 at.% Mg. Beyond this composition, both *B* and *E* behaves normally. The corresponding predicted Poisson's and *B/G* ratio results are presented in figure 9.2.2.2.1(b). For Ti-rich compositions of up to 50 at.% Mg, the value of υ is well below 0.5 and above 0, indicating mechanical stability. However, at around 60 at.% Mg it crosses the 0.5 margin, which is a sign of elastic instability. It is interesting to note that this point corresponds to the anomalous softening of $E_{[100]}$ observed in figure 9.2.2.2.1(a). On the other hand, the measure of ductility or brittleness is also presented on the right y-axis of figure 9.2.2.2.1(b). Besides decreasing from *B/G* value of 2.3 for pure Ti on Mg addition, the HCP ss corresponding to less than or equal to 40 at.% Mg seems to be ductile, since their *B/G* values are at and above critical value of 1.75. However, between 50 and 70 and at 90 at.% Mg, the *B/G* value is either at or below 1.75 threshold value, which is an indication of brittleness at these compositions. It is worth noting that this brittleness corresponds to $E_{[100]}$ softening in figure 9.2.2.2.1(a).

A similar trend in *B* and *E* versus Mg composition is observed for FCC Ti-Mg ss, as shown in figure 9.2.2.2.2(a). However, as shown in figure 9.2.2.2.3(a), in BCC ss only the trend for *B* appears to be following a similar pattern to that of HCP ss. In the FCC

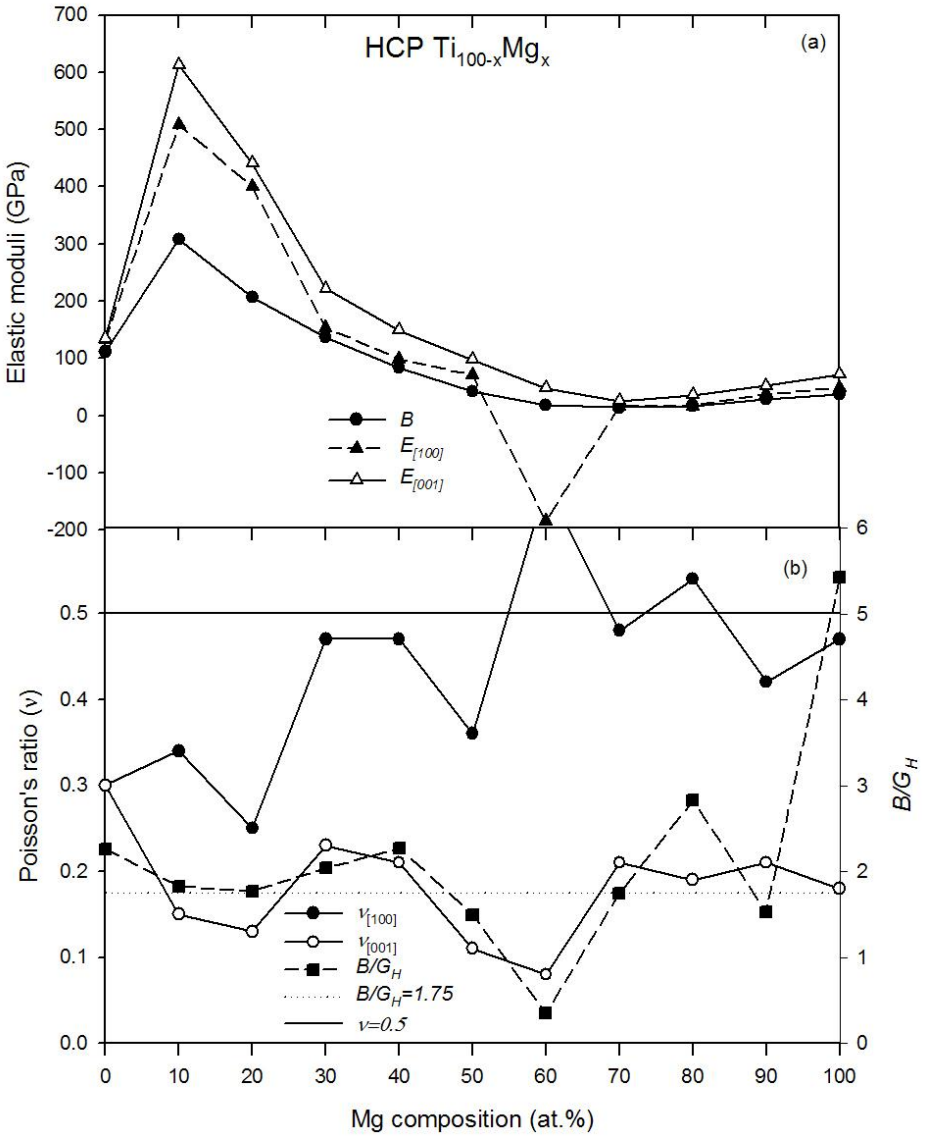

Figure 9.2.2.2.1. The calculated (a) bulk modulus (*B*), Young's modulus (*E*), Poisson's ratio (**ʊ**) and (b) *B/G* of HCP Ti-Mg solid solutions at equilibrium.

ss, the *E* softens to negative values between 60 and 80 at.% Mg but attains a minimum at $Ti_{0.2}Mg_{0.8}$ composition. The negative *E* occurs below 40 at.% Mg for BCC solid solutions but hardens anomalously at $Ti_{0.1}Mg_{0.9}$ composition. In general, these instabilities of crystal structure due to negative *E* are accompanied by a very high positive (above 0.5) value of ʊ, even though the stable BCC ss at 90 at.%Mg shows a large negative ʊ. The *B/G* value for FCC ss at this composition range (80-90 at.% Mg) indicates higher ductility (see figure 9.2.2.2.2(b)) while the BCC ss remains slightly

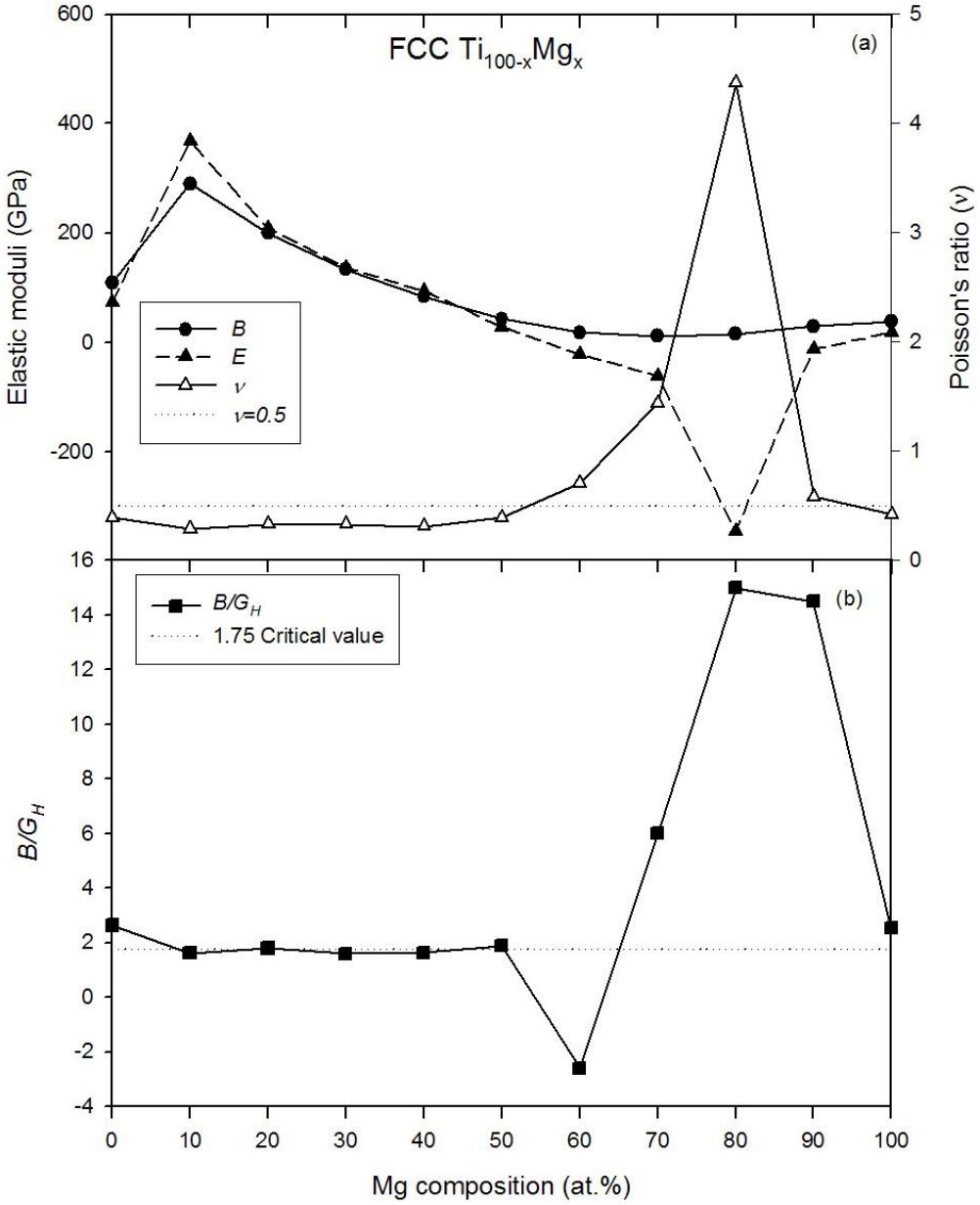

Figure 9.2.2.2.2. The calculated (a) bulk modulus (*B*), Young's modulus (*E*), Poisson's ratio (**υ**) and (b) *B/G* of FCC Ti-Mg solid solutions at equilibrium.

brittle (see figure 9.2.2.2.3(b)) than HCP ss (see 9.2.2.2.1(b)). Furthermore, the Poisson's ratio of FCC ss is less than 0.5 for compositions less or equal to 50 at.% Mg, and otherwise greater than 0.5. The corresponding *B/G* ratio as shown in figure 9.2.2.2.2(b) lies on the 1.75 margin for ≤ 50 at.%, below 1.75 for compositions between 50 and 60 at.%, and above 1.75 for all other remaining compositions. On the other

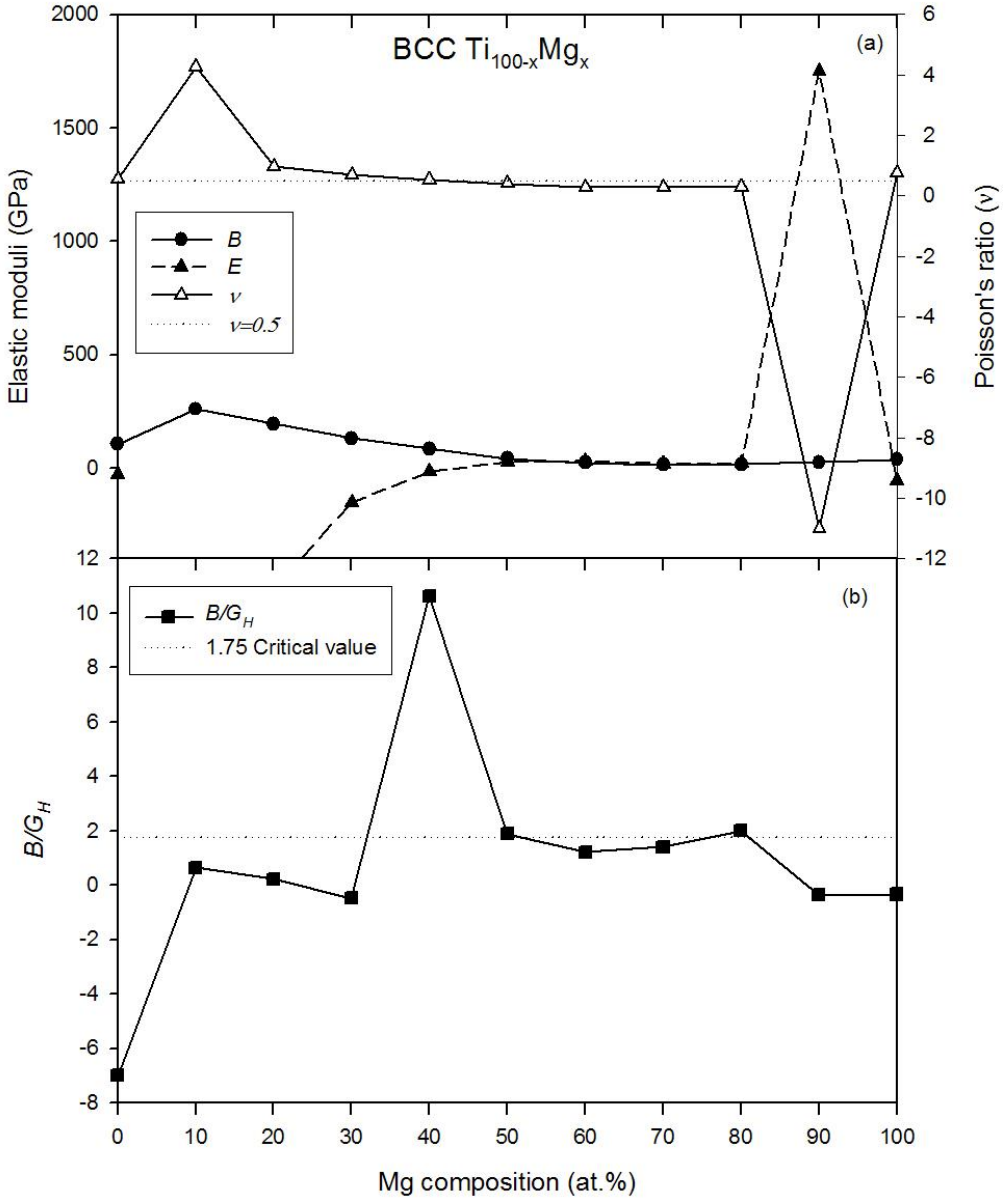

Figure 9.2.2.2.3. The calculated (a) bulk modulus (*B*), Young's modulus (*E*), Poisson's ratio (**υ**) and (b) *B/G* for BCC Ti-Mg solid solutions at equilibrium.

hand, while the *B/G* values as shown in figure 9.2.2.2.3(b) are below 1.75 (indicating brittleness) for BCC ss within compositions showing instability, their corresponding Poisson's ratios are above the 0.5 stability limit. In addition, the abnormal high value of *E* corresponds to the anomalously large and negative υ. In figure 9.2.2.2.4, the predicted mechanical stability for (a) HCP, (b) FCC and (c) BCC ss as defined by the expressions for mechanical stability criterion (equations 7.2.1 and 7.2.3 for cubic and

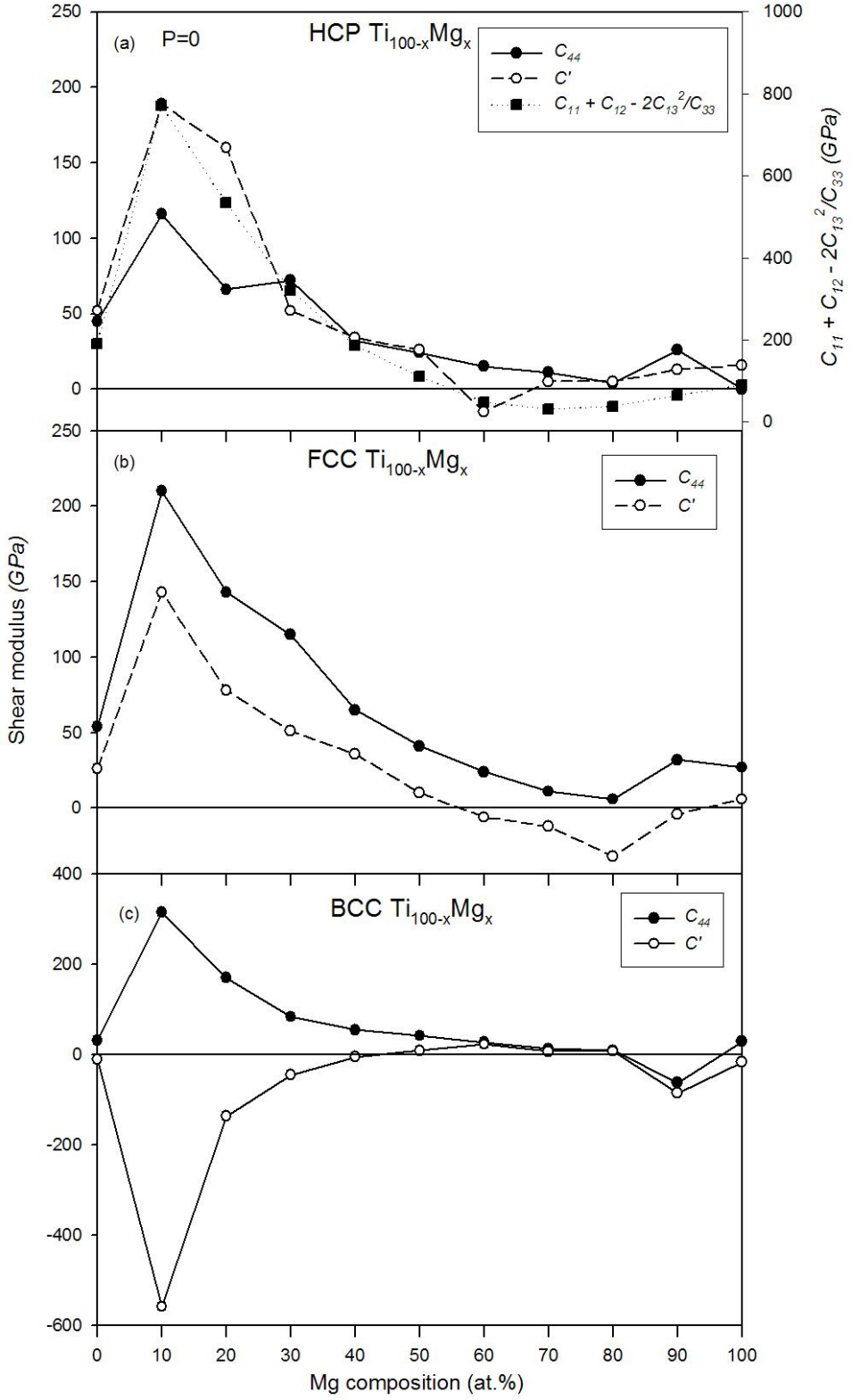

Figure 9.2.2.2.4. The predicted mechanical stability for (a) HCP, (b) FCC and (c) BCC $Ti_{100-x}Mg_x$ solid solutions.

hexagonal crystals, respectively) are presented. As shown in figure 9.2.2.2.4(a), all the elastic moduli of HCP ss are greater than zero for Mg compositions at 50 at.% and below, indicating mechanical stability. However, for compositions above the 50:50 equi-atomic composition only the trigonal shear (C_{44}) remained positive while others became negative. This is an indication of mechanical instability since not all conditions for mechanical stability are satisfied. Despite the tetragonal shear moduli ($C'=C_{66}$) becoming positive above 70 at% Mg, the HCP crystal bearing these compositions remains mechanically unstable. Furthermore, a similar scenario seems to occur for FCC ss as shown in 9.2.2.2.4(b), where the C_{44} remains positive with increase in Mg content while the tetragonal shear moduli (C') is only positive at 50 at.% Mg and below, and negative otherwise. However, on the contrary, the mechanical stability criteria is never satisfied for BCC ss at compositions below 50 at.% Mg since only one stability condition is met. The mechanical stability is fully attained between 50 and 80 at.% Mg. This is shown by negative values of C' below 50 at.% Mg while C_{44} remains positive and both shear moduli being positive between 50 and 80 at.% Mg, as shown in figure 9.2.2.2.4(c). Above this composition range, they both become negative which is again an indication of mechanical instability.

9.2.3. Conclusion

In general, the above two methods used to predict phase and mechanical stability of Ti-Mg ss at equilibrium, namely the formation energy as well as elastic constants, yielded similar stability trends as shown by figures 9.2.2.1.2(b) and 9.2.2.2.4 that can be summarized as follows:

(i) From 0 up to slightly above 50 at.% Mg, the solid solutions with highly close-packed crystal structures, HCP and FCC, are stable.

(ii) Between 50 and 80 at.% Mg, only the loosely packed BCC phase is stable.

(iii) Above 80 at.% Mg, the HCP and FCC seem to be stable even though the stability criteria are only partially satisfied.

9.3. Ti-Mg solid solutions under non-equilibrium conditions (Ideal SS)

9.3.1. Computational procedure

As observed in figure 9.2.2.1.1(c), under equilibrium conditions, the density variation of Ti-Mg solid solution was not linear with Mg change as expected for ideal solid solutions, more especially in the Ti-rich region. Consequently, in this sub-section the theoretical density was varied linearly with composition and the corresponding ideal conditions were predicted. The linear variation was theoretically determined according to the fractional composition, derived from those of optimized pure constituent elements. At each composition, the lattice parameter is altered until the ideal theoretical density is reached. This is followed by single-point energy minimization, in which the total energy and resultant stress (positive pressure) or strain (negative pressure) are calculated. Since under equilibrium conditions the Ti-Mg system does not obey Vegard's law for ideal solid solution, in this sub-section we mimic conditions (pressure) for forced ideal solid solutions herein referred to as far-from-equilibrium conditions. Other parameters such as pseudopotentials, cut-off energy and k-points sets were similar to those employed in 9.2.1. Similarly, elastic properties of each alloy composition in HCP, FCC and BCC phases were computed.

9.3.2. Results and discussions

9.3.2.1. Phase stability

In figure 9.3.2.1.1, the lattice parameters of FCC and BCC ss are plotted against Mg content in (a) whereas their corresponding theoretical densities as well as the resultant pressure are plotted in (b). It follows, from these plots, that if the density is varied linearly, the lattice parameters also change almost linearly, thus very close to resembling Vegard's rule for solid solutions. However, to achieve this ideal behaviour in Ti-Mg system, an expansion (as indicated by negative pressure) of Ti lattice is required for Ti-rich side while compression (positive pressure) of Mg lattice is necessary to obtain

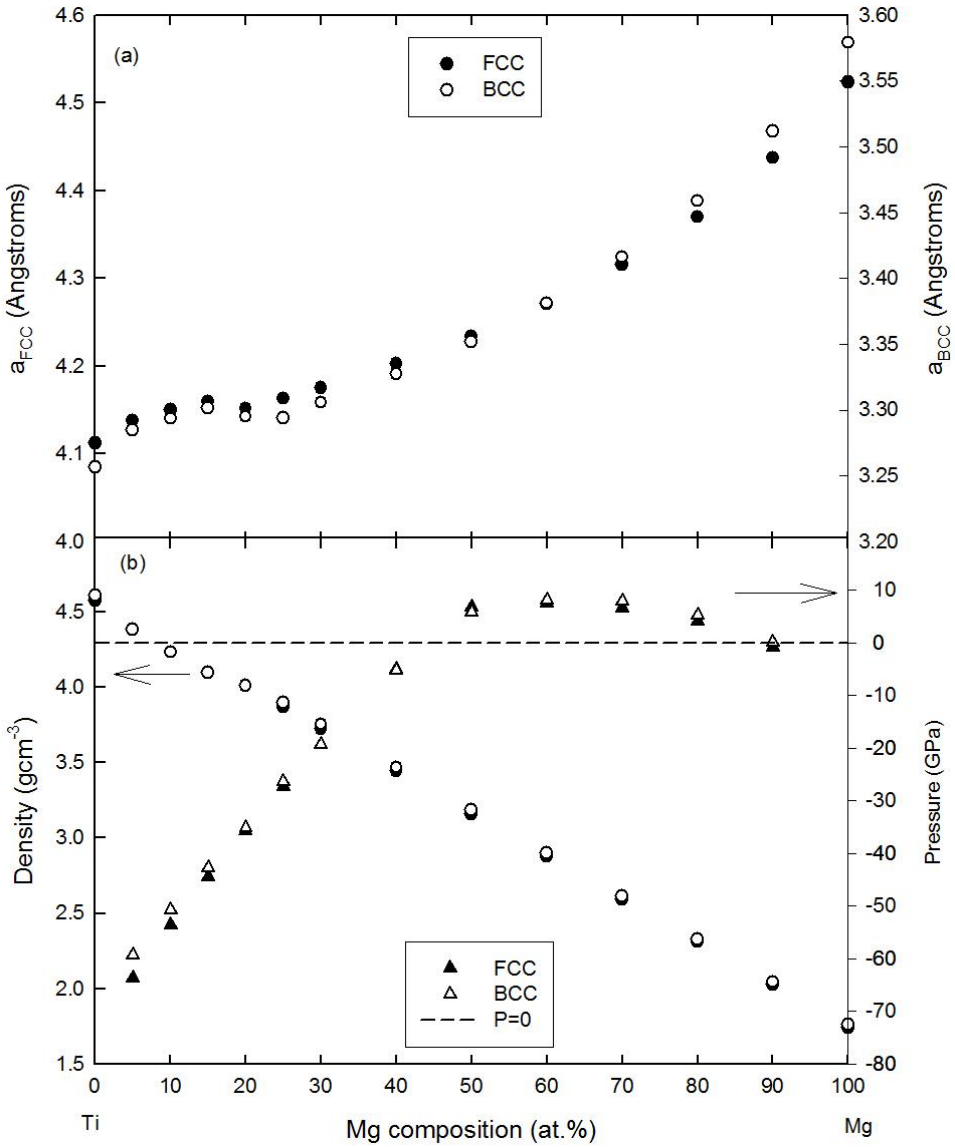

Figure 9.3.2.1.1. Structural properties of Ideal FCC and BCC Ti-Mg ss and the corresponding required conditions.

Mg-rich ss. The pressure sign (- or +) indicates the influence of difference in atomic size. Since Mg is about 10% larger than Ti, then for a successful dissolution Ti needs to expand in order to accommodate (dissolve) larger atoms of Mg while Mg on the other hand has to be compressed to match the smaller size of Ti. Due to high hardness of Ti compared to Mg, more pressure of up to 60 GPa is required to expand Ti, so that it can accommodate larger Mg atoms in its lattice. On the other hand, maximum pressure of 10 GPa is necessary to compress Mg such that it can be host Ti atoms.

When the theoretical density of HCP ss is varied linearly, the lattice parameters *a* and *c* as well as the *c/a* axial ratio have to change linearly as well, as shown in figure 9.3.2.1.2(a) and (b), respectively, together with corresponding required pressure. The lattice parameter, density and pressure trends of HCP ss are similar to those of cubic phases. As expected in accordance with Vegard's law, the plots in figures 9.3.2.1.1(a) and 9.3.2.1.2(a) indicate that introducing a larger atom into smaller one should result in expansion of the latter. In addition, as shown in figures 9.3.2.1.1(b) and 9.3.2.1.2(b), the densities behave as expected since introducing lighter element (Mg) into denser element (Ti) leads to less dense solid solution alloy.

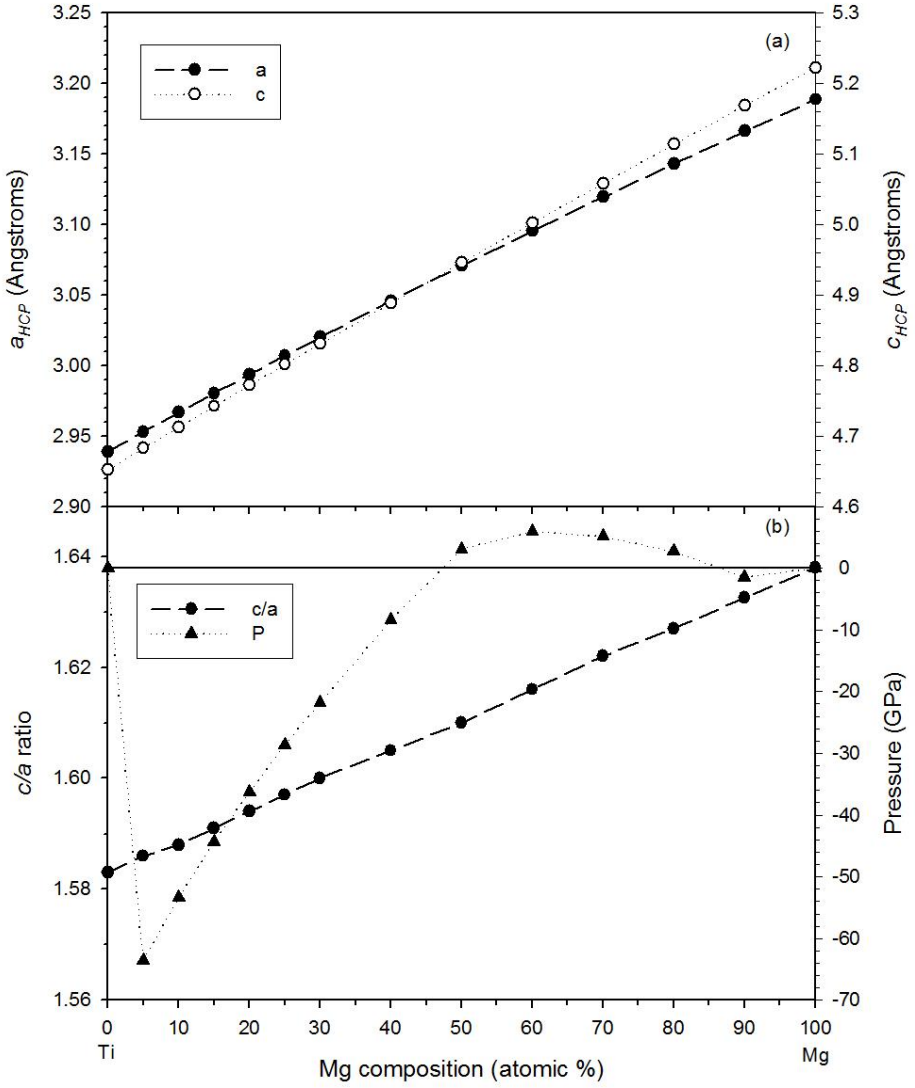

Figure 9.3.2.1.2. Structural properties of Ideal HCP Ti-Mg ss and the corresponding required conditions.

The corresponding required pressures for HCP, FCC and BCC ss are plotted against Mg content in figure 9.3.2.1.3. In comparison, HCP ss requires less compressive and more expansion pressure than FCC and BCC ss at Mg- and Ti-rich compositions, respectively.

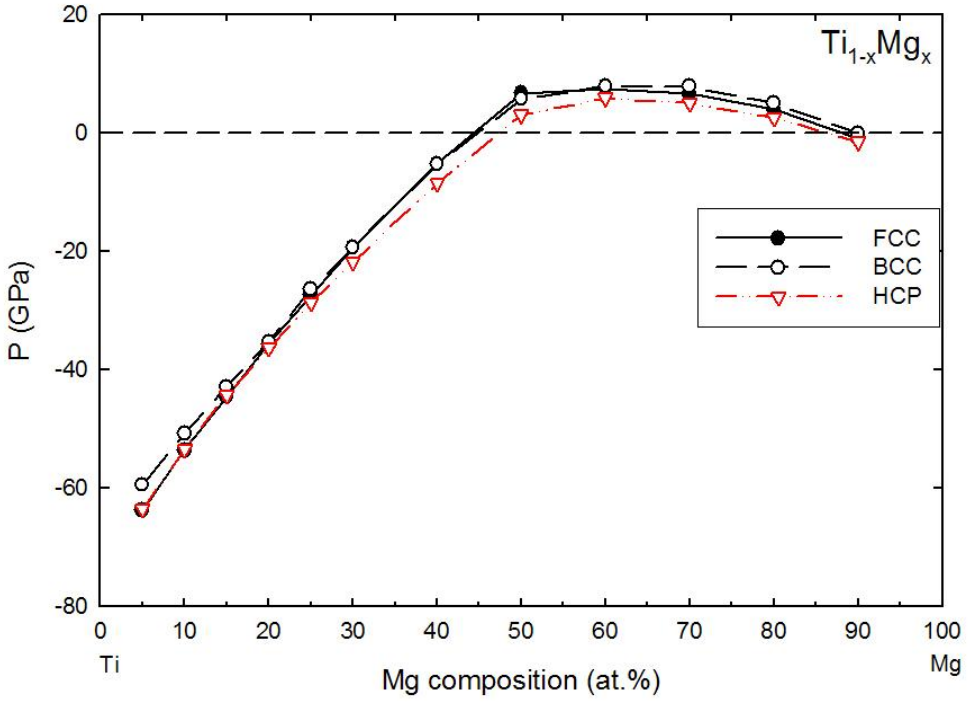

Figure 9.3.2.1.3. Predicted pressures required to obtain ideal HCP, FCC and BCC solid solutions according to Vegard's law.

For ideal Ti-Mg solid solutions, the calculated binding energy, structural energy difference with respect to HCP ss and heats of formation are plotted against Mg composition in figure 9.3.2.1.4 (a), (b) and (c), respectively. As shown in figure 9.3.2.1.4(a) and (c), the trend for Ti-Mg ss at non-equilibrium conditions (P≠0) is similar to that at equilibrium but the values of binding and formation energies increased from those at equilibrium, especially for compositions below 40 at.% Mg. This increase in binding and forming energies indicates unfavourable thermodynamic conditions for the process of alloying to occur. Above 40 at.% Mg these quantities are equal for Ti-Mg ss at equilibrium and non-equilibrium conditions. From Fig. 9.3.2.1.4(c), the heats of formation becomes positive for Mg compositions above 60 at.%. Thus Mg compositions

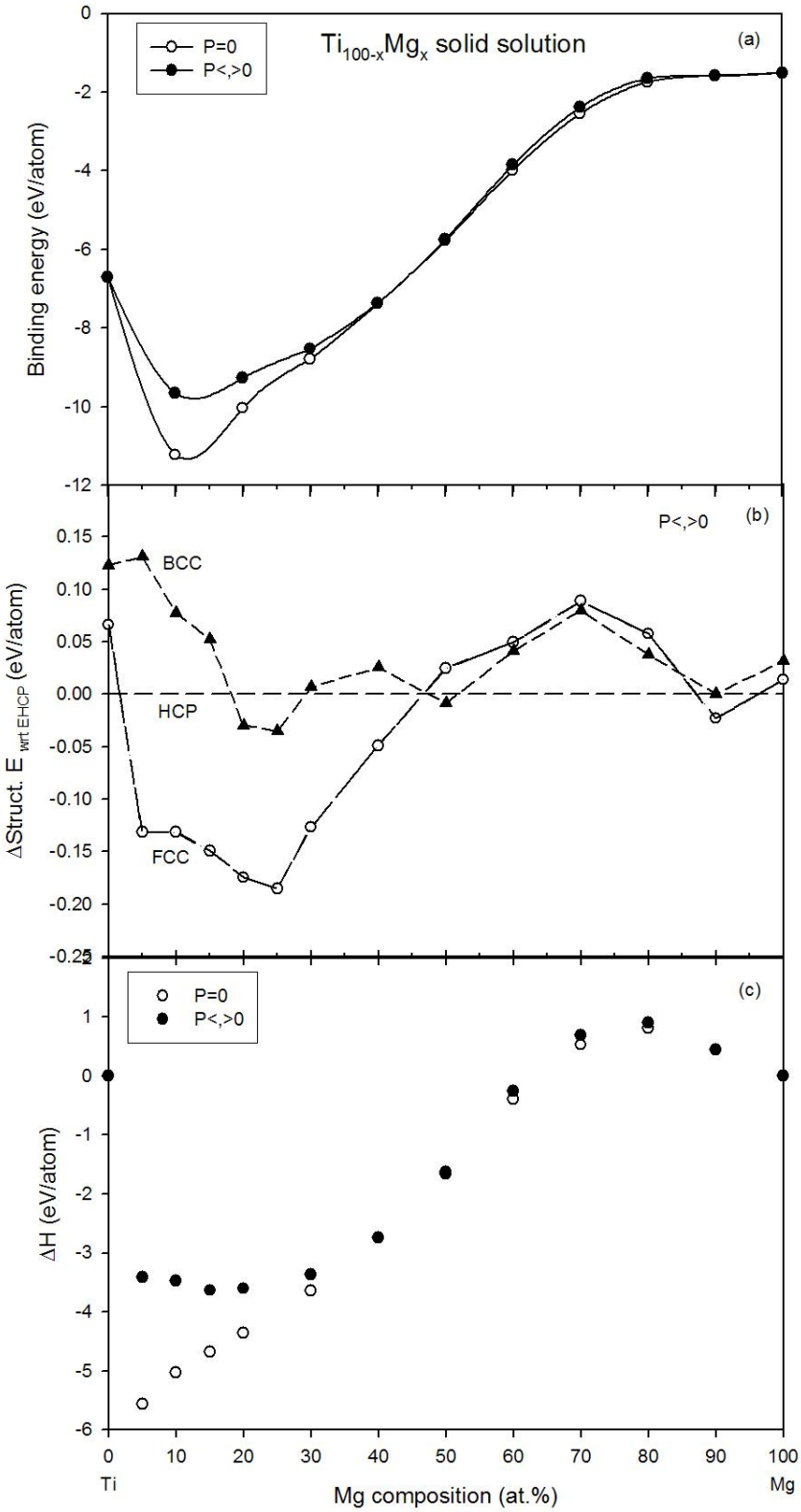

Figure 9.3.2.1.4. The predicted (a) binding energy , (b) structural energy difference and (c) formation energy, for Ti-Mg solid solutions.

below 60 at.% could be dissolved in Ti, hence rendering this value to be the solubility limit. On the other hand, Mg compositions above this solubility threshold are thermodynamically unlikely as evidenced by positive heats of formation.

In regard to phase stability shown in figure 9.3.2.1.4(b), the FCC ss is most stable below 50 at.%, while BCC ss dominates at 50:50 equi-atomic composition, above which HCP is most stable until just less than 90 at.%. The FCC ss is superior in stability over HCP and BCC ss at 90 at.% Mg. The observed trend in formation energy is similar to that reported by Badmos and Bhadeshia (1997) for immiscible system at 1000K.

9.3.2.2. Elastic properties

In figure 9.3.2.2.1, the bulk modulus (*B*), *B/G* and Young's modulus (*E*) are presented in (a), (b) and (c) respectively, for HCP, FCC and BCC Ti-Mg ss at various compositions. An abrupt anomalous drop of *B* in Ti-rich compositions (below 40 at.% Mg) to even below the bulk modulus of pure Mg is observed, as shown in figure 9.3.2.2.1(a). This behaviour is rather strange, since it is expected that harder Ti be slightly softened by the presence of softer Mg. However, this odd behaviour normalizes between 40 and 60 at.% Mg but re-emerges between 70 and 90 at.% Mg. The sharp reduction in *B* could be attributed to the required large expansion (~ 60 GPa) shown in figure 9.3.2.1.3, which then weakens the hardness of Ti.

On the other hand, it is unusual that in Mg-rich compositions, where the resultant pressure is positive, the solid solution remains softer than Mg. Thus far it is not yet clear how pressure influences the behaviour of *B*. However, it is interesting to note that this anomalous behaviour corresponds to brittleness, as indicated by *B/G* values falling below the 1.75 critical value, as shown in figure 9.3.2.2.1(b). The *B/G* values lie almost at 1.75 between 40 and 60 at.% Mg. In figure 9.3.2.2.1(c), the Young's moduli (*E)* for FCC ss remains positive at 50 at.% Mg and below, while it fluctuates for BCC ss between negative and positive values though mostly negative. Above the 50:50 composition, the situation reverses, where *E* for BCC ss is positive while for the FCC ss

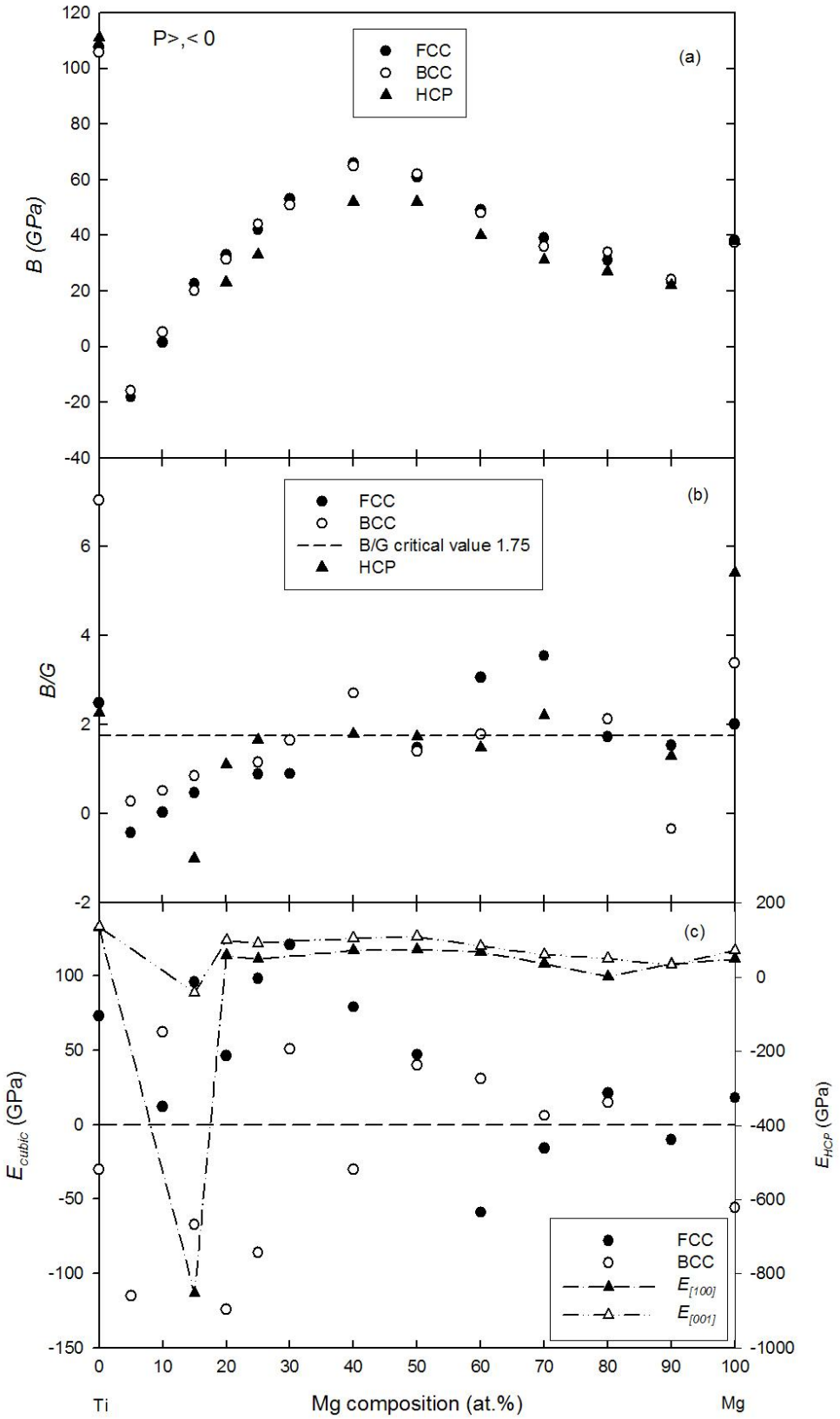

Figure 9.3.2.2.1. Predicted mechanical properties for ideal HCP, FCC and BCC Ti-Mg solid solutions.

is mostly negative. In contrast, for HCP ss the $E_{[100]}$ and $E_{[001]}$ are positive for almost the entire composition range, except for compositions below 20 at.% Mg where they both become negative.

According to mechanical stability criteria given in chapter 7 (equation 7.2.1 and 7.2.3 for cubic and hexagonal crystal structures, respectively), the mechanical phase stability results are plotted against Mg composition in figure 9.3.2.2.2(a), (b) and (c) for HCP, FCC and BCC ss respectively. A similar behaviour to that in figure 9.3.2.2.1(c) for *E* of HCP ss below 20 at.% Mg composition is again observed in all corresponding shear moduli presented in figure 9.3.2.2.2(a). It thus goes without doubt that the HCP ss in this composition range is mechanically unstable. However, for Mg compositions above 20 at.%, all HCP ss are stable since the values of shear moduli responsible for mechanical stability are all greater than zero, thus satisfying the set criteria.

The elastic stability of FCC ss as shown in figure 9.3.2.2.2(b) indicates stability at 50 at.% Mg and below, which corresponds to its positive values of *E* in figure 9.3.2.2.1(c), although some discrepancy is depicted at 20 at.% Mg where *E* is positive but C_{44} being slightly negative. However, above 50 at.% the tetragonal shear modulus (*C'*) of FCC ss becomes negative except for $Ti_{20}Mg_{80}$ composition. This trend again resembles that of Young's modulus observed in figure 9.3.2.2.1(c). The similarity of *E* and *C'* trends is also evident in BCC ss, where *C'* is negative below 50 and above 80 at.% Mg, and remains positive between 50 and 80 at.% Mg, as shown in figure 9.3.2.2.2(c). It seems C_{44} does not play a crucial role as C' in determining the mechanical stability of crystal structures.

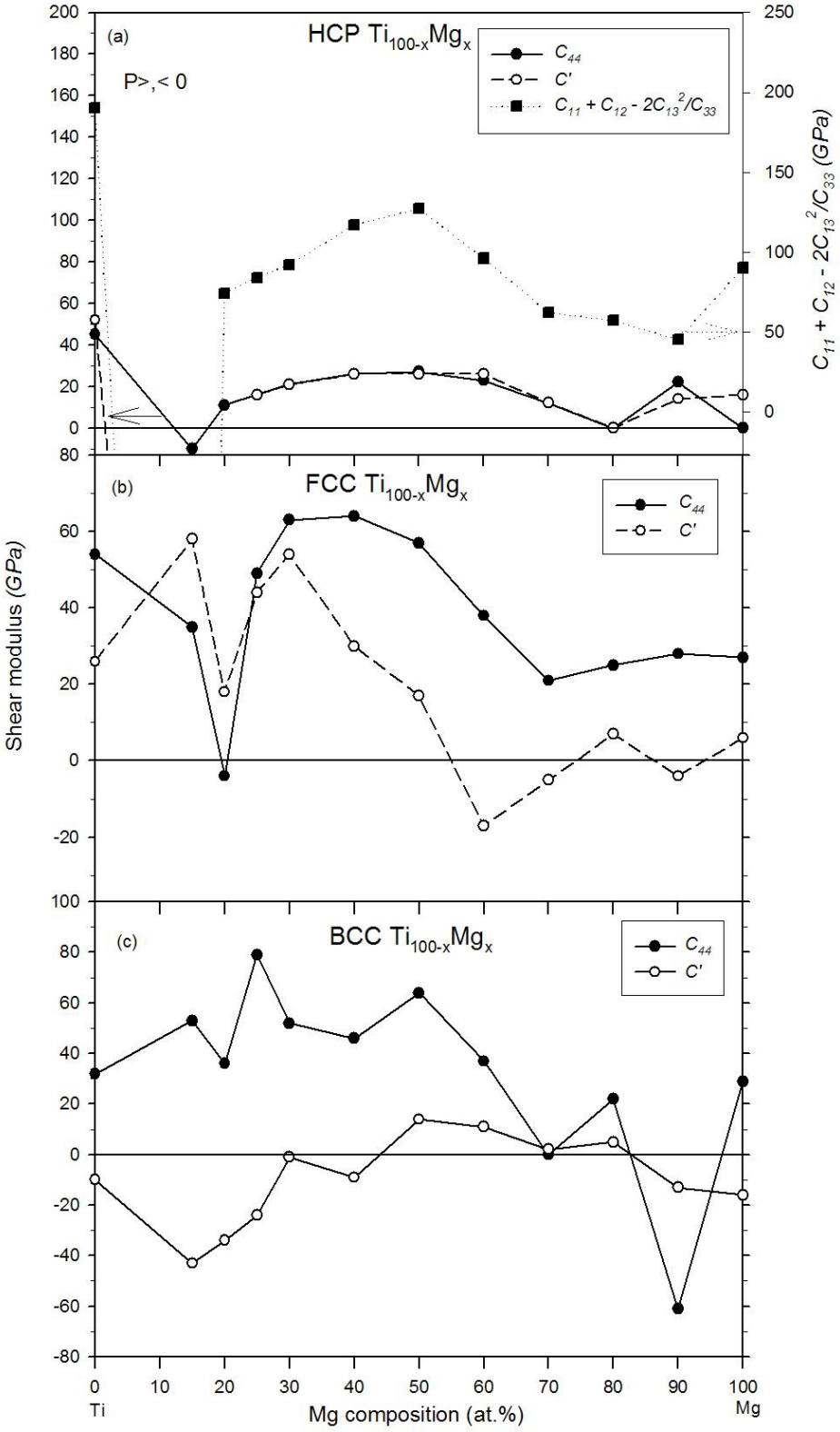

Figure 9.3.2.2.2. Predicted mechanical stability of ideal (a) HCP, (b) FCC and (c) BCC Ti-Mg solid solutions. The units for shear moduli are GPa.

9.3.3. Conclusion

Under non-equilibrium conditions (T=0K, P≠0), i.e. forcing Ti-Mg ss to adhere to Vegard's law, caused the following:

(a) An increase in binding and formation energies, indicating unfavourable thermodynamic process.
(b) Stabilization of FCC ss over HCP at Ti-rich compositions.
(c) Anomalous changes of mechanical properties, especially for Ti-rich compositions where the required expansion is severely high, thus reducing the bulk modulus of the solid solution.

In summary, as observed from elastic properties of Ti-Mg system under equilibrium and non-equilibrium conditions, the trigonal shear modulus (C_{44}) does not appear to play a vital role in determining the mechanical stability of HCP, FCC and BCC crystal structures as the tetragonal shear modulus (C') does. The elasticity trends of Young's modulus and Poisson's ratio are similar to those of C', and therefore may also be used to determine mechanical stability of crystal structures. The mechanical instability (negative E, υ, C') seems to correspond to brittleness (B/G < 1.75) of crystals. From figure 9.3.2.1.4(c) the maximum solubility of Mg in Ti can be deduced, as shown by negative heats of formation. Thus compositions below 60 at.% Mg could be dissolved in Ti, thus rendering this value to be the solubility limit. However, since elemental powders undergo same impacts during ball milling, and the process cannot be controlled such that it expands crystals of one element while at the same time the crystal structure of the other metal is kept the same or compressed in a hydrostatic manner (in all dimensions) as predicted by current calculations. Therefore, besides favourable thermodynamics, the necessary structural kinetics could not be achieved by BM process. This conclusion in is support of our experimental results that yielded no Ti-Mg solid solution.

9.4. Use of norm-conserving pseudopotentials to study Ti-Mg solid solutions at equilibrium

9.4.1. Computational procedure

In the previous chapter, norm-conserving pseudopotentials (NCP) was used to predict reliable structural and elastic properties of well studied binary disordered Mg-Li system. Consequently, in this subsection, we employed them to further investigate phase and elastic stability of Ti-Mg solid solutions under equilibrium conditions. Furthermore, in the recent article by Tegner and Ackland (2012), it was shown that arbitrary choices in the reference configuration (due to the importance of treating the 3s and 3p semi-core states of pure Ti explicitly) can lead to significant differences in the calculated quantities. Despite the valence electron configurations of $3s^2$ and $3d^2 4s^2$ for Mg and Ti, respectively, all other parameters for geometry optimization calculations were kept the same as those in section 9.2.1

9.4.2. Results and discussions

9.4.2.1. Phase stability

In figure 9.4.2.1.1, the predicted equilibrium (T= 0K, P= 0 GPa) lattice parameters of HCP, FCC and BCC Ti-Mg solid solutions plotted against Mg atomic composition are presented in (a), (b) and (c), respectively. As expected, the lattice parameters of pure metals are underestimated (a=2.8994, c=4.6624 Å for Ti and a=3.1307, c=5.1460 Å for Mg) due to known short-comings for the use of norm-conserving pseudopotential (NCP). Common in the above solid solutions, the lattice parameter variation deviates (positively) from Vegard's law (indicated in figure 9.4.2.1.1(c)), since it is not changing linearly with increasing Mg content. In addition, the corresponding theoretical densities presented in 9.4.2.1.1(b) for FCC ss follow the same pattern in all the three crystal structures, which also show deviation from Vegard's law. As shown in figure 9.4.2.1.1(a)-(c), the lattice parameter a of HCP, FCC and BCC ss increases with

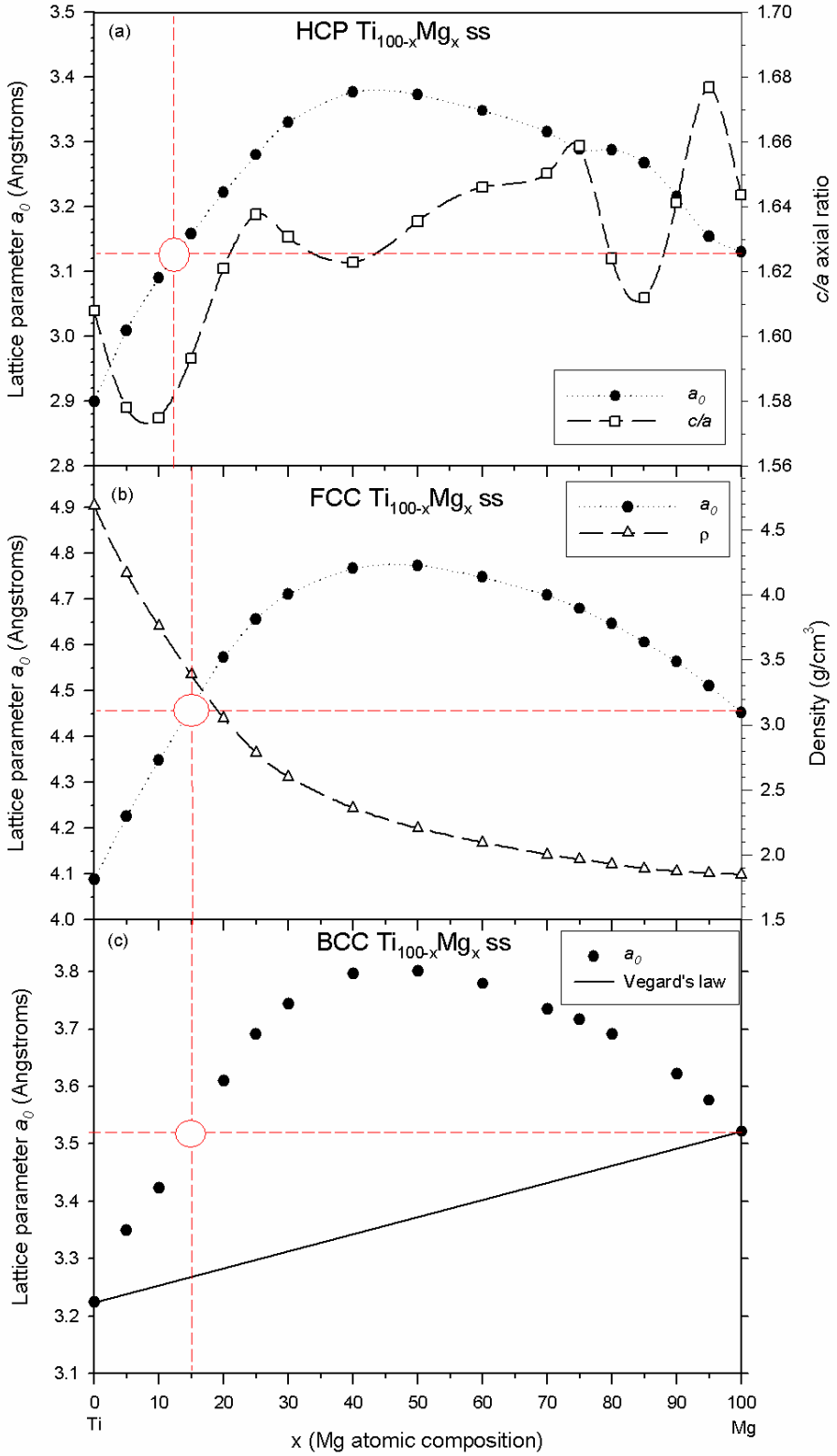

Figure 9.4.2.1.1. Predicted structural properties of Ti-Mg solid solutions under equilibrium conditions, (a) lattice parameter *a*, *c/a* ratio for HCP, (b) lattice parameter *a*, theoretical density for FCC and (c) lattice parameter *a*, Vegard's law variation for BCC, $Ti_{100-x}Mg_x$ ss.

increase in Mg composition until reaching a maximum value at 50 at.% and decreases afterwards. It took about 15 at.% Mg dissolution in Ti to reach the lattice size of pure Mg, as shown by red dashed lines intersecting at red circles. Beyond this Mg composition the lattice sizes become larger than both constituent metals. This behaviour above 15 at.% Mg could be an indication of immiscible region or that temperatures higher than melting point of Ti are required to achieve such solid solutions. Although not presented in figure 9.4.2.1.1(a), the lattice parameter *c* of HCP ss also follows a similar trend. However, the corresponding *c/a* axial ratio fluctuates with increase in Mg composition. Based on proposed MT mechanisms in chapter 6, the minimum and maximum *c/a* ratios at 10 and 25 at.% Mg compositions correspond to lower prismatic and basal slip activation stresses (CRSS), respectively. In comparison to the experimentally claimed HCP, FCC and BCC Ti-Mg solid solutions [Asano *et al* 2009a], our predicted lattice parameter values are quite large. Moreover, using the lattice parameters reported by Asano *et al*, our predicted results show that these values correspond to Mg compositions of less than 10 at.% compared to between 35 and 80 at.% as claimed.

The calculated binding energy, structural energy differences with respect to HCP ss as well as heats of formation for HCP, FCC and BCC solid solutions (ss) are plotted against Mg composition in the lower *x*-axis and *e/a* (valence electron/atom) ratio in the upper *x*-axis in figure 9.4.2.1.2(a), (b) and (c), respectively. The latter is also known to influence the crystal structure upon alloying [Mott and Jones 1936, Paxton *et al* 1997, Phasha *et al* 2010a]. We have again replotted the *c/a* ratio (as shown in figure 9.4.2.1.2(a)) for the sake of clarity when discussing the apparent phase transition. Similar to figure 9.3.2.1.4(a), an anomalous behaviour is observed in Ti-rich side where there is a sharp increase in binding energy on introduction of Mg, reaching maximum at 15 at.% which corresponds to *e/a*=3.70 and intersections in figure 9.4.2.1.2(b) and (c). However, BE decreases significantly upon addition of Mg between 15 and 25 at.% while the gradual linear rise is observed beyond 25 at.% up to pure Mg. On the other hand, the difference in structural energy indicates HCP stability domination in the Mg composition range $0 \leq x < 25$. Interesting, FCC $Ti_{100-x}Mg_x$ ss becomes most stable than

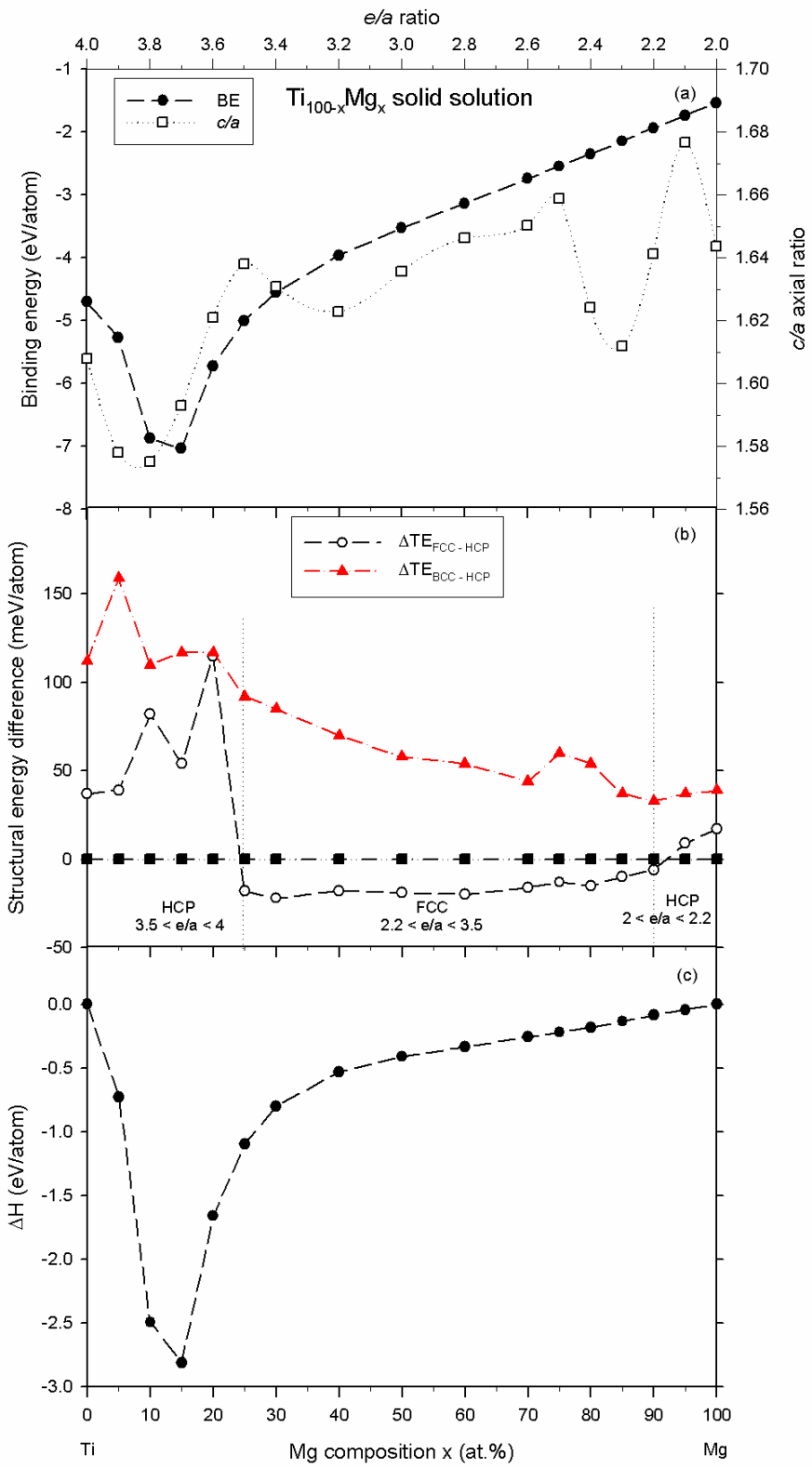

Figure 9.4.2.1.2. The calculated (a) binding energy, *c/a* ratio for HCP, (b) structural energy difference with respect to HCP lattice and (c) heats of formation at equilibrium, for $Ti_{100-x}Mg_x$ ss,. The plotted binding and formation energy were calculated from the most stable phase at every composition of interest.

HCP at 25 at.% Mg and above. This composition corresponds with *c/a*=1.638 for HCP ss which is larger than ideal 1.633 and also with *e/a* ratio of 3.50 when s, d valence electrons are considered to account for crystal structure stability. This HCP→FCC transition in Ti-Mg ss is similar to that shown in figure 8.1.3.2.1 for $Mg_{100-x}Li_x$ ss induced by dissolution of Mg in Li in the concentration range 60≤x≤90 corresponding to 1.10≤*e/a*≤1.40.

Similarly, the FCC $Ti_{100-x}Mg_x$ ss is stable up to 90 at.% Mg corresponding to 2.20≤*e/a*≤3.50, above which the HCP ss is stable. On heats of formation, a similar trend to that in figure 9.4.2.1.2(a) for binding energy is also observed, as shown in figure 9.4.2.1.2(c), though the energy is lower by more a half compared to binding energy. These results again appear to suggest that the formability of the alloy depends strongly on its cohesion ability. However, contrary to USP-based calculations in section 9.2 and 9.3 which predict the solubility limit around 60 at.% Mg concentration, the solid solubility using NCP is predicted to occur over the entire concentration range.

9.4.2.2. Elastic stability

In figure 9.4.2.2.1(a)-(c), we present the predicted mechanical properties such as the bulk modulus (*B*), *B/G* ratio and Young's modulus (*E*) for HCP and FCC $Ti_{100-x}Mg_x$ solid solutions, since the BCC-based ss were not energetically favourable in the entire concentration range as shown in figure 9.4.2.1.2(b). It is evident from figure 9.4.2.2.1(a) and (c) that *B* and *E* of HCP and FCC solid solution increases on Mg addition, reaching maximum values at 10 at.% Mg except for *E* of FCC ss which reach maximum at 15 at.%. The first behaviour is similar to that in figures 9.2.2.2.1(a) and 9.2.2.2.2(a). Thereafter, these values decreases gradually with increasing Mg amount until at 100 at.% Mg. Our results imply that the introduction of Mg in less 15 at.% composition will yield Ti-Mg alloy with bulk and Young's modulus higher than that of pure Ti. This point is futher supported by *B/G* results in figure 9.4.2.2.1(b), which suggest brittleness tendency as indicated reducing *B/G* value to less than the critical 1.75 on addition of Mg. Of significant interest is that $E_{[100]}$ and $E_{[001]}$ for HCP ss become equal at 25 at.%

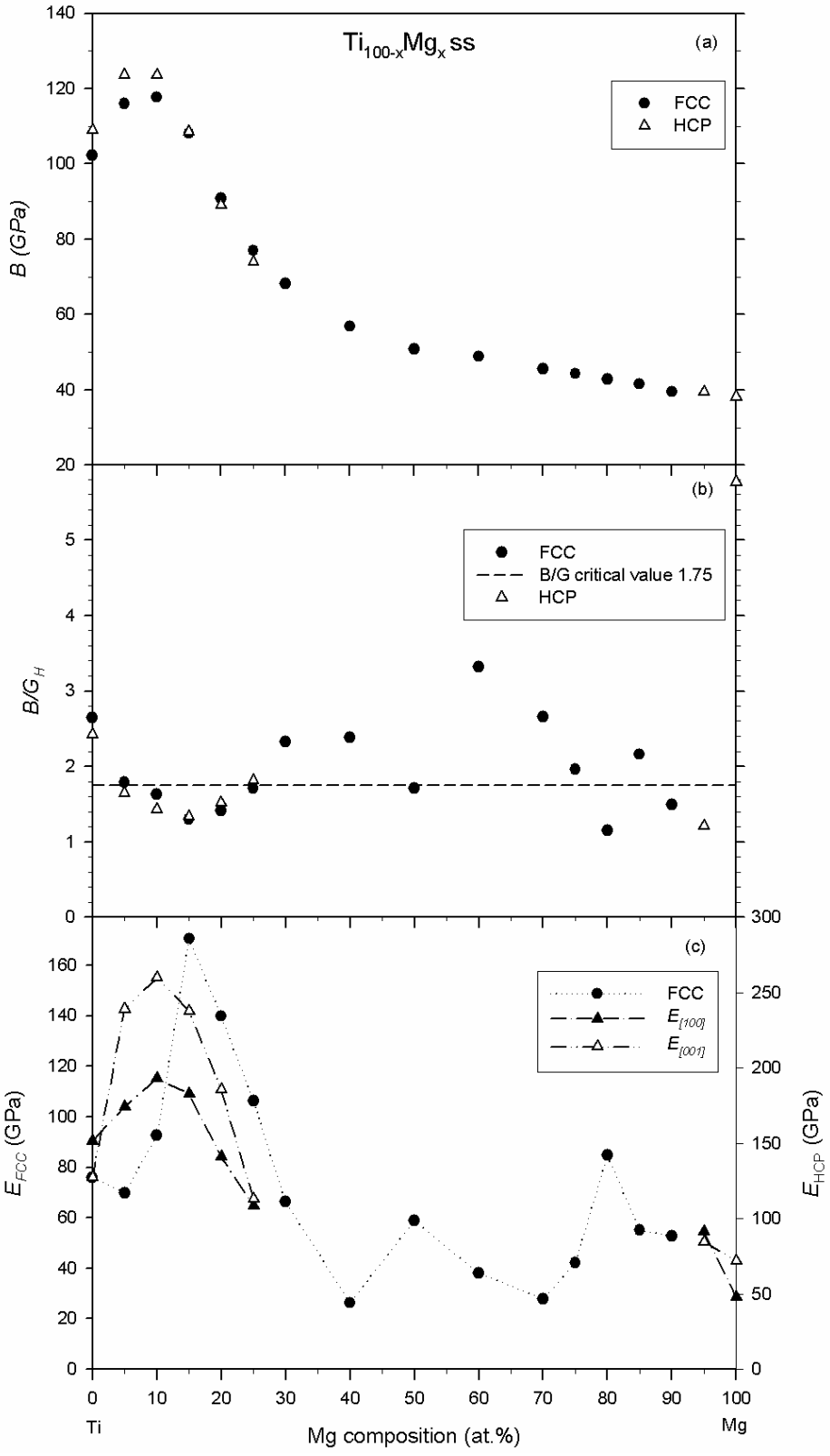

Figure 9.4.2.2.1. The predicted mechanical properties for (a) stable HCP and (b) FCC $Ti_{100-x}Mg_x$ solid solutions.

Mg, which indicates isotropic behaviour compared to the well known anisotropic behaviour in HCP metals, hence the basis for HCP→FCC transition. Generally, all the energetically stable compositions of FCC $Ti_{100-x}Mg_x$ ss are ductile, as shown by *B/G* values higher than 1.75.

In figure 9.4.2.2.2(a) and (b), the predicted mechanical stability for energetically stable HCP and FCC $Ti_{100-x}Mg_x$ ss, respectively, are presented. In terms of mechanical stability, our results comply with the expressions for mechanical stability criterion for hexagonal and cubic crystals.

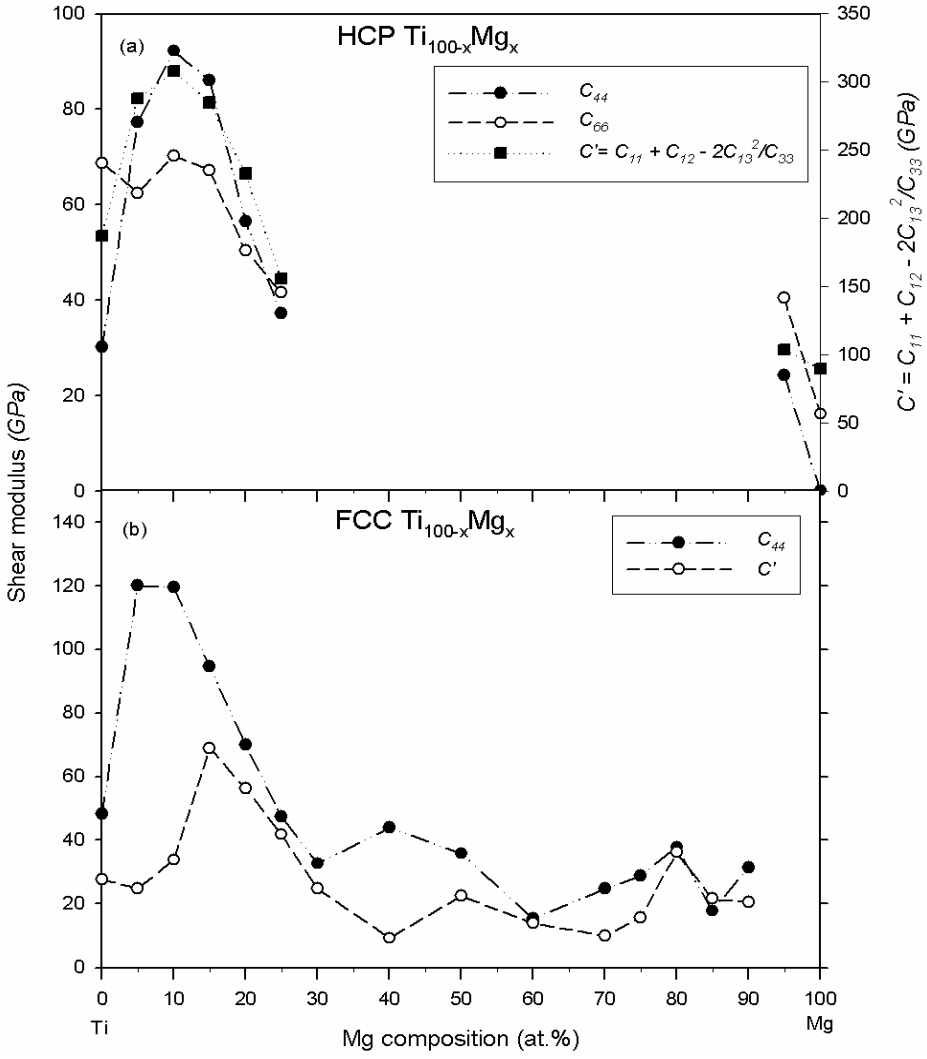

Figure 9.4.2.2.2. The predicted mechanical stability for (a) stabe HCP (0≤x≤25) and (b) FCC $Ti_{100-x}Mg_x$ solid solutions.

Similar to results in figure 9.4.2.2.1(a) and (c), maximum values of C_{44} and C_{66} are observed at 10 at.% Mg for HCP ss while maximum values of C_{44} and C' are shown at 10 and 15 at.% Mg respectively. These results indicates that an increase in *E* shown in figure 9.4.2.2.1 is due to tetragonal shear *C'*, while an increase in *B* is associated with increase in trigonal shear C_{44}. It is therefore apparent from the rise in elastic moduli that when Mg content of less than 15 at.% is introduced into Ti, solid-solution strengthening occurs.

9.4.3. Conclusion

From NCP-based *ab initio* calculations used to predict phase and mechanical stability of Ti-Mg ss at equilibrium, the formation energy as well as elastic constants yielded similar stability trends that can be summarized as follows:

i. From 0 to 20 at.% as well as between 90 and 100 at.% Mg, the solid solutions with HCP crystal structure are both energetically and mechanically stable.
ii. Similarly, the FCC $Ti_{100-x}Mg_x$ ss with composition range $25 \leq x \leq 90$ are both energetically and mechanically stable.
iii. However, in compositions considered in the current study, the formation of BCC $Ti_{100-x}Mg_x$ ss is the least favourable.
iv. Compared to USP-based calculations in section 9.2 and 9.3 which predict the solubility limit around 60 at.% Mg concentration, , the solid solubility using NCP is predicted to occur over the entire concentration range in the following manner: 0 to 20 at.% Mg soluble in α Ti, 25 to 90 at.% Ti soluble in FCC Mg and 0 to 10 at.% Ti soluble in HCP Mg.
v. Maximum increase in *B* is achieved upon addition of 10 at.% Mg in both HCP and FCC ss while maximum *E* is shown at 10 and 15 at.% Mg for HCP ss and FCC ss, respectively, is attributed to solid-solution strengthening effect.

Therefore, owing to the effect of using different pseudopotentials (NCP) which utilizes recpot potentials (extention) to represent Ti and Mg, reasonable atomic properties gave

apparently reliable and different structural properties of $Ti_{100-x}Mg_x$ solid solutions compared to USP. However, the ground-state stability of pure metals was not altered. The results on HCP→FCC transition upon introducing 25 at.% Mg are supported by our predicted values for basal slip, which indicated CRSS of 121 and 658 MPa for Mg and Ti, respectively. Therefore this transition can be described as dissolution of Ti in FCC Mg. From NCP-based calculations, dissolution of Mg in Ti and vice versa is thermodynamically favourable. Nonetheless, for compositions in which the predicted lattice parameters are greater than those of pure constituent metals, current results indicate that either the temperatures higher than melting points of Ti and Mg are required to achieve such solid solutions or addition of Mg beyond 15 at.% leads to solution weakening as shown by decrease in the corresponding elastic properties. Consequently, for practical realisation of Ti_{100-x}-Mg_x solid solutions in the composition range $x > 15$ by conventional methods, the known long standing thermodynamic limitation for dissolving appreciable amount of Mg in Ti will come into play (vapourization temperature of Mg is lower than melting temperature of Ti). On the other hand, in line with our experimental findings, the only obstacle to forming such solid solutions by BM is the quick formation of metastable Ti hydrides or cold welding at early stages of the process.

Chapter 10

Conclusion and Recommendations

A combination of ball milling experiments and *ab initio* calculations in this study successfully yielded results that shed light into understanding the fundamental basis for immiscibility and the concept of mechanical alloying in Ti-Mg system. In addition, the conditions for achieving extended solid solubility in elements that usually do not dissolve in each other under thermodynamic equilibrium conditions have been predicted using ultrasoft (US) and norm-conserving (NC) pseudopotentials. Pressures required to stabilize ordered phases were determined. Our new systematic representation of martensitic transformation (MT) paths as a result of dislocation necessary to induce α→FCC, α→BCC and α→ω phase transitions led to, for the first time, a direct determination of CRSS in Ti and Mg metals. Furthermore, a new crystal structure of ω phase is predicted, which requires uniaxial pressure of 4.167 GPa to be induced.

Attempts to synthesize Ti-Mg solid solutions by means of Simoloyer high energy ball milling were not successful; however, nanocrystalline Mg-TiH_{2-x} composites were instead formed. These results were attributed to quick formation of metastable Ti hydrides or cold welding at early stages of BM prior to alloying. The deformed Ti crystals adsorbed H^+ from the deprotonated stearic acid leading to formation of metastable orthorhombic TiH_{2-x} phase which later transformed to a tetragonal TiH_{2-x} or even cubic TiH_2 when stoichiometric amount of H_2 had been adsorbed. The crystallite sizes of the products formed at higher milling speed were larger than those formed at lower milling speed. However, the kinetics for protonation of Ti crystals were enhanced in powder particles milled at the higher speed. Twins were observed along the grain boundaries in some particles of powders milled for shorter times. The current study noted that starting with a mixture containing coarse magnesium powder particles (300 – 600 μm) that are 10 times larger than the titanium particles led to different process steps than those observed in high-energy ball milling of fine (< 45 μm) titanium and

magnesium particles. Although the yield was significantly lower, product of milling a mixture of coarse Mg and fine Ti particles was comprised of Ti particles adhering around ductile Mg particles in a core shell manner. The adhesion of the fine hard titanium particles on the surface of the large ductile magnesium particles impeded the further plastic deformation of the titanium particles, thus suppressing the formation of the faults necessary for mechanical alloying. The yield dropped drastically when the milling time is longer than 24h owing to an increase in the total area of the fine powder particles not coated by the PCA. This led to an intense cold welding of powder particles on the walls of the jar. Both XRD and TEM techniques revealed the existence of FCC- and BCC-based products together with traces of HCP Mg and Ti phases in materials milled for 24–48h and 72h, respectively at 800 rpm.

Nanocrystalline Ti powder of about 40 nm was produced by ball milling for 30 h. During BM of Ti powder, solid-state transformation from HCP to FCC occurred in the presence of PCA with lattice parameters of 4.242 and 4.240 Å after 24 and 30 h, respectively, due to protonation. Upon sintering, the metastable FCC phase changed to rhombohedral (trigonal) phase and the presence of α phase was detected. The appearance of α phase could suggest that prolonged milling led to dispersion or coating of α Ti particles by FCC/FCT-based Ti hydride particles, hence possibility of resurfacing on sintering. When Ti powder was milled in the absence of PCA, no phase transformation was observed for both uninterrupted and interrupted milling cycles. In addition, nanocrystalline Mg powder with crystallite size varying between 60 and below 40 nm was produced by ball milling. However, no solid-state phase transformation took place even if the powder was milled for 90 h. Therefore, for the first time, we evidently report that the interstitial H^+ is the driving force for α → FCC phase transformation in ball milled Ti powder

Therefore, following current results, we propose a unique mechanism during ball milling of Ti-Mg mixtures in the presence of PCA as follows: Mg particles get enclosed or covered by harder TiH_{2-x} particles, in a “chewing gum-sand” or “core-shell” manner. These results show that a cross-section of milled powders is vital to confirm mechanical alloying; otherwise the drawn conclusions could be misleading. As a result and in

accordance with Hume-Rothery rules, there is no confirmation for solid solution between Ti and Mg induced by MM but only formation of homogeneous nanocrystalline Mg-TiH_{2-x} composite. This is further evidenced by the fact that the crystal structures of either Mg or Ti remained HCP when milling of each metal powder was carried out in the absence of PCA.

Calculations based on pure metals are summarized as follows:

Our optimization results predicted the ω (omega) phase to be the ground-state structure of Ti at 0 K and 0 GPa, in support of other previously reported *ab initio* results. This stability was further confirmed by the density of states (DOS) results. However, for the usual ω phase, current results show no sign of phase transition up to 200 GPa, except for the distinct anomalous behaviour in all Ti phases between 80 and 100 GPa. Since the stability of the α phase is surpassed by that of the FCC lattice at ~ (about) 100 GPa, therefore this anomaly which corresponds with sudden sharp rise of *c/a* ratio is attributed to α → FCC phase transition. Almost at the same pressure range, the atomic energy of RHL (#166 R-3m) phase is being almost equal to that of FCC phase, although slightly more stable than the FCC above 100 GPa, suggesting a further FCC→RHL transition. According to our knowledge, the correlation of *c/a* ratio and α → FCC phase transition in Ti has never been reported before.

Similarly, the crossing of total energy difference curves between FCC and BCC lattices was also observed at 50 GPa for Mg. However, in this case the crossing coincides with minimum *c/a* around 50 GPa. It is interesting to note that in literature HCP Mg is reported to transform to BCC at this pressure. It may consequently be summarised from our results that the reported Mg HCP→BCC transition at 50 GPa is *c/a* driven shown by rapid *c*-lattice compression over *a*-axis. However, following our proposed HCP→BCC MT path mechanism for Mg, it is evident that the minimum *c/a* at 50 GPa corresponds to a change in the preferred deformation slip from basal (below 10 GPa) to prismatic rather than phase transition since BCC phase remains unstable at this point.

The PDOS plots for Ti at and above 250 GPa indicated the $p \rightarrow s$ electron transfer character as shown by coinciding decrease and increase rates in *p* and *s* orbital fillings, respectively. These changes became rapid between 200 and 250 GPa. Similarly, $p \rightarrow s$ electron transfer is observed at high pressures for Mg, attaining ideal $2p^6 3s^2$ electron configuration at 200 GPa. Hence, the HCP→BCC phase transition commencing above 200 GPa could be linked to $p \rightarrow s$ hybridization after obtaining the ideal $2p^6 3s^2$ electron configuration. As shown by the free-energy difference curves, this transition is only obtained at 250 GPa, which is exactly 50 GPa above ideal electronic structure attainment, in accordance with experimental observations. According to our knowledge, this correlation between the electronic structure and energetic phase transition, especially for Mg, has not been made before.

In spite of smaller energy barrier for basal slip in both metals, our proposed new MT model predicts that elemental Ti and Mg prefers to deform via prismatic slip as indicated by lower shear stress as well as CRSS values compared to those calculated for basal slip. Additionally, the proposed systematic MT paths for Ti reveal that an increase in *c/a* favours the MEP (minimum energy path) for α→FCC transition observed around 100 GPa. Current results therefore indicate that deformation in metals requires stress-assisted activation as opposed to being solely energy driven. In addition, a new ω phase which is less stable than α phase at 0 GPa is proposed. Based on this phase, α→ω deformation path which yielded the onset transition pressure of 4.167 GPa is reported for the first time directly from *ab initio* calculations.

Our theoretical findings from *ab initio* calculations on hypothetical ordered Ti-Mg phases can be summarized as follows:

Phase stability

- The predicted heats of formation for all considered hypothetical ordered Ti-Mg phases were positive at equilibrium, thus confirming inability to form intermetallic compounds.

- The positive heats of formation become negative at 80 GPa and above, with respect to *c/a* ratio. This crossing of miscibility barrier line indicates that there is a transition from the tendency towards phase separation between Ti and Mg at lower pressure to the tendency towards alloying at pressures above 80 GPa.
- With respect to stable lattices, tendency towards alloying requires pressure above 200 GPa for most intermetallic phases while some phases remain immiscible.
- Nonetheless, both approaches (with respect to stable lattice and *c/a*) indicated that forming an intermetallic compound between immiscible Ti and Mg requires activation of basal deformation slip or crystal structure change from α→FCC for Ti and HCP→BCC or prismatic slip for Mg.
- It also emerged from the current study that the necessary deformation or phase change can be obtained by applying high pressure. Thus, due to the entropy contribution, the observed miscibility behaviour could be expected to accelerate further at elevated temperatures.

Mechanical properties

- The calculated high pressure dependence elastic properties of simple cubic phases were presented. It was evident from these results that the stability at 50:50 and for Ti-rich phases increases with pressure as indicated by rising shear moduli, C_{44} and C'. It is also clear from values of *B/G* ratio that the ductility is improving as a function of pressure. Furthermore, the bulk and Young's moduli as well as the Posson's ratio also increase with pressure.
- In cubic Mg-rich compounds, below 50 at.% Ti, conversely, the stability is negatively affected (suffers) by an increase in pressure. This is indicated by ever declining shear moduli C' and *G* in addition to Poisson's ratio larger than 0.5. It is also apparent that the only Ti-Mg compound that behaves isotropically is C15 structure with $TiMg_2$ composition, since all shear moduli C_{44} , C' and G are equal.
- Using calculated heats of formation, elasticity and DOS, it has been possible to show that $L1_2$ $TiMg_3$ could not form even at high pressure as 250 GPa.

- In general, the DOS for formable alloys are characteristic of a strong hybridization between *d*-states of Ti, which serves as electron acceptor and *s*-states of Mg, which acts as electron donor. In compounds where this electron transfer does not occur, it is apparently difficult to stabilize them or for them to cross the miscibility barrier.

A proposed DFT-based solid solution model successfully predicted reliable phase stability and elastic property trends of binary random Mg-Li alloys comparable to available theoretical and experimental results. These results which were generated using NCP calculations can be summarized as follows:

- The predicted phase stability trends at 0K resemble those observed experimentally in Mg-Li phase diagram, especially at lower temperatures.
- Furthermore, the mechanical properties of random binary Mg-Li alloys, spanning the entire composition range, were predicted for the first time using DFT-based calculations and were found to be in excellent agreement with earlier experiments.
- The proposed model for random alloys is not only accurate but also less computationally expensive compared to traditional supercell approach.
- Following correct prediction of structural, cohesive as well as mechanical properties of binary Mg-Li alloys, this approach will enable researchers to study other properties such as surface properties of disordered binary Mg-Li alloys with ease.
- Therefore the use of correct crystal structure, symmetry and choice of reliable pseudopotentials to mimic the experimental solid solutions is a crucial benchmark. The current approach does not only predict correct structural properties but it is also computationally and time efficient.

Similar to the proposed model for Mg-Li system with 100% solid solubility, the findings from *ab initio* calculations on binary Ti-Mg solid solutions can be summarized as follows:

Under equilibrium conditions (T=0K, P=0) using USP, we observed the following:

- The lattice parameters as well as density deviate significantly from Vegard's rule of ideal solid solutions.
- According to our predicted heats of formation, up to 60 at.% Mg could be dissolved in HCP Ti to form a solid solution, obviously much higher than experimentally observed.
- On introducing small amounts of Mg into Ti, the mechanical properties increases abruptly to above those of pure constituent elements. This behaviour changes on further Mg addition towards 50:50 atomic composition.

Under non-equilibrium conditions (T=0K, P≠0) using USP, i.e. compelling Ti-Mg ss to adhere to Vegard's law, causes the following:

- A decrease in binding and formation energies, indicating unfavourable thermodynamic process.
- Stabilization of FCC ss over HCP at Ti-rich compositions.
- Anomalous changes of mechanical properties are noted, especially for Ti-rich compositions where the required expansion is severely high (~60 GPa), thus reducing the bulk modulus of the solid solution in this region.

In general, as observed from elastic properties of Ti-Mg solid solutions under equilibrium and non-equilibrium conditions, the trigonal shear modulus (C_{44}) does not appear to play a vital role in determining the mechanical stability of HCP, FCC and BCC crystal structures as the tetragonal shear modulus (C') does. The elasticity trends of Young's modulus and Poisson's ratio are similar to those of C', and therefore may also be used to determine mechanical stability of crystal structures. The mechanical instability (negative E, υ, C') seems to correspond to brittleness (B/G < 1.75) of crystals. From figure 9.3.2.1.4(c) the maximum solubility of Mg in Ti can be deduced, as shown by negative heats of formation. Thus compositions below 60 at.% Mg could be dissolved in Ti, thus rendering this value to be the solubility limit.

Finally, as they were successfully tested for Mg-Li system, we employed NCP to study Ti-Mg solid solutions at equilibrium. In accordance with NCP-based calculations, the formation energy as well as elastic constants, yielded similar stability trends that can be summarized as follows:

- From 0 to 20 at.% as well as between 90 and 100 at.% Mg, the solid solutions with HCP crystal structure are both energetically and mechanically stable.
- Similarly, the FCC $Ti_{100-x}Mg_x$ ss with composition range $25 \leq x \leq 90$ are both energetically and mechanically stable.
- However, in compositions considered in the current study, the formation of BCC $Ti_{100-x}Mg_x$ ss is the least favourable.
- Compared to USP-based calculations in section 9.2 and 9.3 which predict the solubility limit around 60 at.% Mg concentration, the NCP-based calculations predicted the solid solubility to occur over the entire concentration range in the following manner: 0 to 20 at.% Mg soluble in α Ti, 25 to 90 at.% Ti soluble in FCC Mg and 0 to 10 at.% Ti soluble in HCP Mg.
- Maximum increase in *B* achieved upon addition of 10 at.% Mg in both HCP and FCC ss, as well as the maximum *E* is shown at 10 and 15 at.% Mg for HCP ss and FCC ss, respectively, are attributed to solid-solution strengthening effect.

Congruently, owing to usage of NC pseudopotentials which utilizes recpot potentials (extentions) to represent Ti and Mg as opposed to usp potentials, reasonable atomic properties gave apparently reliable and different structural properties of $Ti_{100-x}Mg_x$ solid solutions, as was the case with Mg-Li system. However, the only set back remains underestimation of structural properties. On the other hand, in spite of predicting accurate structural properties for constituent pure metals as well as ordered phases, the USP-based calculations fail to provide meaningful trends for disordered alloys. Moreover, the NCP-based results which predicted HCP→FCC transition upon

introducing 25 at.% Mg are supported by our predicted values for basal slip, which indicated CRSS of 121 and 658 MPa for Mg and Ti, respectively. Hence, this transition can be described as dissolution of Ti in FCC Mg. Therefore NCP seem to be useful and reliable in predicting properties of disordered alloys containing alkali and/or alkaline earth metals.

In summary, our theoretical results based on binding and formation energy of Ti-Mg solid solutions predicted for the first time that the solubility of up to 60 and 100 at.% Mg into Ti with the use of USP and NCP, respectively, to be thermodynamically favourable. However, both approaches predicted that such solid solubility extentions requires massive lattice expansions of Ti lattice, a condition only achievable at very high temperatures (increasing further the melting temperature difference between Ti and Mg). Evidently, this factor seems to be responsible for the limited solid solubility. Moreover, the challenge in dissolving an appreciable amount of Mg in Ti is also made difficult by the high coefficient of thermal expansion for the former. In line with our experimental findings, some of the obstacles to realisation of such solid solutions by ball milling process are the quick formation of metastable Ti hydrides and cold welding at early stages of BM prior to alloying.

Recommendations

Although formation of binary disordered Ti-Mg alloys is predicted to be thermodynamically favourable, suitable non-equilibrium processing techniques that are able to deposit each metal unto one another from different vapour sources, should be given more priority in synthesizing such solid solutions, for example, chemical vapour deposition.

It is more likely for these binary solid solutions to be formed from stable solid solution compounds such as mixed metal hydrides and oxides.

Stearic acid could be used as a safe source of H_2 in studying potential hydrogen storage materials, as it produces H^+ which yields HCP to FCT/FCC transition in Ti at room temperature.

References

Aghion E., Bronfin B. and Eliezer D., J. Mater. Process. Technol. **117** (2001) 381.

Aghion E., Bronfin B., Friedrich H. and Rubinovich Z, Magnesium Technology 2004 Ed. Luo AA in TMS (The Minerals, Metals & Materials Society), 2004.

Agnew S.R., Yoo M.H. and Tomé C.N., Acta Mater. **49** (2001) 4277.

Agnew S.R., Horton J.A. and Yoo M.H., Metall. Mater. Trans. A **33** (2002) 851.

Ahmadieh A., Mitchell J. and Dorn J.E., Trans. Metall. Soc. AIME **233** (1965) 1130.

Ahuja R., Wills J.M., Johansson B. and Eriksson O., Phys. Rev. B **48** (1993) 16269.

Ahuja R., Dubrovinsky L., Dubrovinskaia N., Guillen J.M.O., Mattesini M., Johansson B. and Le Bihan T., Phys. Rev. B **69** (2004) 184102.

Ahahama Y., Kawamura H. and Le Bihan T., Phys. Rev. Lett. **87** (2001) 275503.

Amirkhiz B.S., Zahiri B., Kalisvaart P. and Mitlin D., Inter. J. H. Energy **36** (2011) 6711.

Anusionwu BC. Physica B **311** (2002) 272.

Asada T. and Terakura K., Phys. Rev. B **47** (1993) 15992.

Asano K., Enoki H. and Akiba E., Mater. Trans. **48** (2007) 121.

Asano K., Enoki H. and Akiba E, J. Alloys Compd. **486** (2009a) 115.

Asano K., Enoki H. and Akiba E., J. Alloys Compd. **480** (2009b) 558.

Asano K., Enoki H. and Akiba E., J. Alloys Compd. **478** (2009c) 117.

Atou T., Hasegawa M., Parker L.J., and Badding J.V., J. Am. Chem. Soc. **118** *(*1996) 12104.

Bach F-W., Schaper M. and Jaschik C., Mater. Sci. Forum **419-422** (2003) 1037.

Badmos A.Y. and Bhadeshia H.K.D.H., Metall. Mater. Trans. A **28** (1997) 2189.

Bain E.G., Trans. AIME **70** (1924) 24.

Bao S., Tajima K., Yamada Y., Okada M. and Yoshimura K., Solar Energy Materials & Solar Cells **92** (2008) 224.

Banerjee R., Zhang X.-D., Dregia S.A. and Fraser H.L., Acta Mater. **47** (1999) 1153.

Barrett C.S. and Trautz O.R., Trans. AIME **175** (1948) 579.

Battaini M, PhD thesis, Monash University, 2008.

Becerra A. and Pekguleryuz M., J. Mater. Res. **23** (2008) 3379.

Becke A.D., Phys. Rev. A **38** (1988) 3098.

Benjamin J.S., Metall. Trans. **1** (1970) 2943.

Benjamin J.S., Scientific American **234** (1976) 40.

Benjamin J.S., Metal Powder Rep. **45** (1990) 122.

Benjamin J.S., Mater. Sci. Forum **88-90** (1992) 1.

Benjamin J.S. and Vollin T.E., Metall. Trans. **5** (1974) 1929.

Bhatia M.L., Singh A.K. and Nandy T.K., Intermetallics **4** (1996) 635.

Bhatia M.L., Singh A.K. and Nandy T.K., Intermetallics **6** (1998) 141.

Bhatia M.L. and Cahn R.W., Intermetallics **13** (2005) 474.

Bhattacharya B. and Niewczas M., Philos. Mag. **91** (2011) 2227.

Bialobrzeski A., Saja K. and Hubner K., Archives of Foundry Engineering **7** (2007) 11.

Bloch F., Z. Physik **57** (1929) 545.

Borsa D.M., Gremaud R., Baldi A., Schreuders H., Rector J.H., Kooi B., Vermeulen P., Notten P.H.L., Dam B. and Griessen R., Phys. Rev. B **75** (2007) 205408.

Boyer R.R., Advan. Perf. Mater. **2** (1995) 349.

Bracconi P., Andrès C., N'diaye A. and Pourcelot Y., Thermochimica Acta **429** (2005) 43.

Burgers W.G., Physica **1** (1934) 561.

Byun J.-S., Shim J.-H. and Cho Y.W., J. Alloys Compd. **365** (2004) 149.

Cahn R.W., Intermetallics **7** (1999) 1089.

Callister W.D. Jr., Fundamentals of Materials Science and Engineering, 5th Edition,John Wiley & Sons , Inc., USA, 2001.

Caspersen K.J. and Carter E.A., PNAS **102** (2005) 6738.

Ceperly D.M. and Alder B.J., Phys. Rev. Lett. **45** (1980) 566.

Chakraborty J., Kumar K., Ranjan R., Chowdhury S.G. and Singh S.R., Acta Mater. **59** (2011) 2615.

Chakravorty C.R., Bull. Mater. Sci. **17** (1994) 733.

Chandra U., Indian Journal of Pure & Applied Physics **45** (2007) 790.

Chang T-C., Wang J-Y., Chu C-L. And Lee S., Mater. Lett. **60** (2006) 3272.

Chattopadhyay P.P., Pabi S.K. and Manna I, Mater. Sci. Eng. A **304-306** (2001) 424.

Chavarria G.R., Physics Lett. A **336** (2005) 210.

Chen W., Yamamoto Y. and Peter W.H., Key Eng. Mater. **436** (2010) 123.

Chia T.L., Easton M.A., Zhu S.M., Gibson M.A., Birbilis N. and Nie J.F., Intermetallics **17** (2009) 481.

Choi Y.J., Lu J., Sohn H.Y. and Fang Z.Z., J. Power Sources **180** (2008) 491.

Choi H.J., Kim Y., Shin J.H. and Bae D.H., Mater. Sci. Eng. A **527** (2010) 1565.

Clendenen G.L. and Drickamer H.G., Phys. Rev. **135** (1964) A1643.

Cocco G., Delogu F. and Schiffini L, J. Mat. Synt. Process. **8** (2000) 167.

Cole G.S., Mater. Sci. Forum **419-422** (2003) 43.

Conrad H., Prog. Mater. Sci. **26** (1981) 123.

Coreño-Alonso O. and Coreño-Alonso J., Intermetallics **12** (2004) 117.

Coreño-Alonso O., Intermetallics **14** (2006) 475.

Counts W.A., Friák M., Raabe D. and Neugebauer J., Acta Mater. **57** (2009) 69.

Counts W.A., Friák M., Battaile C.C., Raabe D. and Neugebauer J., Phys. stat. sol. (b) **245** (2008) 2630.

Couret A. and Caillard D., Acta Metall. **33** (1985) 1447.

de Boer F.R., Boom R., Mattens W.C.M., Miedema A.R. and Niessen A.K., Cohesion in Metals: Transition Metals Alloys (North-Holland, Amsterdam, 1989).

Demazeau G, High Pressure Research **28** (2008) 483.

Dabhade V.V., Rama Mohan T.R. and Ramakrishnan P., Powder Technol. **171** (2007) 177.

David E., J. Achievements Mater. Manuf. Eng. **20** (2007) 87.

Duan W., Current Opinion in Solid State and Materials Science **10** (2006) 1.

Dubrovinskaia N., Dubrovinsky L., Kantor I., Crichton W.A., Dmitriev V., Prakapenka V., Shen G., Vitos L., Ahuja R., Johansson B., and Abrikosov I.A., Phys. Rev. Lett. **95** (2005) 245502.

Ducastelle F. "*Order and Phase Stability in Alloys*", Cohesion and Structure series, Vol. **3**, ed. by de Boer FR and Pettifor DG (North-Holland, Amsterdam, 1991).

El-Eskandarany M.S., Aoki K. and Suzuki K., J. Jpn Society of Power and Powder Metall. **38** (1991) 59.

El-Eskandarany M.S., J. Alloys Compd. **279** (1998) 263.

El-Eskandarany M.S., Itoh F., Aoki K. and Suzuki K., J. Non-Cryst. Solids **118** (1990)

729.
El-Eskandarany M.S., Mechanical alloying for fabrication of advanced engineering materials published by William Andrew Publishing, Norwich, New York, USA, 2001.
Elias C.N., Lima J.H.C., Valiev R. and Meyers M.A., JOM **60** (2008) 46.
Eto T., Endo S., Imai M., Katayama Y. and Kikegawa T., Phys. Rev. B **61** (2000) 14984.
Farangis B., Nachimuthu P., Richardson T.J., Slack J.L., Meyer B.K., Perera R.C.C. and Rubin M.D., Solid State Ionics **165** (2003) 309.
Feng J., Hennig R.G., Ashcroft N.W. and Hoffmann R., Nature **451** (2008) 445.
Feng H., Jia D. and Zhou Y., J. Mater. Process. Technol. **182** (2007) 79.
Fermi E., Z. Physik **48** (1928) 73.
Feynman R.P., Phys. Rev. **56** (1939) 340.
Fischer T.H. and Almlof J., J. Phys. Chem. **96** (1992) 9768.
Freeth W.E. and Raynor G.V., J. Inst. Metals **82** (1953) 575.
Friedrichs O., Sánchez-López J.C., López-Cartes C., Dornheim M., Klassen T., Bormann R. and Fernández A., et al 2006 Appl. Surf. Sci. **252** (2006) 2334.
Froes F.H., Ward-Close C.M. and Baeslack W., J. Advan. Mater. **25** (1993) 20.
Froes F.H.S., Suryanarayana C., Russell K. and Li C.-G., Mat. Sci. Eng. A **192/193** (1995) 612.
Froes F.H., Developments in Titanium P/M, http://www.webs1.uidaho.edu/imap/MPR%20Paper.pdf.
Frost P.D., Parris W.M., Hirsch L.L., Doig J.R. and Schwartz C.M.,Trans. Amer. Soc. Metals **46** (1954) 231.
Furui M., Xu C., Aida T., Inoue M., Anada H. and Langdon T.G., Mater. Sci. Eng. A **410-411** (2005) 439.
Furuya H., Matunaga S. and Kogizo N., Mater. Sci. Forum **419-422** (2003) 261.
Gan K. and Gu M., J. Mater. Process. Technol. **199** (2008) 173.
Ganeshan S., Shang S.L., Zhang H., Wang Y., Mantina M. And Liu Z-K., Intermetallics **17** (2009) 313.
Ganeshan S., Shang S.L., Wang Y. and Liu Z-K., Acta Mater. **57** (2009) 3876.
Gardiner R.W., Goodwin P.S., Dodd S.B. and Viney B.W., Advan. Perf. Mater. **3** (1996) 343.

Gasior W., Moser Z. and Pstruś J., J. Phase Equilibria **19** (1998) 568.

Gerasimov K.B., Konstanchunk I.G., Chizhik S.A. and Bobet, J.-L., Int. J. H Energy **34** (2009) 1916.

German R.M., Powder Metallurgy Science 2nd edition, published by Metal Powder Industries Federation, New Jersey, USA, 1994.

Ghosh G. and Olson G.B., Acta Mater. **50** (2002) 2655.

Gillan M.J., Computer Simulation in Materials Science, edited by Meyer M. and Poutikis V. (Dordrecht: Kluwer) p. 257 (1991).

Goumri-Said S. and Kanoun M.B., Comput. Mater. Sci. **43** (2007) 243.

Gleiter H., Acta Mater. **48** (2000) 1.

Gleiter H., NanoStructured Materials **6** (1995) 3.

Gray III G.T., Morris C.E. and Lawson A.C., in Titanium 92: Science and Technology, edited by Froes F.H. and Caplan I.L. (Warrendale, PA: Minerals Metals & Materials Society, 1993) 225.

Greeff C.W., Trinkle D.R. and Albers R.C., J. Appl. Phys. **90** (2001) 2221.

Gong J. and Wilkinson A.J., Acta Mater. **59** (2011) 5970.

Grosjean M-H., Zidoune M., Roué L., Huot J. and Schulz R., Electrochimica Acta **49** (2004) 2461.

Grube G., Zeppelin H.V. and Bumm H., Ztsch. Elektrochemie **40** (1934) 160.

Gubicza J., Kassem M. And Ungar T., Mat. Sci. Forum **443-444** (2004) 103.

Haferkamp H., Niemeyer M., Boehm R., Holzkkamp U., Jaschik C. and Kaese V., Mater. Sci. Forum **350/351** (2000) 31.

Hafner J, J. Phys. F **6** (1976) 1243.

Hafner J, Acta Mater. **48** (2000) 71.

Hall E.O., Proc. Phys. Soc. B **64** (1951) 747.

Harrison W.A., Electronic Structure and the Properties of Solids, edited by Freeman, San Francisco (1980).

Hauser F.E., Landon P.R. and Dorn J.E., Trans. ASM **48** (1956) 986.

Hellmann H., Einfukrung in die Quantumchemie (Deuticke, Leipzzig, 1937) p. 61 and 285.

Hennig R.G., Trinkle D.R., Bouchet J., Srinivasan S.G., Albers R.C. and Wilkins J.W.,

Nature Mater. **4** (2005) 129.
Herbstein F.H. and Averbach B.L., Acta Metall. **4** (1956) 407.
Herbstein F.H. and Averbach B.L., Acta Metall. **4** (1956) 414.
Hess J.B. and Barrett C.S., J. Met. **4** (1952) 645.
Hida M., Asai K., Takemoto Y. and Sakakibara A., Mat. Sci. Forum **235-238** (1997) 187.
Hill R., Proc. Phys. Soc. A **65** (1952) 349.
Hohenberg P. and Kohn W., Phys. Rev. B **136** (1964) 864.
Hu Q.M. and Yang R., Current Opinion in Solid State and Materials Science **10** (2006) 19.
Huang H., Huang K., Liu S., Chen D., Powder Technol. **198** (2010) 144.
Huang J.Y., Wu Y.K. and Ye H.Q., Appl. Phys. Lett. **66** (1995) 308.
Hult E., Andersson Y. and Lundqvist B.I., Phys. Rev. Lett. **77** (1996) 2029.
Hume-Rothery W., Raynor G.V. and Butchers E. J., Inst. Metals **71** (1945) 589.
Hume-Rothery W., Smallman R.E, Haworth C.W, Structure of Metals and Alloys. London: Institute of Metals (1969).
Huot J., Liang G., Boily S., Van Neste A. And Schuly R., J. Alloys Compd. **293** (1999) 495.
Huot J., Liang G., Schulz R., Appl. Phys. A **72** (2001) 187.
Hutchinson W.B. and Barnett M.R., Scripta Mater. **63** (2010) 737.
Hwang S., Nishimura C. and McCormick P.G., Mater. Sci. Eng. A **318** (2001) 22.
Iñiguez M.P. and Alonso J.A., J. Phys. F: **11** (1981) 2045.
Iñiguez M.P., Alonso J.A., González D.J. and Zorita M.L., J. Phys. F: **12** (1982) 1907.
Inoue A., Kawamura Y., Matsushita M., Hayashi K. and Koike J., J. Mater. Res. **16** (2001) 1894.
Jackson J.H., Frost P.D., Loonam A.C., Eastwood L.W. and Lorig C.H., Metals Trans. AIME **185** (1949) 149.
Jain I.P., Lal C. And Jain A., Inter. J. H Energy **35** (2010) 5133.
Jamieson J.C., Science **140** (1963) 72.
Jayaraman A., Klement Jr. W. And Kennedy G.C., Phys. Rev. **131** (1963) 644
Johnson D.F. and Carter E.A., J. Chem. Phys. **128** (2008) 104703.
Jomard G., Magaud L. and Pasturel A., Philos. Mag. B **77** (1998) 67.

Jona F and Marcus P.M, Phys. stat. sol. (b) **242** (2005) 3077.

Jones W.R.D. and Hogg G.V., J. Inst. Metals **85** (1956-7) 255.

Josell D., Shechtman D. and Van Heerden D., Mater. Lett. **22** (1995) 275.

Kalisvaart W.P., Wondergem H.J., Bakker F. and Notten P.H.L., J. Mater. Res. **22** (2007) 1640.

Kalisvaart W.P. and Notten P.H.L., J. Mater. Res. **23** (2008) 2179.

Kamrani S., Simchi A., Riedel R. and Seyed-Reihani S.M., Powder Metall. **50** (2007) 276.

Kamran S., Chen K., and Chen L., Phys. Rev. B **77** (2008) 094109.

Kamran S., Chen K., and Chen L., Phys. Rev. B **79** (2009) 024106.

Kelley E.W. and Hosford W.F. Jr., Trans. Metall. Soc. AIME **242** (1968) 654.

Kim S.K., Jona F. and Marcus P.M. J. Phys.: Condens. Matter **8** (1996) 25.

King H.W., J. Mater. Sci. **1** (1966) 79.

Kirillova M.M, Magnitskaya M.V, Makhnev A.A, Lobov I.D, Nomerovannaya L.V, Tsvyashchenko A.V and Fomicheva L.N, J. Experimental and Theoretical Physics **100** (2005) 983.

Kleinman L. and Bylander D.M., Phys. Rev. Lett. **48** (1982) 1425.

Koch C.C, Cavin O.B., McKamey C.G.and Scarbrough J.O., Appl. Phys. Lett., **43** (1983) 1017.

Koch C.C. and Whittenberger J.D., Intermetallics **4** (1996) 339.

Koch C.C., NanoStructured Materials **9** (1997) 13.

Kohanoff J. and Gidopoulos N.I., Density Functional Theory: Basics, New Trends and Applications Vol. 2, Part 5, Chapter 26, pp 532, in Hanbbook of Molecular Physics and Quantum Chemistry, John Wiley & Sons, Ltd, Chichester, 2003.

Kohn W. and Sham L.J., Phys. Rev. A **140** (1965) 1133.

Kohn W., Meir Y. and Makarov D.E., Phys. Rev. Lett. **80** (1998) 4153.

Kong Y., Li J.H., Kong L.T. and Liu B.X., Phys. Rev. B **72** (2005) 24209.

Korzhavyi P.A., Ruban A.V., Abrikosov I.A. and Skriver H.L., Phys. Rev. B **51** (1995) 5773.

Kovalev D.Y., Prokudina V.K., Ratnikov V.I. and Ponomarev V.I., Int. J. SHS **19** (2010) 253.

Kral M.V., Muddle B.C. and Nie J.F., Mater. Sci. Eng. A **460-461** (2007) 227.
Kresse G., Furthmüller J. and Hafner J., Phys. Rev. B **50** (1994) 13181.
Kutepov A.L. and Kutepova S.G., Phys. Rev. B **67** (2003) 132102.
Kwon S-N., Baek S-H., Mumm D.R., Hong S-H and Song M-Y., Int. J. H. Energy **33** (2008) 4586.
Kwon S-N., Hong S-H., Park H-R. and Song M-Y., Int. J. H. Energy **35** (2010) 13055.
Labusch R., Acta Metall. **20** (1972) 917.
Leu J-S., Chiang C-T., Lee S., Chen Y-H. and Chu C-L., J. Mater. Eng. Performance **19** (2010) 1235.
Leung T.C., Chan C.T., and Harmon B.N., Phys. Rev. B **44** (1991) 2923.
Levinson D.W., Acta Met. **3** (1955) 294.
Li J., Ngan A.H.W. and Gumbsch P., Acta Mater. **51** (2003) 5711.
Liang G. and Schulz R., J. Mater. Sci. **38** (2003) 1179.
Liang C.P. and Gong H.R., J. Alloys Compd. **489** (2010) 130.
Lieb E.H. and Oxford S., Int. J. Quantum Chem. **19** (1981) 427.
Lin C., Yang G.W. and Liu B.X., Phys. Rev. B **61** (2000) 15649.
Lin J.S., Qteish A., Payne M.C. and Heine V., Phys. Rev. B **47** (1993) 4174.
Liu B.X., Johnson W.L., Nicolet M.A. and Lau SS, J. Appl. Phys. **73** (1993) 2794.
Liu J.B., Li Z.F., Zhang J.X., Liu B.X., Kresse G. and Hafner J., Phys. Rev. B **64** (2001) 054102.
Liu J.B. and Johnson D.D., Phys. Rev. B **79** (2009) 134113.
Liu L.J. and Schlesinger M., Corrosion Science **51** (2009) 1733.
Liu Y., Chen L.F., Tang H.P., Liu C.T., Liu B. and Huang B.Y., Mater. Sci. Eng. A **418** (2006) 25.
Lofvander J.P.A., Dary F.-C., Ruschewitz U. and Levi C.G., Mater. Sci. Eng. A **202** (1995) 188.
Lu L. and Lai M.O., Materials & Design **16** (1995) 33.
Lu L., Lai M.O. and Zhang S., J. Mater. Process. Technol. **67** (1997) 100.
Lu L. and Zhang Y.F., J. Alloys Compd. **290** (1999) 279.
Luo A.A., Magnesium Technology 2001, Ed. Hryn J.N (Warrendale, PA: TMS, 2001) 89.
Luo A.A., JOM **54** (2002) 42.

Lynch R.W. and Edwards L.R., J. Appl. Phys. **41** (1970) 5135.

Ma E., Prog. Mater. Sci. **50** (2005) 413.

Ma E. and Atzmon M., Materials Chemistry and Physics **39** (1995) 249.

Manna I, Chattopadhyay PP, Banhart F, Fecht H-J., Appl. Phys. Lett. **22** (2002) 4136.

Manna I, Chattopadhyay PP, Banhart F, Fecht H-J., J. Appl. Phys. **93** (2003) 1520.

Mashkovetz V.P. and Puchkov L.V., Zh. Prikl. Chem. 1965, 1875.

Massalski T., Okamoto H., Subramanian P., Kacprzak L. (Eds.), Binary Alloy Phase Diagram, 2nd ed., American Society for Metals, Metals Park, OH, 1990.

Massalski T.B. (Ed.), Binary Alloy Phase Diagrams, ASM International, Metals Park (OH), 1992.

Mattsson A.E., Schultz P.A., Desjarlais M.P., Mattsson T.R. and Leung K., Modelling Simul. Mater. Sci. Eng., **13** (2005) R1.

Maurice D.R. and Courtney T.H., Metall. Trans. A **21** (1990) 289.

Maweja K., Phasha M.J. and Van der Berg N., Powder Technol. **199** (2010) 256.

McMahan A.K. and Moriarty J.A., Phys. Rev. B **27** (1983) 3235.

McMillan P.F., Chem. Soc. Rev. **35** *(*2006) 855.

Mehl M.J., Klein B.M., and Papaconstantopoulos D.A., Intermetallic Compounds: Vol. **1**, Principles. Edited by J.H. Westbrook and Fleischer R.L., 1994, John Wiley & Sons Ltd.

Meng X., Wu R., Zhang M., Wu L. and Cui C., J. Alloys Compd. **486** (2009) 722.

Meyer P.Y, Automotive Engineering (1992) 89.

Meyers M.A., Mishra A., Benson D.J., Prog. Mater. Sci. **51** (2006) 427.

Milman V., Winkler B., White J.A., Pickard C.J., Payne M.C., Akhmatskaya E.V. and Nobes R.H., Int. J. Quantum Chem. **77** (2000) 895.

Miraghaei S., Abachi P., Madaah-Hosseini H.R. and Bahrami A., J. Mater. Process. Technol. **203** (2008) 554.

Molladavoudi A., Amirkhanlou S., Shamanian M. and Ashrafizadeh F., Intermetallics **29** (2012) 104.

Monkhorst H.J. and Pack J.D., Phys. Rev. B **13** (1976) 5188.

Mordike B.L. and Ebert T., Mater. Sci. Eng. A **302** (2001) 37.

Moriarty J.A and McMahan A.K., Phys. Rev. Lett. **48** (1982) 809.

Morinaga M. and Yukawa H., Mater. Sci. Eng. A **329-331** (2002) 268.
Mousavi T., Karimzadeh F., Abbasi M.H., Enayati M.H., J. Mater. Process. Technol. **204** (2008) 125.
Mott N.F. and Jones H., The theory of the properties of metals and alloys (1936). Oxford: Clarendon Press.
Munroe N., Tan X. and Gu H., Scripta Metall. **36** (1997) 1383.
Nabarro F.R.N., Phil. Mag. **35** (1977) 613.
Nayeb-Hashemi AA, Clark JB, Pelton AD. Bull. Alloy Phase Diagrams **5** (1984) 365.
Nye J.F., Physical Properties of Crystals, Oxford University Press, Oxford, 1985.
Olijnyk H. and Holzapfel W.B., Phys. Rev. B **31** (1985) 4682.
Olijnyk H, Jephcoat AP. J. Phys.: Condens. Matter **12** (2000) 10423.
Orimo S. And Fujii H., Appl. Phys. A **72** (2001) 167.
Ozdemir I., Ahrens S., Mücklich S., Wielage B., J. Mater. Process. Technol. **205** (2008) 111.
Paidar V., Mater. Sci. Eng. A **481-482** (2008) 243.
PalloneE.M.J.A., Trombini V., Botha, W.J. and Tomasi F.R., J. Mater. Process. Technol. **143-144** (2003) 185.
Parker L.J, Atou T, Badding J.V, Science **273** (1996) 95.
Paxton A.T., Methfessel M. and Pettifor D.G., Proc. R. Soc. Lond. A **453** (1997) 1493.
Paxton A.T., Methfessel M. and Polatogiou H.M., Phys. Rev. B **41** (1990) 8127.
Payne M.C., Teter M.P., Allan D.C., Ariar T.A. and Joannopoulos J.D., Rev. Mod. Phys. **64** (1992) 1045.
Perdew J.P., Burke K. and Ernzerhof M., Phys. Rev. Lett. **77** (1996) 3865.
Perdew J.P. and Wang Y., Phys. Rev. B **45** (1992) 13244.
Perdew J.P., Phys. Rev. B, **33** (1986) 8822.
Perdew J.P. and Zunger A., Phys. Rev. B **23** (1981) 5048.
Perdew J.P., Burke K. and Ernzerhof M., Phys. Rev. Lett. **78** (1996) 1396.
Perdew J.P. and Wang Y., Phys. Rev. B **33** (1986) 8800.
Perdew J.P., Nogueira F. and Fiolhais C., J. Molecular Structure (Theochem) **501-502** (2000) 261.
Perez-Albuerne E.A., Clendenen R.L., Lynch R.W. and Drickamer H.G., Phys. Rev. **142**

(1966) 392.
Petch N.J., Iron Steel Inst. **174** (1953) 25.
Pettifor D.G., J. Phys. C **3** (1970) 367.
Pezda J., Advan. Manufac. Sci. Technol. **33** (2009) 55.
Phasha M.J., Ngoepe P.E., Chauke H.R., Pettifor D.G. and Nguyen-Mann D., Intermetallics **18** (2010a) 2083.
Phasha M.J., Maweja K. and Babst C., J. Alloys Compd. **492** (2010b) 201.
Phasha M.J., Bolokang A.S. and Ngoepe P.E., Mater. Lett., **64** (2010c) 1215.
Phillips J.C. and Kleinman L., Phys. Rev. **116** (1959) 287.
Polmear I.J., *Light Metals: Metallurgy of the Light Metals*, 3rd ed., Edward Arnold, London, 1995.
Prakapenka V., Shen G., Vitos L., Ahuja R., Johansson B., and Abrikosov I.A., Phys. Rev. Lett. **95** (2005) 245502.
Pugh S.F., Philos. Mag. **45** (1954) 823.
Pulay P., Molec. Phys. **17** (1969) 197.
Punz G. And Hafner J., Z. Phys. B – Condens. Matter **65** (1987) 465.
Qu Z., Liu X., Wu R. and Zhang M., Mater. Sci. Eng. A **527** (2010) 3284.
Rajput S.S., Prasad R. and Singru R.M., J. Phys. Condens. Matter **5** (1993) 6419.
Ram S., Acta Mater. **49** (2001) 2297.
Rappe A.M. and Joannopoulos J.D., Computer Simulation in Materials Science, edited by Meyer M. and Poutikis V. (Dordrecht: Kluwer) p. 409 (1991).
Reddy L.K., Principles of Engineering Metallurgy, 2nd edition, 2008.
Reed-Hilland R.E. and Robertson W.D., Trans. Metall. Soc. AIME **209** (1957) 496.
Roth W.L., Phys. Rev. **110** (1958) 1333.
Rousselot S., Bichat M.P., Guay D., Roué L., J. Power Sources **175** (2008) 621.
Sahu B.R., Mater. Sci. Eng. B **49** (1997) 74.
Sakintuna B., Lamari-Darkrim F. And Hirscher M., Inter. J. H. Energy **32** (2007) 1121.
Salo P.T. and Kokko K., J. Phys. Condens. Matter **5** (1993) 3325.
Sandim H.R.Z., Morante B.V. and Suzuki P.A., Mater. Res. **8** (2005) 293.
Saunders N., CALPHAD **14** (1990) 61.
Schaffer. G.B. and McCormick P.G., Mat. Sci. Forum **16** (1992) 91.

Schwarzer R.A., Micron **28** (1997) 249.

Seelam U.M.R. and Suryanarayana C., J. Appl. Phys. **105** (2009) 063524.

Seelam U.M.R., Barkhordarian G. and Suryanarayana C., J. Mater. Res. **24** (2009) 3454.

Segall M.D., Lindan P.J.D., Probert M.J., Pickard C.J., Hasnip P.J., Clark S.J. and Payne M.C., J. Phys.: Condens. Matter **14** (2002) 2717.

Senkov O.N., Cavusoglu M. and Froes F.H.S., J. Alloys Compd. **297** (2000) 246.

Shao H., Asano K., Enoki H. And Akiba E., Scripta Mater. **60** (2009) 818.

Shechtman D., Van Heerden D. and Josell D., Mater. Lett. **20** (1994) 329.

Sheikh K.A., Kang Y.B., Rouse J.J. and Eccleston G.M., Int. J. Pharm. **411** (2011) 121.

Shtremel M.A., Metal Science and Heat Treatment **44** (2002) 324.

Sikka S.K., Vohra Y.K. and Chidambaram R., Prog. Mater. Sci. **27** (1982) 245.

Singh A.K., Bull. Mater. Sci. **5** (1983) 219.

Snider T.S and Badding J.V, Solid State Commun. **131** (2004) 157.

Sort J., Nogués J., Suriñach S. And Baró M.D., Philos. Mag. **83** (2003) 439.

Song M-Y., J. Mater. Sci. **30** (1995) 1343.

Song M-Y., Ahn D-S., Kwon I-H. And Ahn H-J., Metals and Materials **5** (1999) 485.

Song M-Y., Baek S-H., Bobet J-L., Kwon S-N. And Hong S-H., J. Mater. Sci. **44** (2009) 4827.

Süleyman E., van Setten M.J., de Wijs G.A. and Brocks G., J. Phys.: Condens. Matter **22** (2010) 074208.

Šob M., Friák M., Legut D., Fiala J. and Vitek V., Mater. Sci. Eng. A **387-389** (2004) 148.

Sun F. And Froes F.H.S., J. Alloys Compd. **340** (2002) 220.

Sundaresan R. and F.H. Froes F.H., Key Eng. Mater. **29–31** (1988) 199.

Suryanarayana C. and Froes F.H., J. Mater. Res. **5** (1990) 1880.

Suryanarayana C., Ivanov E. and Boldyrev V.V., Mater. Sci. Eng. A **304-306** (2001) 151.

Suryanarayana C., Prog. Mater. Sci. **46** (2001) 1.

Tanaka H., Yamada T., Sato E. and Jimbo I., 2006 Scripta Mater. **54** (2006) 121.

Tanigawa S. and Doyama M., J. Phys. F: **2** (1972) L95.

Tanigawa S. and Doyama M., J. Phys. F **3** (1973) 977.

Taylor RH, Curtarolo S, Hart GLW. Phys. Rev. B **81** (2010) 024112.

Tegner B.E. and Ackland G.J., Comput. Mater. Sci. **52** (2012) 2.

Tepper T., Shechtman D., Van Heerden D. and Josell D., Mater. Lett. **33** (1997) 181.

Thomas L.H., Proc. Camb. Phil. Soc. **23** (1927) 542.

Todaka Y., Sasaki J., Moto T. and Umemoto M., Scripta Mater. **59** (2008) 615.

Tonda H. and Ando S., Metall. Mater. Trans. A **33** (2002) 831.

Trinkle D.R, Hennig R.G, Srinivasan S.G, Hatch D.M, Jones M.D, Stokes H.T, Albers R.C, Wilkins J.W, Phys. Rev. Lett. **91** (2003) 025701.

Troullier N. and Martins J.L., Phys. Rev. B **43** (1991) 1993.

Turchi PEA. "*Electronic Theories of Alloy Stability*", in Intermetallic Compounds: Principles and Practice, Vol. **1**, Chap. 2, ed. by Westbrook JH and Fleischer RL (John Wiley & Sons, Ltd., New York, 1995).

Tyson W., Acta Metall. **15** (1967) 574.

Uesugi T., Kohyama M., Kohzu M. and Higashi K., Mater. Sci. Forum **350-351** (2000) 49.

Uesugi T., Kohyama M., Kohzu M. and Higashi K., Mater. Trans. **42** (2001) 1167.

Uesugi T. and Higashi K., Mater. Sci. Forum **488-489** (2005) 131.

Urretavizcaya G., Garcia G., Serafini D. and Meyer G., Latin American Applied Research **32** (2002) 289.

Usikov M.P. and Zilbershtein V.A., Phys. Stat. Sol. (a) **19** (1973) 53.

Vaks V.G. and Trefilov A.V., J. Phys. F: Met. Phys. **18** (1988) 213.

Vanderbilt D., Phys. Rev. B **41** (1990) 7892.

Van Heerden D., Josell D. and Shechtman D., Acta Mater. **44** (1996) 297.

Vegard L, Z. Physik, **5** (1921) 17.

Vermeulen P., Niessen R.A.H. and Notten P.H.L., Electrochem. Commun. **8** (2006) 27.

Vermeulen P., PhD Thesis (2009), Technische Universiteit Eindhoven.

Vohra Y.K., Sikka S.K., Vaidya S.N. and Chidambaran R., J. Phys. Chem. Solids **38** (1977) 1293.

Vohra Y.K. and Spencer P.T., Phys. Rev. Lett. **86** (2001) 3068.

Vullum E., Pitt M., Walmsley J., Hauback B. and Holmestad R., Appl. Phys. A **94** (2009)

787.
Wang J., Wen H. and Desai D., Eur. J. Pharm. Biopharm. **75** (2010) 1.
Ward-Close C.M. and Partridge P.G., Mater. Lett. **11** (1991) 295.
Ward-Close C.M., Lu G., and Partridge P.G., Mat. Sci. and Eng. A**189** (1994) 247.
Ward Flynn P., Mote J. and Dorn J.E., Trans. Metall. Soc. AIME **221** (1961) 1148.
Warren B, X-ray Diffraction, Addison-Wesley Publishing, Massachusetts (1969) 253.
Wassermann G., Metallwirtsch **11** (1932) 61.
Wentzovitch R.M. and Cohen M.L., Phys. Rev. B **37** (1988) 5571.
Williamson G.K. and Hall W.H., Acta Metall. **1** (1953) 22.
Wilkes D.M.J., Goodwin P.S., Ward-Close C.M., Bagnall K. and Steeds J., Mater. Lett. **27** (1996) 47.
Winkler B., Juarez-Arellano E.A., Friedrich A., Bayarjargal L., Yan J. and Clark S.M., J. Alloys Compd. **478** (2009) 392.
Wu R. and Zhang M., Mater. Sci. Eng. A **520** (2009) 36.
Wu R.Z., Qu Z.K. and Zhang M.L., Rev. Adv. Mater. Sci. **24** (2010) 35.
Wyss R.K., Advances in Magnesium Alloys and Composites, edited by H. Paris and W.H. (The Minerals and Metals and Materials Society, Warrendale, Pennsylvania, 1988) p. 25.
Yamakov V., Wolf D., Phillpot S.R. and Gleiter H., Acta Mater. **50** (2002) 61.
Yoo M.H., Metall.Trans. A **12** (1981) 409.
Yoshinaga H., Obara T. and Morozumi S., Mater. Sci. Eng. **12** (1973) 255.
Zakeri M., Allahkarami M., Kavei G., Khanmohammadian A., Rahimipour M.R., J. Mater. Process. Technol. **209** (2009) 96.
Zaluska A., Zaluski L. and Ström-Olsen J.O., J. Alloys Compd. **288** (1999) 217.
Zeng Q.-S., Ding Y., Mao W.L., Luo W., Blomqvist A., Ahuja R., Yang W., Shu J., Sinogeikin S.V., Meng Y., Brewe D.L., Jiang J.-Z. and Mao H.-k., PNAS **106** (2009) 2515.
Zeppelin F., Reule H. And Hirscher M., J. Alloys Compd. **330** (2001) 723.
Zhang D.L., Prog. Mat. Sci., **49** (2004) 537.
Zhang Y.F., Lu L. and Yap S.M., Mater. Process. Technol. **89–90** (1999) 260.
Zhang Y., Tsushio Y., Enoki H. and Akiba E., J. Alloys Compd. **393** (2005) 147.

Zhang H., Shang S.L., Saal J.E., Saengdeejing A., Wang Y., Chen L.-Q. and Liu Z.-K, Intermetallics **17** (2009) 878.

Zhang Z., Dallek S., Vogt R., Li Y., Topping T.D., Zhou Y., Schoenung J.M. and Lavernia E.J., Metall. Mater. Trans. A **41** (2010) 532.

Zheng J.G., Partridge P.G., Steeds J.W., Wilkes D.M.J. and Ward-Close C.M., J. Mater. Sci. **32** (1997) 3089.

Zhou E., Suryanarayana C. and Froes F.H., Mater. Lett. **23** (1995) 27.

Zidoune M., Grosjean M.-H., Roué L., Huot J. and Schulz R., Corrosion Science **46** (2004) 3041.

Zilbershtein V.A. Nosova G.I. and Estrin E.I., Fiz. Met. Metalloved. **35** (1973) 584.